

**PROCESS-STRUCTURE-PROPERTY RELATIONSHIPS IN
SELECTIVE LASER MELTING OF AEROSPACE ALLOYS**

Process-Structure-Property Relationships in Selective Laser Melting of Aerospace Alloys

By

Mostafa Yakout Mohamed, B.Sc., M.Sc.

A Thesis

Submitted to the School of Graduate Studies in Partial Fulfillment of the Requirements
for the Degree Doctor of Philosophy

McMaster University

© Copyright by Mostafa Yakout Mohamed, April 2019

DOCTOR OF PHILOSOPHY (2019)

McMaster University

(Mechanical Engineering)

Hamilton, Ontario

TITLE: Process-Structure-Property Relationships in Selective
Laser Melting of Aerospace Alloys

AUTHOR: Mostafa Yakout Mohamed
B.Sc. in Production Engineering (Alexandria University)
M.Sc. in Production Engineering (Alexandria University)

SUPERVISORS: Dr. M. A. Elbestawi
Dr. Stephen C. Veldhuis

NUMBER OF PAGES: XXVIII, 248

In memory of my grandfather

A. Elkastawy (1919-1994)

To my beloved mother

Mrs. Alia Elkastawy

We are at the very beginning of time for the human race. It is not unreasonable that we grapple with problems. But there are tens of thousands of years in the future. Our responsibility is to do what we can, learn what we can, improve the solutions, and pass them on.

- Richard Feynman (1918-1988)

Preface

This book is the integrated article thesis, known as a sandwich thesis, of **Mostafa Yakout Mohamed**, the sole author. The sole author is inclined to use **Mostafa Yakout** as his formal name in publications. The book consists of eight main chapters and presents the experimental and analytical work carried out by the sole author at McMaster University from 2015 to 2019. The sole author received his B.Sc. in Production Engineering from Alexandria University, where he was ranked the first among the class of 2010. He obtained his M.Sc. from the same university in 2013. He is a member of the Canadian Society for Mechanical Engineering (CSME), Ontario Society of Professional Engineers (OSPE), American Society of Mechanical Engineers (ASME), and International Institute of Acoustics and Vibrations (IIAV). He is a voting member of the American Society for Testing and Materials (ASTM): Committee F42 on Additive Manufacturing and Committee A01 on Steel, Stainless Steel and Related Alloys.

This thesis contributes to the selective laser melting of three selected aerospace alloys: Invar 36, stainless steel 316L, and Ti-6Al-4V. It is a compilation of seven peer-reviewed journal articles and one conference proceeding, written in accordance with the regulation stipulated by the School of Graduate Studies at McMaster University. All experiments and analyses have been done by the sole author. Advice and guidance have been provided by the academic supervisors, Dr. M. A. Elbestawi and Dr. Stephen C. Veldhuis. Assist from colleagues at McMaster University has been provided: A. Cadamuro assisted me during the density measurements reported in Section 2.4.3 and Dr. S. Nangle-Smith provided help on the boundary conditions of the heat transfer model presented in Section 7.2.2. Any information presented from outside sources has been cited where appropriate.

Chapter 1 provides an introduction and is partially reprinted from one journal review paper; Chapters 2-7 are reprinted from six journal papers; and Chapter 8 presents conclusions and closing remarks.

The author has been involved in a side project on additive manufacturing of composite materials, that resulted in one book chapter and one conference proceeding. The work done on these side projects influenced the knowledge provided in the introductory chapter of this thesis and it is thus worthwhile to enumerate these works here. The book chapter is co-authored with Eskandar Fereiduni, first author, and Dr. M. A. Elbestawi, third author, while the conference proceeding is co-authored with Dr. M. A. Elbestawi, second author. Neither the book chapter nor the conference proceeding are presented in this thesis.

I declare that this thesis has been composed solely by myself and that no part of this book has been submitted for a higher degree at any other institution.

Mostafa Yakout

February 2019

Abstract

Metal additive manufacturing can be used for producing complex and functional components in the aerospace industry. This thesis deals with the process-structure-property relationships in selective laser melting of three aerospace alloys: Invar 36, stainless steel 316L, and Ti-6Al-4V. These alloys are weldable but hard to machine, which make them good candidates for the selective laser melting process. Invar 36 has a very low coefficient of thermal expansion because of its nickel concentration of 36% and stainless steel 316L contains 16-18% chromium that gives the alloy a corrosion resistance property. Ti-6Al-4V offers high strength-to-weight ratio, high biocompatibility, and outstanding corrosion resistance. Any changes in the chemical composition of these materials could affect their performance during application. In this thesis, a full factorial design of experiments is formulated to study a wide range of laser process parameters. The bulk density, tensile mechanical properties, fractography, microstructure, material composition, material phases, coefficient of thermal expansion, magnetic dipole moments, and residual stresses of the parts produced are experimentally investigated. An optimum process window has been suggested for each material based on experimental work. The thermal cycle, residual stresses, and part distortions are examined using a thermo-mechanical finite element model. The model predicts the residual stress and part distortion after build plate removal. The thesis introduces two laser energy densities for each material: brittle-ductile transition energy density, E_T , and critical laser energy density, E_C . Below the brittle-ductile transition energy density, the parts exhibited void formation, low density, and brittle fracture. Above the critical energy density, the parts showed vaporization of some alloying elements that have low boiling temperatures. Additionally, real-time measurements were taken using a pyrometer and a high-speed camera during the selective laser melting process. The trends found in the numerical results agree with those found experimentally.

Acknowledgments

Albert Einstein once said, “Wisdom is not a product of schooling but of the lifelong attempt to acquire it.” And so, I am very grateful that both of my co-supervisors, Dr. Mo Elbestawi and Dr. Stephen Veldhuis, acquired wisdom from lifelong attempt. Dr. Mo Elbestawi has been a role model for me in which he amazes me with his commitments, publications and experimental findings review, and research outcomes discussions. Since I started my program under his supervision, I found that whenever I go to his office with a problem or a challenge, I leave the office with a solid solution. I would also like to thank Dr. Stephen Veldhuis for always being available to provide me with research guidance and discuss challenges that have come up over the years. Together, both supervisors provided me with all the tools to work independently and to start a career in the field of manufacturing engineering.

I am also so grateful to the members of my supervisory committee, Dr. Saeid Habibi and Dr. Hatem Zurob, for their valuable and constructive feedback. In addition, this thesis would not have been possible without the encouragement of my cheerful colleagues in the Additive Manufacturing Group (AMG) at McMaster University. I also thank my former supervisor, Dr. Ahmed Elkhatib, whose encouragement has led me to where I am now.

Words fail me to express my deepest appreciation to family and friends. I thank my sweetheart mother who is unconditionally always there for me and never gives up. No success would be achieved without the support and love of my sister and brother. I would like also to thank my grandma, auntie, and uncles who played a vital role in my life. I finally thank my friends for their encouragement and company during such a challenging time as they always made me feel at home.

Contents

	Page
Preface	v
Abstract	vii
Acknowledgments	viii
Contents	ix
List of Figures	xvii
List of Tables	xxv
1 Introduction and Background	1
1.1 A Note to the Reader.....	2
1.2 Literature Review.....	2
1.2.1 Metal Additive Manufacturing Processes.....	2
1.2.2 Applications of Metal Additive Manufacturing	5
1.2.2.1 Aerospace Industry.....	5
1.2.2.2 Automotive Industry	6
1.2.2.3 Tooling Industry.....	6
1.2.2.4 Healthcare Industry	7
1.2.3 Materials Used in This Study	8
1.2.4 Quality of Additive Manufacturing Parts	9

1.2.4.1	Residual Stresses	10
1.2.4.2	Void Formation	12
1.3	Motivation.....	14
1.4	Research Objectives.....	14
1.5	Thesis Outline	15
1.6	References.....	17
2	Selective Laser Melting of Invar 36.....	27
2.1	Introduction.....	31
2.2	Research background	32
2.2.1	Metal additive manufacturing processes	32
2.2.2	Process parameters of selective laser melting (SLM).....	34
2.2.3	Density of additive manufacturing parts.....	35
2.3	Experimental design.....	37
2.3.1	Design range for the SLM process parameters.....	37
2.3.2	Experimental design for the SLM process parameters	40
2.4	Experimental work.....	42
2.4.1	Material and machine	42
2.4.2	SLM processing.....	42
2.4.3	Density measurement	43
2.4.4	Surface microstructure and material composition	44
2.5	Results and discussion	45
2.5.1	Density of selective laser melted Invar 36.....	45
2.5.2	Surface microstructure.....	49
2.5.3	Material composition.....	53

2.5.4	Effect of laser energy density	54
2.5.5	Recommended sets of SLM process parameters for Invar 36	56
2.6	Conclusions.....	57
2.7	References.....	58
3	Selective Laser Melting of Stainless Steel 316L	63
3.1	Introduction.....	67
3.2	Selective laser melting process	68
3.3	Experimental work.....	72
3.3.1	Part design	72
3.3.2	Material and machine	73
3.3.3	Geometrical measurements.....	76
3.3.4	Surface microstructure and material composition	77
3.3.5	Phase identification and residual stress measurements	77
3.4	Results and discussion	79
3.4.1	Profile errors of samples.....	79
3.4.2	Surface microstructure.....	80
3.4.3	Material composition.....	82
3.4.4	Phase identification	85
3.4.4.1	Phase identification using XRD method	85
3.4.4.2	Phase identification using selective etching method	85
3.4.5	Residual stress	88
3.4.5.1	Horizontal residual stress	88
3.4.5.2	Vertical residual stress	90
3.5	Conclusions.....	98

3.6	References.....	99
4	Residual Stresses and Mechanical Properties of Invar 36 and Stainless Steel 316L Produced Using Selective Laser Melting	107
4.1	Introduction.....	112
4.2	Materials and methods	115
4.2.1	Feedstock materials and SLM apparatus	115
4.2.2	Density measurement	118
4.2.3	Tensile testing.....	118
4.2.4	Microscopic residual stress measurement	119
4.2.5	Macroscopic residual stress measurement.....	121
4.2.6	Fractography analysis	124
4.3	Results and discussion	124
4.3.1	Part density	124
4.3.1.1	Part density as a function of the laser process parameters	125
4.3.1.2	Part density as a function of the laser energy	128
4.3.2	Tensile mechanical properties	131
4.3.3	Microscopic residual stress via XRD method	137
4.3.4	Macroscopic residual stress via cantilever method	141
4.3.5	Fractography and material composition analyses.....	146
4.3.6	Optimum SLM process parameters for Invar 36 and SS 316L.....	149
4.4	Conclusions.....	151
4.5	References.....	152

5	Thermal Expansion and Metallurgical Changes Associated with Selective Laser Melting of Invar 36 and Stainless Steel 316L	157
5.1	Introduction.....	160
5.2	Experimental procedures	162
5.2.1	Feedstock materials	162
5.2.2	Selective laser melting processing.....	164
5.2.3	Microstructural analysis and phase identification	164
5.2.4	Magnetic and thermal testing	165
5.3	Experimental results.....	166
5.3.1	Powder characterization	166
5.3.2	Microstructural characterization.....	168
5.3.3	Material composition.....	171
5.3.4	Crystallographic characterization.....	172
5.3.5	Coefficient of thermal expansion	173
5.3.6	Magnetic dipole moment.....	179
5.4	Discussion.....	180
5.4.1	Void formation	180
5.4.2	Vaporization phenomenon.....	182
5.4.3	Thermal expansion variation	184
5.5	Conclusions.....	185
5.6	References.....	186
6	Thermal Expansion and Residual Stresses During Selective Laser Melting of Ti-6Al-4V	195
6.1	Introduction.....	198

6.2	Experimental work.....	200
6.2.1	Feedstock, test samples, and methods	200
6.2.2	Density measurement	204
6.2.3	Thermal expansion measurement	204
6.2.4	Part deflection characterization	205
6.2.5	Residual stress characterization.....	205
6.2.6	Metallurgical analysis.....	206
6.3	Results and analysis	206
6.3.1	Part density	206
6.3.2	Thermal expansion	207
6.3.3	Part deflection.....	211
6.3.4	Residual stress	213
6.3.5	Internal microstructures	215
6.4	Discussion.....	216
6.4.1	Process-Property relationship	216
6.4.2	Process-Structure relationship	218
6.5	Conclusions.....	220
6.6	References.....	220
7	Residual Stresses and Dimensional Distortions During Selective Laser Melting of Invar 36, Stainless Steel 316L, and Ti-6Al-4V	225
7.1	Introduction.....	228
7.2	Methodology	230
7.2.1	Test parts and experiments	230
7.2.2	Model development and boundary conditions.....	232

7.3	Results.....	235
7.3.1	Thermal cycle	235
7.3.2	Dimensional distortion	237
7.3.3	Residual stress evolution	238
7.4	Discussion and conclusions	239
7.5	References.....	242
8	Conclusions and Closing Remarks	245

List of Figures

Figure 1.1: Adhesion and bonding methods in additive manufacturing [1].	4
Figure 1.2: Selective laser melting process [8, 9].	4
Figure 1.3: Stress distributions within a cross-section [75].	10
Figure 2.1: Effect of nickel content on the coefficient of thermal expansion (CTE) [1].	31
Figure 2.2: Overview of a typical selective laser melting process. [10, 13, 14]	33
Figure 2.3: Illustration of the SLM process parameters. (a) Top view and (b) side view of a build layer.	35
Figure 2.4: The energy ratio e at different parameter sets of (a) laser power, (b) scanning speed, (c) hatch spacing, (d) stripe width, and (e) stripe overlap. Each plot shows the parameter sets available for Invar 36 (from reference [7]), maraging steel, as well as the designed sets in the current study.	41
Figure 2.5: (a) The first build plate with the groups that caused vibrations. (b) The second build plate after deactivating the groups at the boundaries.	43
Figure 2.6: Influence of the SLM process parameters on the relative density of Invar 36. (a) Laser power. (b) Scanning speed. (c) Hatch spacing. (d) Laser energy density. (e) Stripe width. (f) Stripe overlap.	47
Figure 2.7: Influence of the SLM process parameters on the relative density of Invar 36. (a) Laser power and scanning speed. (b) Scanning speed and hatch spacing. (c) Laser power and hatch spacing.	50
Figure 2.8: Microstructures of the <i>side</i> surfaces of some cubes at (a) low energy density with more voids (cube CL5), (b) energy density required for maraging steel (cube EB3), (c) optimum energy density with less voids (cube BD5), and (d) high energy density with no voids but geometrical distortion (cube BA5).	51
Figure 2.9: Microstructures of the <i>top</i> surfaces of some cubes at (a) low energy density with more voids (cube CO4), (b) energy density required for maraging steel (cube CD3), (c) optimum energy density with less voids (cube CC1), and (d) high energy density with no voids but geometrical distortion (cube CA5).	52

Figure 2.10: Microstructures of (a) virgin Invar 36 powder, (b) Invar 36 powder after one build, and (c) maraging steel powder after many builds.....	53
Figure 2.11: Relationship between the optimum laser energy density and the quality of the parts produced.....	55
Figure 2.12: Effect of laser energy density on the relative density of the parts produced for different sets of SLM process parameters.....	57
Figure 3.1: Overview of a typical selective laser melting (SLM) process [24].	69
Figure 3.2: The SLM process parameters. (a) Top view and (b) side view of a build layer [24].	71
Figure 3.3: A simplified airfoil blade.	72
Figure 3.4: Dimensions of the designed samples and build plate.	73
Figure 3.5: Laser scanning strategies in the SLM process. (a) Meander, (b) stripe, (c) chessboard, and (d) spiral.	75
Figure 3.6: Profile error of an airfoil blade.....	76
Figure 3.7: An airfoil blade (a sample) after cutting.....	77
Figure 3.8: XRD diffractogram of a “typical” austenitic steel (γ -Fe) structure extracted from Mercury software version 3.0 (build RC5).	77
Figure 3.9: The measured (a) surfaces, (b) points along the top surface, (c) points along the side surface 1, and (d) points along the side surface 2.....	78
Figure 3.10: Microstructures of the <i>side</i> surfaces of some samples showing (a) large particles sticking on the surface, (b) vertical lines perpendicular to the scanning direction, (c) surface voids and partially melted powders, and (d) cracks between subsequent layers.	82
Figure 3.11: Microstructures of the <i>side</i> surfaces of five samples (1, 3, 5, 7, and 8) from each group.....	83
Figure 3.12: (a) Microstructure of a selected area of interest and (b) EDS spectrum of the selected area.....	84

Figure 3.13: XRD diffractograms of two different locations. (a) Top surface. (b) Side surface.....	85
Figure 3.14: Micrographs of the <i>etched</i> (a) top surface and (b) side surface at low magnification.	86
Figure 3.15: Micrographs of the <i>etched</i> (a) top surface and (b) side surface at high magnification.	87
Figure 3.16: Microstructures of the <i>etched</i> (a) top surface and (b) side surface.....	88
Figure 3.17: Horizontal residual stress along the top surface. (a) Maximum principal stress. (b) Minimum principal stress.....	90
Figure 3.18: (a) Trend of horizontal residual stress along the top surface, (b) effect of the scan track on the horizontal residual stress, and (c) effect of the surface hardening on the residual stress.....	90
Figure 3.19: Directions and magnitudes of principal residual stresses along the vertical direction of samples in group A.....	91
Figure 3.20: Measurement directions for studying the residual stress evolution.....	92
Figure 3.21: Directions and magnitudes of principal residual stresses along the vertical direction of samples in group B.	92
Figure 3.22: Evolution of the vertical residual stress along the build direction.....	94
Figure 3.23: Evolution of the vertical residual stress along the scanning direction.....	95
Figure 3.24: Evolution of the vertical residual stresses along the build plate (B1 is located at the top side of the build plate, B5 is located at the center, and B9 is located at the bottom side).	96
Figure 3.25: Effect of (a) part location on the build plate, (b) build direction, and (c) scanning direction on the quality of the parts produced.	97
Figure 4.1: Illustration of selective laser melting process parameters [2].	115
Figure 4.2: (a, c) Differential and cumulative powder size distribution and (b, d) morphology of powders used in this study: (a, b) Invar 36 and (c, d) SS 316L.	116

Figure 4.3: Illustration of the (a) SLM cantilever showing the coordinate measuring machine (CMM) measurement locations in one side of the cantilever “red points” and (b) deflected cantilever after residual stress relief.....	118
Figure 4.4: Illustration of the (a) measured points along the top and lateral surfaces and (b) relative position between the X-ray source, detector and sample.....	120
Figure 4.5: Directions of maximum and minimum residual stresses from the (a) top and (b) lateral surfaces measurements.....	121
Figure 4.6: Mesh shape, size and configuration of the numerical model in this study...	123
Figure 4.7: Estimation of relieved residual stress via finite element method: (a) cantilever deflection distribution (CMM results), as well as residual stress distribution along (b) Z-direction, (c) X-direction, and (d) Y-direction.....	123
Figure 4.8: Relative density as a function of laser energy density for the production of (a) Invar 36, (b) SS 316L samples by selective laser melting.	125
Figure 4.9: Contour plots for the relative density of (a) Invar 36 and (b) SS 316L. The plots show the effect of laser power and scanning speed on the relative density at constant hatch spacings of 0.08, 0.10, and 0.12 mm.	126
Figure 4.10: Stress-strain curves for (a) Invar 36, (b) SS 316L parts manufactured at various laser energy density levels.	132
Figure 4.11: Ultimate tensile strength and yield strength of (a) Invar 36, (b) SS 316L parts produced at various laser energy densities.....	133
Figure 4.12: Maximum elongation at break of (a) Invar 36, (b) SS 316L parts produced at various laser energy densities.	133
Figure 4.13: Approximate modulus of resilience and modulus of toughness of (a) Invar 36, (b) SS 316L parts produced at various laser energy densities.	134
Figure 4.14: Horizontal and vertical principal residual stresses induced in (a) Invar 36 and (b) SS 316L samples produced at various laser energy densities.	139

Figure 4.15: Plastic deformation of (a) cantilevers, (b) tensile test samples, and (c) cubes when melted at laser energy densities much higher than the critical laser energy density of each material.	139
Figure 4.16: Deflections of Invar 36 and SS 316L cantilevers produced at the critical energy density (86.8 J/mm ³ for Invar 36 and 104.2 J/mm ³ for SS 316L).....	142
Figure 4.17: The height of the cantilever from the build plate and the cantilever deflection from the center of the cantilever for (a) Invar 36 and (b) SS 316L samples produced at various laser energy densities.	143
Figure 4.18: Average cantilever deflection for (a) Invar 36 and (b) SS 316L.....	143
Figure 4.19: Minimum cantilever height and dimensional height error for (a) Invar 36 and (b) SS 316L.....	144
Figure 4.20: Simulation results for the relieved residual stress via cantilever deflection for (a) Invar 36 and (b) SS 316L.	146
Figure 4.21: Fractography of Invar 36 and stainless steel 316L samples produced at laser energy density of (a) 41.7 J/mm ³ with more voids present “brittle fracture”, (b) 62.5 J/mm ³ with less voids present “the beginning of ductile fracture”, and (c) 156.3 J/mm ³ with over melting and mass loss.	148
Figure 4.22: SLM process map for (a) Invar 36 and (b) SS 316L, showing the process parameters that could provide stable melting.	150
Figure 5.1: Illustration of (a) selective laser melting machine and (b) selective laser melting process parameters [3, 7, 16]. These process parameters were used for calculating the laser energy density E_v during this study.....	162
Figure 5.2: (a) Differential and (b) cumulative powder size distribution for both Invar 36 and stainless steel 316L powders.....	167
Figure 5.3: Microstructures of (a, b) virgin and recycled Invar 36 and (c, d) virgin and recycled stainless steel 316L powders.	167
Figure 5.4: Microstructures of (a-d) top and (e-h) side surfaces of <i>Invar 36</i> parts produced at laser energy density of (a, e) 41.7 J/mm ³ , (b, f) 52.1 J/mm ³ , (c, g) 86.8 J/mm ³ , and (d, h) 156.3 J/mm ³ . 100x and 500x magnifications were used.....	169

Figure 5.5: Microstructures of (a-d) top and (e-h) side surfaces of <i>stainless steel 316L</i> parts produced at laser energy density of (a, e) 41.7 J/mm ³ , (b, f) 62.5 J/mm ³ , (c, g) 104.2 J/mm ³ , and (d, h) 156.3 J/mm ³ . 100x and 500x magnifications were used.....	170
Figure 5.6: XRD diffractograms of (a) SLM Invar 36 samples, (b) SLM stainless steel 316L samples, and (c) typical austenite crystal.....	172
Figure 5.7: (a) thermal expansion and (b) average coefficient of thermal expansion for Invar 36 and stainless steel 316L samples manufactured at the critical laser energy density (E_C).	175
Figure 5.8: Thermal expansion of (a) Invar 36 and (b) stainless steel 316L samples manufactured at various laser energy densities.....	175
Figure 5.9: Thermal expansion of (a) Invar 36 and (b) stainless steel samples at instantaneous temperature $T_i = 50$ °C.	176
Figure 5.10: Contour plots for the thermal expansion of (a) Invar 36 and (b) stainless steel 316L samples at temperature of 200 °C. The plots show the effect of laser power and scanning speed on thermal expansion at hatch spacings of 0.08, 0.10, and 0.12 mm. ...	178
Figure 5.11: Illustration of SLM melt pool formation highlighting the expected defects.	181
Figure 5.12: Physics of (a) void formation and (b) particles vaporization.	183
Figure 6.1: Morphology of Ti-6Al-4V Grade 23 powder used in this study.	201
Figure 6.2: Dimensions of test coupons: (a) cantilevers, and (b) cubes.	203
Figure 6.3: Relative density of Ti-6Al-4V as a function of laser energy density.	207
Figure 6.4: Effect of laser power and scanning speed on the relative density of Ti-6Al-4V at hatch spacing of (a) 0.08 mm, (b) 0.10 mm, and (c) 0.12 mm.	207
Figure 6.5: (a) Linear thermal expansion, and (b) average coefficient of thermal expansion of Ti-6Al-4V parts manufactured at various laser energy densities.	209
Figure 6.6: Thermal expansion of Ti-6Al-4V samples produced (a) at the critical laser energy density E_C , and (b) at various laser energy densities.....	209

Figure 6.7: Thermal expansion of Ti-6Al-4V samples (a) at 100 °C, and (b) at 200 °C as a function of laser energy density.	209
Figure 6.8: Effect of laser power, scanning speed, and hatch spacing on the thermal expansion of Ti-6Al-4V at 100 °C.	210
Figure 6.9: Deflection of cantilevers produced (a) at the critical laser energy density, and (b) at various laser energy densities.	211
Figure 6.10: (a) Minimum height, and (b) average deflection of cantilevers produced at various laser energy densities.	212
Figure 6.11: Relationship between laser processing parameters and Ti-6Al-4V cantilever height.	212
Figure 6.12: Relationship between laser processing parameters and Ti-6Al-4V cantilever deflection.	212
Figure 6.13: (a) Longitudinal horizontal, and (b) transverse horizontal residual stress profiles in the build direction of Ti-6Al-4V samples produced at various laser energy densities. .	214
Figure 6.14: (a) Vertical, and (b) horizontal residual stress profiles in the layer direction of Ti-6Al-4V samples produced at various laser energy densities.	214
Figure 6.15: Micrographs of etched cross-sections of samples produced at different laser energy densities.	215
Figure 6.16: Relationship between laser processing parameters and Ti-6Al-4V cantilever deflection.	217
Figure 6.17: Relationship between laser processing parameters and Ti-6Al-4V cantilever deflection.	218
Figure 7.1: Schematic of (a) transient thermal, (b) static structural models.	229
Figure 7.2: Dimensions of (a) cantilever beams and (b) cubes for residual stress measurements.	231
Figure 7.3: Relative density as a function of laser energy density for (a) Invar 36 [7, 17], (b) stainless steel 316L [7, 17, 20], and (c) Ti-6Al-4V [18].	231
Figure 7.4: CMM measurements highlighting EDM cut planes.	232

Figure 7.5: (a) Thermal cycles, (b) temperature profile of Ti-6Al-4V.	236
Figure 7.6: (a) Ti-6Al-4V thermal cycles using two-colour pyrometer, (b) melt pool shape visualization.	236
Figure 7.7: Average deflections on the top surfaces of the cantilevers: (a) measured by using CMM, (b) predicted by using the ANSYS© model.	237
Figure 7.8: (a) Comparison between the numerical and experimental deflections, in which maximum deflection represents the edges of the top surface and minimum deflection represents the centre of the top surface; (b-d) directional deformation profiles (z-axis) of Ti-6Al-4V, stainless steel 316L, and Invar 36 cantilevers predicted by using the ANSYS© model.	238
Figure 7.9: (a-b) Experimental and numerical evolutions of longitudinal horizontal, lateral horizontal, and vertical residual stresses (σ_x , σ_y , σ_z), (c) residual stress profiles of Ti-6Al-4V.	240

List of Tables

Table 2.1: The Invar 36 powder used compared with reference [7].	39
Table 2.2: Material composition of maraging steel and Invar 36 powder.	39
Table 2.3: Material properties of maraging steel and Invar 36 alloys.	39
Table 2.4: The designed range for each process parameter.	39
Table 2.5: Parameter sets of the fabrication groups (45 groups).	41
Table 2.6: Summary of the correlation results between the process parameters and the relative density.	48
Table 2.7: Summary of the ANOVA results between the process parameters and the relative density.	48
Table 2.8: Recommended sets of SLM process parameters for fabricating dense Invar 36 components.	56
Table 3.1: Dimensions of the designed samples.	73
Table 3.2: Material composition of stainless steel 316L powder (wt%).	75
Table 3.3: List of SLM process parameters reported in the literature for producing stainless steel 316L.	75
Table 3.4: SLM process parameters for producing the stainless steel 316L samples.	76
Table 3.5: Constants used in the determination of residual stresses using the XRD method.	79
Table 3.6: Profile errors of airfoils (CMM results).	80
Table 3.7: Material composition of the selected area shown in Figure 3.12 (wt%).	84
Table 4.1: Process parameters reported in the literature for producing Invar 36 and SS 316L.	114
Table 4.2: SLM process parameters used in this study (DOE matrix based on full factorial design).	117

Table 4.3: Constants used in the determination of residual stresses using the XRD method.	121
Table 4.4: Materials properties used in the finite element model as provided in the ASTM standards [39-41].	124
Table 4.5: Regression model for Invar 36 and SS 316L density as a function of individual process parameters.....	127
Table 4.6: Regression model for Invar 36 and SS 316L density as a function of laser energy density.....	129
Table 4.7: Comparison between the ANOVA results from the two models for Invar 36 and SS 316L.....	130
Table 4.8: Empirical “regression” equations from the two models for both Invar 36 and SS 316L.....	130
Table 4.9: Predicted densities compared with measured densities for validation.....	131
Table 4.10: Summary of the ANOVA results for the tensile mechanical properties of Invar 36 and SS 316L.....	136
Table 4.11: Empirical “regression” equations for the tensile mechanical properties of both Invar 36 and SS 316L.	137
Table 4.12: Summary of the ANOVA results for the residual stress induced in Invar 36 and SS 316L.....	140
Table 4.13: Empirical “regression” equations for the residual stress induced in both Invar 36 and SS 316L.....	140
Table 4.14: Summary of the ANOVA results for the cantilever deflection and macroscopic residual stress induced in Invar 36 and SS 316L.	145
Table 4.15: Empirical “regression” equations for the macroscopic residual stress induced in both Invar 36 and SS 316L.	146
Table 4.16: Comparison between the experimental and numerical residual stress results.	146

Table 4.17: Material composition of Invar 36 and SS 316L tensile-test samples compared with the wrought material (wt.%) and powder composition.....	148
Table 5.1: Process parameters reported in the literature for producing Invar 36 and stainless steel 316L.....	163
Table 5.2: SLM process parameters used in this study (DOE matrix based on full factorial design).....	165
Table 5.3: Powder diameter at cumulative volume percent of particles 10%, 50%, and 90% for both materials.	167
Table 5.4: Material composition of Invar 36 parts (wt.%).....	171
Table 5.5: Material composition of stainless steel 316L parts (wt.%).....	171
Table 5.6: Regression model for Invar 36 and stainless steel 316L thermal expansions.	176
Table 5.7: Empirical “regression” equations for thermal expansion of both Invar 36 and stainless steel 316L parts.	177
Table 5.8: Magnetic dipole moment of Invar 36 and stainless steel 316L samples.....	180
Table 5.9: Material properties of alloying elements [96, 97].....	184
Table 6.1: Process parameters reported in the literature for selective laser melting of Ti-6Al-4V.	198
Table 6.2: Laser process parameters used in this study.	201
Table 7.1: SLM process conditions for Ti-6Al-4V, stainless steel 316L, and Invar 36.	232
Table 7.2: Build conditions used to calculate heat transfer coefficients.....	235
Table 7.3: Thermal properties at room temperature.....	241

Chapter 1

Introduction and Background

Complete Citation:

Yakout, M., Elbestawi, M.A., Veldhuis, S.C. (2018). A review of metal additive manufacturing technologies. *Solid State Phenomena*, 278, 1-14. DOI: 10.4028/www.scientific.net/SSP.278.1

Copyright:

Reprinted by permissions from Trans Tech Publications (2018). M. Yakout presented this paper in the 7th International Conference on Manufacturing Engineering and Process (ICMEP 2018) held in Barcelona, Spain, February 5-7, 2018.

Relative Contributions:

M. Yakout: Reviewed the literature and wrote the first draft of the manuscript.
Helped with submitting the final manuscript to the journal.

M. A. Elbestawi: Co-supervisor of M. Yakout. Revised the manuscript.

S. C. Veldhuis: Co-supervisor of M. Yakout. Revised the manuscript.

1.1 A Note to the Reader

Since this thesis is a compilation of seven peer-reviewed journal articles, the introduction and background sections in Chapters 2-7 may contain some similarities. However, the reader is encouraged to read these introductory sections in each chapter as the material is targeted towards specific aspects of the investigation covered in the chapter. In addition, a condensed literature review is provided in Section 1.2 to highlight the gap in the literature, which prompted the work presented in the thesis. Furthermore, Chapter 8 provides a summary of the key findings and contributions that are stated in Chapters 2-7.

1.2 Literature Review

1.2.1 Metal Additive Manufacturing Processes

ASTM International [1] defines additive manufacturing (AM) as “*the process of joining materials to make objects from 3D model data, usually layer upon layer, as opposed to subtractive manufacturing methodologies*”. There are various classifications of AM processes in the literature [2-5]. ASTM ISO F52900 [1] categorizes the AM processes into seven main categories, according to the adhesion and bonding method. These categories are: (i) VAT photopolymerization, (ii) material jetting, (iii) material extrusion, (iv) powder bed fusion, (v) binder jetting, (vi) direct energy deposition, and (vii) sheet lamination. VAT polymerization or material jetting could be used in liquid AM processes, while material extrusion could be used in filament processes. Powder AM processes could use powder fusion, binder jetting, or direct energy deposition for binding the powder particles. Figure 1.1 classifies the bonding techniques according to the state of the raw material “*feedstock*”. AM has been developed in 1986 by Charles W. Hull [6]. Since then various processes have been introduced. Material extrusion, powder bed fusion (PBF), and direct energy deposition

(DED), are the most commonly used processes for metal additive manufacturing [7]. Selective laser melting (SLM) and electron beam melting (EBM) are powder bed fusion AM processes. In SLM, full melting of powders is achieved to produce fully dense objects with mechanical properties comparable to the wrought material. The powder is evenly distributed and spread to create a level, uniform surface that completely covers the build area, as shown in Figure 1.2. A focused laser beam is then precisely directed at the powder layer and scans over the cross-section of the part. The build platform is lowered, and the process is repeated until all layers have been built [8, 9]. All metals can be candidates but some act differently when processed. Such differences include reactions to laser absorption, surface tensions, and material viscosities [10]. SLM powders can be broken down into two categories: single material powders or alloyed powders. Single material powders consist of strictly one type of metal, such as pure titanium. In this case, tests showed almost 100% part density; however, high thermal stresses could be induced and cause internal cracks [11]. Alloyed powders consist of alloyed materials (e.g., Ti-6Al-4V, stainless steel 316L, Invar 36, etc.). The mechanical properties of alloyed materials are comparable to wrought materials apart from ductility, which is significantly reduced [12]. A big benefit of SLM is the ability to process non-ferrous metals such as titanium, aluminum and copper. As the process uses higher energy, problems arise with instabilities in the melt pool along with part shrinkage [13]. EBM is typically similar to SLM except that an electron gun is used for melting preheated powder instead of using a laser source for melting a powder, which makes the EBM more powerful because its build rate is faster than SLM [14, 15]. Powder bed fusion processes are commonly used for metallic applications, especially for complex designs. EBM is currently the preferred process for metals, but it is limited by the electrical conductivity of the material and the need to maintain a high level of vacuum; however, SLM is more versatile [16].

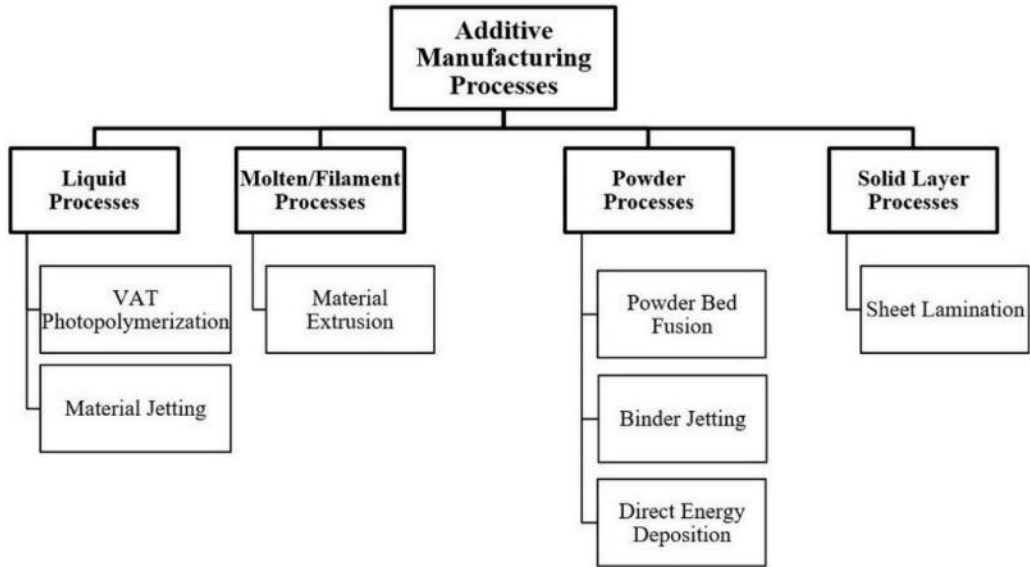


Figure 1.1: Adhesion and bonding methods in additive manufacturing [1].

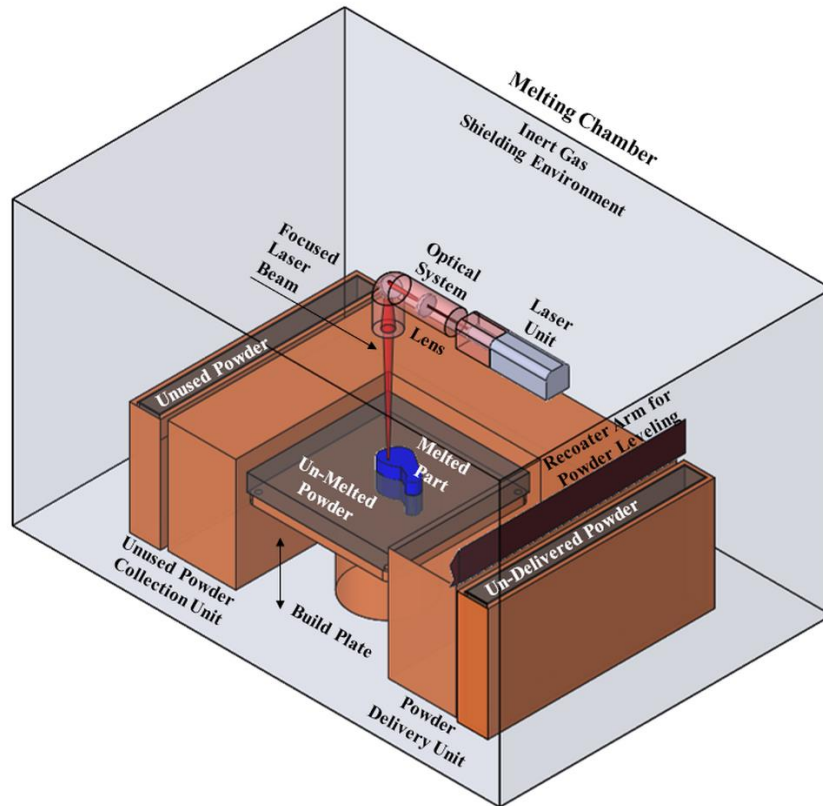


Figure 1.2: Selective laser melting process [8, 9].

SLM has been chosen in this study to process three aerospace alloys; Invar 36, stainless steel 316L, and Ti-6Al-4V. The work in this thesis contributes to the SLM of Invar 36, stainless steel 316L, and Ti-6Al-4V. These alloys are widely used in the aerospace and biomedical industries because of their unique properties. Invar 36 is a ferromagnetic alloy that has a very low coefficient of thermal expansion for applications below its Curie temperature (279 °C), stainless steel 316L offers corrosion resistance and high strength, and Ti-6Al-4V offers high strength-to-weight ratio and is biocompatible.

1.2.2 Applications of Metal Additive Manufacturing

1.2.2.1 Aerospace Industry

An important requirement for the aerospace industry is to consistently produce light complex geometries with good mechanical properties in small quantities. These reasons make AM a very efficient manufacturing method for aerospace applications. The most common AM processes used in the aerospace industry are material extrusion [17], PBF [18, 19], and DED [20]. These techniques are used to fabricate low-volume complex aerospace parts, aircraft wings, and replacement parts in the aerospace industry along with fabricating specialized parts, lightweight structures, parts with minimal waste, on-demand parts, and replacement parts to support long term space exploration [21]. Advanced materials such as aluminum alloys, titanium alloys, nickel super-alloys, and special steels have been manufactured in the aerospace industry using AM technologies [3]. AM technologies open the door for developing new materials and designs in the aerospace industry. The main challenges reported in the literature include mechanical anisotropy, microstructural inhomogeneity, residual stresses, dimensional accuracy, and surface finish [22-28].

1.2.2.2 Automotive Industry

Metal AM has significant implications on part design as well as supply chains and inventory systems, which is particularly relevant for the automotive industry. An important feature of using metal AM processes in the automotive sector is producing complex lightweight structures. The weight of the automotive parts can be reduced significantly by leveraging the ability of AM processes to produce parts with complex geometries while maintaining relative strengths. Examples of automotive parts produced by AM include structural composite components, engine valves, and turbocharger turbines [29, 30]. A significant advantage is in-house and on demand production, which reduces inventory needs, shipping costs, and material procurement costs [31]. Notwithstanding the capabilities of the AM processes in the automotive industry, the parts produced should comply with the standards to perform a certain level of performance. The main challenges in the AM of automotive components are: (i) the thermal stresses induced in the AM parts which affect the repeatability and performance of these parts, (ii) the surface finish and dimensional accuracies, and (iii) the size of the parts produced [24, 32, 33] in addition to this, processing speed is critical due to typical production volumes.

1.2.2.3 Tooling Industry

For the tooling industry, AM can offer time saving through the reduction of the fabrication steps and cost reduction through the elimination of material loss associated with traditional subtractive manufacturing. In addition, the AM technology offers the ability to produce customized molds with optimized cooling channels which can impart unique properties to parts and reduce production cycle time. AM molds made with integrated conformal cooling also prolong their service life as it provides the designer with the ability to reduce the thermal stress loading that the die experiences [34, 35].

1.2.2.4 Healthcare Industry

The use of metal AM processes in the healthcare industry is briefly reviewed. In the dental industry, AM processes are used for creating precise dental crowns, bridges, and implants. The capability of the SLM process to manufacture custom, complex, accurate, and fully dense objects makes it suitable for dental applications. The process of creating crowns and bridges consists of scanning the dental impression of the patient's teeth, digital modeling of the part, and then SLM production [36]. This process provides a competitive market for AM of dental implants that rivals traditional casting and milling production methods. Additionally, a similar process is used for the manufacturing of personalized prosthesis and supports for artificial teeth made of titanium or cobalt-chromium [37]. Moreover, metal AM processes are used in the medical sector due to its ability to quickly produce highly custom components. The technology is very useful for fabricating custom-made medical implants as well as surgical tools and fixtures for use in operation rooms. There is no doubt that fabricating custom implants is more accurate than the previous traditional methods [38]. The main advantage of AM in the medical industry is its capability to produce very complex components with low production cost as well as customized components [39]. Recently, AM technologies have been integrated with nano-technology to fabricate parts from new nano-composites. The main benefit of using nano-materials in AM processes is enhancing the material properties of the fabricated parts. Parts with better optical, thermal, electrochemical, and mechanical properties have been obtained. Over the past few decades, a wide variety of nanomaterials were used in AM processes, including carbon nanotubes, nanowires, metal nanoparticles, nano-graphene, and quantum dots [40]. Nano-scale AM plays a vital role in producing metal parts with nanopores, thus eliminating or minimizing the formation of pores and voids [41].

1.2.3 Materials Used in This Study

This thesis deals with the characteristics of Ti-6Al-4V (*UNS R56400*), stainless steel 316L (*UNS S31603*), and Invar 36 (*UNS K93600*) parts produced using SLM process. These three materials have unique thermal and mechanical properties and are commonly used in the aerospace and biomedical industries. The characteristics of titanium Ti-6Al-4V produced by different AM processes to meet aerospace standards were reported in the literature. A study showed that the mechanical and fatigue behaviors of the SLM Ti-6Al-4V parts are significantly affected by the internal voids as well as the residual stresses in the parts produced. The tensile strength and fatigue strength are strongly affected by the pore size. However, the crack growth is influenced by the residual stresses [42, 43]. Another study demonstrated that the microstructure of the SLM Ti-6Al-4V components also alters the mechanical properties of these parts [44]. The SLM process parameters such as scanning parameters, scanning strategies, and laser melting parameters exhibited a strong influence on the surface quality [45], voids characteristics [46], microstructure [47], and mechanical properties [44, 48] of Ti-6Al-4V parts. Other studies were performed to find the optimum SLM process parameters for producing Ti-6Al-4V parts suitable for aerospace [49, 50]. Similar studies performed using other AM processes such as DED [51, 52] and EBM [52-55] achieved similar results. In EBM production of Ti-6Al-4V, a function is developed to control the beam speed and energy during the process in order to enhance the thermal properties of the parts produced [56]. The influence of thermal properties of Ti-6Al-4V on the characteristics of the parts produced is one of the research gaps in the literature. Stainless steel 316L is one of the most common iron-based alloys in powder-based AM processes. Starting from the raw material, the powder grain size affects the density and consequently the mechanical properties of the produced parts [57, 58]. In

SLM of stainless steel 316L, some studies showed that point distance, exposure time, scan speed, layer thickness, and building direction have a strong influence on the quality of the parts produced. These parameters should be controlled during the fabrication process in order to achieve good surface finish and high mechanical properties [9, 59-61]. AM technology makes the processing of special alloys such as nickel-based alloys easier. Some studies showed that Inconel 718 parts, produced via SLM, contain small cracks that may affect mechanical properties in all directions especially in the building direction [62-64]. These cracks can be attributed to the phase transition and the formation of columnar dendrites during the melting process [65, 66]. Only a few studies illustrated the selection of SLM process parameters for producing dense parts from Invar 36 [8, 67].

1.2.4 Quality of Additive Manufacturing Parts

Starting from the raw material, the powder grain size affects the density and consequently the mechanical properties of the parts produced in a SLM process [68, 69]. Moreover, point distance, exposure time, scanning speed, layer thickness, and building direction show a strong influence on the quality of the parts produced. This includes surface microstructure, fatigue strength, hardness, density, and surface roughness of parts produced. These parameters should be controlled during the fabrication process to get a reasonable surface finish and fair mechanical properties [60, 61, 69, 70]. The SLM process has some limitations and challenges compared to subtractive manufacturing processes. The thermal stresses and material degradations (i.e. changes in the material microstructure and chemical composition) that could occur during the process are challenging for some applications, especially in the aerospace industry. These factors affect the density of SLM parts and consequently all the mechanical properties, particularly the fatigue properties. SLM parts differ from wrought or forged parts in that they can have a large number of defects/stress

risers including, but not limited to, voids either from gas pores or imperfections, partially melted powder, lack of adhesion/pre-existing cracks formed between subsequent printed layers, and powder particles stuck on the surface [71]. There are currently two options to overcome these challenges. The first solution is to refine the quality of the additive parts through carefully controlled post processing techniques [42, 43]. The second solution is to optimize and control the process parameters to produce high quality parts [8, 60, 72-74].

1.2.4.1 Residual Stresses

Residual stresses are internal stresses present in materials and structures without any external loads. The tensile and compressive residual stresses are in equilibrium within the whole volume of the material or structure as shown in Figure 1.3. Almost all manufacturing processes cause residual stresses in the parts produced. The residual stresses are induced due to one of the following mechanisms:

1. Non-uniform plastic deformation (e.g., forging, bending, and extrusion)
2. Subtracting manufacturing (e.g., machining and grinding)
3. Material phase changes (e.g., welding, casting, and additive laser melting)

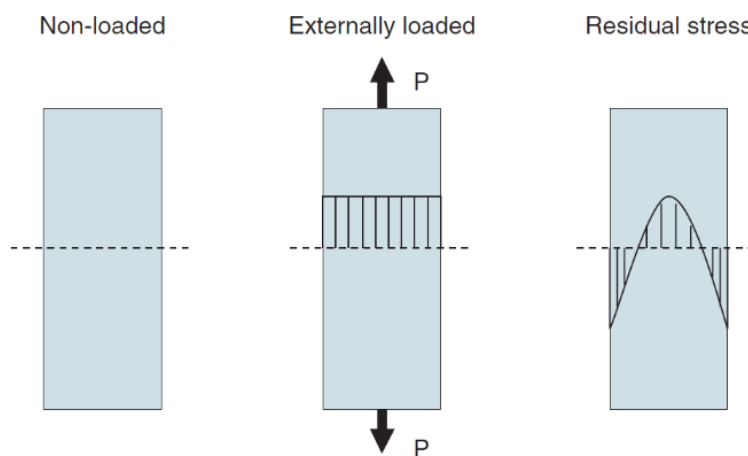


Figure 1.3: Stress distributions within a cross-section [75].

Residual stresses can be classified according to the scale on which they occur [75]:

1. Type I: macro residual stresses that vary over large distances
2. Type II: micro residual stresses that vary over small distances
3. Type III: atomic-scale residual stresses that occur due to atomic dislocations

The SLM process is associated with thermal stresses due to rapid heating and cooling during the powder melting and part solidification. These thermal stresses are the main cause of the residual stresses in the parts produced. These residual stresses are due to material phase and/or density changes, and they are of Types I, II and III [75]. These induced residual stresses significantly affect the mechanical and material properties of the parts produced [76]. Mercelis and Kruth [77] explained the formation of residual stresses in SLM process using numerical models. The experimental work was based on investigating the influence of the number of layers, build plate height, material yield strength, laser post-scanning parameter, and build plate removal method on the residual stress distribution. They found that the residual stress distribution starts with tensile stresses at the top surface, followed by compressive stresses in the middle and ends with tensile stresses at the bottom. They suggested a heat treatment procedure and the pre-heating of the build plate for reducing the residual stresses. Their findings include the influence of the build-plate removal method on the residual stresses. They concluded that the yield strength of the printed material, part height, build plate height, laser scanning strategy, and heating conditions all affect the residual stress distribution. Casavola et al. [78] studied the influence of the part location in the build plate and part height on the surface residual stresses in a SLM process. The experimental work in this study was based on maraging steel parts with 1.4% porosity, measured by the Archimedes method. For residual stress measurement by the hole-drilling method, the authors found that the parts in the center of

the build plate have less residual stresses than the parts on the edges. They argued that the laser is probably lined up orthogonally to the layer surface in the center of the build plate. Their findings also illustrated that the residual stresses are fairly small for small thicknesses, large for intermediate thicknesses, and small again for large thicknesses. They argued that the laser heat caused a heat treatment procedure for thick parts, which is the reason for having a fairly small amount of residual stresses in the thick parts. Van Belle et al. [79] studied the influence of the part height, layer thickness, and cooling time between successive layers on the residual stresses of maraging steel produced using the SLM process. They found that the residual stresses increase with the increase of cooling time, decrease of part height, and decrease of layer thickness. Various methods are suggested in the literature for measuring residual stresses in AM parts. These methods include, but not limited to, layer removal method [76, 79], crack compliance method [77], hole drilling method [78], contour method [75], sectioning method [75], neutron diffraction [80], X-ray diffraction (XRD) [81], and indentation correlation method (hardness test) [82].

1.2.4.2 Void Formation

Void formation in SLM parts is one of the most challenging problems in the industry. This impacts many applications, especially applications requiring high stress and fatigue strength. Mass/volume measurement, Archimedes method, X-ray computed tomography (CT) scan, and ultrasonic pulse-echo velocity technique are reported in the literature for measuring the amount of porosity in SLM parts [83]. These voids could be either gas pores or imperfections. The gas pores have almost a spherical shape and come from inclusion of gases inside the printing chamber. The imperfections have a non-uniform shape and come from partially melted powder. The amount of voids is dependent on the build chamber as well as the process parameters [84, 85].

The following methods are suggested in the literature to reduce void formation:

1. Efficient drying of the powder and tight control of the process parameters [84]
2. Increasing the laser power for processing materials with high reflectivity and low energy absorption [86]
3. Experimenting with the scanning speed, scanning strategy, and scanning overlap for controlling the type of the pores and reducing the amount of pores [86, 87]
4. Hot isostatic pressing (HIP) of the SLM parts for porosity elimination, fatigue damage refinement, powder compaction, and material joining enhancement

Simonelli et al. [88] studied the microstructural features and phases of titanium parts produced by SLM. The mechanical behaviors of the SLM parts are significantly affected by the formation of voids and residual stresses. The tensile strength, fatigue strength, and ductility are strongly affected by the pores size; however, the fatigue crack growth is influenced by the residual stresses [42, 43]. A study showed that the microstructure of SLM parts has a significant effect on the mechanical properties, such as fatigue behavior, mechanical strength, elongation, etc. The microstructure of the AM parts is influenced by the imperfections formed during the process and/or the post-processing. The mechanical properties of SLM parts could be enhanced by controlling the process parameters and/or performing heat treatments [72, 89]. HIP process and heat treatments have been used to eliminate void formation and reduce residual stresses, and consequently enhance the mechanical properties of parts produced [42, 43, 76]. Micro-cracks are formed during the SLM process either from separation between subsequent layers or due to large thermal gradients during the powder melting and/or part solidification. These cracks can be controlled and/or eliminated by optimizing the process parameters. A clear understanding of the relationship between process parameters and crack initiation is needed [71, 90].

1.3 Motivation

The above survey showed that SLM parts differ from wrought parts in that they can have many defects including, but not limited to, voids, lack of adhesion between subsequent printed layers, and substandard mechanical/fatigue properties. Developments in metal additive manufacturing offer significant possibilities for the creation of new types of products. Research and development priorities have been discussed in the literature. A summary of the main research issues includes:

1. Enhancing the mechanical properties of the SLM parts through post-processing techniques or tuning the SLM process parameters [73, 74]
2. Developing new alloys and functionally graded materials based on the capabilities of the additive processes [53, 91]
3. Establishing rules and protocols to design for additive manufacturing [24, 31]
4. Creating a real-time process control for the additive manufacturing systems [91]
5. Exploring the hybrid and multi-materials manufacturing [3, 53]
6. Improving the productivity of the additive manufacturing systems [18, 32, 91]

Understanding the influence of process parameters and material properties on part quality is the main goal of this thesis.

1.4 Research Objectives

The main objective of this thesis is to investigate the process-structure-property relationships and to optimize the SLM process parameters for three aerospace alloys: Ti-6Al-4V, stainless steel 316L, and Invar 36. The practical merit of this research will be the selection of an optimized set of SLM process parameters necessary to process each of these materials for aerospace and automotive applications.

This thesis provides a better understanding of:

1. Residual stresses formation that occur during the SLM process by experimental and numerical methods
2. Changes in the material composition and microstructure that occur during the SLM process
3. Mechanisms of residual stress formation and metallurgical changes associated with SLM process
4. Thermal properties that affect the residual stress formation

The study will include two complementary approaches:

1. Experimental approach to study the influence of process parameters on the residual stresses, thermal expansion, microstructures, chemical compositions, and mechanical properties of the parts produced
2. Numerical approach to define what is happening during the SLM process, in which this approach will compare the induced residual stresses and part deflections of the three materials

1.5 Thesis Outline

Overall, the main results of this thesis have been published in seven journal articles, in which five articles are already published and the other two articles are submitted to journals for peer-review. In addition, one conference proceeding has been published from part of the results presented in Chapter 4.

Chapter 1 introduces the background and motivation of the research as well as the thesis objectives and main contributions. It shows the research gaps in metal additive manufacturing and explains how this thesis contributes to explore one of these gaps.

Very few publications [67] on selective laser melting of Invar 36 was available in the open literature when this research started. No process window was available for selective laser melting of Invar 36. It was important to find thresholds of selective laser melting process parameters for Invar 36. Hence, Chapter 2 presents pilot experiments on selective laser melting of Invar 36 to determine the “optimum” range of process parameters to produce dense parts. The surface microstructures and material compositions of parts produced are analyzed. The analysis is based on one-factor-at-a-time (OFAT).

Chapter 3 deals with the selective laser melting of stainless steel 316L. Since many publications are available for laser melting of stainless steel 316L, this chapter presents a preliminary study on the effect of part location in the build plate on the characteristics of stainless steel 316L produced using selective laser melting. The main goal of this study is to understand the characteristics of stainless steel 316L produced using selective laser melting.

Chapter 4 presents an extensive study on the density, mechanical properties, and residual stresses of Invar 36 and stainless steel 316L parts produced using selective laser melting. The study is based on full factorial design of experiments to develop an optimum process map for each material. Void formation and alloying element vaporization that occur during selective laser melting of Ni- and Fe-based alloys are studied.

Chapter 5 explains the relationship between the laser process parameters and thermal expansion of parts produced. A process window is determined for Invar 36 and stainless steel 316L based on stable melting. The metallurgical changes, microstructures, material phases, and the chemical compositions of parts produced are studied.

Chapter 6 deals with the metallurgical changes, residual stresses, and thermal expansion variations of Ti-6Al-4V parts produced using selective laser melting. The study is based on full factorial design of experiments. A process map is presented based on stable melting and compared with process maps available in the literature for Ti-6Al-4V.

Chapter 7 compares the residual stresses induced in Invar 36, stainless steel 316L, and Ti-6Al-4V parts produced using selective laser melting. The study discusses the relationship between the material properties and induced residual stresses by experimental and numerical work. It explains the mechanisms of forming residual stress in a material that have a low coefficient of thermal expansion (i.e., Invar 36) when compared to stainless steel 316L and Ti-6Al-4V.

Chapter 8 summarizes the main contributions of this thesis and presents closing remarks for future work.

1.6 References

- [1] *Standard Terminology for Additive Manufacturing - General Principles - Terminology*, 2015.
- [2] Youssef, H. A., El-Hofy, H. A., and Ahmed, M. H., *Manufacturing Technology: Materials, Processes, and Equipment*. International Edition: Taylor & Francis Group, CRC Press, 2012.
- [3] Guo, N. and Leu, M. C., "Additive Manufacturing: Technology, Applications and Research Needs," *Frontiers of Mechanical Engineering*, vol. 8, no. 3, pp. 215-243, 2013.
- [4] Gibson, I., Rosen, D., and Stucker, B., *Additive Manufacturing Technologies; 3D Printing, Rapid Prototyping, and Direct Digital Manufacturing*. New York, USA: Springer, 2015.
- [5] Wong, K. V. and Hernandez, A., "A Review of Additive Manufacturing," *International Scholarly Research Network (ISR) Mechanical Engineering*, vol. 2012, 2012.

- [6] Hull, C. W., "Apparatus for Production of Three-Dimensional Objects by Stereolithography," Unites States, 1986.
- [7] Wohlers, T. and Gornet, T., "Wohler's Report (2014), History of Additive Manufacturing," Wohlers Associates Inc.2014.
- [8] Yakout, M., Cadamuro, A., Elbestawi, M. A., and Veldhuis, S. C., "The selection of process parameters in additive manufacturing for aerospace alloys," *International Journal of Advanced Manufacturing Technology*, journal article vol. 92, no. 5, pp. 2081-2098, September 01 2017.
- [9] Yakout, M., Elbestawi, M. A., and Veldhuis, S. C., "On the characterization of stainless steel 316L parts produced by selective laser melting," *International Journal of Advanced Manufacturing Technology*, vol. Online First, pp. 1-22, 2017.
- [10] Kruth, J.-P., Mercelis, P., Froyen, L., and Rombouts, M., "Binding Mechanisms in Selective Laser Sintering and Selective Laser Melting," in *International Solid Freeform Fabrication Symposium, USA, 2004*.
- [11] Miller, F., "Schneller Zahn aus Titan (Fast Tooth made of Titanium)," *Fraunhofer Magazin*, vol. 4, 2002.
- [12] Over, C., Meiners, W., Wissenbach, K., Lindemann, M., and Hammann, G., "Selective Laser Melting: A New Approach for the Direct Manufacturing of Metal Parts and Tools," in *International Conference on Laser Assisted Net Shape Engineering*, Germany, 2001.
- [13] Gu, D. D., Meiners, W., Wissenbach, K., and Poprawe, R., "Laser Additive Manufacturing of Metallic Components: Materials, Processes and Mechanisms," *International Materials Reviews*, vol. 57, no. 3, pp. 133-164, 2012.
- [14] Murr, L. E. *et al.*, "Fabrication of Metal and Alloy Components by Additive Manufacturing: Examples of 3D Materials Science," *Journal of Materials Research and Technology*, vol. 1, no. 1, pp. 42-54, 2012.
- [15] Vora, P., Derguti, F., Mumtaz, K., Todd, I., and Hopkinson, N., "Investigating a Semi-Solid Processing Technique using Metal Powder Bed Additive Manufacturing Processes," in *International Solid Freeform Fabrication Symposium, USA, 2013*.
- [16] Taminger, K. M. and Hafley, R. A. (2006) Electron Beam Freeform Fabrication for Cost Effective Near-Net Shape Manufacturing. *Cost Effective Manufacture via Net-Shape Processing (RTO-MP-AVT-139)*. 16 (1-10).
- [17] Yagnik, D., "Fused Deposition Modeling - A Rapid Prototyping Technique for Product Cycle Time Reduction Cost Effectively in Aerospace Applications," *IOSR Journal of Mechanical and Civil Engineering*, vol. 5, pp. 62-68, 2014.
- [18] Wohlers, T. (2011) Making Products By Using Additive Manufacturing. *Manufacturing Engineering Magazine*. 70-77.

- [19] Michaleris, P., "Modeling Metal Deposition in Heat Transfer Analyses of Additive Manufacturing Processes," *Finite Elements in Analysis and Design*, vol. 86, pp. 51-60, 2014.
- [20] Dey, N. K., "Additive Manufacturing Laser Deposition of Ti-6Al-4V for Aerospace Repair Application," M.Sc. Thesis Missouri University of Science and Technology, Missouri, USA, 2014.
- [21] Coykendall, J., Cotteleer, M., Holdowsky, J., and Mahto, M., "3D Opportunity in Aerospace and Defense: Additive Manufacturing Takes Flight," in "A Deloitte Series on Additive Manufacturing," Deloitte University Press UK2014.
- [22] National Research Council, *3D Printing in Space*. Washington, DC, USA: National Academies Press, 2014, p. 100.
- [23] Kobryn, P. A., Ontko, N. R., Perkins, L. P., and Tiley, J. S., "Additive Manufacturing of Aerospace Alloys for Aircraft Structures," in *Cost Effective Manufacture via Net-Shape Processing (RTO-MP-AVT-139)*, Neuilly-sur-Seine, France, 2006, pp. (3) 1-14: NATO Research and Technology Organization (RTO).
- [24] Scott, J., Gupta, N., Weber, C., Newsome, S., Wohlers, T., and Caffrey, T., "Additive Manufacturing: Status and Opportunities," IDA Science and Technology Policy Institute, Washington, DC, USA 2012.
- [25] Frazier, W. E., Polakovics, D., and Koegel, W., "Qualifying of Metallic Materials and Structures for Aerospace Applications," *JOM*, vol. 53, no. 3, pp. 16-18, 2001.
- [26] Guessasma, S., Zhang, W., Zhu, J., Belhabib, S., and Nouri, H., "Challenges of Additive Manufacturing Technologies from an Optimisation Perspective," *International Journal for Simulation and Multidisciplinary Design Optimization*, vol. 6, pp. (A9) 1-13, 2015.
- [27] Smith, C. J. *et al.*, "Dimensional Accuracy of Electron Beam Melting (EBM) Additive Manufacture with Regard to Weight Optimized Truss Structures," *Journal of Materials Processing Technology*, vol. 229, pp. 128-138, 2016.
- [28] Energetics Incorporated, "Measurement Science Roadmap for Metal-Based Additive Manufacturing," in "Roadmap Workshop on Measurement Science for Metal-Based Additive Manufacturing," National Institute of Standards and Technology (NIST), U.S. Department of Commerce, Columbia, Maryland 2013.
- [29] Cooper, D., Thornby, J., Blundell, N., Henrys, R., Williams, M. A., and Gibbons, G., "Design and Manufacture of High Performance Hollow Engine Valves by Additive Layer Manufacturing," *Materials & Design*, vol. 69, pp. 44-55, 2015.
- [30] Biamino, S., Klöden, B., Weißgärber, T., Kieback, B., and Ackelid, U., "Properties of a TiAl Turbocharger Wheel Produced by Electron Beam Melting," in *Fraunhofer Direct Digital Manufacturing Conference*, Berlin, Germany, 2014.

- [31] Beyer, C., "Strategic Implications of Current Trends in Additive Manufacturing," *Journal of Manufacturing Science and Engineering*, vol. 136, no. 6, pp. 064701 (1-6), 2014.
- [32] Gao, W. *et al.*, "The Status, Challenges, and Future of Additive Manufacturing in Engineering," *Computer-Aided Design*, 2015.
- [33] Giffi, C. A., Gangula, B., and Illinda, P., "3D Opportunity in the Automotive Industry: Additive Manufacturing hits the Road," in "A Deloitte Series on Additive Manufacturing " Deloitte University Press 2014.
- [34] Cotteleer, M., Neier, M., and Crane, J., "3D Opportunity in Tooling: Additive Manufacturing Shapes the Future," in "A Deloitte Series on Additive Manufacturing," Deloitte University Press 2014.
- [35] Villalon, A. V., "Electron Beam Fabrication of Injection Mold Tooling with Conformal Cooling Channels," M.Sc. Thesis Industrial Engineering North Carolina State University, Raleigh, North Carolina, USA 2005.
- [36] Gebhardt, A., Schmidt, F.-M., Hötter, J.-S., Sokalla, W., and Sokalla, P., "Additive Manufacturing by Selective Laser Melting the Realizer Desktop Machine and its Application for the Dental Industry," *Physics Procedia*, vol. 5, no. B, pp. 543-549, 2010.
- [37] Vandenbroucke, B. and Kruth, J. P., "Selective Laser Melting of Biocompatible Metals for Rapid Manufacturing of Medical Parts," *Rapid Prototyping Journal*, vol. 13, no. 4, pp. 196-203, 2007.
- [38] Banks, J., "Adding Value in Additive Manufacturing: Researchers in the United Kingdom and Europe Look to 3D Printing for Customization," *IEEE Pulse*, vol. 4, no. 6, pp. 22-26, 2013.
- [39] Mertz, L., "Dream it, Design it, Print it in 3-D: What Can 3-D Printing do for you?," *IEEE Pulse*, vol. 4, no. 6, pp. 15-21, 2013.
- [40] Campbell, O., Christopher, I., and Thomas, W., "Additive Manufacturing (AM) and Nanotechnology: Promises and Challenges," *Rapid Prototyping Journal*, vol. 19, no. 5, pp. 353-364, 2013.
- [41] Lee, J.-K. and Xu, T. T., "Recent Progress in Scalable Nanomanufacturing," *JOM*, vol. 67, no. 1, pp. 27-28, 2015.
- [42] Leuders, S. *et al.*, "On the Mechanical Behaviour of Titanium Alloy TiAl6V4 Manufactured by Selective Laser Melting: Fatigue Resistance and Crack Growth Performance," *International Journal of Fatigue*, vol. 48, pp. 300-307, 2013.
- [43] Kasperovich, G. and Hausmann, J., "Improvement of Fatigue Resistance and Ductility of TiAl6V4 Processed by Selective Laser Melting," *Journal of Materials Processing Technology*, vol. 220, pp. 202-214, 2015.

- [44] Simonelli, M., "Microstructure Evolution and Mechanical Properties of Selective Laser Melted Ti-6Al-4V," PhD Thesis School of Aeronautical, Automotive, Chemical and Materials Engineering, Loughborough University, Leicestershire, UK, 2014.
- [45] Vaithilingam, J., Goodridge, R. D., Hague, R. J. M., Christie, S. D. R., and Edmondson, S., "The Effect of Laser Remelting on the Surface Chemistry of Ti6Al4V Components Fabricated by Selective Laser Melting," *Journal of Materials Processing Technology*, vol. 232, pp. 1-8, 2016.
- [46] Kasperovich, G., Haubrich, J., Gussone, J., and Requena, G., "Correlation between Porosity and Processing Parameters in TiAl6V4 Produced by Selective Laser Melting," *Materials & Design*, vol. 105, pp. 160-170, 2016.
- [47] Thijs, L., Verhaeghe, F., Craeghs, T., Humbeeck, J. V., and Kruth, J.-P., "A Study of the Microstructural Evolution during Selective Laser Melting of Ti-6Al-4V," *Acta Materialia*, vol. 58, pp. 3303-3312, 2010.
- [48] Vrancken, B., Thijs, L., Kruth, J.-P., and Humbeeck, J. V., "Heat Treatment of Ti6Al4V Produced by Selective Laser Melting: Microstructure and Mechanical Properties," *Journal of Alloys and Compounds*, vol. 541, no. 0, pp. 177-185, 2012.
- [49] Song, B., Dong, S., Liao, H., and Coddet, C., "Process Parameter Selection for Selective Laser Melting of Ti6Al4V based on Temperature Distribution Simulation and Experimental Sintering," *International Journal of Advanced Manufacturing Technology*, vol. 61, pp. 967-974, 2012.
- [50] Uhlmann, E., Kersting, R., Klein, T. B., Cruz, M. F., and Borille, A. V., "Additive Manufacturing of Titanium Alloy for Aircraft Components," *Procedia CIRP*, vol. 35, pp. 55-60, 2015.
- [51] Baufeld, B., Biest, O. v. d., and Gault, R., "Microstructure of Ti-6Al-4V Specimens Produced by Shaped Metal Deposition," *International Journal of Material Research*, vol. 100, no. 11, pp. 1536-1542, 2009.
- [52] Zhai, Y., Galarraga, H., and Lados, D. A., "Microstructure Evolution, Tensile Properties, and Fatigue Damage Mechanisms in Ti-6Al-4V Alloys Fabricated by Two Additive Manufacturing Techniques," *Procedia Engineering*, vol. 114, pp. 658-666, 2015.
- [53] Hrabec, N. and Quinn, T., "Effects of Processing on Microstructure and Mechanical Properties of a Titanium Alloy (Ti-6Al-4V) Fabricated using Electron Beam Melting (EBM), Part 1: Distance from Build Plate and Part Size," *Materials Science & Engineering A*, vol. 375, pp. 264-270, 2013.
- [54] Hrabec, N. and Quinn, T., "Effects of Processing on Microstructure and Mechanical Properties of a Titanium Alloy (Ti-6Al-4V) Fabricated using Electron Beam Melting (EBM), Part 2: Energy Input, Orientation, and Location," *Materials Science & Engineering A*, vol. 573, pp. 271-277, 2013.

- [55] Gong, H., Rafi, K., Starr, T., and Stucker, B., "The Effects of Processing Parameters on Defect Regularity in Ti-6Al-4V Parts Fabricated By Selective Laser Melting and Electron Beam Melting," in *International Solid Freeform Fabrication Symposium*, USA, 2013, pp. 424-439.
- [56] Price, S., Cheng, B., Lydon, J., Cooper, K., and Chou, K., "On Process Temperature in Powder-Bed Electron Beam Additive Manufacturing: Process Parameter Effects," *Journal of Manufacturing Science and Engineering*, vol. 136, pp. 061019 (1-10), 2014.
- [57] Spierings, A. B. and Levy, G., "Comparison of Density of Stainless Steel 316L Parts Produced with Selective Laser Melting using Different Powder Grades," in *International Solid Freeform Fabrication Symposium*, USA, 2009, pp. 342-353.
- [58] Spierings, A. B., Herres, N., and Levy, G., "Influence of the Particle Size Distribution on Surface Quality and Mechanical Properties in Additive Manufactured Stainless Steel Parts," in *International Solid Freeform Fabrication Symposium*, USA, 2010, pp. 397-406.
- [59] Cherry, J. A., Davies, H. M., Mehmood, S., Lavery, N. P., Brown, S. G. R., and Sienz, J., "Investigation into the Effect of Process Parameters on Microstructural and Physical Properties of 316L Stainless Steel Parts by Selective Laser Melting," *International Journal of Advanced Manufacturing Technology*, vol. 76, pp. 869-879, 2015.
- [60] Delgado, J., Ciurana, J., and Rodríguez, C. A., "Influence of Process Parameters on Part Quality and Mechanical Properties for DMLS and SLM with Iron-Based Materials," *International Journal of Advanced Manufacturing Technology*, vol. 60, pp. 601-610, 2012.
- [61] Król, M., Kujawa, M., Dobrzański, L. A., and Tański, T., "Influence of Technological Parameters on Additive Manufacturing Steel Parts in Selective Laser Sintering," *Archives of Materials Science and Engineering*, vol. 67, no. 2, pp. 84-92, 2014.
- [62] Kistler, N. A., "Characterization of Inconel 718 Fabricated through Powder Bed Fusion Additive Manufacturing," B.Sc. Thesis, Materials Science and Engineering, Pennsylvania State University, USA, 2015.
- [63] Lewandowski, J. J. and Seifi, M., "Metal Additive Manufacturing: A Review of Mechanical Properties," *Annual Review of Materials Research*, vol. 46, pp. 151-186, 2016.
- [64] Frazier, W. E., "Metal Additive Manufacturing: A Review," *Journal of Materials Engineering and Performance*, vol. 23, no. 6, pp. 1917-1928, 2014.
- [65] Gong, X. and Chou, K., "Microstructures of Inconel 718 by Slective Laser Melting," in *TMS 2015 Annual Meeting Supplemental Proceedings*, Orlando, Florida, USA, 2015, pp. 461-468.

- [66] Song, H. Y., "Multi-Scale Microstructure Characterization for Improved Understanding of Microstructure-Property Relationship in Additive Manufacturing " PhD, Welding Engineering, Ohio State University, Ohio, USA, 2016.
- [67] Qiu, C., Adkins, N. J. E., and Attallah, M. M., "Selective Laser Melting of Invar 36: Microstructure and Properties," *Acta Materialia*, vol. 103, pp. 382-395, 2016.
- [68] Spierings, A. B. and Levy, G., "Comparison of Density of Stainless Steel 316L Parts Produced with Selective Laser Melting using Different Powder Grades," in *Annual International Solid Freeform Fabrication Symposium*, Texas, USA, 2009, pp. 342-353: University of Texas in Austin.
- [69] Spierings, A. B., Herres, N., and Levy, G., "Influence of the Particle Size Distribution on Surface Quality and Mechanical Properties in Additive Manufactured Stainless Steel Parts," in *Annual International Solid Freeform Fabrication Symposium*, Texas, USA, 2010, pp. 397-406: University of Texas in Austin.
- [70] Cherry, J. A., Davies, H. M., Mehmood, S., Lavery, N. P., Brown, S. G. R., and Sienz, J., "Investigation into the Effect of Process Parameters on Microstructural and Physical Properties of 316L Stainless Steel Parts by Selective Laser Melting.," *International Journal of Advanced Manufacturing Technology*, vol. 76, pp. 869-879, 2014.
- [71] Song, B. *et al.*, "Differences in Microstructure and Properties between Selective Laser Melting and Traditional Manufacturing for Fabrication of Metal Parts: A Review," *Frontiers of Mechanical Engineering*, vol. 10, no. 2, pp. 111-125, 2015.
- [72] Siddique, S., Imran, M., Wycisk, E., Emmelmann, C., and Walther, F., "Influence of Process-Induced Microstructure and Imperfections on Mechanical Properties of AlSi12 Processed by Selective Laser Melting," *Journal of Materials Processing Technology*, vol. 221 pp. 205-213, 2015.
- [73] Hanzl, P., Zetek, M., Bakša, T., and Kroupa, T., "The Influence of Processing Parameters on the Mechanical Properties of SLM Parts," *Procedia Engineering*, vol. 100, pp. 1405-1413, 2015.
- [74] Górski, F., Kuczko, W., and Wichniarek, R., "Influence of Process Parameters on Dimensional Accuracy of Parts Manufactured Using Fused Deposition Modelling Technology," *Advances in Science and Technology Research Journal*, vol. 7, no. 19, pp. 27-35, 2013.
- [75] Schajer, G. S. and Ruud, C. O., "Overview of Residual Stresses and Their Measurement," in *Practical Residual Stress Measurement Methods*, G. S. Schajer, Ed. 1st ed. United Kingdom: John Wiley & Sons Ltd, 2013.
- [76] Shiomi, M., Osakada, K., Nakamura, K., Yamashita, T., and Abe, F., "Residual Stress within Metallic Model Made by Selective Laser Melting Process," *CIRP Annals - Manufacturing Technology*, vol. 53, no. 1, pp. 195-198, 2004.

- [77] Mercelis, P. and Kruth, J.-P., "Residual Stresses in Selective Laser Sintering and Selective Laser Melting," *Rapid Prototyping Journal*, vol. 12, no. 5, pp. 254-265, 2006.
- [78] Casavola, C., Campanelli, S. L., and Pappalettere, C., "Experimental Analysis of Residual Stresses in the Selective Laser Melting Process," in *Proceedings of the XIth International Congress and Exposition*, Orlando, Florida USA, 2008: Society for Experimental Mechanics Inc.
- [79] Belle, L. V., Boyer, J.-C., and Vansteenkiste, G., "Investigation of Residual Stresses induced during the Selective Laser Melting Process," *Key Engineering Materials*, vol. 554-557, pp. 1828-1834, 2013.
- [80] Ibraheem, A. K., Derby, B., and Withers, P. J., "Thermal and Residual Stress Modelling of the Selective Laser Sintering Process," in *Materials Research Society Symposium Proceedings*, Boston, Massachusetts, United Kingdom, 2003, vol. 758: Materials Research Society.
- [81] Yadroitsava, I. and Yadroitsev, I., "Residual Stress in Metal Specimens Produced by Direct Metal Laser Sintering," in *Annual International Solid Freeform Fabrication Symposium*, Texas, USA, 2015.
- [82] Wang, X. and Chou, K., "Residual Stress in Metal Parts Produced by Powder-Bed Additive Manufacturing Processes," in *Annual International Solid Freeform Fabrication Symposium*, Texas, USA, 2015.
- [83] Slotwinski, J. A., Garboczi, E. J., and Hebenstreit, K. M., "Porosity Measurements and Analysis for Metal Additive Manufacturing Process Control," *Journal of Research of the National Institute of Standards and Technology*, vol. 119, pp. 494-528, 2014.
- [84] Weingarten, C., Buchbinder, D., Pirch, N., Meiners, W., Wissenbach, K., and Poprawe, R., "Formation and Reduction of Hydrogen Porosity During Selective Laser Melting of AlSi10Mg," *Journal of Materials Processing Technology*, vol. 221, pp. 112-120, 2015.
- [85] Yasa, E. and Kruth, J.-P., "Microstructural Investigation of Selective Laser Melting 316L Stainless Steel Parts Exposed to Laser Re-Melting," *Proceedings of the 1st CIRP Conference on Surface Integrity (CSI)* vol. 19, pp. 389-395, 2011.
- [86] Bland, S. and Aboulkhair, N. T., "Reducing Porosity in Additive Manufacturing," *Metal Powder Report*, vol. 70, no. 2, pp. 79-81, 2015.
- [87] Aboulkhair, N. T., Everitt, N. M., Ashcroft, I., and Tuck, C., "Reducing Porosity in AlSi10Mg Parts Processed by Selective Laser Melting," *Additive Manufacturing*, vol. 1-4, pp. 77-86, 2014.

- [88] Simonelli, M., Tse, Y. Y., and Tuck, C., "Microstructure of Ti-6Al-4V Produced by Selective Laser Melting," *Journal of Physics: Conference Series*, vol. 371 (012084), 2012.
- [89] Kempen, K., L.Thijs, Humbeeck, J. V., and Kruth, J.-P., "Mechanical Properties of AlSi10Mg Produced by Selective Laser Melting," *Physics Procedia*, vol. 39, pp. 439-446, 2012.
- [90] Harrison, N. J., Todd, I., and Mumtaz, K., "Reduction of Micro-Cracking in Nickel Superalloys Processed by Selective Laser Melting: A Fundamental Alloy Design Approach," *Acta Materialia*, vol. 94, pp. 59-68, 2015.
- [91] Bourell, D. L., Leu, M. C., and Rosen, D. W., "Roadmap for Additive Manufacturing: Identify the Future of Freeform Processing," in "International Solid Freeform Fabrication Symposium," USA2009

Chapter 2

Selective Laser Melting of Invar 36

Complete Citation:

Yakout, M., Cadamuro, A., Elbestawi, M.A., Veldhuis, S.C. (2017). The selection of process parameters in additive manufacturing for aerospace alloys. *The International Journal of Advanced Manufacturing Technology*, Volume 92, Issue 5-8, pp 2081-2098.

Doi: 10.1007/s00170-017-0280-7

Copyright:

Reprinted with permission copyrighted by Springer Nature, 2017.

Relative Contributions:

M. Yakout: Performed experiments, analysis, and data interpretation. Wrote the first draft of the manuscript. Helped with submitting the final manuscript to the journal (corresponding author).

A. Cadamuro: Was involved in the density measurements.

M. A. Elbestawi: Co-supervisor of M. Yakout. Revised the manuscript. Was responsible of submitting the final manuscript to the journal (corresponding author).

S. C. Veldhuis: Co-supervisor of M. Yakout. Revised the manuscript.

Abstract:

Invar 36 has gained considerable popularity in many industries, including the aerospace industry, because of its low coefficient of thermal expansion. In this paper, a brief overview for the research needs in metal additive manufacturing is presented. A thorough study for the influence of process parameters on the quality of the parts produced is presented. This study is beneficial for the long-term growth of the additive manufacturing industry. The paper aims to select the process parameters that can be used to fabricate dense parts from Invar 36 (UNS K93600) using the selective laser melting process. In this research, a group of cubes was fabricated using different process parameters from Invar 36 powder using a selective laser melting machine. The density, microstructures, and surface features of these cubes were measured. Experimental observations were drawn from the results of the preliminary analyses. The influence of the process parameters on the density of the parts produced is discussed in this paper.

Keywords:

Selective laser melting; Invar 36 fabrication; Metal additive manufacturing; Aerospace industry; Microstructure analysis; Density measurement.

Acronyms:

AM	Additive manufacturing
CTE- α	Coefficient of thermal expansion
FCC	Face centered cubic
SLM	Selective laser melting
PBF	Powder bed fusion

DED	Direct energy deposition
EBM	Electron beam melting
HIP	Hot isostatic pressing
OFAT	one-factor-at-a-time
SEM	Scanning electron microscopy
EDS	Energy-dispersive X-ray spectroscopy
ANOVA	Analysis of variance

Notations:

P	Laser power (W)
v	Laser scanning speed (mm/s)
h	Hatch spacing (mm)
t	Layer thickness (mm)
E_v	Laser energy density (J/mm ³)
PD	Point distance (mm)
θ	Exposure time (s)
w	Stripe width (mm)
γ	Stripe overlap (mm)
δ	Beam offset (μm)
E_m	Energy density of melting (J/mm ³)
c	Specific heat capacity (J/kg.K)
ρ	Density (kg/mm ³)
T_m	Melting temperature (K)
T_a	Ambient temperature (K)

e	Energy ratio
Y	Yield strength (MPa)
E	Modulus of elasticity (GPa)
W	Weight (kg)

Acknowledgment:

The authors thank the COM DEV International Ltd. (currently part of Honeywell Aerospace) team in Cambridge, ON Canada for highlighting the importance of Invar 36 in the aerospace industry. The authors also thank the Additive Metal Manufacturing Inc. team in Concord, ON Canada for offering their facility for testing.

2.1 Introduction

This paper provides a brief review of various technologies for metal additive manufacturing (AM). Metal AM processes are classified based on the state of the raw material. It shows an overview of the research needs in AM for aerospace alloys. Invar 36 (UNS K93600), known as Fe-36wt%Ni alloy, is an iron-nickel alloy with a very low coefficient of thermal expansion (CTE- α) as shown in Figure 2.1.

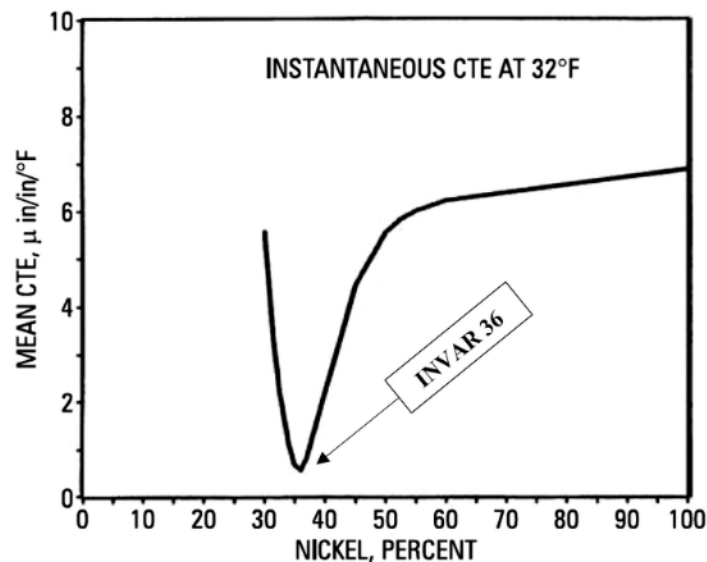


Figure 2.1: Effect of nickel content on the coefficient of thermal expansion (CTE) [1].

The face centered cubic (FCC) structure of Invar 36 shows excellent toughness and fair mechanical properties. Invar 36 has been used in the aerospace industry for applications that require high dimensional stability since 1985. Subtractive processes have been used to manufacture Invar 36 parts and components for a long time but these processes are not suitable for very complex geometries. There is therefore a limitation on the use of Invar 36 in some applications because maintaining its mechanical properties when welded or otherwise joined is very difficult [1-4]. Recently, AM processes have been used to

produce very complex geometries with acceptable mechanical properties. Finding the optimal process parameters for fabricating each material and design is a big challenge [5-7]. This paper illustrates the selection of the process parameters to produce dense parts of Invar 36 using the selective laser melting (SLM) process. The microstructure and material composition of the parts produced have been studied. The analysis obtained is helpful in determining the capability of the SLM process for fabricating Invar 36 parts in industries such as aerospace, automotive, etc.

2.2 Research background

2.2.1 Metal additive manufacturing processes

Material extrusion, direct energy deposition (DED), and powder bed fusion (PBF) are the most commonly used processes for additive metal manufacturing [8]. SLM and electron beam melting (EBM) are powder bed fusion processes. SLM is a powder bed process, in which a metal powder is distributed and spread evenly to create a layer in a bed. Then, a laser source is used to fully melt the powder layer by layer over the cross-sections of the part [9]. Figure 2.2 shows a typical SLM process. The SLM process is available for many metals and composites. It starts with the full melting of metallic powders to produce dense objects layer by layer with certain mechanical properties like tensile strength, hardness, elongation, etc. being comparable to traditionally produced bulk materials while properties related to fatigue being considerably lower. The ability of the SLM process to fabricate non-ferrous metals such as titanium, aluminum, and copper makes it beneficial for several industries, especially aerospace and automotive [10, 11]. EBM is typically similar to SLM except that an electron gun is used for melting preheated powder instead of using a laser source for melting powder, which makes the EBM more powerful because the build rate in EBM is faster than SLM. Also, EBM must take place in high vacuum [12].

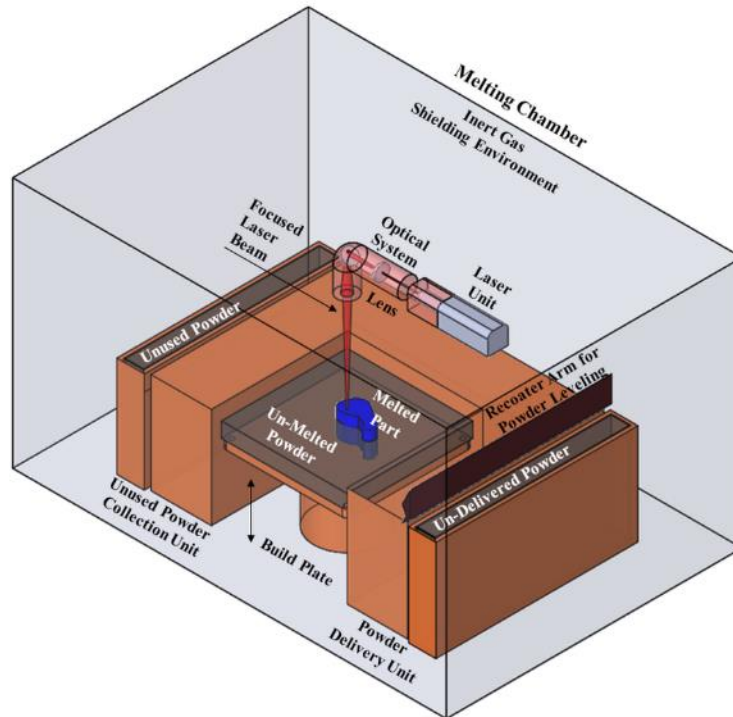


Figure 2.2: Overview of a typical selective laser melting process. [10, 13, 14]

The dimensional accuracy and surface finish in powder bed fusion are typically better than those in material extrusion process because the resolution of material extrusion processes is dictated by the wire diameter versus powder particle size [15-18]. Although DED processes have the unique ability to repair metallic parts that cannot be repaired by powder bed fusion processes (SLM and EBM) [19], they do not have the same ability to produce beneficial mechanical properties like SLM and EBM [20]. Powder bed fusion processes are commonly used for metallic applications, especially for complex designs. EBM is currently the preferred process for fabricating metals, but it is limited by the electrical conductivity of the material and component size due to the need to maintain a high level of vacuum; however, SLM is more versatile [21]. Thus, SLM has been chosen in this study to fabricate several aerospace alloys.

2.2.2 Process parameters of selective laser melting (SLM)

Starting from the raw material, the powder grain size affects the density and consequently the mechanical properties of the parts produced in a SLM process [22, 23]. Moreover, point distance, exposure time, scanning speed, layer thickness, and building direction show a strong influence on the quality of the parts produced; including surface microstructure, fatigue strength, hardness, density, and surface roughness. These parameters should be controlled during the fabrication process to get a reasonable surface finish and fair mechanical properties [23-26]. The SLM process parameters include laser power (P), scanning speed (v), point distance (PD), exposure time (θ), hatch spacing (h), stripe width (w), stripe overlap (γ), beam offset (δ), and layer thickness (t) as shown in Figure 2.3. These parameters define the laser energy density (E_v) as follows:

$$E_v = \frac{P}{(v \times h \times t)} \quad (2.1)$$

$$v = PD / \theta \quad (2.2)$$

where P is the laser power in (W), v is the scanning speed in (mm/s), h is the hatch spacing in (mm), t is the layer thickness in (mm), and E_v is the laser energy density in (J/mm³).

The energy density required for melting a certain material (E_m) depends on the thermal properties of the material and is estimated by the following equation:

$$E_m = c\rho(T_m - T_a) \quad (2.3)$$

where c is the specific heat capacity in (J/kg.K), ρ is the material density in (kg/mm³), T_m is the melting temperature in (K), T_a is the ambient temperature in (K), and E_m is the melting energy density in (J/mm³).

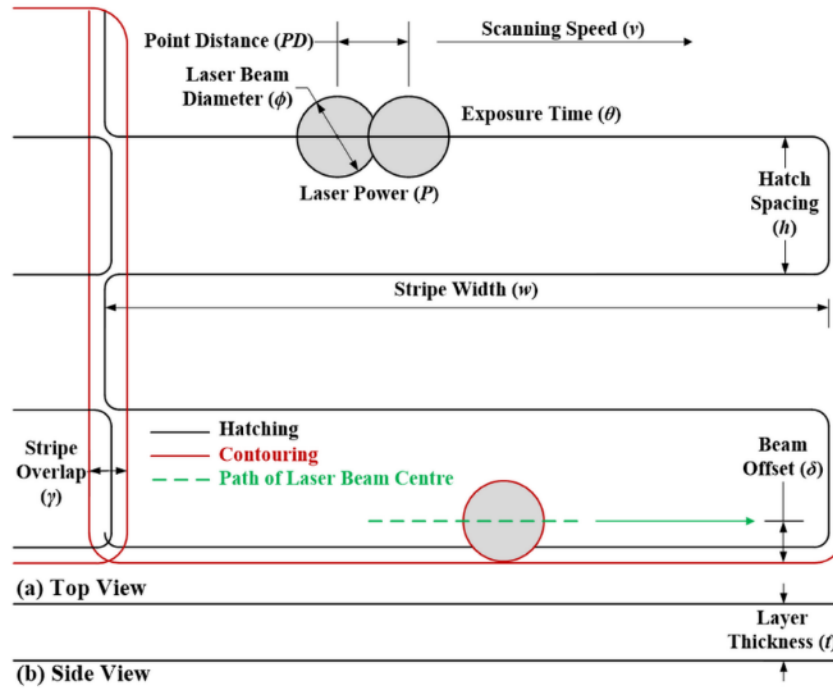


Figure 2.3: Illustration of the SLM process parameters. (a) Top view and (b) side view of a build layer.

A dimensionless ratio between the laser energy density and the required energy density for melting can be defined as the (e) ratio. This ratio describes the relationship between the energy density of the laser source and the energy required for melting the metal powder.

$$e = E_v / E_m \quad (2.4)$$

2.2.3 Density of additive manufacturing parts

AM parts differ from wrought or forged parts in that they can have a large number of defects/stress risers including, but not limited to, voids either from gas pores or imperfections, partially melted powder, lack of adhesion/pre-existing cracks formed between subsequent printed layers, and powder particles stuck on the surface [27].

Void formation in AM parts is one of the most challenging problems in this industry. This impacts many applications, especially high stress and high fatigue applications. These voids could be either gas pores or imperfections. The gas pores have a spherical shape and come from the entrapment of gases in a build layer. However, imperfections have a non-uniform shape and come from partially melted powder. The amount of voids present in a part is dependent on the melting chamber as well as the process parameters, especially the laser source and melting energy [28, 29]. The following methods are suggested in the literature to reduce void formation:

1. Efficient drying of the powder and tight control of the process parameters [29]
2. Increasing the laser power for processing materials with high reflectivity and low energy absorption [30]
3. Experimenting with the scanning speed, scanning paths, and overlap for controlling the type of the pores and reducing the amount of pores [31]
4. Hot isostatic pressing (HIP) of the AM parts for porosity elimination, fatigue damage refinement, powder compaction, and material joining enhancement [32]

The mechanical behaviors of the AM parts are significantly affected by the amount of voids formed between the layers during the process, as well as the residual stresses in those parts. The tensile strength, fatigue strength, and ductility are strongly affected by pore size. The fatigue crack growth is influenced by the residual stresses [33, 34]. A study showed that the microstructure of AM parts has a significant effect on the mechanical properties such as fatigue behavior, mechanical strength, percent elongation, etc. The microstructure of the AM parts is influenced by the imperfections formed during the process and/or the post-processing. Thus, the mechanical properties could be enhanced by controlling the process parameters or by heat treatment. Although AM parts show better mechanical properties

than cast parts, they still have a lot of challenges due to the presence of pores and anisotropy [35, 36]. In the SLM process, the steep thermal gradients as well as fast solidification have a negative effect on the mechanical properties. Recently, most AM research has focused on enhancing the mechanical properties of metals through heat treatment procedures, especially for aluminum and titanium alloys [37, 38]. HIP processes and heat treatments have also been used to reduce the voids as well as the residual stresses, and consequently, to enhance mechanical properties [39]. Oftentimes, there are also micro-cracks that are formed during the SLM process either from separation between two subsequent layers or due to the large thermal gradients associated with the heat energy added when melting nearby powder and/or contraction due to solidification and subsequent cooling of a region of the part [40]. These cracks can be controlled and/or eliminated by optimizing the process parameters. They also may be controlled by modifying the material composition to increase the thermal shock resistance. Thus, a clear understanding of the relationship between process parameters and quality of the parts produced is recommended.

2.3 Experimental design

2.3.1 Design range for the SLM process parameters

In this paper, a specific range for each process parameter was suggested based on a preliminary energy density calculation. In reference [7], Invar 36 samples were fabricated using a concept laser CL M2 machine. The effect of increasing the scanning speed of a SLM system on the porosity, microstructure, and mechanical properties of the parts produced was studied. The authors did not study other parameters such as laser power, hatch spacing, stripe width, and stripe overlap. Their results were taken into consideration throughout this study. Table 2.1 illustrates the specifications of the powder that was used in reference [7] and the current study. The SLM process parameters that would be used to

fabricate Invar 36 parts with high density are not defined in the literature. The process parameters for fabricating dense components from 18Ni (300) maraging steel (*UNS K93120*) powder were experimentally defined and suggested by the supplier. As shown in Table 2.2, the material composition of Invar 36 is very close to that of maraging steel. It is noted that the thermal properties are similar in both materials except for the coefficient of thermal expansion. Table 2.3 illustrates the material properties of maraging steel and Invar 36 where ρ is density, T_m is melting temperature, k is thermal conductivity, c is specific heat capacity, α is coefficient of thermal expansion, Y is yield strength, and E is modulus of elasticity. The authors assumed that the coefficient of thermal expansion would have a strong influence on the induced residual stresses but a minor influence on the density and other mechanical properties. Thus, the SLM process parameters set for maraging steel fabrication was used as an initial estimate to optimize the SLM process parameters for fabricating the Invar 36 components with a high density. P is the laser power in (W), v is the scanning speed in (mm/s), h is the hatch spacing in (mm), w is the stripe width in (mm), γ is the stripe overlap in (mm), δ is the beam offset in (μm), and t is the layer thickness in (μm). Table 2.4 shows the process parameter set that was used in reference [7] for the Invar 36 fabrication process using a CL M2 machine as well as the parameter set for fabricating dense maraging steel components using a SLM machine. These two sets of parameters were used to define a specific range for each parameter as follows:

1. Use the process parameters of maraging steel fabrication as a reference.
2. Change one parameter at a time while keeping the other parameters fixed, based on a one-factor-at-a-time (OFAT) design.
3. Define threshold values for each parameter based on reference [7].
4. Calculate the energy ratio e in each case and compare the values.

Table 2.1: The Invar 36 powder used compared with reference [7].

Source	Supplier	Powder size	Machine	Laser source
Reference [7]	TLS Technik	25-50 μm	SLM machine	Nd, YAG laser
Current study	Sandvik Osprey	15-45 μm	SLM machine	Yb fiber laser

Table 2.2: Material composition of maraging steel and Invar 36 powder.

Maraging steel powder (wt%)											
Fe	Ni	Co	Mo	Ti	Cr	Cu	Mn	Si	Al	C	P&S
Bal.	17-19	8.5-9.5	4.5-5.2	0.6-0.8	<0.5	<0.5	<0.1	<0.1	<0.15	<0.03	<0.02
Invar 36 powder (wt%)											
Fe	Ni						Mn	Si			C
Bal.	35.5-36.5						<0.5	<0.25			<0.02

Table 2.3: Material properties of maraging steel and Invar 36 alloys.

Property	ρ (kg/m^3)	T_m ($^{\circ}\text{C}$)	k (W/m.K)	c (J/kg.K)	α (m/m.K^{-1})	Y (MPa)	E (GPa)
Maraging steel	8100	1413	15	450	8.6×10^{-6}	1000	180
Invar 36	8050	1427	10.5	515	≈ 0	248	141

Table 2.4: The designed range for each process parameter.

Parameter	P (W)	v (mm/s)	h (mm)	w (mm)	γ (mm)	δ (μm)	t (μm)	
Reference [7]	400	1800 \rightarrow 4300	0.30	Not mentioned			30	
Maraging steel	285	960	0.11	10	0.08	55	40	
Families	A	150 \rightarrow 370	960	0.11	10	0.08	55	40
	B	285	700 \rightarrow 3000	0.11	10	0.08	55	40
	C	285	960	0.08 \rightarrow 0.32	10	0.08	55	40
	D	285	960	0.11	7 \rightarrow 10	0.08	55	40
	E	285	960	0.11	10	0.06 \rightarrow 0.10	55	40

Based on the above procedure, a specific range for each process parameter was defined as shown in Table 2.4 and Figure 2.4 forming five different families to study the influence of laser power, scanning speed, hatch spacing, stripe width, and stripe overlap, respectively. The first family (A) involved varying the laser power from 150 to 370 W, the second family (B) varied the scanning speed from 700 to 3000 mm/s, the third family (C) varied the hatch spacing from 0.08 to 0.32 mm, the fourth family (D) varied the stripe width from 7 to 10 mm, and the fifth family (E) varied the stripe overlap from 0.06 to 0.10 mm. Figure 2.4a shows that increasing the laser power increases the energy ratio (this means that the energy density of the laser will increase). However, increasing either the scanning speed or the hatch spacing decreases the energy ratio as shown in Figure 2.4b and c. The stripe width and stripe overlap do not have any effect on the energy ratio because they do not have any influence on the energy density of the laser.

2.3.2 Experimental design for the SLM process parameters

The OFAT method was used to design the experiments for studying a wide range of each individual process parameter and its effect on the density, microstructure, and material composition of the parts produced. Although the OFAT method will not show the interactions among the factors, it will allow testing multi-factors at multiple levels as well as a wide range of each factor (process parameter). Using the designed range, the 45 different groups as prepared are shown in Table 2.5. Family A consists of 7 groups to study the laser power, family B consists of 19 groups to study the scanning speed, family C consists of 13 groups to study the hatch spacing, family D consists of 3 groups to study the stripe width, and family E consists of 3 groups to study the stripe overlap. Group CD represents the parameters set for fabricating maraging steel which was included in family

C during fabrication but was included in all families during the analysis. Each group was marked with two letters; the first represents the family and the other represents the group.

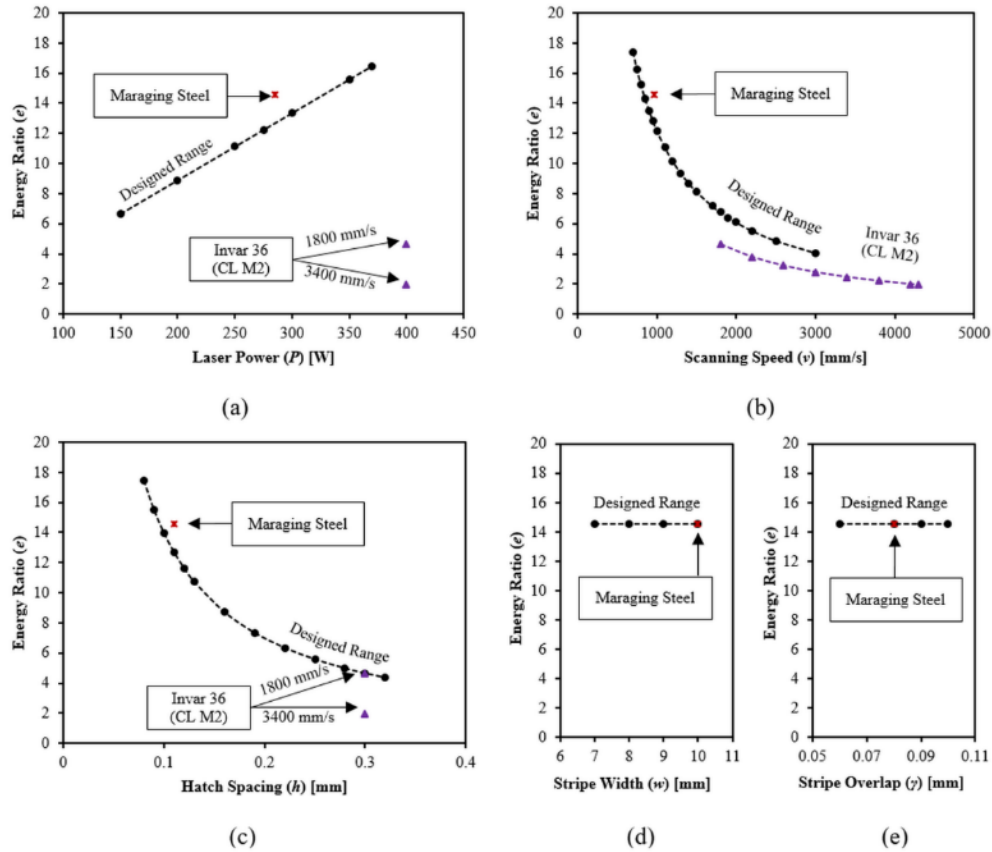


Figure 2.4: The energy ratio e at different parameter sets of (a) laser power, (b) scanning speed, (c) hatch spacing, (d) stripe width, and (e) stripe overlap. Each plot shows the parameter sets available for Invar 36 (from reference [7]), maraging steel, as well as the designed sets in the current study.

Table 2.5: Parameter sets of the fabrication groups (45 groups).

P (W)		v (mm/s)		h (mm)		w (mm)		γ (mm)	
AA	150	BA	700	CA	0.08	DA	7	EA	0.06
↓	↓	↓	↓	↓	↓	DB	8	CD	0.08
CD	285	CD	960	CD	0.11	DC	9	EB	0.09
↓	↓	↓	↓	↓	↓	CD	10	EC	0.1
AG	370	BZ	3000	CO	0.32				
7 Groups		19 Groups		13 Groups (with CD)		3 Groups		3 Groups	

2.4 Experimental work

2.4.1 Material and machine

Invar 36 powder, supplied by Sandvik Osprey UK, was used to fabricate samples for density measurement and microstructure analysis. The size range of the powder was 15-45 μm and the powder was manufactured by inert gas atomization. A SLM machine (EOS M290) was used to fabricate 225 cubes (5 cubes in each group of parameter sets) with a nominal size of 10 \times 10 \times 10 mm. The cubes were fabricated directly to the build plate. The contouring parameters were deactivated during the fabrication process so that only the hatching parameters were considered.

2.4.2 SLM processing

After melting a few layers, the recoater arm started to vibrate causing non-uniform distribution of the metal powder in some groups. This problem occurs when the recoater arm bumps over the edge of an improperly melted layer and causes vibration, this is unacceptable. This vibration is present at excessively high energy levels [41]. Vibration was found in groups AF ($P = 350 \text{ W}$), AG ($P = 370$), and EC ($\gamma = 0.10 \text{ mm}$), which are the groups at the upper and lower boundaries of the A and E families respectively as shown in Figure 2.5a. Once vibration was observed, the build process was stopped and build plate removed. The process was restarted on a new build plate without these group's build parameters. Figure 2.5b shows the cubes as-built before being removed from the build plate. The cubes did not undergo any post-processing procedures and were removed using a band saw with coolant applied to keep the temperature low.

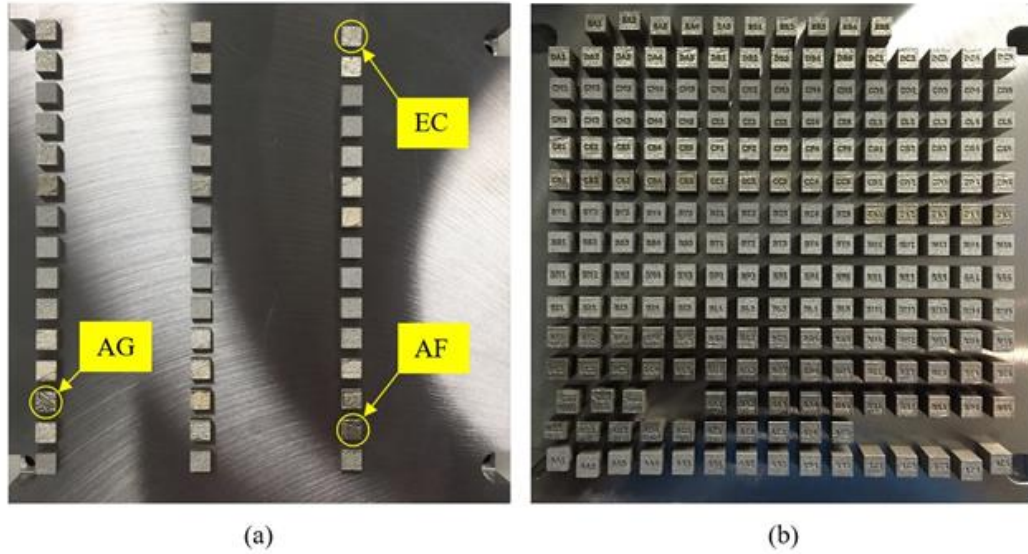


Figure 2.5: (a) The first build plate with the groups that caused vibrations. (b) The second build plate after deactivating the groups at the boundaries.

2.4.3 Density measurement

There are several non-destructive techniques used for measuring the amount of porosity within AM parts such as mass/volume measurement, Archimedes method, X-ray computed tomography (CT) scan, ultrasonic pulse-echo velocity technique, etc. [42].

The density of each cube was measured using Archimedes method. Each cube was weighed twice using a scale; the first time directly on the scale ($W1$) and the second time immersed in distilled water ($W2$) in order to obtain the apparent immersed weight. The density of each sample was calculated using:

$$\rho = \rho_w \times \frac{W1}{W1 - W2} \quad (2.5)$$

The resolution of the scale was ± 0.01 g, water density (ρ_w) was 1 g/cm^3 , and Invar density (ρ_{Bulk}) was 8.05 g/cm^3 . The relative density of each cube was calculated using the following formula:

$$\rho_r \% = \frac{\rho}{\rho_{\text{Bulk}}} \% \quad (2.6)$$

The density error ($\Delta\rho$) was calculated based on the scale error ($\Delta W1 = \Delta W2 = 0.01$). Using the propagation of error effect, the following formula was used to calculate the density error:

$$\Delta\rho = \rho \times \sqrt{\left(\frac{\Delta W1}{W1}\right)^2 + \left(\frac{\sqrt{(\Delta W1)^2 + (\Delta W2)^2}}{W1 - W2}\right)^2} \quad (2.7)$$

Groups BY ($v = 2500$ mm/s) and BZ ($v = 3000$ mm/s) were dropped from the analysis because significant amounts of air bubbles were present in the parts due to internal voids. These two groups were at the lower boundary of the B family build parameters.

2.4.4 Surface microstructure and material composition

The surface morphology and material composition of the fresh (virgin) Invar 36 powder were analyzed using scanning electron microscopy (SEM) and energy-dispersive X-ray spectroscopy (EDS). The results were compared to those obtained in non-virgin powder after processing. The surface microstructure and material composition of the fabricated cubes were studied. The analysis was performed for one cube from each group (45 cubes were analyzed). The microstructural analysis included the morphology, topography, and chemical contrast of the surfaces. The analysis was performed on the side of the cubes to investigate the crack initiation between subsequent layers. However, extra images were taken on the upper surface of specific cubes for comparison.

2.5 Results and discussion

2.5.1 Density of selective laser melted Invar 36

The relative density as well as the density error of each cube were calculated based on the weight measurements. The following observations were noted during the density calculations:

1. The density (relative density) error varies between 0.09 g/cm³ (1.10%) to 0.10 g/cm³ (1.26%), so the maximum relative density error is $\pm 1.26\%$.
2. The density (relative density) tolerance within the same group varies from 0.02 g/cm³ (0.30%) to 0.12 g/cm³ (1.46%).
3. The maximum recorded density (relative density) is 7.98 g/cm³ (99.07%) in sample CA3 ($h = 0.08$ mm) and sample BA4 ($v = 700$ mm/s).
4. The minimum density (relative density) is 7.07 g/cm³ (87.84%) in sample CO5 ($h = 0.32$ mm).

For each family, the relative density of each cube was examined against the process parameter that was varied throughout this family as shown in Figure 2.6. The influence of laser power, scanning speed, hatch spacing, stripe width, and stripe overlap on the relative density of Invar 36 was studied. From the results, it was observed that:

1. Increasing the laser power increases the density (less voids) until reaching a maximum point in which the density will start to decrease due to over melting (the maximum point is 271 W in the current study) as shown in Figure 2.6a.
2. Increasing either the scanning speed or the hatch spacing decreases the density as shown in Figure 2.6b and Figure 2.6c.

3. The stripe width and stripe overlap do not have any effect on the density as shown in Figure 2.6e and Figure 2.6f.

As defined in Section 2.2.2, the laser energy density is dependent on the laser power, scanning speed, and hatch spacing. The laser energy increases with the increase of laser power and/or the decrease of the scanning speed and hatch spacing. The laser energy density was calculated for each cube and the relative density was plotted against it as shown in Figure 2.6d.

Pearson and Spearman correlation tests [43] were conducted between each process parameter and the resultant relative density using Minitab software. The tests show the linear and monotonic dependency of the relative density on the process parameters. Table 2.6 shows the correlation coefficient and p -value for the association between each parameter and the relative density.

From the correlation tests, it is concluded that the laser power, scanning speed, and hatch distance have a strong influence on the density of the parts produced (high coefficients and p -value less than 0.05). In contrast, the stripe width and stripe overlap have a negligible effect (low coefficients and p -value greater than 0.05).

One-way analysis of variance (ANOVA) was conducted to study the proposed relationship between the response variable (relative density) against each factor (process parameter). Table 2.7 summarizes the ANOVA results. These results showed that the laser power, scanning speed, and hatch spacing (combined in the laser energy density) are significantly affecting the relative density of the parts produced.

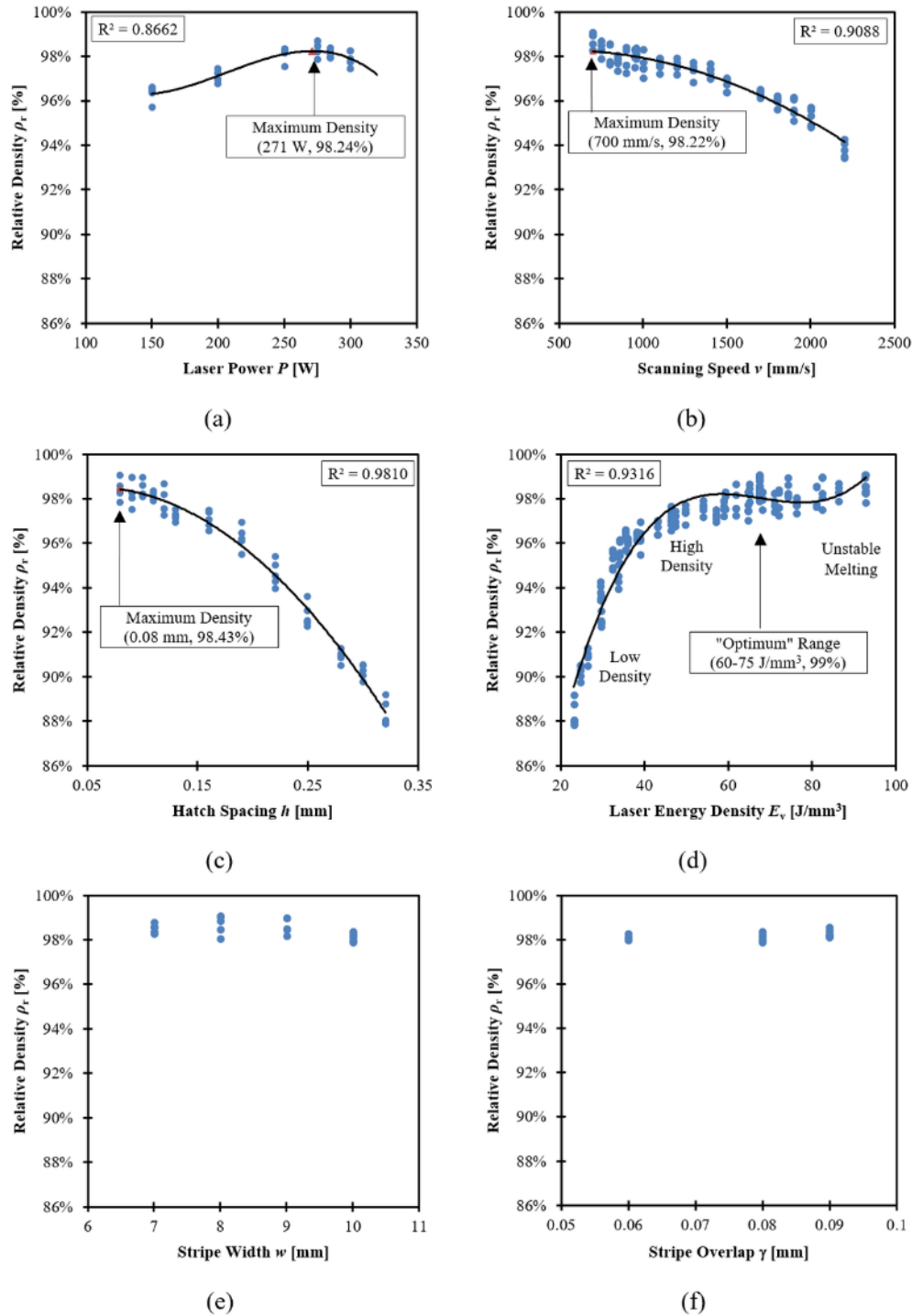


Figure 2.6: Influence of the SLM process parameters on the relative density of Invar 36. (a) Laser power. (b) Scanning speed. (c) Hatch spacing. (d) Laser energy density. (e) Stripe width. (f) Stripe overlap.

Table 2.6: Summary of the correlation results between the process parameters and the relative density.

Dependent variable	Process parameter	Pearson correlation		Spearman correlation	
		r coefficient	p-value	Rho coefficient	p-value
Relative density ρ_r (%)	Laser power P (W)	0.862	0.000	0.637	0.000
	Scanning speed v (mm/s)	-0.932	0.000	-0.898	0.000
	Hatch spacing h (mm)	-0.970	0.000	-0.960	0.000
	Stripe width w (mm)	-0.390	0.089	-0.427	0.061
	Stripe overlap γ (mm)	0.421	0.118	0.435	0.105
	Energy density E_v (J/mm ³)	0.786	0.000	0.872	0.000

Table 2.7: Summary of the ANOVA results between the process parameters and the relative density.

Factors	Levels	Values				
Laser power P (W)	6	150, 200, 250, 275, 285, 300				
	Analysis of variance (ANOVA)					
	Source	DF	Sum of squares	Mean of squares	F value	p -value
	Laser power	5	0.001455	0.000291	31.48	0.000
	Error	24	0.000222	0.000009		
	Total	29	0.001677			
Scanning speed v (mm/s)	18	700, 750, 800, 850, 900, 950, 960, 1000, 1100, 1200, 1300, 1400, 1500, 1700, 1800, 1900, 2000, 2200				
	Analysis of variance (ANOVA)					
	Source	DF	Sum of squares	Mean of squares	F value	p -value
	Scanning speed	17	0.013519	0.000795	68.38	0.000
	Error	72	0.000837	0.000012		
	Total	89	0.014356			
Hatch spacing h (mm)	13	0.08, 0.09, 0.10, 0.11, 0.12, 0.13, 0.16, 0.19, 0.22, 0.25, 0.28, 0.30, 0.32				
	Analysis of variance (ANOVA)					
	Source	DF	Sum of squares	Mean of squares	F value	p -value
	Hatch spacing	12	0.075488	0.006291	297.49	0.000
	Error	52	0.001100	0.000021		
	Total	64	0.076588			
Energy density E_v (J/mm ³)	35	23.2, 24.7, 26.5, 29.4, 29.7, 32.4, 33.8, 34.1, 35.5, 36.0, 38.1, 39.1, 43.2, 46.3, 46.4, 47.3, 49.8, 54.0, 57.1, 58.9, 59.2, 61.8, 64.8, 65.1, 67.5, 68.2, 71.0, 72.0, 74.2, 76.2, 81.0, 82.5, 86.4, 92.5, 92.8				
	Analysis of variance (ANOVA)					
	Source	DF	Sum of squares	Mean of squares	F value	p -value
	Energy density	34	0.113479	0.003338	223.95	0.000
	Error	165	0.002459	0.000015		
	Total	199	0.115938			

To study the expected interactions between the individual parameters, every two parameters were examined together as shown in Figure 2.7. From the analysis of the laser energy density, the following observations were made:

1. Increasing the laser energy density increases the density (and consequently the relative density) of the parts produced.
2. For laser energy density from 20 to 60 J/mm³, the relative density of Invar 36 parts increased from 89% to reach 98%.
3. High relative density (99%) was observed at a laser energy density of approximately 60-75 J/mm³. At that energy level, the material reached a saturated limit and became fully melted and dense.
4. Starting at a laser energy density of approximately 75 J/mm³, high values of residuals were observed.
5. In the SLM process, the laser energy density is a good parameter for studying the material properties because it includes most of the effective process parameters.

Family A showed that the maximum relative density is predicted to be 98.24% at process parameters ($P = 271$ W, $v = 960$ mm/s, and $h = 0.11$ mm) but family B predicted a maximum of 98.22% at process parameters ($P = 285$ W, $v = 700$ mm/s, and $h = 0.11$ mm). Family C predicted the highest relative density of 98.43% at process parameters ($P = 285$ W, $v = 960$ mm/s, and $h = 0.08$ mm).

2.5.2 Surface microstructure

In addition to the density, it was found that the laser power, scanning speed, and hatch distance have a strong influence on the microstructure of the parts produced. From the microstructure analysis, it was observed that increasing the laser energy density reduces the amount of surface voids and increases the material packing factor during the melting

process as shown in Figure 2.8a-c. If the laser energy density exceeded the “optimum” range during the melting of a certain layer, the layer would be over melted and the molten metal would spill over the sides, leaving marks on the preceding layers as shown in Figure 2.8d.

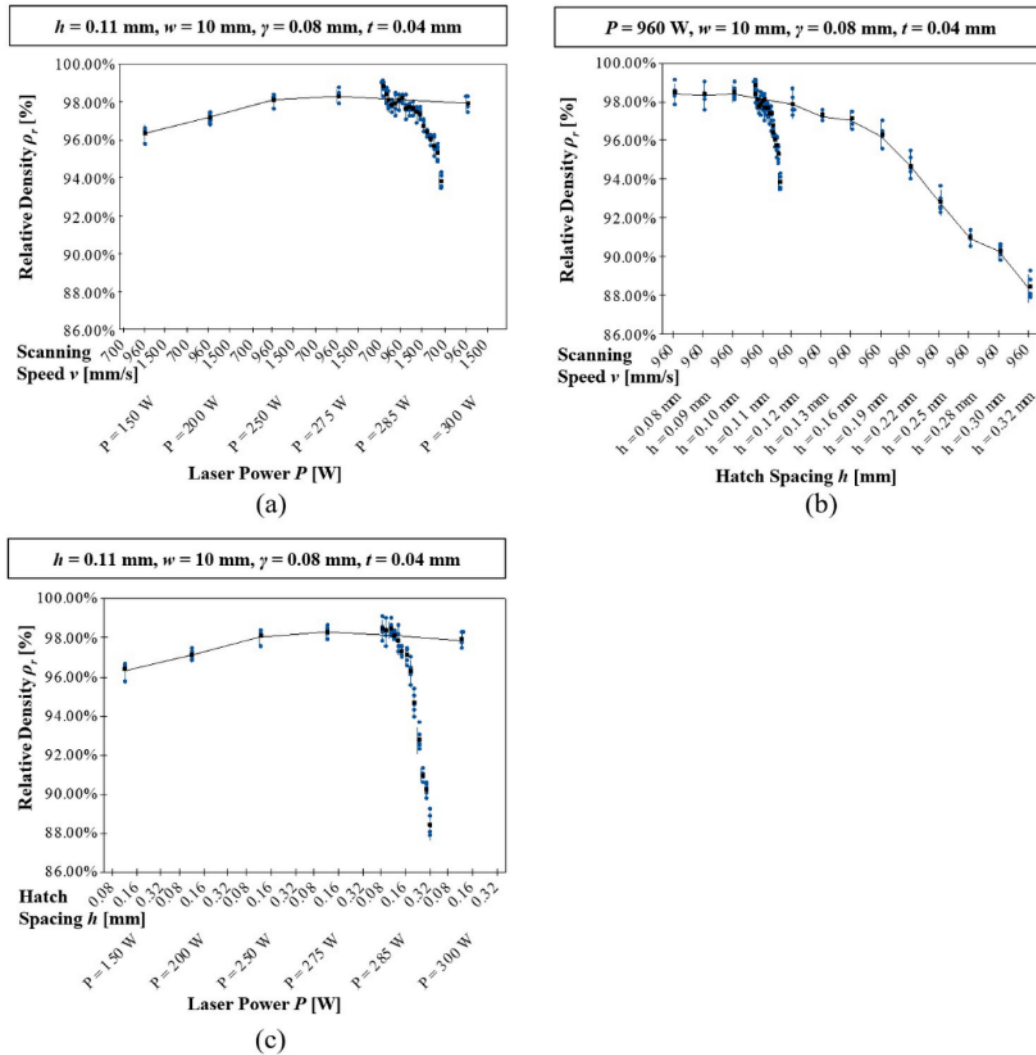


Figure 2.7: Influence of the SLM process parameters on the relative density of Invar 36. (a) Laser power and scanning speed. (b) Scanning speed and hatch spacing. (c) Laser power and hatch spacing.

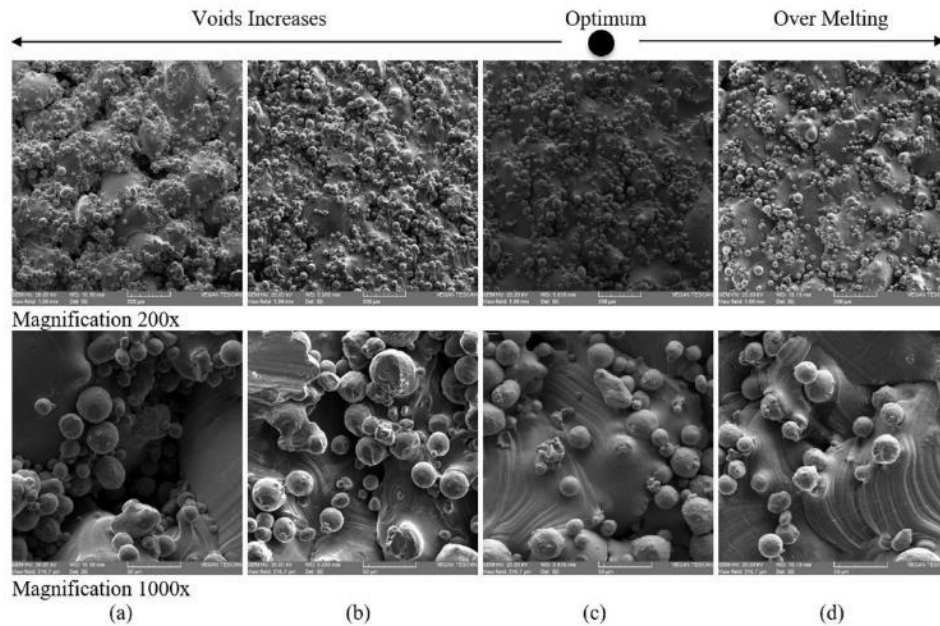


Figure 2.8: Microstructures of the *side* surfaces of some cubes at (a) low energy density with more voids (cube CL5), (b) energy density required for maraging steel (cube EB3), (c) optimum energy density with less voids (cube BD5), and (d) high energy density with no voids but geometrical distortion (cube BA5).

From the microstructure analysis, it is concluded that:

1. At a low energy density, the densities of the parts produced were very low due to the internal voids that were formed during the melting process. In this case, the powder was not fully melted. It is reasonable to expect that the melting pool size was very small and the laser energy density was not enough to melt all of the distributed powder in the immediate area.
2. At a very high energy density, the surface showed footprints of spilled over molten metal. This molten metal on the surface supports the conclusion that the layers were over melted.
3. At the laser energy density of 60-75 J/mm³, the densities of the parts produced were at their greatest value and the surface showed less metal being spilled over.

By performing the SEM analysis on the top surface, the results revealed the same evidences as shown in Figure 2.9. It was also clear that any combination of process parameters that have the same laser energy density showed similar microstructures (and similar densities). The microstructure analysis (see Figure 2.8 and Figure 2.9) showed that porous parts are produced at a laser energy density lower than 60 J/mm^3 . For energy densities higher than approximately 75 J/mm^3 , over melted parts with high distortions are observed.

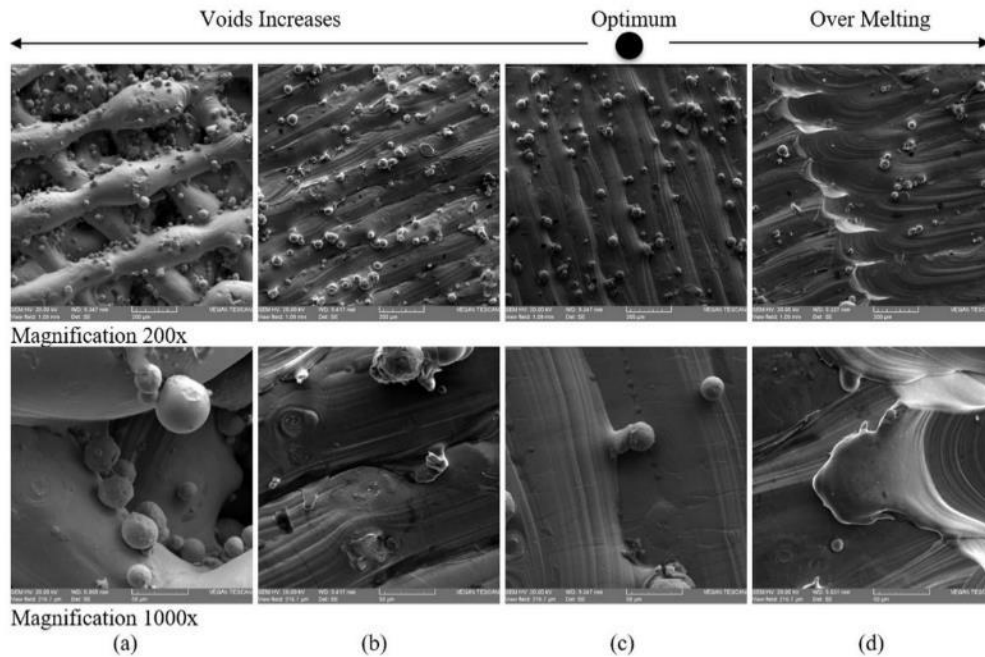


Figure 2.9: Microstructures of the *top* surfaces of some cubes at (a) low energy density with more voids (cube CO4), (b) energy density required for maraging steel (cube CD3), (c) optimum energy density with less voids (cube CC1), and (d) high energy density with no voids but geometrical distortion (cube CA5).

The state of the metal powder is another factor that may affect the optimum laser energy density. It was observed that virgin powder required an optimum laser energy density to be fully melted, which may be different from the amount that is required when processing recycled powder. Figure 2.10a-c shows the microstructure of fresh Invar 36

powder, Invar 36 powder after fabrication, and maraging steel powder recycled many times. The analysis showed that the size of the powder would be different and irregular after recycling as well as the surface of the powder would have micro-cracks (as shown in case of maraging steel). The effect of powder recycling on the optimum energy density is recommended for future work.

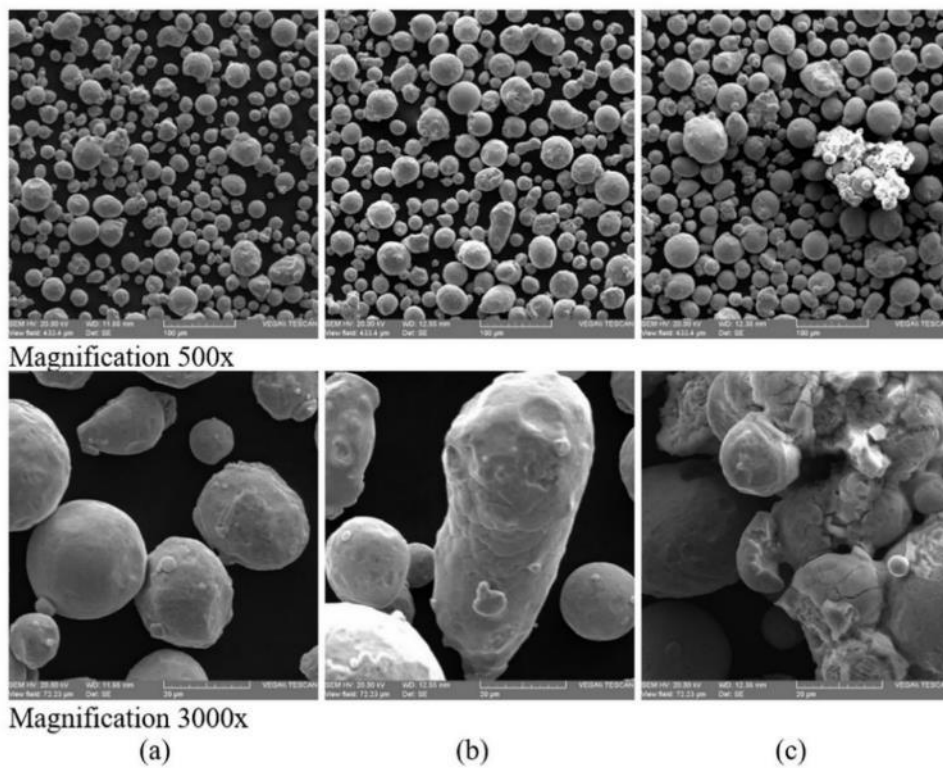


Figure 2.10: Microstructures of (a) virgin Invar 36 powder, (b) Invar 36 powder after one build, and (c) maraging steel powder after many builds.

2.5.3 Material composition

The material composition of the parts did not show that much difference from the wrought material except for the following observations:

1. At a very low energy density, the parts showed irregular distribution of the elements, which means that some particles were not fully melted enough to be evenly distributed.
2. At a very high energy density, some parts showed less Ni content than the rest. This loss in Ni can be attributed to either microsegregation of Ni or vaporization and ejection of some Ni particles from the melting pool during the process. These elements will be converted into soot, this phenomenon is commonly observed during the laser welding process. For such a material (i.e., Invar 36), the Ni content is an important factor for achieving the desired near zero CTE.
3. Evidence of a few inclusions in the SLM Invar 36 cubes. These inclusions might be contaminations if the parts were fabricated after a light material (e.g., aluminum and titanium) was processed in the machine.

It is concluded that any excessive amount of heat in the melting pool may cause some other elements to be splashed around inside the melting chamber and form soot. A small amount of heat in the melting pool would cause partially melted powder and thus voids to be formed [44, 45].

2.5.4 Effect of laser energy density

In the SLM process, the laser energy density includes most of the effective process parameters that affect the mechanical properties and density. It is a function of the laser power, scanning speed, hatch spacing, and layer thickness. Empirically, it was shown that increasing the laser energy density increases the density and reduces the internal voids in the parts produced. These results correspond with some research results from the literature involving different materials [22, 46-50]. Furthermore, the laser energy density combined with the thermal properties of the material affected the quality of the produced parts and

the induced residual stresses. The melting pool size depends on the amount of energy coming from the source and the thermal properties [48, 49]. In conclusion, the effect of increasing the laser energy density is as follows:

1. Increasing the energy density increases the density and reduces void formation because it maintains full melting of the powder.
2. The use of a massive amount of energy generating a very high density will cause high thermal stresses and form a large amount of tensile residual stress.
3. Very high energy density will also cause either microsegregation or vaporization of some elements at their vaporization temperature and eject those elements from the melting pool which will affect the composition of the parts produced.
4. A lower energy density will cause the formation of partially melted powder particles inside the parts produced.

Hence, an optimized range of laser energy density needs to be determined for each material based on experimental verification as shown in Figure 2.11. Optimizing the process parameters for different materials is one of the biggest challenges in the AM sector.

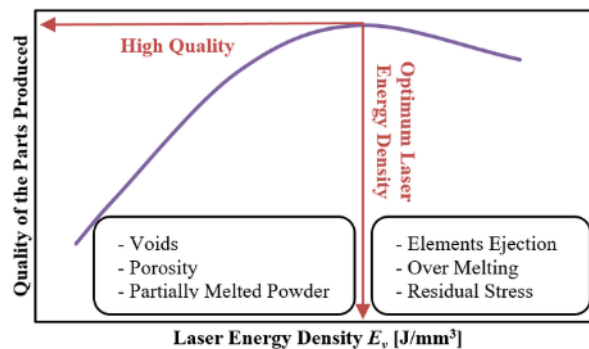


Figure 2.11: Relationship between the optimum laser energy density and the quality of the parts produced.

2.5.5 Recommended sets of SLM process parameters for Invar 36

Based on the energy density calculations, the set of process parameters corresponding to the maximum density in each family (A, B, and C) showed high relative density (approximately 99%). The “optimum” range of laser energy density for fabricating dense components from Invar 36 was between 60 to 75 J/mm³. The laser energy density for fabricating dense maraging steel was 67.5 J/mm³. Although the thermal conductivity of Invar 36 is less than that of maraging steel, they require similar or close energy densities to be fully melted because the energy density depends on a combination of several material properties. Table 2.8 shows the three sets of process parameters corresponding to the maximum density in the three families (A, B, and C). A very high energy density is not recommended because it may affect the performance of the parts produced (over melting) and result in a lower density than expected.

The laser energy density is function of laser power, scanning speed, and hatch spacing. Various combinations of these parameters, which have similar laser energy densities, were grouped and the corresponding relative densities were plotted. It is observed that the densities of the parts produced were dependent on the laser energy density for all combinations of these three parameters. As shown in Figure 2.12, the groups that had the same energy densities showed similar relative densities and similar microstructures.

Table 2.8: Recommended sets of SLM process parameters for fabricating dense Invar 36 components.

Set number	<i>P</i> (W)	<i>v</i> (mm/s)	<i>h</i> (mm)	<i>t</i> (mm)	<i>E_v</i> (J/mm ³)	Within the “optimum” range of laser energy density (60-75 J/mm ³)
1	300	940	0.11	0.04	72.53	
2	285	880	0.11	0.04	73.61	
3	285	960	0.10	0.04	74.22	

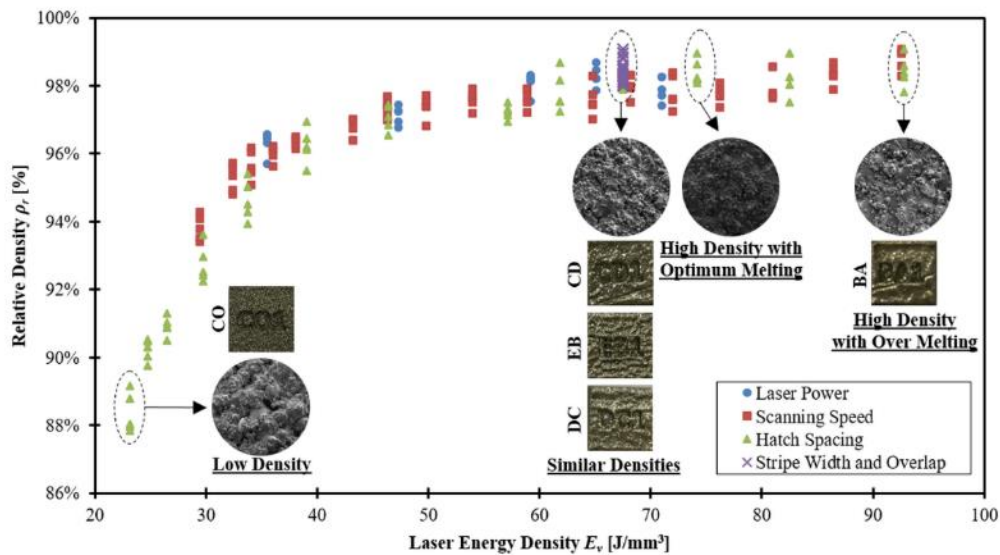


Figure 2.12: Effect of laser energy density on the relative density of the parts produced for different sets of SLM process parameters.

2.6 Conclusions

The purpose of this paper was to determine and recommend sets of SLM process parameters for fabricating Invar 36 components and structures with high density. Invar 36 is commonly known in the aerospace industry for its low thermal expansion coefficient. It has been used in different applications that require high dimensional stability. In this extensive study, a complete analysis for the influence of SLM process parameters on the density of the parts produced from Invar 36. Maraging steel 18Ni (300) was used as a comparator for this study.

The study showed that the laser energy density has a strong influence on the density of the parts produced. As the energy density increases, the density increases until reaching a certain limit associated with melting. After that, the part quality starts to deteriorate due to thermal stresses and induced residual stresses. The analysis showed that Invar 36 needs a set of SLM process parameters that can generate approximately between

60 to 75 J/mm³ of laser energy density to be fully melted (maraging steel needs around 67.5 J/mm³). Although Invar 36 has a lower value of thermal conductivity than maraging steel, this higher level of energy density is attributed to the fact that Invar 36 has a higher melting temperature than maraging steel. Thus Invar 36 needs high laser energy to be fully melted.

The recommended energy density range that results in high part density and better microstructure may affect other factors. These factors include residual stress, tensile strength, percent elongation, hardness, etc. Hence, additional tests are needed to analyze other influencing factors. These tests should provide the optimum range of the laser energy densities that would result in complete melting of Invar 36 without deteriorating its performance.

2.7 References

- [1] Smith, R. J., Lewi, G. J., and Yates, D. H., "Development and Application of Nickel Alloys in Aerospace Engineering," *Aircraft Engineering and Aerospace Technology*, vol. 73, no. 2, pp. 138-147, 2001.
- [2] Jasthi, B. K., Arbegast, W. J., and Howard, S. M., "Thermal Expansion Coefficient and Mechanical Properties of Friction Stir Welded Invar (Fe-36%Ni)," *Journal of Materials Engineering and Performance*, vol. 18, no. 7, pp. 925-934, 2009.
- [3] Zhao, Y., Wu, A., Yao, W., Wang, Z., Sato, Y. S., and Kokawa, H., "Microstructure and Mechanical Properties of Nd:YAG Laser Welded Invar 36 Alloy," *Materials Science Forum*, vol. 675-677, pp. 739-742, 2011.
- [4] Zhao, Y. *et al.*, "Temperature and Force Response Characteristics of Friction Stir Welding on Invar 36 Alloy," *Science and Technology of Welding and Joining*, vol. 18, no. 3, pp. 232-238, 2013.
- [5] National Research Council (U.S.), "3D Printing in Space," National Academy of Sciences, Washington, D.C., USA2014.
- [6] Hofmann, D. C. *et al.*, "Developing Gradient Metal Alloys through Radial Deposition Additive Manufacturing," *Scientific Reports*, vol. 4, 2014, Art. no. 5357.

- [7] Qiu, C., Adkins, N. J. E., and Attallah, M. M., "Selective Laser Melting of Invar 36: Microstructure and Properties," *Acta Materialia*, vol. 103, pp. 382-395, 2016.
- [8] Wohlers, T. and Gornet, T., "Wohler's Report (2014), History of Additive Manufacturing," Wohlers Associates Inc.2014.
- [9] Thijs, L., Verhaeghe, F., Craeghs, T., Humbeeck, J. V., and Kruth, J.-P., "A Study of the Microstructural Evolution during Selective Laser Melting of Ti-6Al-4V," *Acta Materialia*, vol. 58, pp. 3303-3312, 2010.
- [10] Kruth, J.-P., Mercelis, P., Froyen, L., and Rombouts, M., "Binding Mechanisms in Selective Laser Sintering and Selective Laser Melting," in *Annual International Solid Freeform Fabrication Symposium*, Texas, USA, 2004: University of Texas in Austin.
- [11] Over, C., Meiners, W., Wissenbach, K., Lindemann, M., and Hammann, G., "Selective Laser Melting: A New Approach for the Direct Manufacturing of Metal Parts and Tools," in *International Conference on Laser Assisted Net Shape Engineering*, Germany, 2001.
- [12] Murr, L. E. *et al.*, "Fabrication of Metal and Alloy Components by Additive Manufacturing: Examples of 3D Materials Science," *Journal of Materials Research and Technology*, vol. 1, no. 1, pp. 42-54, 2012.
- [13] Kempen, K., Thijs, L., Yasa, E., Badrossamay, M., Verheecke, W., and Kruth, J.-P., "Process Optimization and Microstructural Analysis for Selective Laser Melting of AlSi10Mg," in *Annual International Solid Freeform Fabrication Symposium*, 2011.
- [14] UDROIU, R., "Powder Bed Additive Manufacturing Systems and its Applications," *Academic Journal of Manufacturing Engineering*, vol. 10, no. 4, pp. 122-129, 2012.
- [15] Boschetto, A. and Bottini, L., "Accuracy Prediction in Fused Deposition Modeling," *The International Journal of Advanced Manufacturing Technology*, vol. 73, pp. 913-928, 2014.
- [16] Bual, G. S. and Kumar, P., "Methods to Improve Surface Finish of Parts Produced by Fused Deposition Modeling," *Manufacturing Science and Technology*, vol. 2, no. 3, pp. 51-55, 2014.
- [17] Radu, S.-A., Popescu, A. C., Balc, N., and Panc, N., "Experimental Determination of Surface Roughness of Parts Obtained by Rapid Prototyping," in *The 3rd Advanced Research in Scientific Areas (ARSA) Conference*, 2014, vol. 3, no. 1, pp. 342-345: EDIS - Publishing Institution of the University of Zilina.
- [18] Barari, A., Kishawy, H. A., Kaji, F., and Elbestawi, M. A., "On the Surface Quality of Additive Manufactured Parts," *International Journal of Advanced Manufacturing Technology*, 2016.
- [19] Mudge, R. P. and Wald, N. R., "Laser Engineered Net Shaping Advances Additive Manufacturing and Repair," *Welding Journal*, vol. 86, pp. 44-48, 2007.

- [20] Baufeld, B., Biest, O. V. d., and Gault, R., "Additive Manufacturing of Ti-6Al-4V Components by Shaped Metal Deposition: Microstructure and Mechanical Properties," *Materials & Design*, vol. 31, pp. S106-S111, 2010.
- [21] Taminger, K. M. and Hafley, R. A. (2006) Electron Beam Freeform Fabrication for Cost Effective Near-Net Shape Manufacturing. *NATO Research and Technology Organization (RTO) AVT-139 Cost Effective Manufacture via Net Shape Processing*. 16 (1-10).
- [22] Spierings, A. B. and Levy, G., "Comparison of Density of Stainless Steel 316L Parts Produced with Selective Laser Melting using Different Powder Grades," in *Annual International Solid Freeform Fabrication Symposium*, Texas, USA, 2009, pp. 342-353: University of Texas in Austin.
- [23] Spierings, A. B., Herres, N., and Levy, G., "Influence of the Particle Size Distribution on Surface Quality and Mechanical Properties in Additive Manufactured Stainless Steel Parts," in *Annual International Solid Freeform Fabrication Symposium*, Texas, USA, 2010, pp. 397-406: University of Texas in Austin.
- [24] Delgado, J., Ciurana, J., and Rodríguez, C. A., "Influence of Process Parameters on Part Quality and Mechanical Properties for DMLS and SLM with Iron-Based Materials," *International Journal of Advanced Manufacturing Technology*, vol. 60, pp. 601-610, 2012.
- [25] Cherry, J. A., Davies, H. M., Mehmood, S., Lavery, N. P., Brown, S. G. R., and Sienz, J., "Investigation into the Effect of Process Parameters on Microstructural and Physical Properties of 316L Stainless Steel Parts by Selective Laser Melting," *International Journal of Advanced Manufacturing Technology*, vol. 76, pp. 869-879, 2014.
- [26] Król, M., Kujawa, M., Dobrzański, L. A., and Tański, T., "Influence of Technological Parameters on Additive Manufacturing Steel Parts in Selective Laser Sintering," *Archives of Materials Science and Engineering*, vol. 67, no. 2, pp. 84-92, 2014.
- [27] Song, B. *et al.*, "Differences in Microstructure and Properties between Selective Laser Melting and Traditional Manufacturing for Fabrication of Metal Parts: A Review," *Frontiers of Mechanical Engineering*, vol. 10, no. 2, pp. 111-125, 2015.
- [28] Yasa, E. and Kruth, J.-P., "Microstructural Investigation of Selective Laser Melting 316L Stainless Steel Parts Exposed to Laser Re-Melting," *Proceida Engineering - 1st CIRP Conference on Surface Integrity (CSI)* vol. 19, pp. 389-395, 2011.
- [29] Weingarten, C., Buchbinder, D., Pirch, N., Meiners, W., Wissenbach, K., and Poprawe, R., "Formation and Reduction of Hydrogen Porosity During Selective Laser Melting of AlSi10Mg," *Journal of Materials Processing Technology*, vol. 221, pp. 112-120, 2015.
- [30] Bland, S. and Aboulkhair, N. T., "Reducing Porosity in Additive Manufacturing," *Metal Powder Report*, vol. 70, no. 2, pp. 79-81, 2015.

- [31] Aboulkhair, N. T., Everitt, N. M., Ashcroft, I., and Tuck, C., "Reducing Porosity in AlSi10Mg Parts Processed by Selective Laser Melting," *Additive Manufacturing*, vol. 1-4, pp. 77-86, 2014.
- [32] Frazier, W. E., "Metal Additive Manufacturing: A Review," *Journal of Materials Engineering and Performance*, vol. 23, no. 6, pp. 1917-1928, 2014.
- [33] Kasperovich, G. and Hausmann, J., "Improvement of Fatigue Resistance and Ductility of TiAl6V4 Processed by Selective Laser Melting," *Journal of Materials Processing Technology*, vol. 220, pp. 202-214, 2015.
- [34] Leuders, S. *et al.*, "On the Mechanical Behaviour of Titanium Alloy TiAl6V4 Manufactured by Selective Laser Melting: Fatigue Resistance and Crack Growth Performance," *International Journal of Fatigue*, vol. 48, pp. 300-307, 2013.
- [35] Siddique, S., Imran, M., Wycisk, E., Emmelmann, C., and Walther, F., "Influence of Process-Induced Microstructure and Imperfections on Mechanical Properties of AlSi12 Processed by Selective Laser Melting," *Journal of Materials Processing Technology*, vol. 221 pp. 205-213, 2015.
- [36] Kempen, K., L.Thijs, Humbeeck, J. V., and Kruth, J.-P., "Mechanical Properties of AlSi10Mg Produced by Selective Laser Melting," *Physics Procedia*, vol. 39, pp. 439-446, 2012.
- [37] Thöne, M., Leuders, S., Riemer, A., Tröster, T., and Richard, H. A., "Influence of Heat Treatment on Selective Laser Melting Products – e.g. Ti6Al4V," in *International Solid Freeform Fabrication Symposium, An Additive Manufacturing Conference*, Austin, Texas, USA, 2012.
- [38] Vrancken, B., Thijs, L., Kruth, J.-P., and Humbeeck, J. V., "Heat Treatment of Ti6Al4V Produced by Selective Laser Melting: Microstructure and Mechanical Properties," *Journal of Alloys and Compounds*, vol. 541, no. 0, pp. 177-185, 2012.
- [39] Shiomi, M., Osakada, K., Nakamura, K., Yamashita, T., and Abe, F., "Residual Stress within Metallic Model Made by Selective Laser Melting Process," *CIRP Annals - Manufacturing Technology*, vol. 53, no. 1, pp. 195-198, 2004.
- [40] Harrison, N. J., Todd, I., and Mumtaz, K., "Reduction of Micro-Cracking in Nickel Superalloys Processed by Selective Laser Melting: A Fundamental Alloy Design Approach," *Acta Materialia*, vol. 94, pp. 59-68, 2015.
- [41] Jacobson, D. M. and Bennett, G., "Practical Issues in the Application of Direct Metal Laser Sintering," in *Annual International Solid Freeform Fabrication Symposium*, Texas, USA, 2006, pp. 728-739: University of Texas in Austin.
- [42] Slotwinski, J. A., Garboczi, E. J., and Hebenstreit, K. M., "Porosity Measurements and Analysis for Metal Additive Manufacturing Process Control," *Journal of Research of the National Institute of Standards and Technology*, vol. 119, pp. 494-528, 2014.

- [43] Oehlert, G. W., *A First Course in Design and Analysis of Experiments*. W. H. Freeman, 2000.
- [44] He, X., DebRoy, T., and Fuerschbach, P. W., "Alloying Element Vaporization during Laser Spot Welding of Stainless Steel," *Journal of Physics D: Applied Physics*, vol. 36, pp. 3079-3088, 2003.
- [45] Mukherjee, T., Zuback, J. S., De, A., and DebRoy, T., "Heat and Fluid Flow Modeling to Examine 3D-Printability of Alloys," in *7th International Symposium on High-Temperature Metallurgical Processing*, 2016, pp. 471-478: The Minerals, Metals & Materials Society.
- [46] Attallah, M. M., Jennings, R., Wang, X., and Carter, L. N., "Additive Manufacturing of Ni-Based Superalloys: The Outstanding Issues," *MRS Bulletin*, vol. 41, no. 10, pp. 758-764, 2016.
- [47] Louvis, E., Fox, P., and Sutcliffe, C. J., "Selective Laser Melting of Aluminium Components," *Journal of Materials Processing Technology*, vol. 211, pp. 275-284, 2011.
- [48] Ocylok, S., Alexeev, E., Mann, S., Weisheit, A., Wissenbach, K., and Kelbassa, I., "Correlations of Melt Pool Geometry and Process Parameters During Laser Metal Deposition by Coaxial Process Monitoring," *Physics Procedia*, vol. 56, pp. 228-238, 2014.
- [49] Kusuma, C., "The Effect of Laser Power and Scan Speed on Melt Pool Characteristics of Pure Titanium and Ti-6Al-4V alloy for Selective Laser Melting," M.Sc. Thesis, Mechanical Engineering Department, Wright State University, 2016.
- [50] Hu, Z., Zhu, H., Zhang, H., and Zeng, X., "Experimental Investigation on Selective Laser Melting of 17-4PH Stainless Steel," *Optics & Laser Technology*, vol. 87, pp. 17-25, 2017.

Chapter 3

Selective Laser Melting of Stainless Steel 316L

Complete Citation:

Yakout, M., Elbestawi, M.A., Veldhuis, S.C. (2018). On the characterization of stainless steel 316L parts produced by selective laser melting. *The International Journal of Advanced Manufacturing Technology*, Volume 95, Issue 5-8, pp 1953-1974. DOI: 10.1007/s00170-017-1303-0

Copyright:

Reprinted with permission copyrighted by Springer Nature, 2017.

Relative Contributions:

M. Yakout: Performed experiments, analysis, and data interpretation. Wrote the first draft of the manuscript. Helped with submitting the final manuscript to the journal (corresponding author).

M. A. Elbestawi: Co-supervisor of M. Yakout. Revised the manuscript. Was responsible of submitting the final manuscript to the journal (corresponding author).

S. C. Veldhuis: Co-supervisor of M. Yakout. Revised the manuscript.

Abstract:

Metal additive manufacturing has employed several technologies and processes to advance from rapid prototyping to rapid manufacturing. Additive manufacturing technologies compete with traditional manufacturing methods through their ability to produce complex structures and customized products. This paper aims to study the characteristics of stainless steel 316L (UNS S31603) parts produced using a selective laser melting machine. In the aerospace industry, turbine blades are typically manufactured from nickel-based alloys, titanium alloys, and stainless steels. Several geometries typical of airfoil blades were examined. The main goal is to investigate the material characteristics and surface features of the airfoil blades. The study included the geometrical errors, surface microstructures, material compositions, material phases, and residual stresses of the samples produced. The characteristics of the parts produced were investigated based on experimental observations. The paper also discusses the influence of the part dimension and orientation on the profile error, surface microstructure, and residual stress.

Keywords:

Metal additive manufacturing; Stainless steel 316L; Surface microstructure; Residual stress; Phase transformation; Selective laser melting; Aerospace industry.

Abbreviations:

AM	Additive manufacturing
SLM	Selective laser melting
YFL	Ytterbium fiber laser
XRD	X-ray diffraction

CMM	Coordinate measuring machine
SEM	Scanning electron microscopy
EDS	Energy-dispersive X-ray spectroscopy
FCC	Face-centered cubic
BCT	Body-centered tetragonal
CAD	Computer-aided drafting
STL	Stereolithography
LPB	Lower prediction boundary
UPB	Upper prediction boundary

Notations:

P	Laser power (W)
v	Laser scanning speed (mm/s)
h	Hatch spacing (mm)
t	Layer thickness (mm)
E_v	Laser energy density (J/mm^3)
PD	Point distance (mm)
θ	Exposure time (s)
w	Stripe width (mm)
γ	Stripe overlap (mm)
δ	Beam offset (μm)
φ	Effective diameter of laser beam (mm)
FP	Focal position (mm)
D	Leading edge diameter (mm)

d	Trailing edge diameter (mm)
C	Center distance (mm)
α	Inclination angle (degree)
$S1$	X-ray elastic constant 1
$S2$	X-ray elastic constant 2

Acknowledgment:

The authors thank the Renishaw (Canada) Ltd. team for offering their facility for testing.

3.1 Introduction

ASTM International [1] defines additive manufacturing (AM) as “the process of joining materials to make objects from 3D model data, usually layer upon layer, as opposed to subtractive manufacturing methodologies.” Over the last decade, AM has been used for metal fabrication in many industries, including aerospace and automotive [2, 3]. AM processes have been developed to produce complex, customized, and cost-effective components with acceptable mechanical properties. However, metal AM still has many challenges in industries that require high quality manufacturing, especially in the aerospace industry. Stainless steel 316L (UNS S31603) has an advantage over other stainless steels because it contains nickel and molybdenum elements that increase its corrosion resistance. It also has a relatively low carbon percentage so it has better welding characteristics [4].

Turbine blades have been produced using materials that have high temperature resistance, corrosion resistance, fatigue strength, tensile strength, and bending strength. Nickel-based alloys, titanium alloys, and stainless steels are commonly used for turbine blades [5-7]. AM processes allow the manufacture of conformal cooling channels in turbine blades [8-10]. A previous study [11] showed the characteristics of various turbine blades manufactured from different aerospace alloys including stainless steel 316L. Another study [12] showed the additive manufacturing of turbine blades with conformal cooling channels using stainless steel 316L and Inconel 718. Stainless steel 316L has shown good weldability and has gained popularity in AM applications. The thermal stresses that are introduced during the selective laser melting (SLM) process cause flaws and residual stresses in the parts produced. Several studies were performed to characterize the density and mechanical properties of stainless steel 316L samples produced by the SLM process. Some of these studies included the effect of different powder grades [13, 14], process

parameters [15-18], and part orientation [19, 20] on the mechanical properties and material characteristics of the parts produced. Other studies covered the material composition and corrosion resistance changes that occur during the SLM of stainless steel 316L [15, 20-22]. It can be concluded from the literature that the following parameters/factors are significantly affecting the mechanical properties and surface quality of the stainless steel 316L parts produced by the SLM process [13-22].

1. SLM process parameters (e.g., laser power, scanning speed, scanning strategy, etc.)
2. Powder characteristics (e.g., particles distribution, particles size, etc.)
3. Part design and dimensions
4. Part location on the build plate

The research presented in this study investigates the material characteristics and surface features of simplified airfoil blades produced by SLM process. The design of the blades is a realistic AM application that could be used to study the staircase effect which delineates the differences between the surface features of the top and bottom layers. The effect of the part location (on the build plate) on the material characteristics of the parts produced by SLM is also evaluated. The paper examines the surface defects, profile error, microstructure, material composition, material phases, and residual stress of parts produced from stainless steel 316L. The main causes of these defects are discussed in the paper.

3.2 Selective laser melting process

SLM is an AM process that belongs to powder bed processes. The process starts with distributing a metal powder in a bed, then melting predefined sections using a focused laser beam. The process is repeated by lowering the build plate and melting another layer until all the layers have been built [3, 23]. Figure 3.1 shows a typical SLM process as mentioned in reference [24].

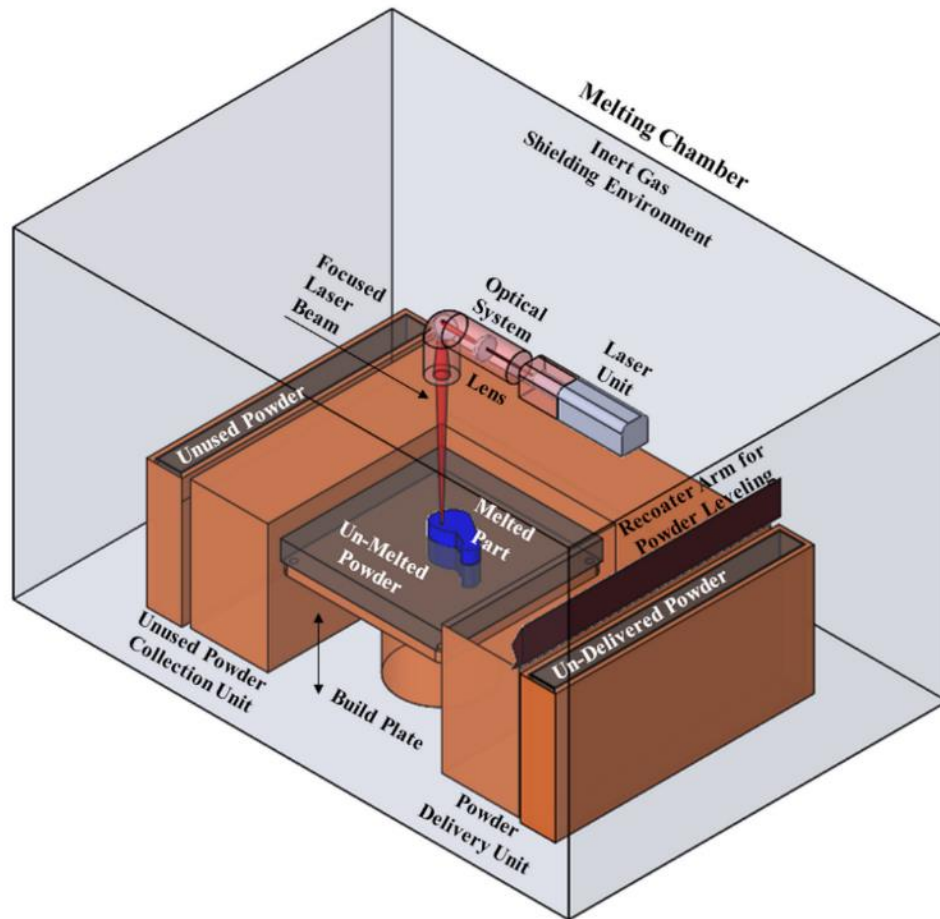


Figure 3.1: Overview of a typical selective laser melting (SLM) process [24].

As opposed to wrought parts, SLM parts can have stress risers such as internal voids, partially melted powder, and powder particles stuck on the surface, and there is the potential for cracks between layers [24, 25]. The SLM process generates highly localized changes in both heating rate during the powder melting and cooling rate during the part solidification process. These thermal changes cause thermal stresses, and consequently cause residual stress in the resulting parts. These residual stresses significantly affect the mechanical properties and dimensional accuracy of the parts produced [26-33]. The following methods are suggested in the literature to reduce the amount of residual stress in the SLM parts:

1. Heat treating the parts for residual stress reduction [26, 27, 33].
2. Preheating the build plate before melting the powder to limit the temperature difference from one layer to another [26, 27, 33].
3. Controlling the part location on the build plate and the process parameters for controlling the heating and cooling rates to reduce the residual stress formation [26, 28, 29, 32, 33].

Residual stress can be measured using different methods such as layer removal method [26, 29], crack compliance method [27, 31, 34], hole drilling method [28, 31], contour method [35], sectioning method [35], neutron diffraction [36], X-ray diffraction (XRD) [30, 37], and indentation correlation method (hardness test) [38]. Previous studies showed that the amounts of residual stress in the parts produced is influenced by the process parameters [26, 32, 33], part dimensions [27, 29, 31], part location on the build plate [28], part removal [27], and post processing [32, 33]. The residual stress differs from one layer to another in the build direction as well as its distribution in the build direction differs from that in the scanning direction [30, 31, 37, 38].

As shown in Figure 3.2, the laser system generates a peak power (P) on a certain spot for a fixed exposure time (θ). Then, the laser moves a distance, called point distance (PD), to a consecutive spot on the scan line (hatch line). The average scanning speed (v) equals the point distance divided by the exposure time as shown in Equation (3.3). At the end of each scan line, the laser moves a distance, called hatch spacing (h), to apply exposures on another scan line. The width of each scan line is called stripe width (w) and the overlap between each two lines is called stripe overlap (γ). After finishing one layer, the build plate moves down a given distance called the layer thickness (t). The focal position of the laser system controls the laser effective diameter (ϕ) and the beam offset

(δ). For a SLM machine that operates with a pulsed wave emission, these parameters define the volumetric energy density of the laser (E_v) [24, 39-41].

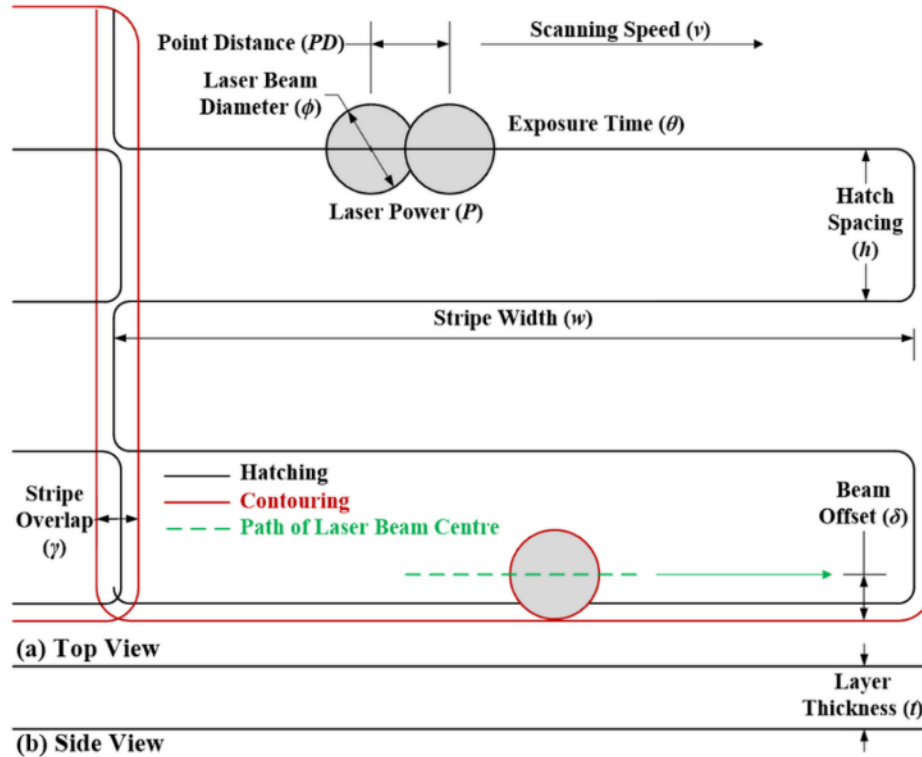


Figure 3.2: The SLM process parameters. (a) Top view and (b) side view of a build layer [24].

$$E_v = \frac{P}{(v \times h \times t)} \quad \text{in the hatch step} \quad (3.1)$$

$$E_v = \frac{P}{(v \times \phi \times t)} \quad \text{in the contouring step} \quad (3.2)$$

$$v = PD / \theta \quad (3.3)$$

where P is the laser power in (W), v is the average scanning speed in (mm/s), h is the hatch spacing in (mm), t is the layer thickness in (mm), ϕ is the effective laser diameter in (mm), and E_v is the laser energy density in (J/mm^3).

This paper investigates the profile errors and surface microstructures of the stainless steel 316L parts produced by the SLM process. The residual stress distribution among the scanning and build directions has been measured using the XRD method. A correlation between the surface microstructure and residual stress distribution has been made.

3.3 Experimental work

3.3.1 Part design

Simplified airfoil blade geometries were selected for this study. The dimensions of a typical airfoil blade were simplified into inclination angle, center distance, and leading-edge diameter and trailing-edge diameter as shown in Figure 3.3. Four groups of samples A-D were designed, and each group consisted of nine samples as shown in Figure 3.4. These groups were used for studying the effect of two factors: (i) part dimensions; and (ii) part location on the build plate. Group A to study the inclination angle, group C to study the center distance, and group D to study the thickness (trailing- and leading-edge diameters). Group B consists of identical samples to study the part location on the build plate. Table 3.1 illustrates the dimensions of the samples in each group.

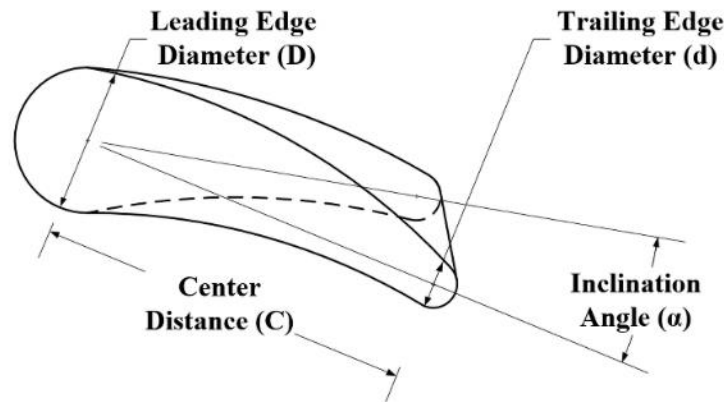


Figure 3.3: A simplified airfoil blade.

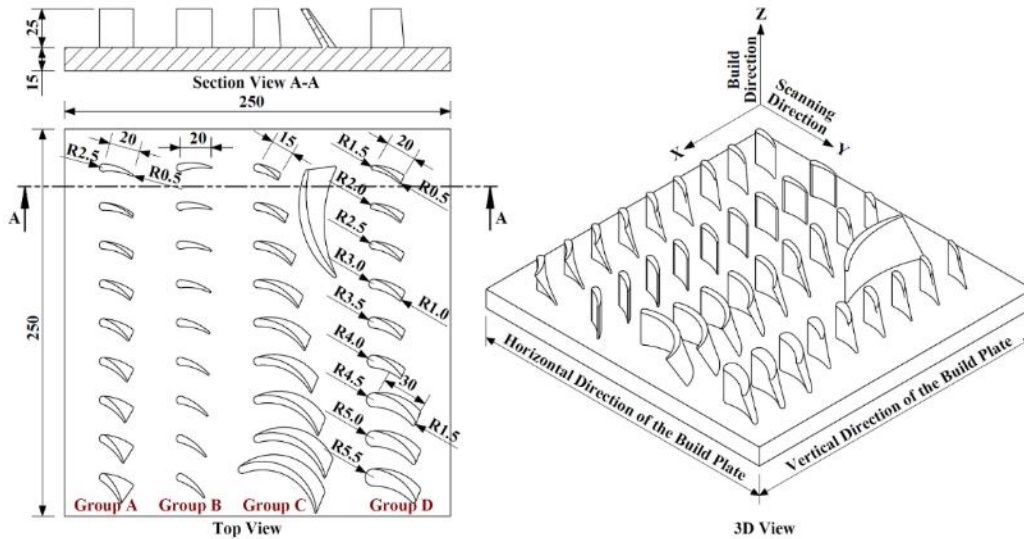


Figure 3.4: Dimensions of the designed samples and build plate.

Table 3.1: Dimensions of the designed samples.

Group	Inclination angle α (degree)	Center distance C (mm)	Leading edge diameter D (mm)	Trailing edge diameter d (mm)
A	$0^\circ \rightarrow 40^\circ$	20	5	1
B	0°	20	5	1
C	15°	$15 \rightarrow 55$	5	1
D	15°	20	$3 \rightarrow 5$	1
	15°	20	$6 \rightarrow 8$	2
	15°	30	$9 \rightarrow 11$	3

3.3.2 Material and machine

The samples were produced from stainless steel 316L powder (supplied by Renishaw Canada) using a Renishaw AM250 machine. The machine is equipped with a 200-watt ytterbium fiber laser (YFL). The powder particles were spherical and the grain size was 15-45 μm . The powder was manufactured using a gas atomization process. Table 3.2 shows the powder composition as provided by the supplier. The samples were built directly to the build plate without supports. Each layer was built in three different steps: hatching,

contouring, and finishing. The most commonly used strategies for laser scanning in SLM are meander, stripe, chessboard, and spiral as shown in Figure 3.5. Both the stripe and chessboard scanning are used for large cross section areas while spiral scanning is commonly used for inhomogeneous cross sections. Hence, for this study the designed parts were fabricated using a meander-like scanning pattern as the cross section is small and homogeneous. In the hatching step, a certain area is melted according to a meander scanning strategy. Then, the profile of this area is re-melted in the contouring step. The finishing step is also performed to smooth the outside surface of the parts produced. Table 3.3 shows a list of SLM process parameters that have been reported in the literature. The laser power, scanning speed, layer thickness, and hatch spacing were approximately 50-400 W, 100-1600 mm/s, 40-60 μm , and 80-130 μm , respectively. Based on these values and the experimental recommendations from the supplier, a laser power of 200 W, an average scanning speed of 750 mm/s, a layer thickness of 50 μm , and a hatch spacing of 110 μm were recommended. The scanning speed was controlled by the exposure time (80 μs) and point distance (60 μm). The focal position was zero, in which the layer being melted was in the focal plane. At zero focal position, the calculated effective diameter was 150 μm . The process parameters used for hatching and contouring each layer is shown in Table 3.4. Once the building process was finished, an air blasting procedure was used to remove the supporting powders and to clean the parts. After that, the build plate was removed from the machine for testing. Each sample was marked with a letter that represents the group and a number that represents the sample count in the group (e.g., A4). The parts did not undergo any post-processing procedures and were not removed from the build plate at this stage of testing.

Table 3.2: Material composition of stainless steel 316L powder (wt%).

Fe	Cr	Ni	Mo	Mn	Si	N	O	P	C	S
Balance	16-18	10-14	2-3	< 2	< 1	< 0.1	< 0.1	< 0.045	< 0.03	< 0.03

Table 3.3: List of SLM process parameters reported in the literature for producing stainless steel 316L.

Laser power P (W)	Scanning speed v (mm/s)	Layer thickness t (mm)	Hatch spacing h (mm)	Laser energy density E_v (J/mm^3)	Reference
50	100	0.04	0.07	179	[37]
50	100	0.05	0.06	167	[42]
50	100	0.05	0.07	143	[30]
50	100-300	0.05	0.08	42-125	[22, 41]
50	120	0.04	0.12	87	[22, 43]
100	300	0.03	0.081-0.126	88-137	[22, 44]
100	300	0.03	0.112-0.125	89-99	[22, 45]
100	175-380	0.06	0.126	35-76	[22, 46]
100-150	700	0.02	0.05-0.07	102-214	[47]
85-105	300	0.02-0.06	0.112-0.125	38-156	[22, 48]
87	150	0.075	0.13	59	[22, 49]
104	300-800	0.03	0.13	33-89	[14, 22]
105	380	0.02-0.04	0.125	55-111	[22, 50]
75-175	80-200	0.10	0.04-0.06	63-547	[22, 51]
150	400	0.035	0.08	134	[31]
150-400	1200	0.03	0.15	28-74	[22]
180	900	0.02	0.06	167	[52]
190	50-800	0.05	0.15	32-507	[53]
190	800	0.02	0.1	119	[54]
200	1600	0.05	0.06	42	[55]

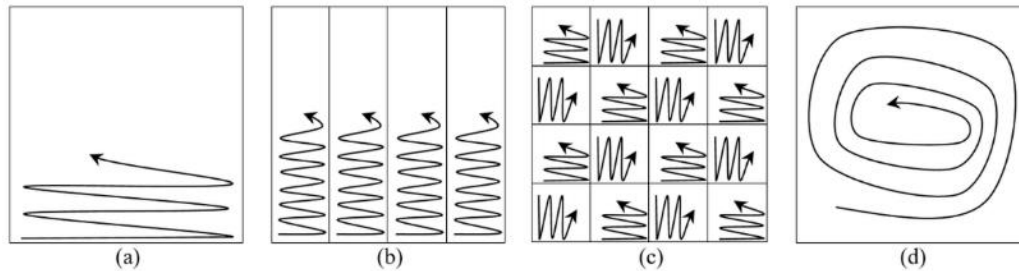
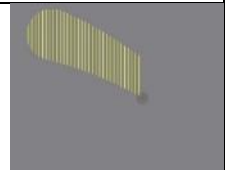
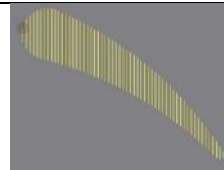
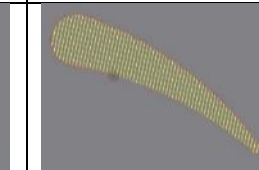


Figure 3.5: Laser scanning strategies in the SLM process. (a) Meander, (b) stripe, (c) chessboard, and (d) spiral.

Table 3.4: SLM process parameters for producing the stainless steel 316L samples.

Parameter	Step I (hatching)	Step II (contouring)	Step III (finishing)
Scanning strategy	Meander	Contour	Fine contour
Focal position FP (mm)	0	0	0
Laser power P (W)	200	200	110
Point distance PD (μm)	60	40	20
Exposure time θ (μs)	80	90	100
Scanning speed v (mm/s)	750	444	200
Layer thickness t (mm)	0.05	0.05	0.05
Hatch spacing h (mm)	0.11	-	-
Effective diameter ϕ (mm)	0.15	0.15	0.15
Beam offset δ (μm)	60	60	60
Laser energy density E_v (J/mm^3)	$E_v = P / (v \cdot t \cdot h)$	$E_v = P / (v \cdot t \cdot \phi)$	$E_v = P / (v \cdot t \cdot \phi)$
	48.5	60.1	73.3
Illustration			

3.3.3 Geometrical measurements

The profile errors of the samples were measured using a coordinate measuring machine (CMM). Five samples were selected for the analysis; A1-A4 and A9. Figure 3.6 shows the profile error of an airfoil blade.

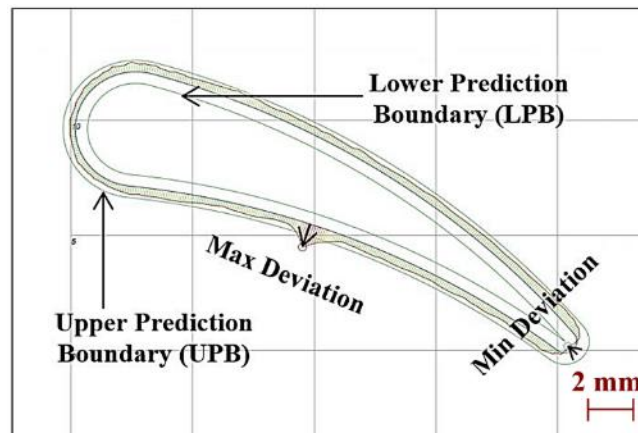


Figure 3.6: Profile error of an airfoil blade.

3.3.4 Surface microstructure and material composition

After geometrical measurements, the samples were not removed from the build plate; however, the build plate was cut to enable the testing of each sample independently as shown in Figure 3.7. The surface microstructure and material composition of the samples were analyzed using scanning electron microscopy (SEM) and energy-dispersive X-ray spectroscopy (EDS) analyses. The microstructural analysis included the morphology, topography, and chemical contrast of the surfaces. The analysis was performed on the side of the samples to investigate the crack initiation between subsequent layers.

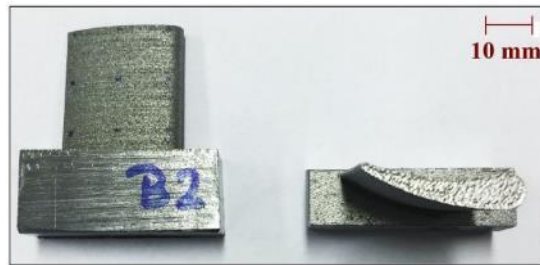


Figure 3.7: An airfoil blade (a sample) after cutting.

3.3.5 Phase identification and residual stress measurements

Stainless steel 316L is an austenitic single-phase steel (γ -Fe) with a face-centered cubic (FCC) crystal structure. Figure 3.8 shows the XRD diffractogram for a “typical” austenitic steel structure as provided from Mercury software version 3.0 (build RC5).

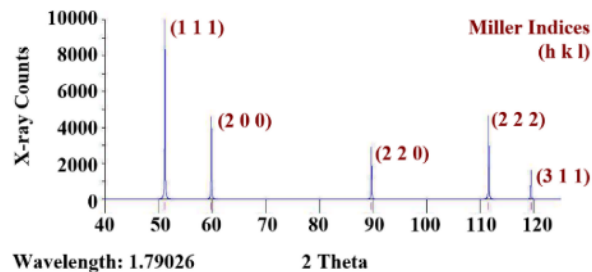


Figure 3.8: XRD diffractogram of a “typical” austenitic steel (γ -Fe) structure extracted from Mercury software version 3.0 (build RC5).

The material phases were identified using the XRD method. The phase identification was performed to identify the material phases in the samples produced and to define the diffracted angle (2θ) that represents the measured lattice plane (hkl). The lattice deformation was obtained using a $\text{CoK}\alpha$ (wavelength 1.79026 \AA) radiation source, then the material phases were identified. The residual stress was calculated from the lattice deformation measurements using the constants shown in Table 3.5. The XRD frames were collected at four different rotation angles ($\Phi = 0, 45, 135, \text{ and } 270$), four different tilting angles ($\Psi = 10^\circ, 25^\circ, 40^\circ, \text{ and } 55^\circ$), detector angle (57.3°), and X-ray angle (59.3°). The residual stress evolutions across the top surface and the side surfaces of each airfoil blade were investigated using the XRD measurements. Figure 3.9a shows the measured surfaces: top surface, side surface 1, and side surface 2. The X and Y directions represent the transverse and longitudinal horizontal directions along the scanning plane, while the Z direction represents the vertical direction along the build “height” direction. The top surface measurements represent the horizontal residual stress (along the scanning direction) and the side surface measurements represent the vertical residual stress (along the build direction). Figure 3.9b-d shows the measured points along the top and side surfaces. The principal residual stresses σ_1 and σ_2 were calculated at each point. For surface measurements, the residual stresses were assumed biaxial.

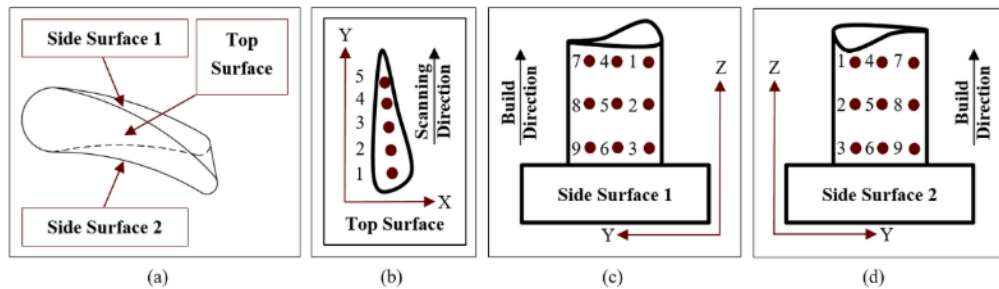


Figure 3.9: The measured (a) surfaces, (b) points along the top surface, (c) points along the side surface 1, and (d) points along the side surface 2.

Table 3.5: Constants used in the determination of residual stresses using the XRD method.

Material	h k l	2Theta	S1	½ S2	Poisson ratio	Young's modulus
Stainless steel 316L	2 2 2	119.050°	-1.559×10^{-6}	7.441×10^{-6}	0.265	170 GPa

3.4 Results and discussion

3.4.1 Profile errors of samples

Table 3.6 summarizes the profile errors of the five samples at three different positions: bottom, middle, and top layers. The actual profile deviation represents the summation of the maximum and minimum deviations as shown in Figure 3.6. The minimum deviation ranges from 0.02 to 0.09 mm, maximum deviation ranges from 0.07 to 0.21 mm, and actual profile error ranges from 0.12 to 0.26 mm. This profile error causes a geometrical distortion that will affect the performance of the airfoil blades.

The analysis showed that the profile error varies based on the inclination angle. It has been reported in the literature that the geometrical distortion in the laser melted parts might be attributed to surface tension due to thermal gradients [56], balling effect due to molten material wettability [17, 53], and/or powder particles sticking and agglomerating on the surface [56, 57]. Some studies showed that the surface features depend also on the inclination of the side surface. This phenomenon is called staircase, which causes differences between the surface features of the top layers and those of the bottom layers [57-60]. By measuring the profile error in three different locations (bottom layer, medium layer, and top layer), it was observed that the profile error of the top layer is larger than that of the bottom layer. This could be attributed to more particles sticking on the surface of the top layers and/or more possibility of balling phenomenon on the top layers. It was also noted

that the profile error is minimal in the blade that is inclined by 10 degrees relative to the substrate (sample A3), which is corresponding with the results obtained in reference [57].

Table 3.6: Profile errors of airfoils (CMM results).

Blade	Inclination	Minimum deviation (mm)			Maximum deviation (mm)			Actual profile deviation (mm)		
		Bottom	Middle	Top	Bottom	Middle	Top	Bottom	Middle	Top
A1	0°	0.0734	0.0840	0.0852	0.1016	0.0921	0.0903	0.1750	0.1761	0.1755
A2	5°	0.0493	0.0680	0.0624	0.1076	0.1186	0.1226	0.1569	0.1866	0.1850
A3	10°	0.0346	0.0408	0.0493	0.0921	0.0977	0.1229	0.1267	0.1385	0.1722
A4	15°	0.0521	0.0445	0.0487	0.0722	0.1269	0.2094	0.1243	0.1714	0.2581
A9	40°	0.0165	0.0256	0.0547	0.1205	0.1595	0.1269	0.1370	0.1851	0.1816

3.4.2 Surface microstructure

The SEM analysis was performed on the side surface of all samples. The results showed large particles “approximately 250 μm” on the surface of some samples as shown in Figure 3.10a. Since the powder size was tested to be consistent with specifications ranging from 15 to 45 μm, these large particles possibly were formed during the melting process due to a spherical balling phenomenon [53] and/or spatter formation (molten droplets) [61]. Some previous studies [53, 62] showed that the balling phenomenon can be attributed to a high oxygen content inside the melting chamber or a low laser energy density. At high scanning speed, low laser power, or large layer thickness, the powder tends to absorb very low energy. This low absorbed energy lowers the wettability of the molten metal, resulting in a lack of flow and a balling phenomenon. Hence, these particles could represent the side view of a balling track that happened in that particular layer. Other studies [61, 63] showed that the melt-pool instabilities could cause powder spattering and splashes, resulting in molten droplets hitting the surface. These molten droplets could be deposited to the side surface of the layer being melted. There was evidence of vertical lines perpendicular to the

scanning direction in some samples as shown in Figure 3.10b. These vertical lines are attributed to the STL format that represents the toolpaths along the surface. When the CAD model is converted into the STL format, discontinuities may occur causing a rough surface [64]. Figure 3.10c, d shows evidence of surface voids, some partially melted powders sticking on the surface, and some cracks between subsequent layers. The bottom layers have less powder sticking on the surface and more surface cracks between subsequent layers than the top layers. These cracks may be caused by thermal residual stresses as discussed in the next section.

As shown in Figure 3.11, the samples located at the center of the build plate (e.g., A5, B5, ...) have less particles sticking on the surface but more surface cracks. This can be attributed to the high energy that is building up at the center of the build plate during the melting process. This high energy will cause high thermal stress that consequently will cause more surface cracks but with better melting (i.e., less powder sticking on the surface). At a low melting energy (samples located at the side of the build plate), the balling phenomenon may occur causing large particles on the surface and some surface voids. The thermal stresses induced in these samples will be relatively small, so there are no cracks between subsequent layers. At a high melting energy (samples located at the center of the build plate), the thermal stresses induced in the samples will be relatively high causing cracks between subsequent layers. During the production of the samples located at the center of the build plate, the flow of the molten metal is relatively high due to the built-up energy. Hence, a successful melting with no balling phenomenon but high thermal stress is most likely expected at the center of the build plate. Since the location of the parts on the build plate affects the microstructure, the process parameters (e.g., laser power, scanning speed, etc.) should be carefully selected for each individual part during the process.

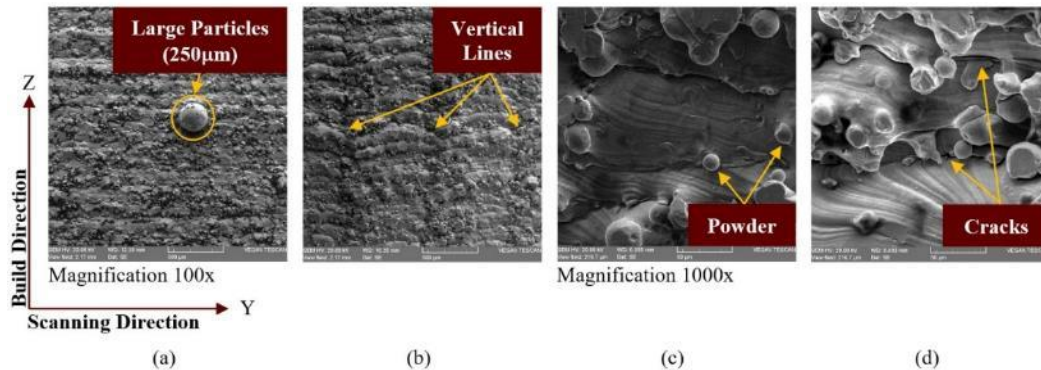


Figure 3.10: Microstructures of the *side* surfaces of some samples showing (a) large particles sticking on the surface, (b) vertical lines perpendicular to the scanning direction, (c) surface voids and partially melted powders, and (d) cracks between subsequent layers.

3.4.3 Material composition

The EDS analysis was performed on the side surface of all samples. The results showed aluminum inclusions in some locations. The stainless steel 316L powder does not have a certified value for aluminum; therefore, a possible source could be aluminum powder remaining in the machine from a previous build. A large amount of carbon and oxygen was observed in some locations as shown in Figure 3.12 and Table 3.7. The carbon and oxygen contents were not consistent with the material composition of the stainless steel 316L powder. Thus, these elements are likely in the form of carbides and oxides of some elements formed from the remaining atmosphere in the build space. The distribution of the material elements was inhomogeneous. The nickel content varied from 5 to 10% and the chromium content varied from 9 to 15%; stainless steel 316L typically contains 10-14% nickel and 16-18% chromium. In some instances, parts did not contain molybdenum; stainless steel 316L is typically have 2-3% molybdenum. It was observed that the parts located at the center of the build plate have less nickel and chromium contents than the rest. This can be attributed to the high built-up energy at the center of the build plate. The high energy will cause microsegregation of these elements or vaporization of some particles. Previous studies showed that some elements will be converted into soot during the melting process due to a

very high energy [24, 65-68]. For stainless steel 316L, the nickel, chromium, and molybdenum contents are obviously important for achieving the desired corrosion resistance.

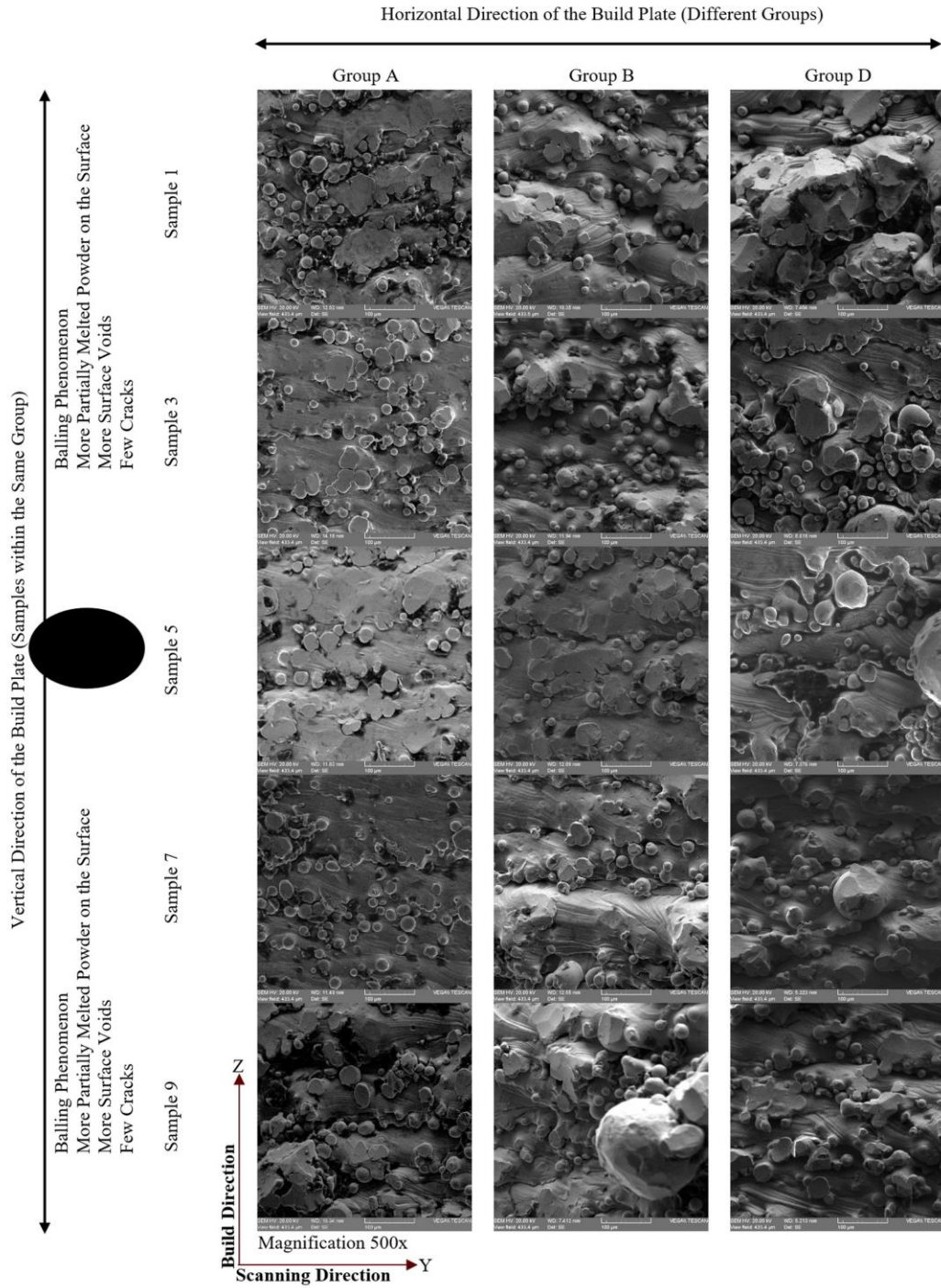


Figure 3.11: Microstructures of the *side* surfaces of five samples (1, 3, 5, 7, and 8) from each group.

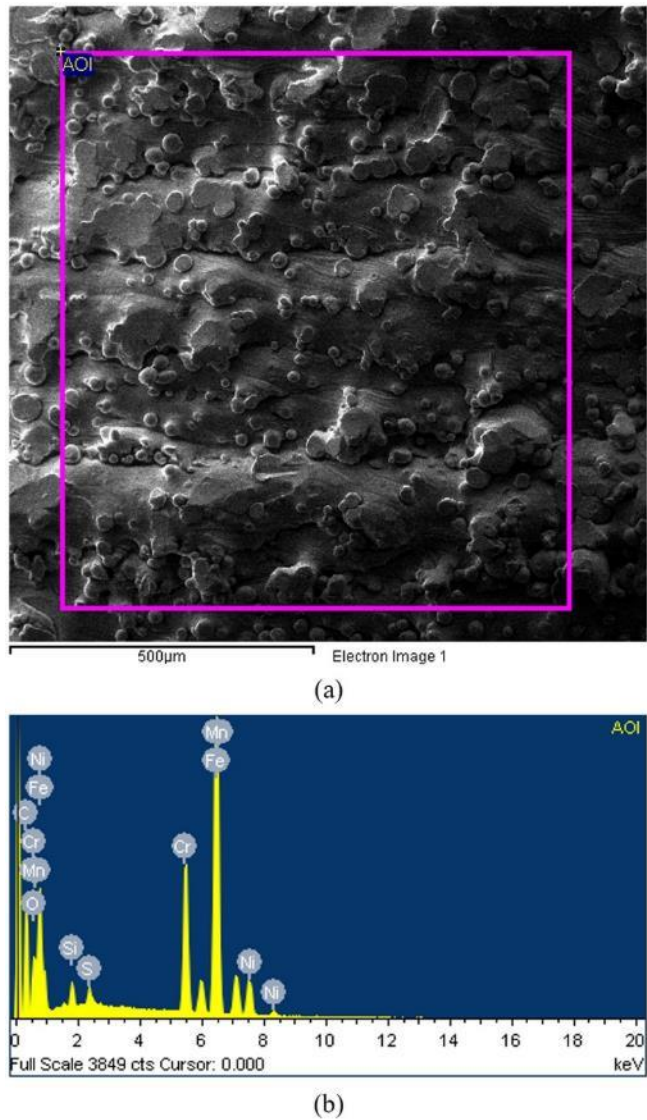


Figure 3.12: (a) Microstructure of a selected area of interest and (b) EDS spectrum of the selected area.

Table 3.7: Material composition of the selected area shown in Figure 3.12 (wt%).

Fe	Cr	Ni	Mn	Si	O	C	S	Mo
42.07	13.11	8.00	1.96	1.05	4.65	28.68	0.48	Not included

3.4.4 Phase identification

3.4.4.1 Phase identification using XRD method

Figure 3.13 shows the XRD diffractograms of two different locations: top surface and side surface. The phase identification results matched the typical austenitic steel structure with a single austenite (γ -Fe) phase. Some locations showed small X-ray counts for a martensite phase as illustrated in Figure 3.13b. The martensitic phase has a body-centered tetragonal (BCT) crystal structure.

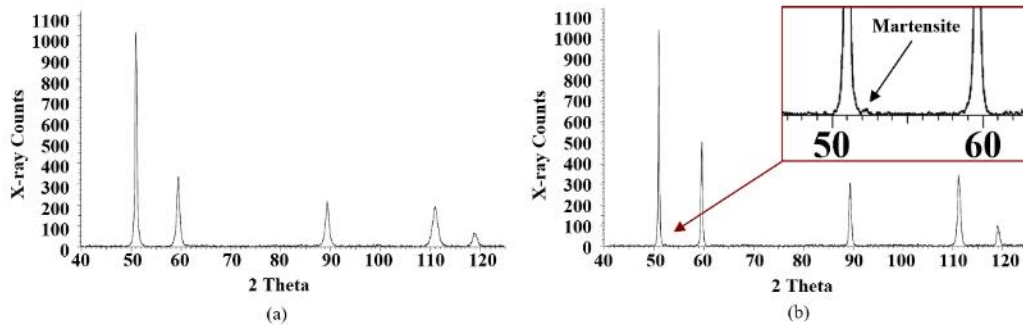


Figure 3.13: XRD diffractograms of two different locations. (a) Top surface. (b) Side surface.

3.4.4.2 Phase identification using selective etching method

To reveal the martensitic phase, two samples (A1 and A5) were cut, mounted in bakelite, polished, and etched with Kalling No. 2 etchant for around 2 min. The etchant formula was 1.25 g of cupric chloride dihydrate, 25 ml of hydrogen chloride, and 25 ml of ethanol. Figure 3.14a shows the etched top surface of sample A5 and Figure 3.14b shows the etched side surface of sample A1. The top surface showed the scan track and the side surface showed the melt pool. The black areas represent the internal voids in the etched samples. The etchant revealed the internal voids, material phases, and scan track.

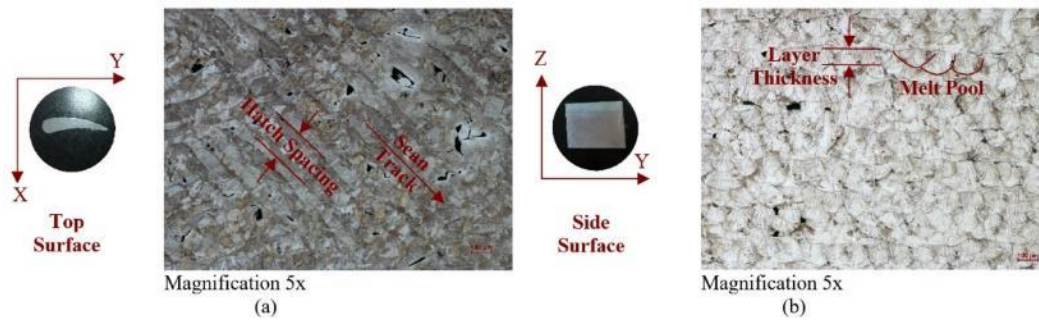


Figure 3.14: Micrographs of the *etched* (a) top surface and (b) side surface at low magnification.

The melt pool height ($80\ \mu\text{m}$) was approximately 1.5 times the layer thickness ($50\ \mu\text{m}$) and the melt pool width ($150\ \mu\text{m}$) was approximately two times the laser spot size ($70\ \mu\text{m}$). Overlaps were observed between subsequent layers and between the scan tracks. The overlapped locations were over melted and would have a high probability of soot formation and phase transformation during the melting process. The micrographs of the samples revealed both austenitic and martensitic phases as shown in Figure 3.15a, b. It was also observed that the martensitic phase occurred in the overlapped locations (e.g., the overlapped scan tracks shown in Figure 3.15a and the overlapped melting pools shown in Figure 3.15b).

The SEM analysis of the etched samples revealed that the overlapped locations have a martensitic phase with a needle-like microstructure. The SEM microstructures revealed a martensitic and a cellular microstructure. The austenitic-martensitic transformation can be attributed to the rapid solidification rate inside the melting pool when the laser moves from one spot to another. The microstructures revealed the epitaxial growth across a track boundary (Figure 3.16a) and across a melt pool boundary (Figure 3.16b). The significant temperature gradients and rapid solidification rates across these boundaries cause martensitic transformation. The austenitic phase has a cellular microstructure due to

micro voids and carbide precipitates as shown in Figure 3.16. These carbide precipitates are the reason for the large amount of carbon that was observed in the EDS analysis. Previous studies showed similar distinct fine and complex columnar microstructures of the additively manufactured parts [69-71].

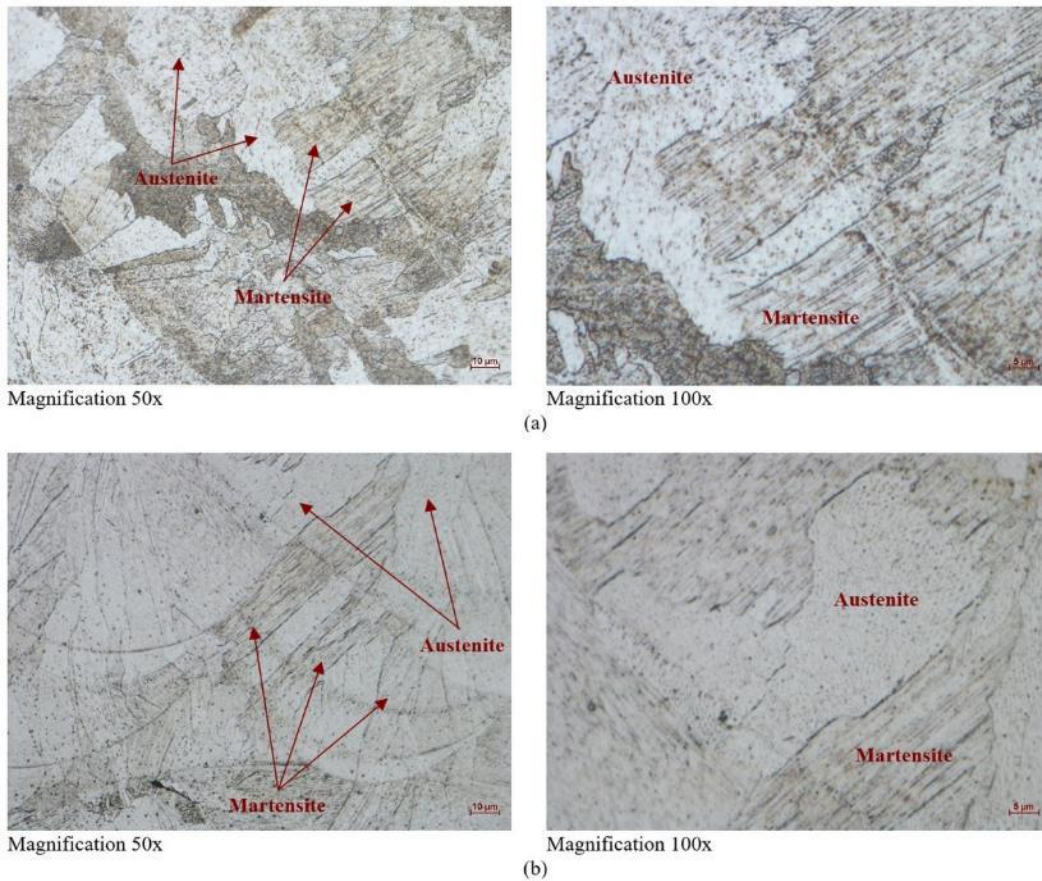


Figure 3.15: Micrographs of the *etched* (a) top surface and (b) side surface at high magnification.

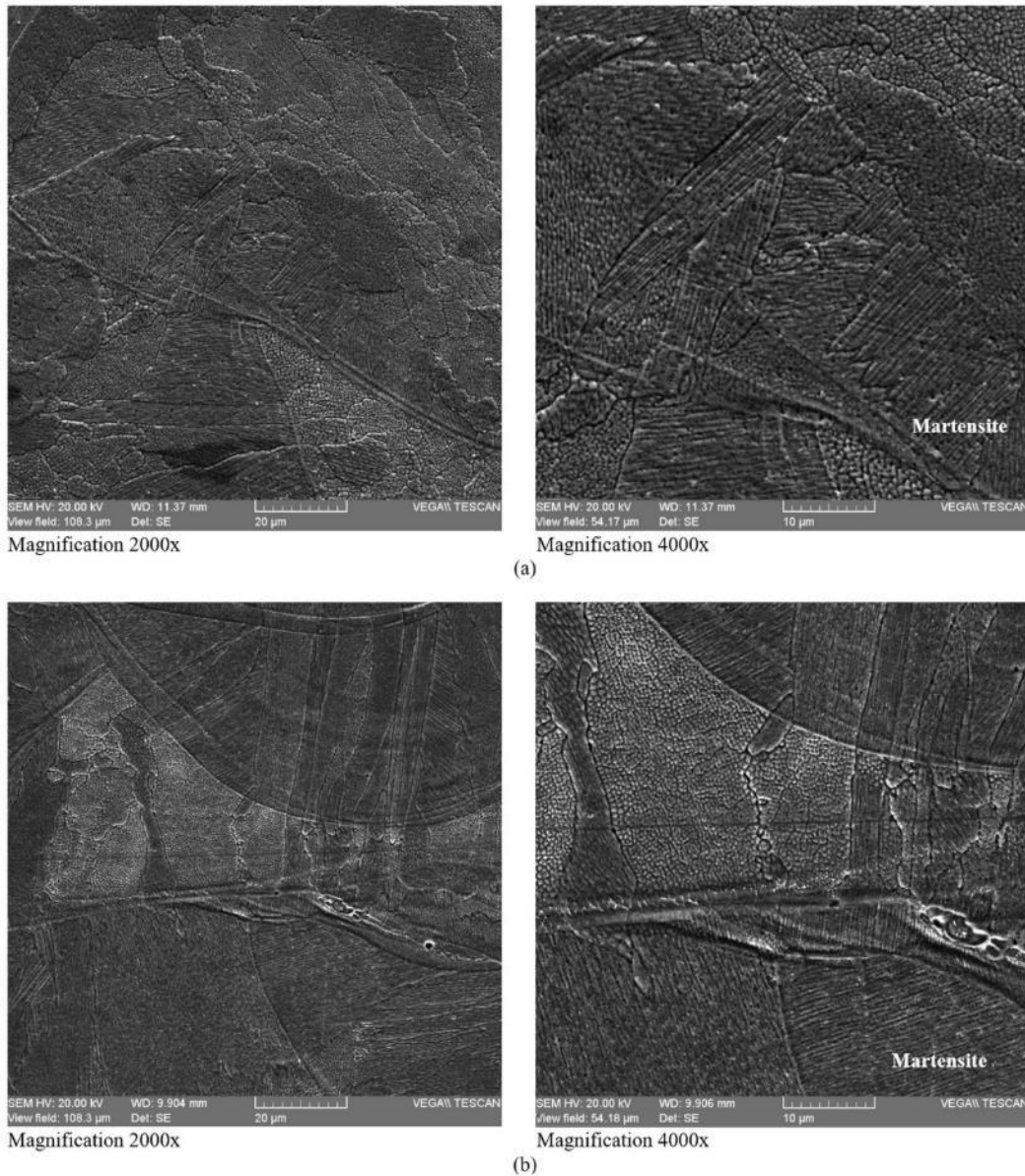


Figure 3.16: Microstructures of the *etched* (a) top surface and (b) side surface.

3.4.5 Residual stress

3.4.5.1 Horizontal residual stress

Samples in group A have identical surface areas, but different inclination angles. Thus, they were prepared for analyzing the horizontal residual stress in the parts produced. The horizontal residual stresses were measured on the top surfaces of the samples. The analysis

showed that the top surfaces have compressive residual stresses in the horizontal plane (i.e., along the scanning direction). Figure 3.17 shows the relationship between the principal residual stresses and the distance from the leading edge of the airfoil blade. The maximum principal stress ranges from -195 MPa to -409 MPa and the minimum principal stress ranges from -93 MPa to -351 MPa. All the observed stresses in the horizontal direction were compressive. The results revealed that the large areas (i.e., near the leading edges) have more compressive residual stresses than the small areas (i.e., near the trailing edges). Figure 3.18a shows the trend of the horizontal residual stresses along the top surfaces of the samples in group A. It was observed that the horizontal residual stress increases with the increase in surface area (towards the trailing edge). This compressive residual stress in the horizontal direction can be attributed to surface hardening [72-74]. There are two driving mechanisms that cause a decrease in the horizontal residual stress towards the end of the scan track: (i) the scan track [31] and (ii) the martensitic phase transformation [74]. At the start of the scan track, the temperature gradient between the molten metal and the surrounding powder is high and induces a large amount of residual stresses [31]. Towards the end of the scan track, the temperature gradient decreases and consequently the residual stress decreases as shown in Figure 3.18b. The martensitic phase transformation also causes residual stresses due to surface hardening. The martensitic transformation causes a compressive stress in the surface and a tensile stress in the core as shown in Figure 3.18c. The rapid cooling in the core will cause martensite formation that results in a volume expansion. This volume expansion will cause a tensile residual stress in the core and a compressive residual stress in the top surface. The volume expansion decreases with the decrease of the surface area of the airfoil.

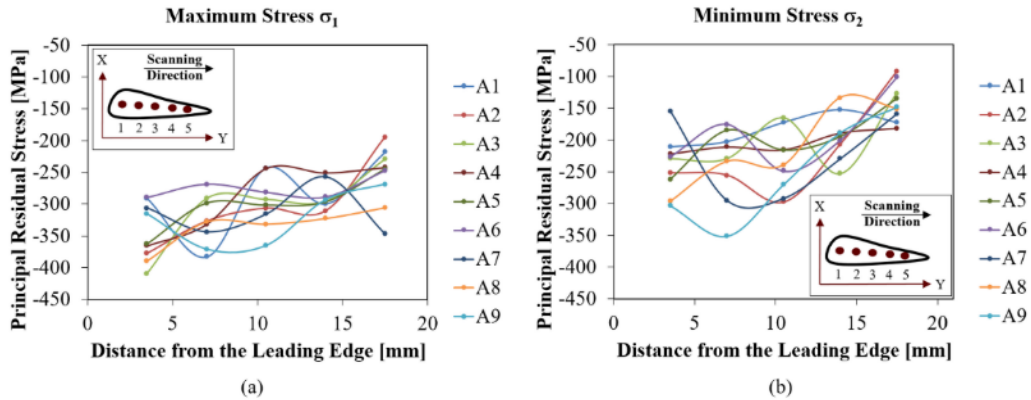


Figure 3.17: Horizontal residual stress along the top surface. (a) Maximum principal stress. (b) Minimum principal stress.

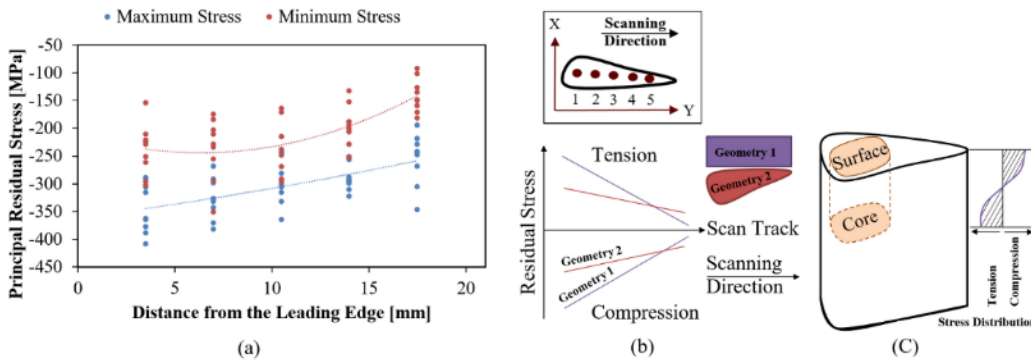


Figure 3.18: (a) Trend of horizontal residual stress along the top surface, (b) effect of the scan track on the horizontal residual stress, and (c) effect of the surface hardening on the residual stress.

3.4.5.2 Vertical residual stress

The vertical residual stress was measured in the build direction Z in the center of the samples from group A as shown in Figure 3.19. The analysis (in the Z direction) showed that the maximum principal stress starts with compression in the top layers, decreases towards the middle layers, and then increases again in the bottom layers. The minimum principal stress starts either with tension in the top layers and ends with compression in the bottom layers or vice versa. The bottom and top layers are surrounded by unmelted powder which causes high temperature gradients during the melting process and consequently high residual stress. It was also observed that the samples located at the center of the build plate

have the largest amount of residual stress. This can be attributed to the amount of heat energy that is building up at the center of the build plate during the melting process. The large heat energy causes more thermal stresses and martensitic transformation, which consequently cause more residual stresses.

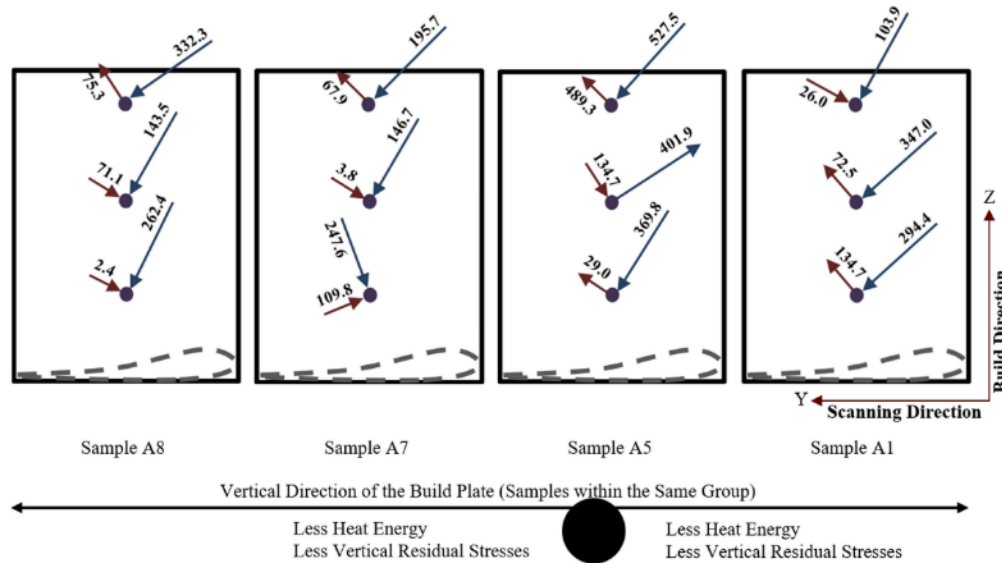


Figure 3.19: Directions and magnitudes of principal residual stresses along the vertical direction of samples in group A.

Samples in group B have identical dimensions, so nine points were measured in both Y and Z directions, in which the Y direction represents the scanning direction and the Z direction represents the build direction as shown in Figure 3.20. These measurements were used for studying the effect of the part location on the build plate. The residual stress evolution along the build direction was identified in three different planes; near the trailing edge, at the center, and near the leading edge as shown in Figure 3.20. From the measurements, it was observed that:

1. The part thickness and scan track affect the residual stress profile (the Y direction).
2. The residual stress magnitude changes along the part height (the Z direction).
3. The residual stress evolution is affected by the part location on the build plate.

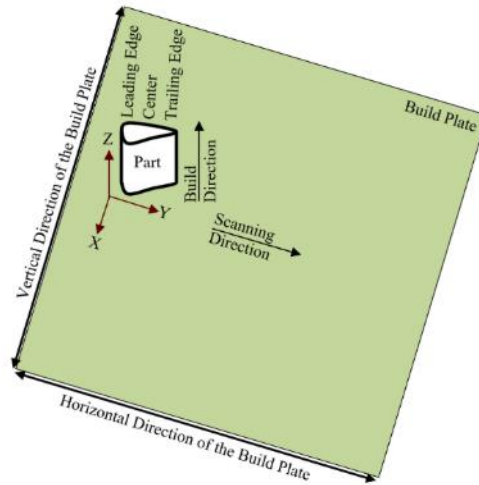


Figure 3.20: Measurement directions for studying the residual stress evolution.

Figure 3.21 shows the directions and magnitudes of the principal residual stresses along the vertical direction. It was observed that the residual stress evolution is affected by: (i) the vertical distance from the top layer, (ii) the part thickness (i.e., difference between leading and trailing edges), and (iii) the part location on the build plate. Three different analyses were performed to study the effect of the part height, part thickness, and part location on the build plate, on the residual stress distribution.

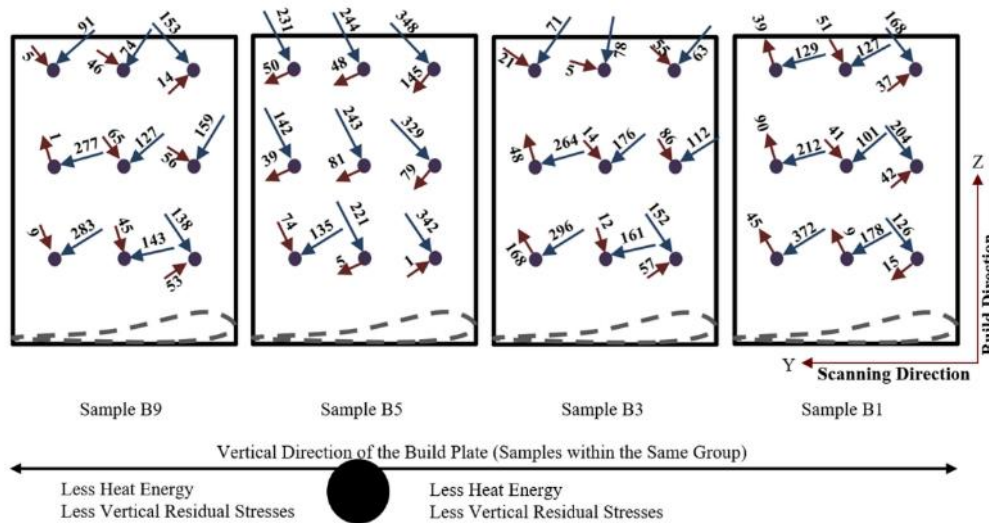


Figure 3.21: Directions and magnitudes of principal residual stresses along the vertical direction of samples in group B.

The first analysis included the evolution of the vertical residual stress along the build direction “the Z direction.” Figure 3.22 shows the vertical residual stress profiles along the build “height” direction in three different planes: near the leading edge, in the center, and near the trailing edge. The analysis showed that the vertical residual stress increases towards the bottom layers for most of the samples. It was also observed that the minimum principal stress is tensile while the maximum principal stress is compressive. The sample located at the center of the build plate (B5) has the largest amount of residual stresses compared with the samples located at the edges of the build plate. This may be attributed to the large amount of heat that is building up at the center of the build plate. This heat energy causes martensitic phase transformation and high residual stress.

For further investigation, the second analysis included the study of the vertical residual stress along the scanning direction (the Y direction) from the leading edge towards the trailing edge. Figure 3.23 shows the vertical residual stress distribution in the scanning direction. The analysis showed that the vertical residual stress decreases towards the small thickness (i.e., near the trailing edge) for most of the samples. It was also observed that the minimum residual stress switches from compression in the leading edge to tension in the trailing edge for few of the samples. This can be attributed to two phenomena: the thickness effect and scan track. It is well known that the temperature gradient decreases with a reduction in thickness which causes a decrease in the thermal residual stresses. The other mechanism is the scan track in which the residual stress decreases towards the end of the scan track. When the melting process starts, the temperature gradient becomes very large causing a large amount of thermal stress. However, the thermal stress decreases towards the end of the scan track which cause a reduction in the residual stress. These two mechanisms are the driving forces for the vertical residual stress distribution.

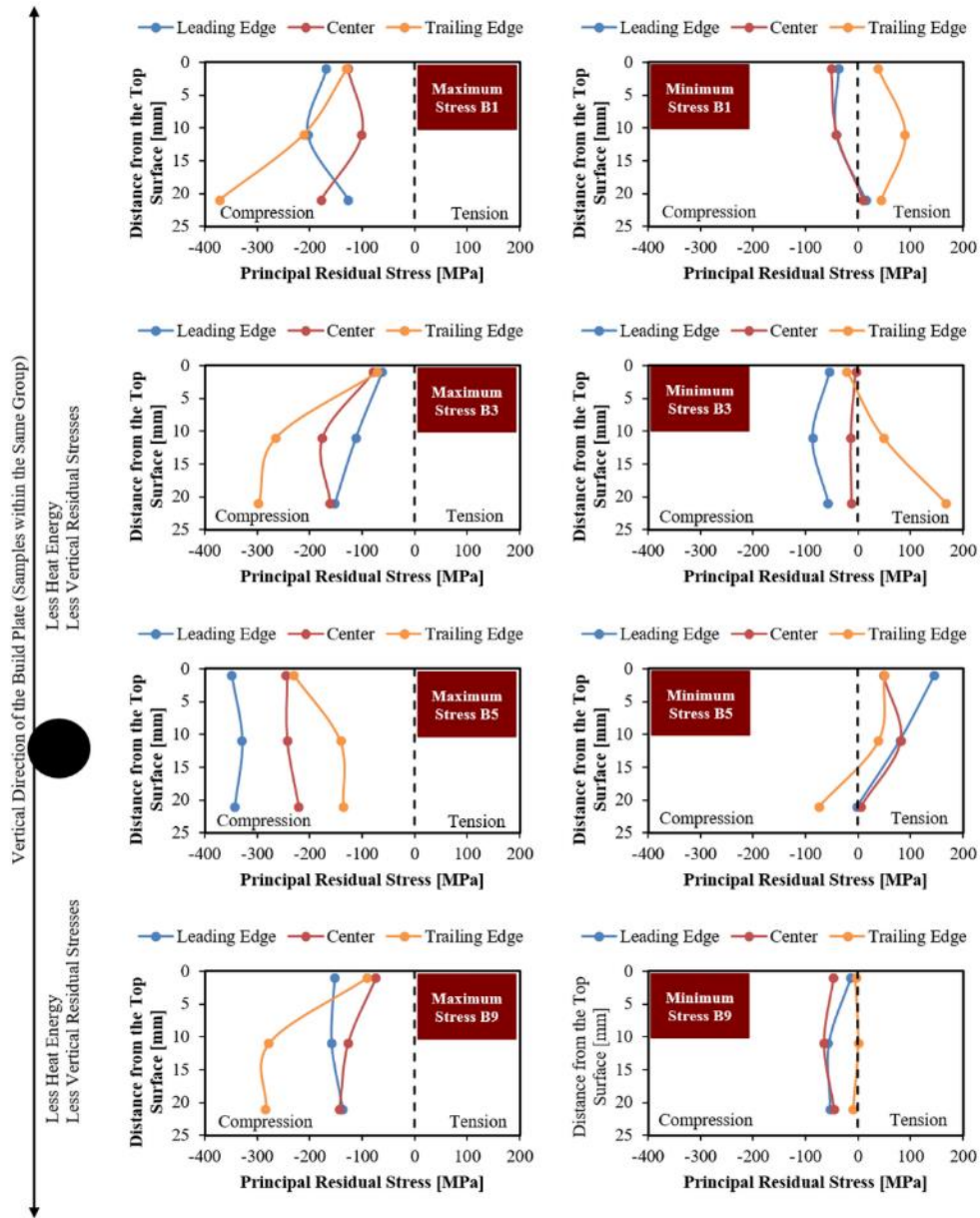


Figure 3.22: Evolution of the vertical residual stress along the build direction.

The third analysis investigated the effect of the part location on the build plate on the residual stress distribution. Figure 3.24 shows the magnitude of the residual stress for samples located at different locations on the build plate. The results showed that both the maximum and minimum residual stress increases toward the center of the build plate and decreases toward both top and bottom sides. These results are consistent with the microstructure

analysis which showed that the parts located at the center of the build plate have more cracks between the layers. This can be attributed to the amount of thermal stress at the center of the build plate during the melting process. The cooling and solidification rates at the center of the build plate are affected by the amount of heat coming from the surrounding parts.

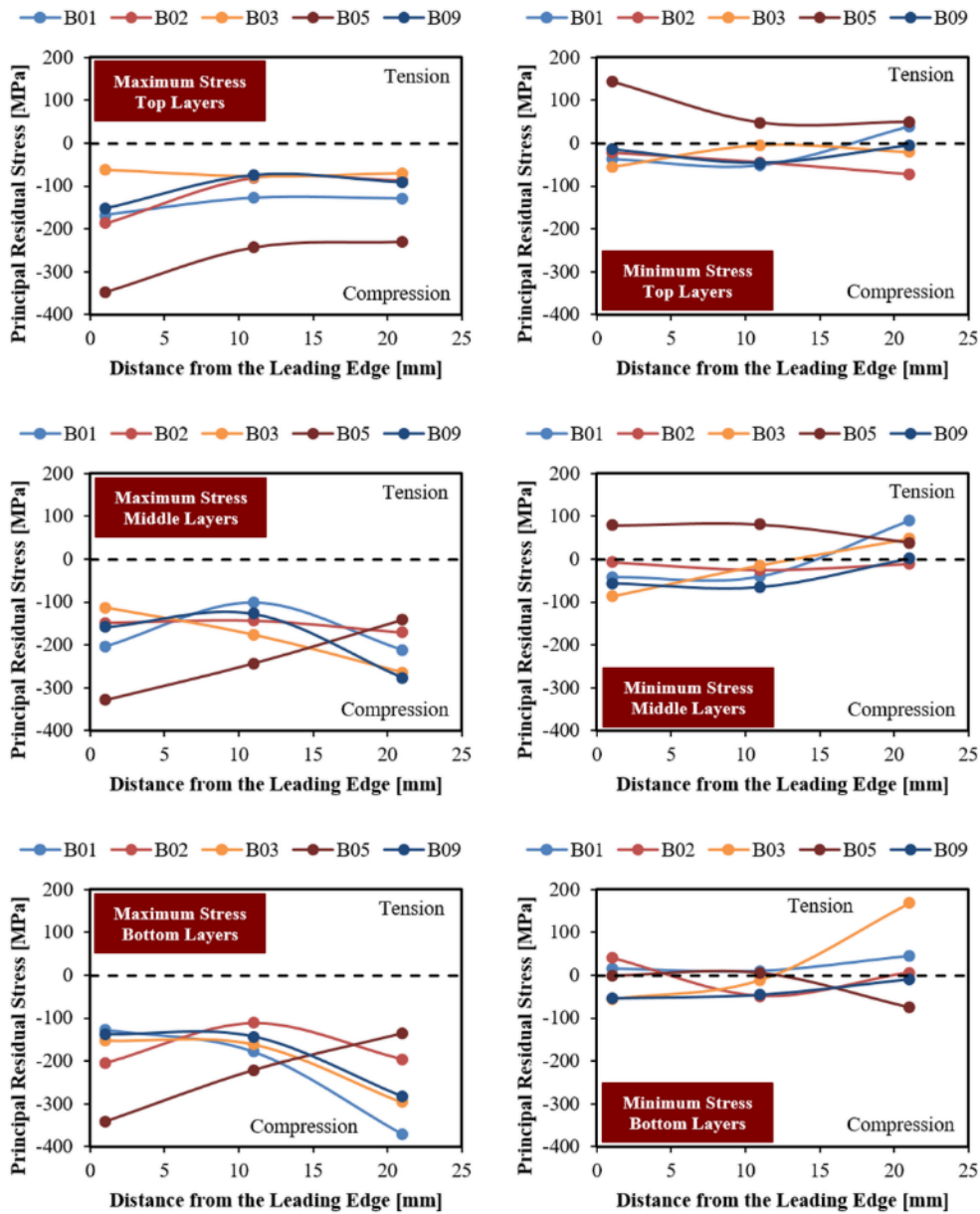


Figure 3.23: Evolution of the vertical residual stress along the scanning direction.

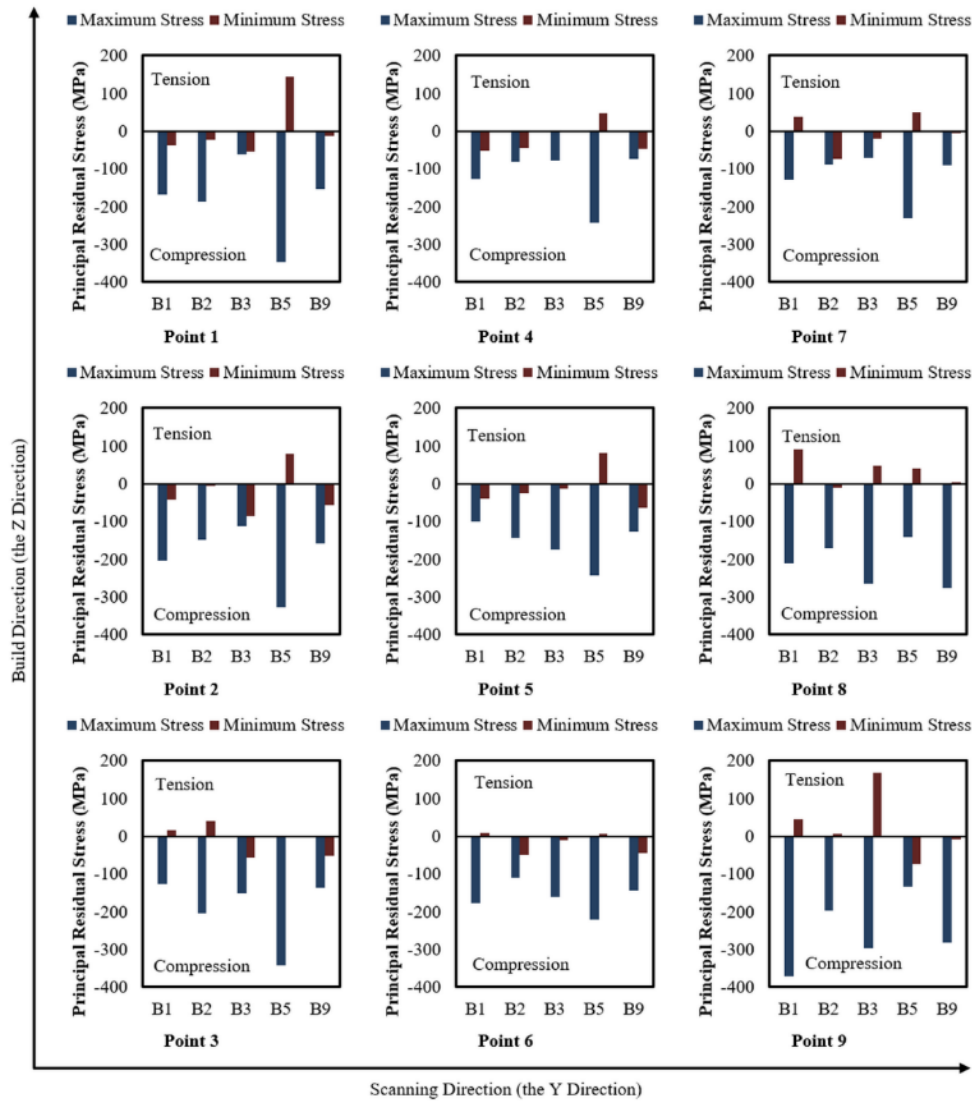


Figure 3.24: Evolution of the vertical residual stresses along the build plate (B1 is located at the top side of the build plate, B5 is located at the center, and B9 is located at the bottom side).

In the SLM process, the part location on the build plate, gas flow direction, scan track and direction, and part height affect the quality of the parts produced [20, 28, 75]. In the current study, the nitrogen gas flow was adjusted from the right side to the left side across the melting chamber, but the parts were melted from the top side to bottom side of the build plate. The residual stress analysis was based on samples in group B which are located perpendicular to the gas flow direction. Hence, the analysis does not include the effect of the

gas flow. It was observed that the parts located at the center of the build plate undergo high built-up laser energy causing microsegregation of some elements, vaporization of some particles, and a martensitic phase transformation as mentioned in Figure 3.25a. This material transformation will induce a large amount of residual stresses in the parts and may initiate cracks between subsequent layers. However, these parts should not experience significant balling phenomenon and may have less partially melted powders due to the high energy. More experiments are recommended for future work to confirm and verify that the laser energy is building up toward the center of the build plate. It was also observed that the top layers have an increased temperature gradient as compared to the bottom layers due to the low temperature of the surrounding powder. This temperature gradient will produce high thermal stresses that will induce high residual stresses in those layers as illustrated in Figure 3.25b. The scan track also affects the temperature gradient within the same layer. The long scan track leads to a small temperature gradient which will decrease the amount of the residual stresses at the end of the scan track. However, it will affect the wettability of the molten metal and may cause a balling phenomenon as shown in Figure 3.25c.

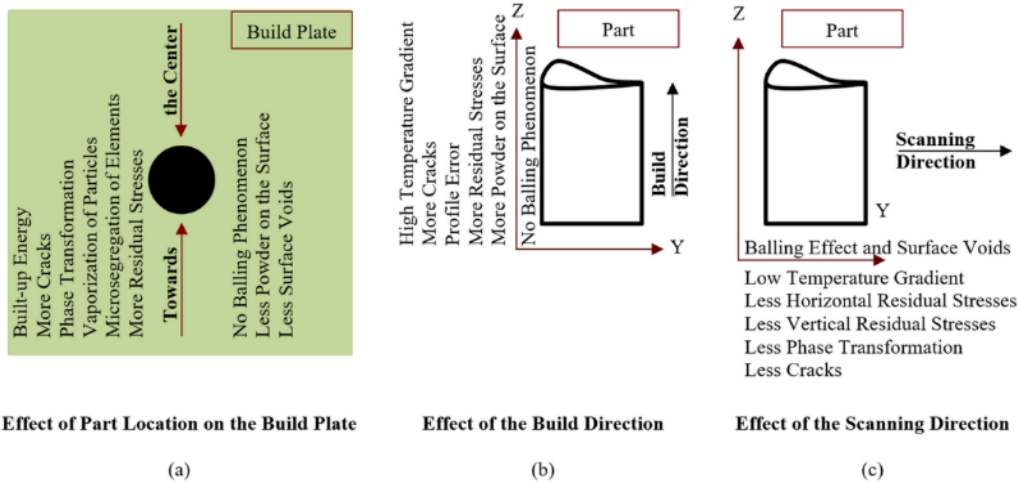


Figure 3.25: Effect of (a) part location on the build plate, (b) build direction, and (c) scanning direction on the quality of the parts produced.

3.5 Conclusions

The main objective of this paper was to perform an extensive experimental study focused on the characterization of stainless steel 316L, simplified air foil blades, produced by selective laser melting. Stainless steel 316L has been used for many applications in the aerospace industry due to its corrosion resistance resulting from the nickel and molybdenum contents in the alloy. The study included an evaluation of the mechanical properties and the quality of the parts produced. A comprehensive analysis is presented including the profile error, microstructure features, material composition, phase transformation, and residual stress of the selective laser melted parts.

The effect of the part location on the build plate, part height, and part dimensions on the microstructure characteristics of the parts was studied. It was observed that the built-up heat energy affects the microstructure of the parts produced. At the center of the build plate, some elements microsegregated and some particles were ejected from the melting pool and converted into soot. This may occur at the center of the build plate due to the built-up energy originating from the surrounding parts. This built-up energy also caused a martensitic transformation in the airfoils, which induced a high amount of residual stresses. At the side of the build plate, the wettability of the molten metal decreases, resulting in the occurrence of a balling phenomenon on the surface. The balling phenomenon has two effects: (i) the molten metal will not be able to complete the scan track with full melting and (ii) the profile error will be affected, causing geometrical distortions in the airfoils. The temperature gradient during the melting process will cause thermal stresses during the process. These thermal stresses are one of the main causes for residual stresses in the parts produced. It can be concluded that the residual stresses are mainly induced during the selective laser melting process by either thermal stresses or phase transformation. These results contribute to improving the application of stainless steel 316L in additive manufacturing of aerospace parts.

3.6 References

- [1] *Standard Terminology for Additive Manufacturing - General Principles - Terminology*, 2015.
- [2] Gu, D. D., Meiners, W., Wissenbach, K., and Poprawe, R., "Laser Additive Manufacturing of Metallic Components: Materials, Processes and Mechanisms," *International Materials Reviews*, vol. 57, no. 3, pp. 133-164, 2012.
- [3] Kruth, J.-P., Mercelis, P., Froyen, L., and Rombouts, M., "Binding Mechanisms in Selective Laser Sintering and Selective Laser Melting," in *Annual International Solid Freeform Fabrication Symposium*, Texas, USA, 2004: University of Texas in Austin.
- [4] Pentair, "The Benefits of Stainless Steel," Pentair, Hoffman and Design 2015.
- [5] Essienubong, I. A., Ikechukwu, O., Ebunilo, P. O., and Ikpe, E., "Material Selection for High Pressure (HP) Turbine Blade of Conventional Turbojet Engines," *American Journal of Mechanical and Industrial Engineering*, vol. 1, no. 1, pp. 1-9, 2016.
- [6] Bhaduri, A. K., Gill, T. P. S., Albert, S. K., Shanmugam, K., and Iyer, D. R., "Repair welding of cracked steam turbine blades using austenitic and martensitic stainless-steel consumables," *Nuclear Engineering and Design*, vol. 206, pp. 249-259, 2001.
- [7] Rawat, M. S., Jayaraman, T. R., Prasad, C. R. K., and Kalpana, Y., "Influence of Shot Peening on Corrosion Properties of Steam Turbine Blading Steel," in *The 7th International Conference on Shot Peening*, Warsaw, Poland, 1999, pp. 184-191.
- [8] Charles, A. P., "Development of a Method to Repair Gas Turbine Blades using Electron Beam Melting Additive Manufacturing Technology," Master of Science, Production Engineering and Management, KTH Royal Institute of Technology, Stockholm 2016.
- [9] Dewangan, R., Patel, J., Dubey, J., Sen, P. K., and Bohidar, S. K., "Gas Turbines Blades - A Critical Review of Failure on First and Second Stages," *International Journal of Mechanical Engineering and Robotics Research*, vol. 4, no. 1, pp. 216-223, 2015.
- [10] Lu, Z. L. *et al.*, "Review of main manufacturing processes of complex hollow turbine blades," *Virtual and Physical Prototyping* vol. 8, no. 2, pp. 87-95, 2013.
- [11] Lewis, J. R., "Design overview of fiber-reinforced superalloy composites for the Space Shuttle main engine," *NASA Marshall Space Flight Center Advanced High Pressure O₂/H₂ Technology*, pp. 93-109, 1985.
- [12] Ugolotti, M. *et al.*, "Cooling System for 0.1 kN Thrust Micro-Engines: Concept Design Using Additive Manufacturing," in *The 58th AIAA/ASCE/AHS/ASC Structures, Structural Dynamics, and Materials Conference*, Texas, USA, 2017.

- [13] Spierings, A. B., Herres, N., and Levy, G., "Influence of the Particle Size Distribution on Surface Quality and Mechanical Properties in Additive Manufactured Stainless Steel Parts," in *Annual International Solid Freeform Fabrication Symposium*, Texas, USA, 2010, pp. 397-406: University of Texas in Austin.
- [14] Spierings, A. B. and Levy, G., "Comparison of Density of Stainless Steel 316L Parts Produced with Selective Laser Melting using Different Powder Grades," in *Annual International Solid Freeform Fabrication Symposium*, Texas, USA, 2009, pp. 342-353: University of Texas in Austin.
- [15] Sun, Z., Tan, X., Tor, S. B., and Yeong, W. Y., "Selective laser melting of stainless steel 316L with low porosity and high build rates," *Materials and Design*, vol. 104, pp. 197-204, 2016.
- [16] Miranda, G. *et al.*, "Predictive models for physical and mechanical properties of 316L stainless steel produced by selective laser melting," *Materials Science & Engineering A*, vol. 657, pp. 43-56, 2016.
- [17] Kruth, J. P., Froyen, L., Vaerenbergh, J. V., Mercelis, P., Rombouts, M., and Lauwers, B., "Selective laser melting of iron-based powder," *Journal of Materials Processing Technology* vol. 149, pp. 616-622, 2004.
- [18] DEWIDAR, M. M., KHALIL, K. A., and LIM, J. K., "Processing and mechanical properties of porous 316L stainless steel for biomedical applications " *Transactions of Nonferrous Metals Society of China* vol. 17, pp. 468-473, 2007.
- [19] Casati, R., Lemke, J., and Vedani, M., "Microstructure and Fracture Behavior of 316L Austenitic Stainless Steel Produced by Selective Laser Melting," *Journal of Materials Science & Technology*, vol. 32, pp. 738-744, 2016.
- [20] Fitzgerald, E. and Everhart, W., "The Effect of Location on the Structure and Mechanical Properties of Selective Laser Melted 316L Stainless Steel," in *Proceedings of the 27th Annual International Solid Freeform Fabrication Symposium*, Texas, USA, 2016.
- [21] Zhang, Y., Liu, F., Chen, J., and Yuan, Y., "Effects of surface quality on corrosion resistance of 316L stainless steel parts manufactured via SLM," *Journal of Laser Applications*, vol. 29, no. 2, pp. 022306 (1-2), 2017.
- [22] Kamath, C., El-dasher, B., Gallegos, G. F., King, W. E., and Sisto, A., "Density of additively-manufactured, 316L SS parts using laser powder-bed fusion at powers up to 400 W," *International Journal of Advanced Manufacturing Technology*, vol. 74, pp. 65-78, 2014.
- [23] UDROIU, R., "Powder Bed Additive Manufacturing Systems and its Applications," *Academic Journal of Manufacturing Engineering*, vol. 10, no. 4, pp. 122-129, 2012.
- [24] Yakout, M., Cadamuro, A., Elbestawi, M. A., and Veldhuis, S. C., "The selection of process parameters in additive manufacturing for aerospace alloys," *The International*

- Journal of Advanced Manufacturing Technology*, vol. 92, no. 5-8, pp. 2081-2098, 2017.
- [25] Song, B. *et al.*, "Differences in Microstructure and Properties between Selective Laser Melting and Traditional Manufacturing for Fabrication of Metal Parts: A Review," *Frontiers of Mechanical Engineering*, vol. 10, no. 2, pp. 111-125, 2015.
- [26] Shiomi, M., Osakada, K., Nakamura, K., Yamashita, T., and Abe, F., "Residual Stress within Metallic Model Made by Selective Laser Melting Process," *CIRP Annals - Manufacturing Technology*, vol. 53, no. 1, pp. 195-198, 2004.
- [27] Mercelis, P. and Kruth, J.-P., "Residual Stresses in Selective Laser Sintering and Selective Laser Melting," *Rapid Prototyping Journal*, vol. 12, no. 5, pp. 254-265, 2006.
- [28] Casavola, C., Campanelli, S. L., and Pappalettere, C., "Experimental Analysis of Residual Stresses in the Selective Laser Melting Process," in *Proceedings of the XIth International Congress and Exposition*, Orlando, Florida USA, 2008: Society for Experimental Mechanics Inc.
- [29] Belle, L. V., Boyer, J.-C., and Vansteenkiste, G., "Investigation of Residual Stresses induced during the Selective Laser Melting Process," *Key Engineering Materials*, vol. 554-557, pp. 1828-1834, 2013.
- [30] Yadroitsev, I. and Yadroitsava, I., "Evaluation of residual stress in stainless steel 316L and Ti6Al4V samples produced by selective laser melting," *Virtual and Physical Prototyping*, vol. 10, no. 2, pp. 67-76, 2015.
- [31] Liu, Y., Yang, Y., and Wang, D., "A study on the residual stress during selective laser melting (SLM) of metallic powder," *International Journal of Advanced Manufacturing Technology*, vol. 87, pp. 647-656, 2016.
- [32] Mishurova, T. *et al.*, "An Assessment of Subsurface Residual Stress Analysis in SLM Ti-6Al-4V," *Materials*, vol. 10, no. 4, pp. 348 (1-14), 2017.
- [33] Vrancken, B., "Study of Residual Stresses in Selective Laser Melting," PhD Degree, Faculty of Engineering Science, KU Leuven, Belgium, 2016.
- [34] Grum, J. and Šturm, R., "A new experimental technique for measuring strain and residual stresses during a laser remelting process," *Journal of Materials Processing Technology*, vol. 147, pp. 351-358, 2004.
- [35] Schajer, G. S. and Ruud, C. O., "Overview of Residual Stresses and Their Measurement," in *Practical Residual Stress Measurement Methods*, G. S. Schajer, Ed. 1st ed. United Kingdom: John Wiley & Sons Ltd, 2013.
- [36] Ibraheem, A. K., Derby, B., and Withers, P. J., "Thermal and Residual Stress Modelling of the Selective Laser Sintering Process," in *Materials Research Society*

- Symposium Proceedings*, Boston, Massachusetts , United Kingdom, 2003, vol. 758: Materials Research Society.
- [37] Yadroitsava, I. and Yadroitsev, I., "Residual Stress in Metal Specimens Produced by Direct Metal Laser Sintering," in *Annual International Solid Freeform Fabrication Symposium*, Texas, USA, 2015.
- [38] Wang, X. and Chou, K., "Residual Stress in Metal Parts Produced by Powder-Bed Additive Manufacturing Processes," in *Annual International Solid Freeform Fabrication Symposium*, Texas, USA, 2015.
- [39] Demir, A. G., Colombo, P., and Previtali, B., "From pulsed to continuous wave emission in SLM with contemporary fiber laser sources: effect of temporal and spatial pulse overlap in part quality," *International Journal of Advanced Manufacturing Technology*, vol. 91, pp. 2701-2714, 2017.
- [40] Wang, S. *et al.*, "Research on High Layer Thickness Fabricated of 316L by Selective Laser Melting," *Materials*, vol. 10, pp. 1055 (1-15), 2017.
- [41] Liu, B., Wildman, R., Tuck, C., Ashcroft, I., and Hague, R., "Investigation the effect of particle size distribution on processing parameters optimisation in selective laser melting process," in *The 22nd International solid freeform fabrication symposium*, Texas, USA, 2011.
- [42] Yadroitsava, I. and Yadroitsev, I., "Evaluation of Residual Stress in Selective Laser Melting of 316L Steel," in *The 1st International Conference on Progress in Additive Manufacturing*, Singapore, 2014.
- [43] Yadroitsev, I. and Smurov, I., "Selective laser melting technology: from the single laser melted track stability to 3d parts of complex shape," *Physics Procedia*, vol. 5, pp. 551-560, 2010.
- [44] Yasa, E., Deckers, J., Kruth, J.-P., Rombouts, M., and Luyten, J., "Investigation of Sectoral Scanning in Selective Laser Melting " in *ASME 2010 10th Biennial Conference on Engineering Systems Design and Analysis*, Istanbul, Turkey, 2010, vol. 4, pp. 695-703.
- [45] Yasa, E., "Manufacturing by combining selective laser melting and selective laser erosion/laser re-melting," PhD Department of Mechanical Engineering, Katholieke Universiteit Leuven, Leuven, 2011.
- [46] Kruth, J. P., Deckers, J., Yasa, E., and Wauthle, R., "Assessing influencing factors of residual stresses in selective laser melting using a novel analysis method," in *The 16th International Symposium on Electromachining (ISEM XVI)*, Shanghai, China, 2010.
- [47] Liverani, E., Toschi, S., Ceschini, L., and Fortunato, A., "Effect of selective laser melting (SLM) process parameters on microstructure and mechanical properties of 316L austenitic stainless steel," *Journal of Materials Processing Technology*, vol. 249, pp. 255-263, 2017.

- [48] Yasa, E., Craeghs, T., Badrossamay, M., and Kruth, J.-P., "Rapid Manufacturing Research at the Catholic University of Leuven," presented at the US Turkey Workshop on Rapid Technologies, Istanbul, Turkey, 2009.
- [49] Dadbakhsh, S., Hao, L., and Sewell, N., "Effect of selective laser melting layout on the quality of stainless steel parts," *Rapid Prototyping Journal*, vol. 18, pp. 241-249, 2012.
- [50] Kruth, J., Badrossamay, M., Yasa, E., Deckers, J., Thijs, L., and Humbeeck, J. V., "Part and material properties in selective laser melting of metals," in *The 16th International Symposium on Electromachining (ISEM XVI)*, Shanghai, China, 2010.
- [51] Laohaprapanon, A. *et al.*, "Optimal Scanning Condition of Selective Laser Melting Processing with Stainless Steel 316L Powder," *Advanced Materials Research*, vol. 341-342, pp. 816-820, 2011.
- [52] Shifeng, W., Shuai, L., Qingsong, W., Yan, C., Sheng, Z., and Yusheng, S., "Effect of molten pool boundaries on the mechanical properties of selective laser melting parts," *Journal of Materials Processing Technology*, vol. 214, pp. 2660-2667, 2014.
- [53] Li, R., Liu, J., Shi, Y., Wang, L., and Jiang, W., "Balling behavior of stainless steel and nickel powder during selective laser melting process," *International Journal of Advanced Manufacturing Technology*, vol. 59, pp. 1025-1035, 2012.
- [54] Saeidi, K., "Stainless steels fabricated by laser melting, Scaled-down structural hierarchies and microstructural heterogeneities," PhD Department of Materials and Environmental Chemistry, Stockholm University, Stockholm, Sweden, 2016.
- [55] Yusuf, S. M., Chen, Y., Boardman, R., Yang, S., and Gao, N., "Investigation on Porosity and Microhardness of 316L Stainless Steel Fabricated by Selective Laser Melting," *Metals*, vol. 7, pp. 64 (1-12), 2017.
- [56] Mumtaz, K. A. and Hopkinson, N., "Selective Laser Melting of thin wall parts using pulse shaping," *Journal of Materials Processing Technology*, vol. 210, pp. 279-287, 2010.
- [57] Krol, M. and Tanski, T., "SURFACE QUALITY RESEARCH FOR SELECTIVE LASER MELTING OF Ti-6Al-4V ALLOY," *Archives of Metallurgy and Materials*, vol. 61, no. 3, pp. 1291-1296, 2016.
- [58] Barari, A., Kishawy, H. A., Kaji, F., and Elbestawi, M. A., "On the surface quality of additive manufactured parts," *International Journal of Advanced Manufacturing Technology*, vol. 89, pp. 1969-1974, 2017.
- [59] Yasa, E. and Kruth, J., "APPLICATION OF LASER RE-MELTING ON SELECTIVE LASER MELTING PARTS " *Advances in Production Engineering & Management*, vol. 6, no. 4, pp. 259-270, 2011.

- [60] Rombouts, M., Maes, G., Hendrix, W., Delarbre, E., and Motman, F., "Surface finish after laser metal deposition," *Physics Procedia* vol. 41, pp. 810-814, 2013.
- [61] Gunenthiram, V. *et al.*, "Experimental analysis of spatter generation and melt-pool behavior during the powder bed laser beam melting process," *Journal of Materials Processing Technology*, vol. 251, pp. 376-386, 2018.
- [62] Yadroitsev, I., Bertrand, P., and Smurov, I., "Parametric analysis of the selective laser melting process," *Applied Surface Science* vol. 253, pp. 8064-8069, 2007.
- [63] Andani, M. T., Dehghani, R., RezanKaramooz-Ravari, M., Mirzaeifar, R., and Ni, J., "Spatter formation in selective laser melting process using multi-laser technology," *Materials & Design*, vol. 131, pp. 460-469, 2017.
- [64] Guessasma, S., Zhang, W., Zhu, J., Belhabib, S., and Nouri, H., "Challenges of additive manufacturing technologies from an optimisation perspective," *International Journal for Simulation and Multidisciplinary Design Optimization*, vol. 6, pp. A9 (1-13), 2015.
- [65] He, X., DebRoy, T., and Fuerschbach, P. W., "Alloying Element Vaporization during Laser Spot Welding of Stainless Steel," *Journal of Physics D: Applied Physics*, vol. 36, pp. 3079-3088, 2003.
- [66] Mukherjee, T., Zuback, J. S., De, A., and DebRoy, T., "Heat and Fluid Flow Modeling to Examine 3D-Printability of Alloys," in *7th International Symposium on High-Temperature Metallurgical Processing*, 2016, pp. 471-478: The Minerals, Metals & Materials Society.
- [67] Attallah, M. M., Jennings, R., Wang, X., and Carter, L. N., "Additive Manufacturing of Ni-Based Superalloys: The Outstanding Issues," *MRS Bulletin*, vol. 41, no. 10, pp. 758-764, 2016.
- [68] Quan, B., Saeidi, K., Kvetkova, L., Lofaj, F., Xiao, C., and Shen, Z., "Defects-tolerant Co-Cr-Mo dental alloys prepared by selective laser melting," *Dental Materials*, vol. 31, no. 12, pp. 1435-1444, 2015.
- [69] Saeidi, K., Gao, X., Zhong, Y., and Shen, Z. J., "Hardened austenite steel with columnar sub-grain structure formed by laser melting," *Materials Science & Engineering A*, vol. 625, pp. 221-229, 2015.
- [70] Casati, R., Lemke, J. N., Tuissi, A., and Vedani, M., "Aging Behaviour and Mechanical Performance of 18-Ni 300 Steel Processed by Selective Laser Melting," *Metals*, vol. 6, pp. 218 (1-13), 2016.
- [71] Chlebus, E., Kuźnicka, B., Kurzynowski, T., and Dybała, B., "Microstructure and mechanical behaviour of Ti—6Al—7Nb alloy produced by selective laser melting," *Materials Characterization*, vol. 62, pp. 488-495, 2011.

- [72] Grum, J., "Comparison of different techniques of laser surface hardening," *Journal of Achievements in Materials and Manufacturing Engineering*, vol. 24, no. 1, pp. 17-25, 2007.
- [73] Ericsson, T., "RESIDUAL STRESSES CAUSED BY THERMAL AND THERMOCHEMICAL SURFACE TREATMENTS " in *Advances in Surface Treatments: Technology - Applications - Effects*, vol. 4 "Residual Stresses", A. Niku-Lari, Ed. Pergamon Press, 1986.
- [74] Coupard, D., Palin-luc, T., Bristiel, P., Ji, V., and Dumas, C., "Residual stresses in surface induction hardening of steels: Comparison between experiment and simulation," *Materials Science and Engineering: A*, vol. 487, no. 1-2, pp. 328-339, 2008.
- [75] John, D. B. S., Joshi, S. B., Simpson, T. W., Qu, M., Rowatt, J. D., and Lou, Y., "A Preliminary Examination of Variability Due to Build Location and Powder Feedstock in Additive Manufacture of Inconel 718 using Laser-Based Powder Bed Fusion," in *The 27th Annual International Solid Freeform Fabrication Symposium*, Texas, USA, 2016.

Chapter 4

Residual Stresses and Mechanical Properties of Invar 36 and Stainless Steel 316L Produced Using Selective Laser Melting

Complete Citation:

Yakout, M., Elbestawi, M.A., Veldhuis, S.C. (2019). Density and mechanical properties in selective laser melting of Invar 36 and stainless steel 316L. *Journal of Materials Processing Technology*, Volume 266, pp 397-420. Doi: 10.1016/j.jmatprotec.2018.11.006

Copyright:

© 2018 The Authors Under CC BY-NC-ND 4.0 License. Published by Elsevier.

Relative Contributions:

- M. Yakout: Performed experiments, analysis, and data interpretation. Wrote the first draft of the manuscript. Helped with submitting the final manuscript to the journal (corresponding author).
- M. A. Elbestawi: Co-supervisor of M. Yakout. Revised the manuscript. Was responsible of submitting the final manuscript to the journal (corresponding author).
- S. C. Veldhuis: Co-supervisor of M. Yakout. Revised the manuscript.

Abstract:

In this study, the process-structure-property relationship for selective laser melting of Invar 36 and stainless steel 316L is discussed. Invar 36 and stainless steel 316L have been used in various industrial applications for their unique properties, especially in the aerospace industry. Invar 36 offers a very low coefficient of thermal expansion while stainless steel 316L offers high corrosion resistance. Since both materials are weldable, but hard to machine, this study is aimed at finding the optimum laser process parameters for producing dense components from both alloys. A full factorial design of experiments was formulated in this paper to study a wide range of process parameters for both materials. The bulk density, tensile mechanical properties, fractography, material composition, and residual stresses of the parts produced were investigated. An optimum process window has been suggested based on experimental work. The induced residual stresses were categorized into two categories: microscopic residual stresses and macroscopic residual stresses. The microscopic residual stresses were measured using X-ray diffraction method and the macroscopic residual stresses were measured using cantilever deflection method and finite element simulations. The paper proposes two laser energy densities for each material: brittle-ductile transition energy density, E_T , and critical laser energy density, E_C . Below the brittle-ductile transition energy density, the parts exhibited void formation, low density, and brittle fracture. Above the critical energy density, the parts showed vaporization of some alloying elements that have low boiling temperatures. Stable melting ranges were found to occur between these two laser energy densities: 52.1-86.8 J/mm³ for Invar 36 and 62.5-104.2 J/mm³ for stainless steel 316L.

Keywords:

Residual stress; Tensile-test; Invar 36; Steel 316L; Fractography; Metal vaporization.

Acronyms:

AM	Additive manufacturing
SLM	Selective laser melting
SS 316L	Stainless steel 316L
CTE	Coefficient of thermal expansion
γ -Fe	Single phase austenite structure
OFAT	One-factor-at-a-time
SEM	Scanning electron microscopy
DOE	Design of experiments
CMM	Coordinate measuring machine
XRD	X-ray diffraction
EDM	Electrical discharge machining
FE	Finite element
MS1	Maraging steel
EDX	Energy dispersive X-ray spectroscopy
ANOVA	Analysis of variance

Notations:

E_v	Volumetric laser energy density (J/mm^3)
E_C	Critical laser energy density (J/mm^3)
E_v	Brittle-ductile transition energy density (J/mm^3)
P	Laser power (W)

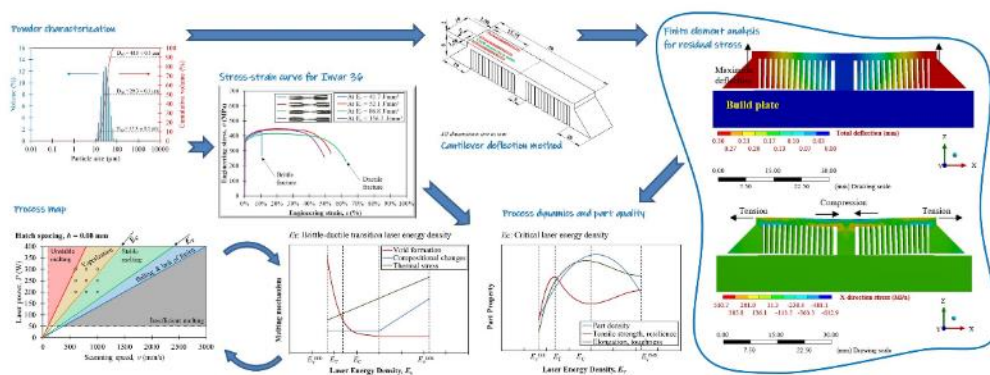
v	Average scanning speed (mm/s)
d	Point distance (mm)
θ	Exposure time (s)
h	Hatch spacing (mm)
t	Layer thickness (mm)
w	Stripe width (mm)
γ	Stripe overlap (mm)
δ	Beam offset (μm)
$W, \Delta W$	Weight and error in weight (g)
$\rho, \Delta\rho$	Density and density error (g/cm^3)
ρ_r	Relative density (%)
R^2	Coefficient of determination
$PRESS$	Predicted residual error sum of squares
S	Standard deviation
σ	Engineering stress (MPa)
ε	Engineering strain (%)
σ_u	Ultimate tensile strength (MPa)
σ_y	0.2% offset yield strength (MPa)
E	Modulus of elasticity (MPa)
ε_f	Engineering strain at fracture (%)
u_R	Modulus of resilience (MJ/m^3)
u_T	Modulus of toughness (MJ/m^3)
$\sigma_{h1, h2}$	Principal horizontal residual stresses (MPa)
$\sigma_{v1, v2}$	Principal vertical residual stresses (MPa)

e_H	Dimensional height error (mm)
ΔH	Maximum cantilever deflection (mm)
H	Minimum cantilever height (mm)
σ_{rh1}	Longitudinal horizontal relieved stress (MPa)
σ_{rh2}	Lateral horizontal relieved stress (MPa)
σ_{rv}	Vertical relieved stress (MPa)
$S1, S2$	X-ray elastic constants
2θ	X-ray diffraction angle

Acknowledgment:

The authors thank the McMaster Analytical X-Ray Diffraction (MAX) team at McMaster University for their assistance during the XRD measurements. The authors also thank the COM DEV International (part of Honeywell Aerospace) team in Cambridge, Ontario, Canada for highlighting the importance of Invar 36 in the aerospace industry. The use of the wire EDM facility at Liburdi Engineering in Dundas, Ontario, Canada is gratefully acknowledged.

Graphical Abstract:



4.1 Introduction

Recently, additive manufacturing (AM) processes have been used in the aerospace industry for producing complex designs from various weldable metals and composite materials. Selective laser melting (SLM), as a powder-bed process, is capable of fulfilling the aerospace industry requirements and produce functional parts, layer-by-layer, via metal powder melting. SLM of Invar 36 and stainless steel 316L (SS 316L) were investigated in this paper. Both materials have a single-phase austenite (γ -Fe) crystal structure. The nickel concentration is different in both alloys: 36% in Invar 36 and 10-14% in SS 316L which makes Invar 36 unique with its very low coefficient of thermal expansion (CTE). However, SS 316L have 16-18% chromium that gives the alloy a corrosion resistance property. Compositional changes in these materials affect their performance during application. DebRoy, et al. [1] reviewed various alloys and processes in metal AM. They explained the weldability of various metals, and they summarized some of the defects and stress risers in AM. Yakout, et al. [2] found that the SLM process parameters affect the density and microstructure of Invar 36. They provided a preliminary study to understand the physical mechanisms involved during the SLM of Invar 36 and Maraging steel. In another publication, Yakout, et al. [3] studied the effect of the part location on the build plate on the residual stress induced in SS 316L components. SLM parts have shown many defects and stress risers including, internal voids, partially melted powder, internal cracks, changes in chemical composition, and thermal stress as mentioned by DebRoy, et al. [1], Yakout, et al. [2], and Yakout, et al. [3]. DebRoy, et al. [1] have suggested parametric studies to better understand what happens during the SLM process and minimize these defects and stress risers. The open literature provides several studies on SS 316L and fewer studies on Invar 36. Qiu, et al. [4] provided a preliminary study of the mechanical properties of Invar

36 produced by SLM. Their study did not cover a wide range of process parameters and did not cover the interactions between the process parameters. Harrison, et al. [5] followed this work and provided CTE measurements and mechanical testing for Invar 36 parts produced via SLM. Their work did not cover the influence of the SLM process parameters on the mechanical properties of parts produced. Spierings and Levy [6] conducted a comparison between SS 316L parts produced with different powder grades. They found that powder agglomeration occurs when using very fine powder particles. Kamath, et al. [7] conducted a density study on SS 316L parts produced at 400 W laser power, and they found that increasing the laser scanning speed will cause an increase in the part density until a peak density, then it decreases. They explained the keyhole pores that could be introduced in the parts when using a very high energy density. However, they have not studied other influencing factors such as mechanical properties and residual stresses. Table 4.1 summarizes the SLM process parameters that have been reported in the literature for producing Invar 36 and SS 316L parts. It is not clear which of these process parameters could be used to produce high quality parts. Previous attempts at optimizing SLM process parameters for part production mainly focused on a one-factor-at-a-time (OFAT) design of experiments and did not include the interactions between factors. Moreover, little insight into the physical mechanisms involved during the SLM process was presented. In this work, the process-structure-property relationships for both materials were studied through experiments based on full factorial design. The SLM process parameters include laser power, P in (W); average scanning speed, v in (mm/s); point distance, d in (mm); exposure time, θ in (s); hatch spacing, h in (mm); layer thickness, t in (mm); stripe width, w in (mm); stripe overlap, γ in (mm); and beam offset, δ in (mm) as shown in Figure 4.1. These

parameters can be combined to calculate the volumetric laser energy density, E_v in (J/mm³), using Equation (4.1).

$$E_v = \frac{P}{(v \times h \times t)}, \quad v = \frac{d}{\theta} \quad (4.1)$$

Table 4.1: Process parameters reported in the literature for producing Invar 36 and SS 316L.

P (W)	v (mm/s)	t (mm)	h (mm)	E_v (J/mm ³)	Reference
Invar 36					
400	1800-4300	0.030	0.300	10-25	[4]
150-300	700-2200	0.040	0.080-0.320	23-93	[2]
300	2500	0.030	0.090	44	[8]
180-200	333-1000	0.020	0.090	100-333	[5]
Stainless steel 316L					
150-400	500-1800	0.030	0.150	28-74	[7]
190	800	0.050	0.150	32	[9]
50-100	300-1250	0.030	0.070-0.140	32-80	[10]
104	175-800	0.030-0.045	0.130	33-107	[6, 11]
100	175-380	0.060	0.126	35-76	[12]
85-105	300	0.020-0.060	0.112-0.125	38-156	[13]
200	1600	0.050	0.060	42	[14]
50	100-300	0.050	0.080	42-125	[15]
200	750	0.050	0.110	48	[3, 16]
105	380	0.020-0.040	0.125	55-111	[17]
87	150	0.075	0.130	59	[18]
100-200	200-220	0.050	0.124	81-150	[19]
50	120	0.040	0.120	87	[20]
100	300	0.030	0.081-0.126	88-137	[21]
100	300	0.030	0.112-0.125	89-99	[22]
380	625-3000	0.050	0.025-0.120	99-109	[23]
100-150	700	0.020	0.050-0.070	102-214	[24]
190	800	0.020	0.100	119	[25]
50	100	0.050	0.070	143	[26]
200	400	0.040	0.080	156	[27]
50	100	0.050	0.060	167	[28]
180	900	0.020	0.060	167	[29]
50	100	0.040	0.070	179	[30]

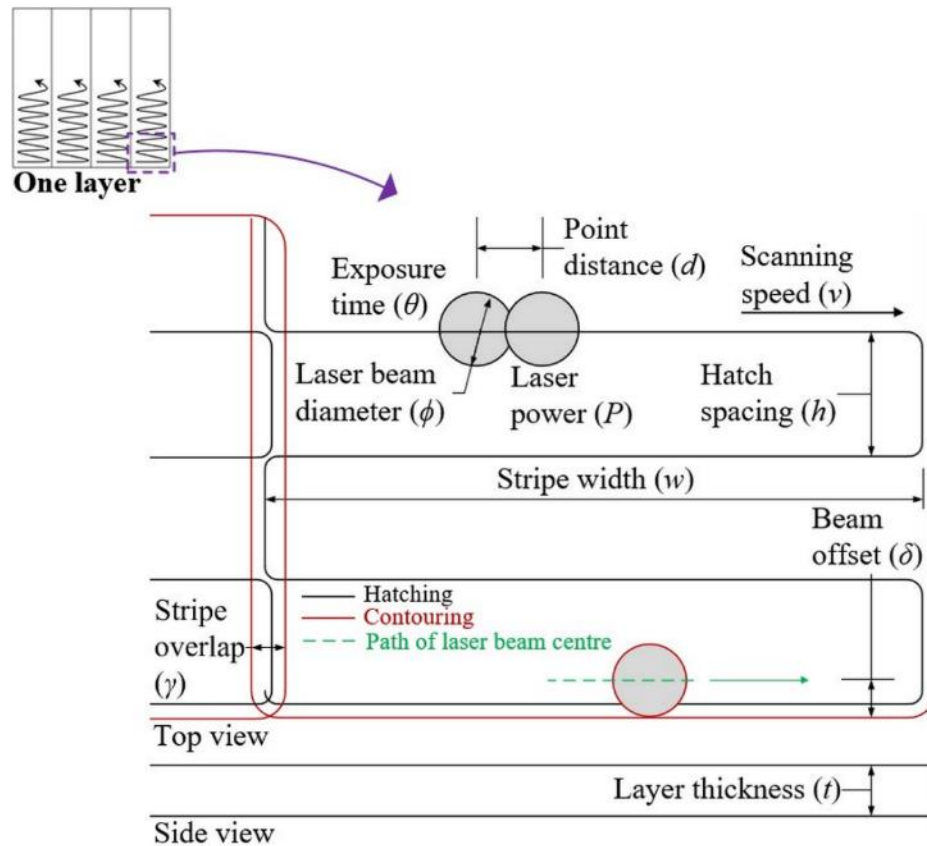


Figure 4.1: Illustration of selective laser melting process parameters [2].

4.2 Materials and methods

4.2.1 Feedstock materials and SLM apparatus

Invar 36 powder provided by Sandvik Osprey LTD and SS 316L powder provided by Carpenter Technology LTD were used in this study. The powders were manufactured via the gas atomization process and sieved using a 200-mesh sieve ($75 \mu\text{m}$) before melting. Prior to SLM, the powder size distribution was determined using a Malvern Mastersizer 2000 instrument via the laser diffraction method and the powder morphology was measured using a scanning electron microscopy (SEM). The particle size of both materials was approximately identical within the repeatability standard deviation ($\pm 1\%$) of the measurement. No significant morphological changes between both powders were observed

as shown in Figure 4.2. The test samples in this study were produced using an EOSINT M280 SLM machine, equipped with a 400 W ytterbium fiber laser. The following conditions were maintained constant during this study: 0.04 mm layer thickness, 10 mm stripe width, 0.08 mm stripe overlap, 67° scanning rotation between subsequent layers, and a stripe scanning strategy. The contouring, up-skin, and down-skin parameters were deactivated so that only the hatching parameters were considered. The laser power, scanning speed, and hatch spacing were considered three independent variables at three levels in a full factorial design of experiments (DOE), as proposed in Table 4.2.

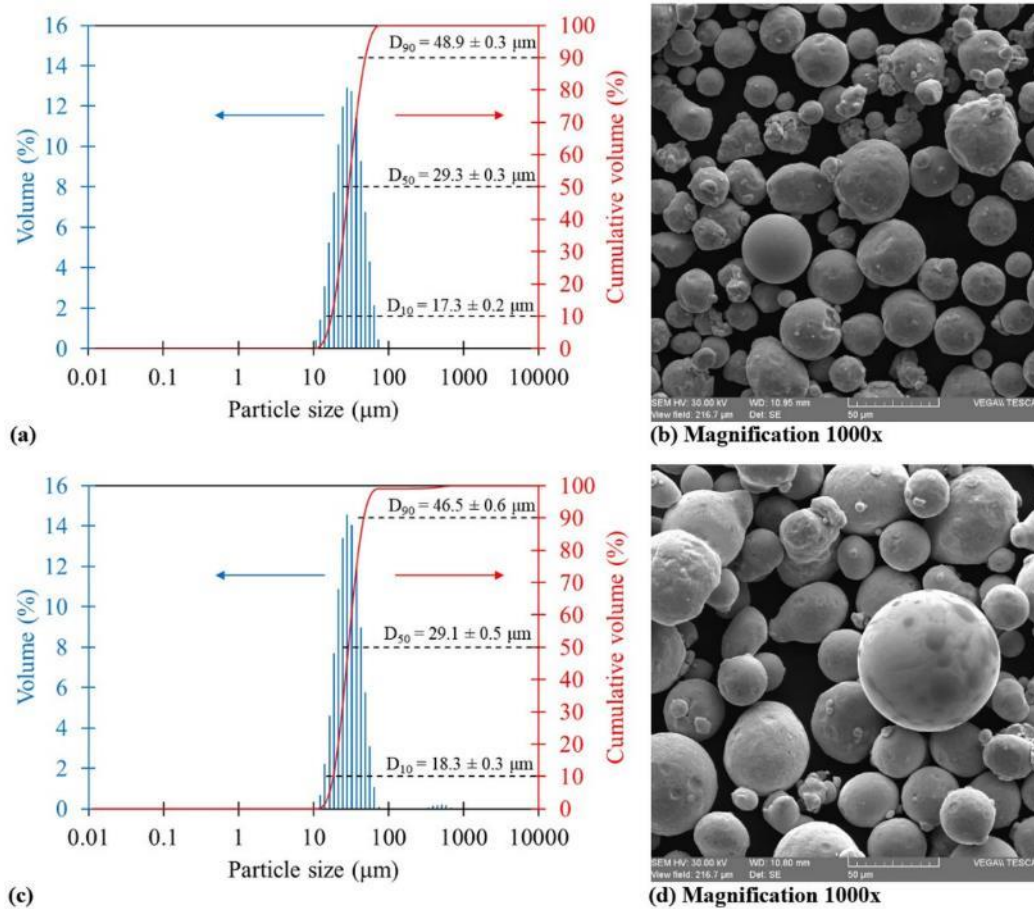


Figure 4.2: (a, c) Differential and cumulative powder size distribution and (b, d) morphology of powders used in this study: (a, b) Invar 36 and (c, d) SS 316L.

Table 4.2: SLM process parameters used in this study (DOE matrix based on full factorial design).

No	P (W)	v (mm/s)	h (mm)	E_v (J/mm ³)	No	P (W)	v (mm/s)	h (mm)	E_v (J/mm ³)
1	200	600	0.08	104.2 **	15	250	800	0.12	65.1
2	200	600	0.10	83.3	16	250	1000	0.08	78.1 ‡
3	200	600	0.12	69.4	17	250	1000	0.10	62.5 †
4	200	800	0.08	78.1 ‡	18	250	1000	0.12	52.1 *
5	200	800	0.10	62.5 †	19	300	600	0.08	156.3
6	200	800	0.12	52.1 *	20	300	600	0.10	125.0
7	200	1000	0.08	62.5 †	21	300	600	0.12	104.2 **
8	200	1000	0.10	50.0	22	300	800	0.08	117.2
9	200	1000	0.12	41.7	23	300	800	0.10	93.8 §
10	250	600	0.08	130.2	24	300	800	0.12	78.1 ‡
11	250	600	0.10	104.2 **	25	300	1000	0.08	93.8 §
12	250	600	0.12	86.8	26	300	1000	0.10	75.0
13	250	800	0.08	97.7	27	300	1000	0.12	62.5 †
14	250	800	0.10	78.1 ‡					
* † ‡ § ** indicate groups that have the same laser energy densities									

Each run of this DOE was used to produce: (i) four cubes with an edge length of 10 mm, (ii) three vertical cylinders with 94 mm length and 16 mm diameter, and (iii) one cantilever beam shown in Figure 4.3 (i.e. a total of 108 cubes, 81 vertical cylinders, and 27 beams were produced from each material). The samples were produced directly on the build plate and did not undergo any post-processing procedures. Prior to manufacturing, the parts were carefully located on the build plate to maintain an even heat distribution. The variations expected in part quality due to part location on the build plate were investigated in previous research work [3]. However, the parts location on the build plate was not considered a major factor in the current study because the thermal history expected during the SLM process was taken into consideration during locating the samples on the build plate. The cubes and cylinders were removed using a band saw, with coolant applied to prevent overheating of the samples.

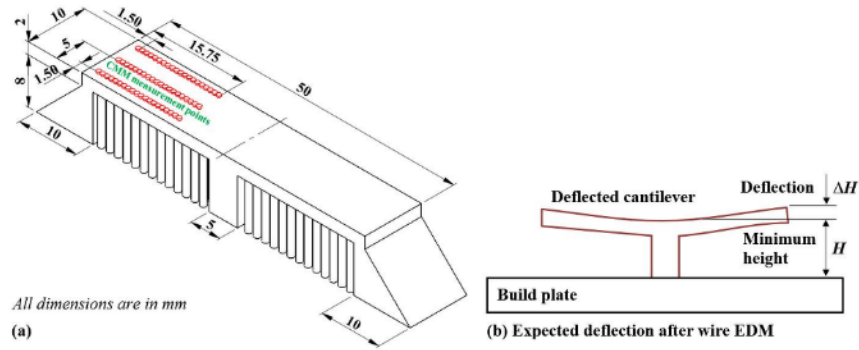


Figure 4.3: Illustration of the (a) SLM cantilever showing the coordinate measuring machine (CMM) measurement locations in one side of the cantilever “red points” and (b) deflected cantilever after residual stress relief.

4.2.2 Density measurement

The density of the cubes was measured at room temperature and atmosphere pressure using the Archimedes method. Each sample was weighed directly on the scale (W_1) as well as immersed in a distilled water (W_2). The water density (ρ_w) is 1 g/cm^3 , Invar 36 bulk density is 8.05 g/cm^3 , and SS 316L bulk density is 8.00 g/cm^3 at room temperature. The resolution of the scale was $\pm 0.01 \text{ g}$, and accordingly the error in weight was ($\Delta W_1 = \Delta W_2 = 0.01 \text{ g}$). The density (ρ), relative density (ρ_r), density error ($\Delta\rho$) of each sample can be calculated using Equation (4.2). The density error ($\Delta\rho$) was determined by propagation of error as mentioned in reference [2].

$$\rho = \rho_w \times \frac{W_1}{W_1 - W_2}, \quad \rho_r \% = \frac{\rho}{\rho_{bulk}} \%, \quad \Delta\rho = \rho \times \sqrt{\left(\frac{\Delta W_1}{W_1}\right)^2 + \left(\frac{\sqrt{(\Delta W_1)^2 + (\Delta W_2)^2}}{W_1 - W_2}\right)^2} \quad (4.2)$$

4.2.3 Tensile testing

The cylinders were machined to the standard specimen size of the tensile-test samples (16 mm gauge length and 4 mm gauge diameter) according to the ASTM F3122-14 and

E8/E8M-16a standards [31, 32]. Tensile tests were carried out at room temperature, and the engineering stress-strain curve was plotted for each sample. The ultimate tensile strength (σ_u), 0.2% offset yield strength (σ_y), modulus of elasticity “Young’s modulus” (E), and percent elongation “engineering strain at fracture” (ϵ_f) were determined and recorded. The estimated modulus of resilience (u_R) and modulus of toughness (u_T) were calculated using Equation (4.3) as mentioned by Budynas, et al. [33].

$$u_R \cong \left(\frac{\sigma_y^2}{2E} \right), \quad u_T \cong \left(\frac{\sigma_u + \sigma_y}{2} \right) \times \epsilon_f - \left(\frac{\sigma_u + \sigma_y}{2} \right)^2 \times \frac{1}{2E} \quad (4.3)$$

4.2.4 Microscopic residual stress measurement

The microscopic residual stress, induced in one cube from each run of experiment, was analyzed via X-ray diffraction (XRD) method, which determines the stress tensor based on lattice strain measurements. The constants of the XRD measurements are shown in Table 4.3 for both materials. Different XRD frames were collected using a CoK α (wavelength 1.79026 Å) radiation source at five different rotation angles ($\Phi = 0^\circ, 70^\circ, 140^\circ, 210^\circ,$ and 280°), four different tilting angles ($\Psi = 10^\circ, 25^\circ, 40^\circ,$ and 55°), detector angle (57.4°), and X-ray angle (59.4°). The microscopic residual stress was measured on the top and lateral surfaces of each cube, where the top surface measurements represent the horizontal residual stress, along the scanning and hatch directions, and the lateral surface measurements represent the vertical residual stress, along the build and layer directions, respectively. Figure 4.4a shows both top and lateral surface measurements, and Figure 4.4b shows the relative position between the sample, X-ray source, and detector. Figure 4.5a shows the directions of the maximum and minimum principal stresses from the top surface measurements. It was observed that the maximum principal stress from the top surface

measurements (σ_{h1}) lies along the laser scanning direction and the minimum principal stress from the top surface measurements (σ_{h2}) lies along the hatch direction. Gusarov, et al. [34] found that the residual stresses in the scanning direction is almost twice the residual stresses in the transverse direction. Cheng, et al. [35] conducted a similar study via finite element analysis that determined the directional stress components. Figure 4.5b shows the directions of the maximum and minimum principal stresses from the lateral surface measurements. It was observed that the maximum principal stress from the lateral surface measurements (σ_{v1}) lies approximately along the build direction and the minimum principal stress from the lateral surface measurements (σ_{v2}) lies along the layer direction as investigated before by Liu, et al. [27]. Thus, σ_{h1} , σ_{h2} , σ_{v1} , and σ_{v2} represent the maximum horizontal stress along the scanning direction, minimum horizontal stress along the hatch direction, maximum vertical stress along the build direction, and minimum residual stress along the layer direction “perpendicular to the build direction”, respectively.

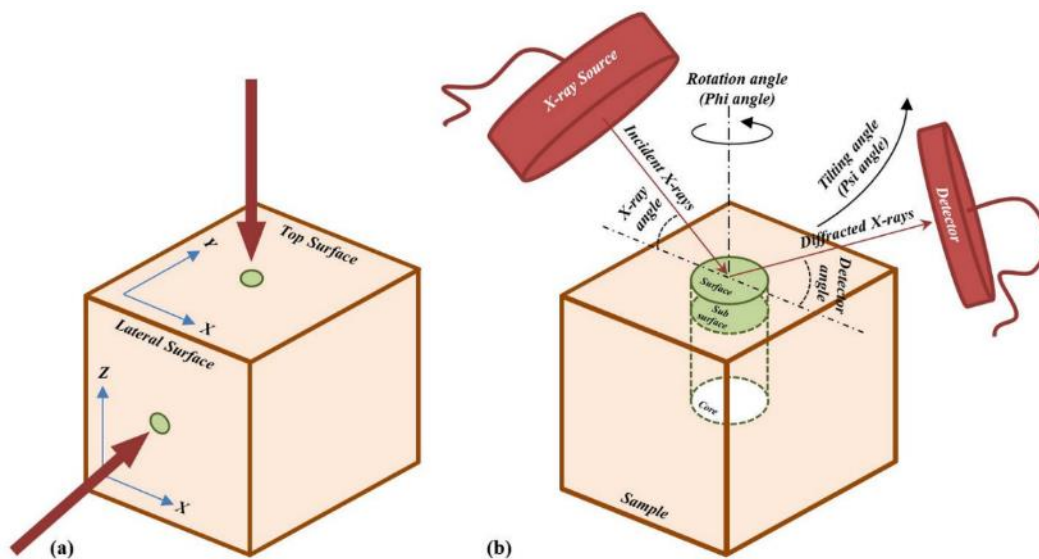


Figure 4.4: Illustration of the (a) measured points along the top and lateral surfaces and (b) relative position between the X-ray source, detector and sample.

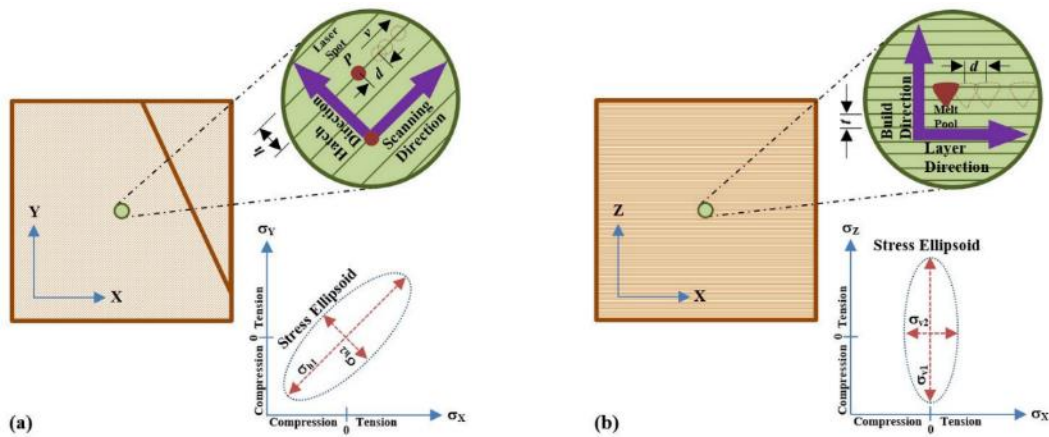


Figure 4.5: Directions of maximum and minimum residual stresses from the (a) top and (b) lateral surfaces measurements.

Table 4.3: Constants used in the determination of residual stresses using the XRD method.

Material	h k l	2θ (degree)	S1	½ S2	Poisson ratio	Young's modulus
Invar 36	3 1 1	111.347°	- 2.057 × 10 ⁻⁶	9.149 × 10 ⁻⁶	0.290	141 GPa
SS 316L	3 1 1	111.245°	- 1.295 × 10 ⁻⁶	6.477 × 10 ⁻⁶	0.250	193 GPa

4.2.5 Macroscopic residual stress measurement

The macroscopic residual stress was estimated via the cantilever method (see Figure 4.3). This method has been reported in the literature for residual stress measurements. Liu, et al. [27] used this method to validate the XRD results of both horizontal and vertical residual stress measurements, while Wang, et al. [36] developed a finite element model to estimate the part deflection after removing the part supports. Zaeh and Branner [37] used SLM process to produce classical cantilever beams for residual stress estimation. The results of the cantilever method agreed with the XRD results as mentioned by Vrancken [38]. After producing 27 cantilevers on the same build plate, the supports were cut from the build plate using wire electrical discharge machining (EDM) and the cantilevers were left attached to the build plate by the middle web. It was assumed that wire EDM minimizes the risk of

introducing additional residual stresses on the samples. After wire EDM, it was observed that the cantilevers manifested convex deflection as shown in Figure 4.3b. This deflection, attributed to the residual stress relief, was measured along the length of each cantilever using a coordinate measuring machine (CMM), with a scale value of 0.1 μm . The measurements were taken along the length of the cantilever every 0.75 mm, resulting in 40 measurement locations along the 50 mm length. Three measurements were taken along the width of the cantilever and averaged to minimize the effect of surface roughness as shown in Figure 4.3a. The measured points were plotted in XY plane in which the maximum deflection, ΔH in (mm), and minimum height, H in (mm) were measured for each cantilever. A finite element (FE) model was developed using ANSYS software to estimate the residual stress that result in this deflection in the cantilever. This estimated stress represents the **macroscopic relieved residual stress**. Table 4.4 lists the material properties used in the FE model, in which Maraging steel (MS1) is used as the build plate material. A static structural modeling approach was used, and the materials were assumed to be isotropic. A steady state adiabatic analysis of the mechanical deflection was considered. The numerical model was validated, and the mesh/grid independence was achieved. Figure 4.6 shows the shape, size and configuration of the mesh convergence. The support was cut from the build plate and the measured deflections were applied in the FE model. The directional and principal residual stress profiles for both Invar 36 and SS 316L were predicted. Figure 4.7 shows an example of stress profiles of a SS 316L cantilever due to a 0.3 mm cantilever deflection. These stress profiles represent the residual stress that caused the deflection in the cantilever after cutting the supports. The numerical model was used to estimate the residual stress that was induced in each cantilever deflection during the SLM process. The simulation results were recorded and compared with the XRD experimental

results. The X-direction stress represents the longitudinal horizontal stress, σ_{rh1} , Y-direction stress represents the lateral horizontal stress, σ_{rh2} , and Z-direction stress represents the vertical stress, σ_{rv} . It was found that the longitudinal horizontal stress (Figure 4.7c) is much higher than the lateral horizontal stress (Figure 4.7d). The XRD microscopic results showed that the residual stress along the scanning direction is much higher than that along the hatch direction, and the values of the XRD results and FE results were comparable. It was also found that the horizontal stresses (Figure 4.7c, d) are higher than the vertical stress (Figure 4.7b), which also match the XRD results along the build direction.

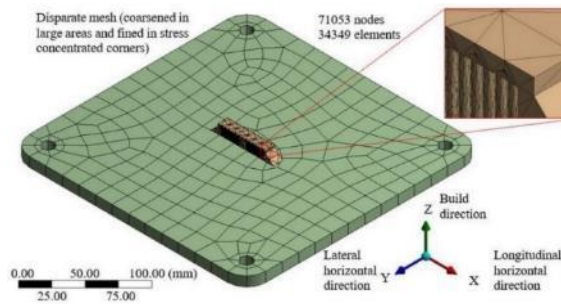


Figure 4.6: Mesh shape, size and configuration of the numerical model in this study.

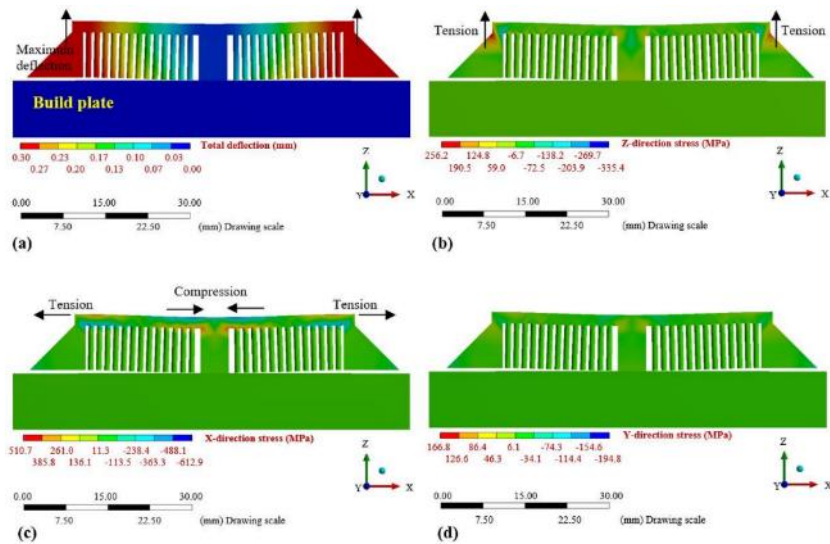


Figure 4.7: Estimation of relieved residual stress via finite element method: (a) cantilever deflection distribution (CMM results), as well as residual stress distribution along (b) Z-direction, (c) X-direction, and (d) Y-direction.

Table 4.4: Materials properties used in the finite element model as provided in the ASTM standards [39-41].

Material	Density	Thermal expansion	Yield strength	Ultimate strength	Poisson ratio	Young's modulus
Invar 36	8.05 g/cm ³	1.3×10 ⁻⁶ °C ⁻¹ at 93 °C	276 MPa	448 MPa	0.290	141 GPa
SS 316L	8.00 g/cm ³	16×10 ⁻⁶ °C ⁻¹ at 100 °C	290 MPa	560 MPa	0.250	193 GPa
MS1	8.00 g/cm ³	10.1×10 ⁻⁶ °C ⁻¹ at 21 °C	758 MPa	1034 MPa	0.300	190 GPa

4.2.6 Fractography analysis

SEM and energy dispersive X-ray spectroscopy (EDX) methods were used to analyze the fractography and material composition of the tensile-test samples. The fractography analysis identified the fracture mechanism during the tensile test; ductile fracture or brittle fracture.

4.3 Results and discussion

4.3.1 Part density

The relative density and the corresponding propagated uncertainty of each cube were calculated using the Archimedes principal “Equation (4.2)”. The relative density and the corresponding measurement uncertainty, error bars, of each sample is plotted against the laser energy density that has been used to produce that sample as shown in Figure 4.8a and b. The graphs indicate a strong relationship between the relative density and laser energy density. The laser energy density is function of laser power, average scanning speed, and hatch spacing which are all considered variable parameters in this study. Two statistical models were developed to study the relationship between the laser process parameters and part density. The first model studies the part density as a function of individual laser parameters, while the second model studied the part density as a function of the laser energy density.

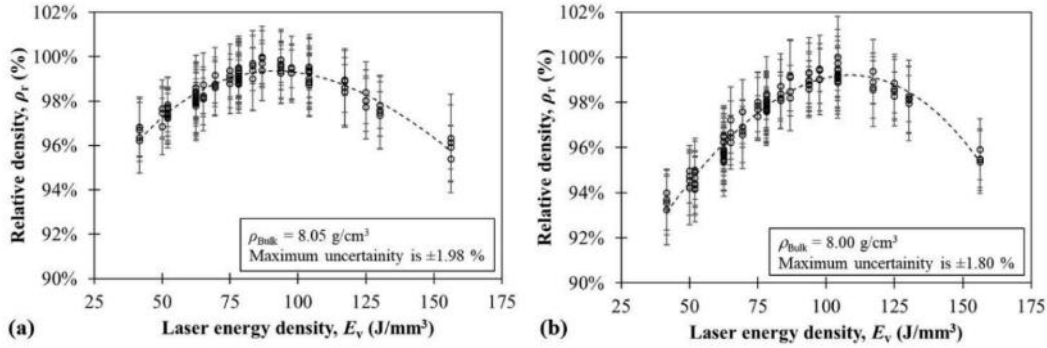


Figure 4.8: Relative density as a function of laser energy density for the production of (a) Invar 36, (b) SS 316L samples by selective laser melting.

4.3.1.1 Part density as a function of the laser process parameters

A regression model that examines the three-way interaction of the independent variables (P , v , h) was developed using Minitab software to study the effect of both individual process parameters and interactions between process parameters on the relative density as described in Equation (4.4).

$$\rho_r = \beta_0 + \beta_1 P + \beta_2 v + \beta_3 h + \beta_{11} P^2 + \beta_{22} v^2 + \beta_{33} h^2 + \beta_{12} Pv + \beta_{13} Ph + \beta_{23} vh + \beta_{123} Pvh + e \quad (4.4)$$

The model included independent variables (P , v , h), quadratic variables (P^2 , v^2 , h^2), two-way interactions ($P \times v$, $P \times h$, $v \times h$), and three-way interaction ($P \times v \times h$). The null hypotheses (H_{01} , H_{02} , H_{03} , and H_{04}) assumed that there is no significant relationship between the response and independent variables, quadratic variables, two-way interactions, and three-way interaction, respectively. The alternative hypothesis (H_a) assumed that there is significant relationship between the response and any of the variables. The null hypotheses were rejected when the confidence level was less than 95% ($p\text{-value} > \alpha$, in which the significant level $\alpha = 0.05$). Hence, the insignificant parameters were removed by a stepwise backward elimination of terms that had confidence level less than 95%. The overall significance of the regression model was tested by F- and t-tests. It can be said that

the regression model is statistically significant when F-value of the accepted terms is greater than a predefined critical value ($F_{\alpha, p-1, n-p-1}$) and t-value of the accepted terms is greater than a predefined critical value ($t_{\alpha/2, n-p-1}$). Table 4.5 shows the regression analysis results for Invar 36 and SS 316L density. Since p-value is less than the specified significance level, F-value is greater than the critical F-statistic, and t-value is greater than the critical t-statistic, then the null hypothesis is rejected, and the model is defined as a statistically significant model. Figure 4.9 shows the influence of laser power, scanning speed, and hatch spacing on the relative density of both Invar 36 and SS 316L. The red areas in the contour plots represent relative densities less than 50% as predicted from the statistical model, but this is not practically applicable except for lattice structures.

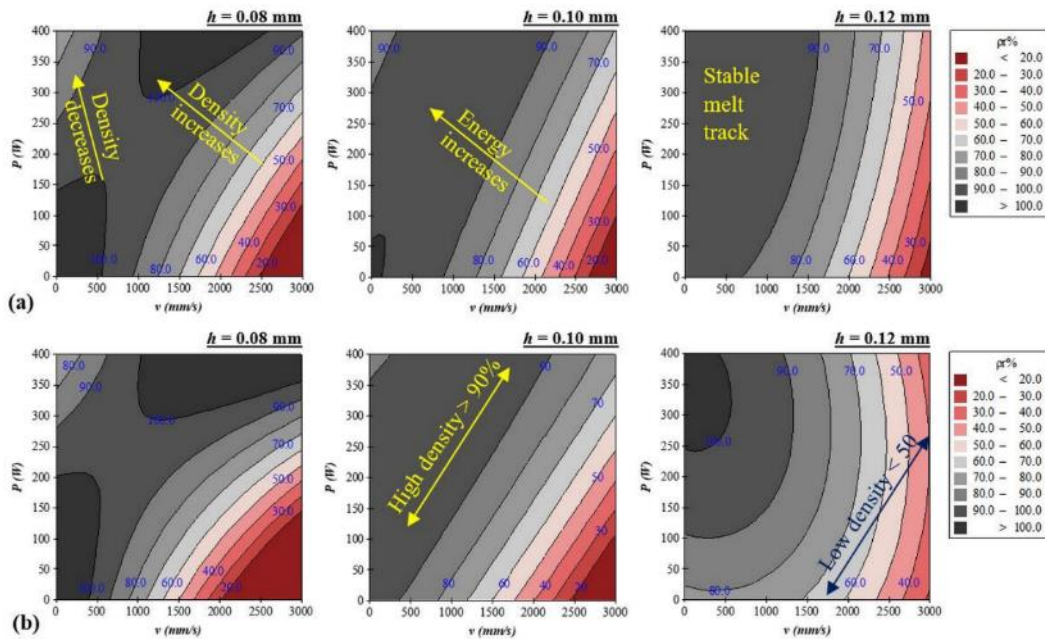


Figure 4.9: Contour plots for the relative density of (a) Invar 36 and (b) SS 316L. The plots show the effect of laser power and scanning speed on the relative density at constant hatch spacings of 0.08, 0.10, and 0.12 mm.

Table 4.5: Regression model for Invar 36 and SS 316L density as a function of individual process parameters.

Source	Degree of freedom	Contribution	Sum of squares	Mean sum of squares	F-value	p-value	t-value	Remarks
Invar 36								
Regression	10	86.02%	89.874	8.9874	59.69	0.000		$\alpha = 0.05$ $F_{0.05, 10, 97} = 1.93$ $t_{0.025, 97} = 1.98$
<i>P</i>	1	1.67%	8.100	8.1001	53.80	0.000	-7.33	
<i>v</i>	1	2.93%	2.813	2.8128	18.68	0.000	-4.32	
<i>h</i>	1	0.99%	2.008	2.0084	13.34	0.000	-3.65	
<i>P</i> ²	1	1.61%	1.679	1.6789	11.15	0.001	-3.34	
<i>v</i> ²	1	3.92%	4.097	4.0975	27.21	0.000	-5.22	
<i>h</i> ²	1	1.70%	1.776	1.7758	11.79	0.001	-3.43	
<i>P</i> × <i>v</i>	1	24.41%	11.631	11.6308	77.25	0.000	8.79	
<i>P</i> × <i>h</i>	1	11.50%	10.698	10.6981	71.05	0.000	8.43	
<i>v</i> × <i>h</i>	1	30.66%	2.837	2.8366	18.84	0.000	4.34	
<i>P</i> × <i>v</i> × <i>h</i>	1	6.62%	6.921	6.9212	45.97	0.000	-6.78	
Error	97	13.98%	14.605	0.1506				
Total	107	100.00%						
SS 316L								
Regression	10	92.52%	295.364	29.5364	119.99	0.000		$\alpha = 0.05$ $F_{0.05, 10, 97} = 1.93$ $t_{0.025, 97} = 1.98$
<i>P</i>	1	14.58%	19.743	19.7430	80.20	0.000	-8.96	
<i>v</i>	1	24.05%	19.311	19.3113	78.45	0.000	-8.86	
<i>h</i>	1	13.83%	14.404	14.4039	58.51	0.000	-7.65	
<i>P</i> ²	1	2.14%	6.830	6.8304	27.75	0.000	-5.27	
<i>v</i> ²	1	0.64%	2.056	2.0564	8.35	0.005	-2.89	
<i>h</i> ²	1	0.55%	1.752	1.7522	7.12	0.009	-2.67	
<i>P</i> × <i>v</i>	1	9.05%	37.134	37.1336	150.85	0.000	12.28	
<i>P</i> × <i>h</i>	1	5.11%	35.969	35.9686	146.12	0.000	12.09	
<i>v</i> × <i>h</i>	1	13.78%	17.291	17.2912	70.24	0.000	8.38	
<i>P</i> × <i>v</i> × <i>h</i>	1	8.79%	28.054	28.0542	113.96	0.000	-10.68	
Error	97	7.48%	23.878	0.2462				
Total	107	100.00%						

As shown in Figure 4.9, increasing the laser power at high scanning speed led to an increase in the part density. This could be attributed to a reduction in the void formation when increasing the laser power at high scanning speed. However, increasing the laser power at low scanning speed led to a decrease in the part density when using small hatch

spacing, which is likely due to the mass loss and compositional changes that happen at very high laser energy (high laser power, low scanning speed, and small hatch spacing). These compositional changes during the SLM of Invar 36 and SS 316L were considered in another work by the authors [42]. The analysis of variance (ANOVA) showed that the part density significantly depends on the interactions between the three process parameters, which are combined in the laser energy density formula.

4.3.1.2 Part density as a function of the laser energy

Another regression model that examines the effect of the independent variable, laser energy density (E_v), was developed to find an empirical equation that could be used to optimize “maximize” the density for both materials. The model included the independent variable (E_v), quadratic variable (E_v^2), and cubic variable (E_v^3) as described in Equation (4.5). The null hypotheses (H_{01} , H_{02} , and H_{03}) assumed that there is no significant relationship between the response and independent variable ($\beta_1 = 0$), quadratic variable ($\beta_{11} = 0$), and cubic variable ($\beta_{111} = 0$), respectively. The alternative hypothesis (H_a) assumed that there is significant relationship between the response and any of the variables (at least one of the $\beta_1, \beta_{11}, \beta_{111} \neq 0$). Table 4.6 shows the regression analysis results for Invar 36 and SS 316L density versus the laser energy density. The insignificant parameters (e.g. E_v^2 in the regression model for SS 316L) were removed by a stepwise backward elimination of terms that had confidence level less than 95%. The null hypothesis is rejected, and the model is defined as statistically significant.

$$\rho_r = \beta_0 + \beta_1 E_v + \beta_{11} E_v^2 + \beta_{111} E_v^3 + e \quad (4.5)$$

Table 4.6: Regression model for Invar 36 and SS 316L density as a function of laser energy density.

Source	Degree of freedom	Contribution	Sum of squares	Mean sum of squares	F-value	p-value	t-value	Remarks
Invar 36								
Regression	3	90.57%	94.6276	31.5425	332.99	0.000		$\alpha = 0.05$ $F_{0.05, 3, 104} = 2.69$ $t_{0.025, 104} = 1.98$
E_v	1	0.26%	9.7785	9.7785	103.23	0.000	10.16	
E_v^2	1	89.38%	4.1629	4.1629	43.95	0.000	-6.63	
E_v^3	1	0.93%	0.9755	0.9755	10.30	0.002	3.21	
Error	104	9.43%	9.8513	0.0947				
Total	107	100.00%						
SS 316L								
Regression	2	95.54%	305.018	152.509	1125.77	0.000		$\alpha = 0.05$ $F_{0.05, 2, 105} = 3.08$ $t_{0.025, 105} = 1.98$
E_v	1	35.26%	276.342	276.342	2039.87	0.000	45.16	
E_v^3	1	60.28%	192.441	192.441	1420.54	0.000	-37.69	
Error	105	4.46%	14.224	0.135				
Total	107	100.00%						

Table 4.7 and Table 4.8 compares the ANOVA results and lists the regression equations from the first and second models for both materials. It was observed that the second model gives lower standard deviation (S), higher coefficient of determination (R^2), and lower predicted residual error sum of squares (PRESS) for both materials. Four samples were manufactured at laser power 250 W, scanning speed 800 mm/s, and hatch spacing 0.10 mm from both materials for validation. Both models were used to predict the relative density of the samples, and the predicted values were compared with the measured densities as listed in Table 4.9. Compared with the measured densities, it was observed that the first model overestimates the relative density and gives a positive error between 0.08% to 0.56%, but the second model underestimates the relative density and gives an error between -0.25% to 0.11%. The first model also leads to a variation in the relative density of the groups that have the same laser energy but different combinations of process parameters, but the second model predicts only one relative density at each laser energy

density. The ANOVA results showed that the second model is better than the first model for both materials, therefore the second model has been selected. It can be summarized that increasing the laser energy density leads to an increase in the part density. This is attributed to the reduction of the void formation when increasing the laser energy, in which the amount of energy will be sufficient for full melting. The void formation at low energy density was studied by Yakout, et al. [42]. At a critical value of the laser energy density (E_C), the part reaches its maximum density as shown in Figure 4.8. Above that limit, the part density decreases due to vaporization and microsegregation of some alloying elements. The critical laser energy density was found to be 86.8 J/mm³ for Invar 36 and 104.2 J/mm³ for SS 316L.

Table 4.7: Comparison between the ANOVA results from the two models for Invar 36 and SS 316L.

	S	R ²	Adjusted R ²	Predicted R ²	PRESS
Invar 36					
1 st model	0.388034	86.02%	84.58%	82.82%	17.9510
2 nd model	0.307773	90.57%	90.30%	89.52%	10.9531
SS 316L					
1 st model	0.496150	92.52%	91.75%	90.59%	30.0442
2 nd model	0.368063	95.54%	95.46%	95.25%	15.1772

Table 4.8: Empirical “regression” equations from the two models for both Invar 36 and SS 316L.

Invar 36	
1 st model	$\rho_r \% = 137.01 - 0.2384 P - 0.04044 v - 296.7 h - 0.000106 P^2 - 0.000010 v^2 - 680 h^2 + 0.000305 P \times v + 2.360 P \times h + 0.3771 v \times h - 0.002325 P \times v \times h$
2 nd model	$\rho_r \% = 87.842 + 0.27800 E_v - 0.001957 E_v^2 + 0.000003 E_v^3$
SS 316L	
1 st model	$\rho_r \% = 181.85 - 0.3721 P - 0.10600 v - 795.0 h - 0.000213 P^2 - 0.000007 v^2 - 676 h^2 + 0.000546 P \times v + 4.328 P \times h + 0.9310 v \times h - 0.004682 P \times v \times h$
2 nd model	$\rho_r \% = 86.206 + 0.17845 E_v - 0.000005 E_v^3$

Table 4.9: Predicted densities compared with measured densities for validation.

Invar 36						SS 316L					
#	Measured density	1 st model		2 nd model		#	Measured density	1 st model		2 nd model	
		density	error	density	error			density	error	density	error
1	99.12%	99.23%	0.11%	99.05%	-0.07%	1	97.99%	98.21%	0.22%	97.76%	-0.23%
2	98.99%	99.23%	0.24%	99.05%	0.06%	2	97.78%	98.21%	0.43%	97.76%	-0.02%
3	99.10%	99.23%	0.13%	99.05%	-0.05%	3	97.65%	98.21%	0.56%	97.76%	0.11%
4	99.15%	99.23%	0.08%	99.05%	-0.10%	4	98.01%	98.21%	0.20%	97.76%	-0.25%

4.3.2 Tensile mechanical properties

Figure 4.10 shows the stress-strain curves for Invar 36 and SS 316L parts manufactured at various laser energy densities. It shows that Invar 36 components exhibited brittle fracture when manufactured at laser energy of 41.7 J/mm³ and ductile fracture when manufactured at 52.1 J/mm³. Parts that were manufactured at 86.8 J/mm³ had lower tensile strength but higher elongation than those were manufactured at 52.1 J/mm³. This is in contrast to parts that were manufactured at 156.3 J/mm³, which had higher tensile strength but lower elongation than those were manufactured at 86.8 J/mm³. SS 316L components showed a similar behavior, albeit at different energy density levels. Figure 4.11 shows the ultimate tensile strength and 0.2% offset yield strength and the corresponding measurement uncertainties for Invar 36 and SS 316L. The uncertainty was defined by the standard deviation of the results from three samples at each set of parameters. The elongation at break, modulus of resilience, and modulus of toughness are shown in Figure 4.12 and Figure 4.13. It was observed that the mechanical properties of the SLM parts strongly depend on the laser energy densities that have been used to produce these parts. It was concluded that:

1. For brittle parts for both materials: the tensile strength, yield strength, elongation, toughness, and resilience increased when increasing the laser energy density until

it reached to the ductile-transition laser energy density (52.1 J/mm^3 for Invar 36 and 62.5 J/mm^3 for SS 316L).

2. For ductile parts for both materials: increasing the laser energy density led to a decrease in the tensile strength, yield strength, and resilience, but an increase in the elongation and toughness until the critical value of laser energy density. Above that critical laser energy density, the tensile strength, yield strength, and resilience started to increase while the elongation and toughness begin to decrease.
3. The mechanical properties of Invar 36 showed very sharp change of slope during the brittle-ductile transition, compared with SS 316L. This sharp change of slope could be attributed to differences in the residual stresses and CTE for both materials. The residual stresses induced in both materials were compared in this study, but the CTE measurements were considered in another study [42].

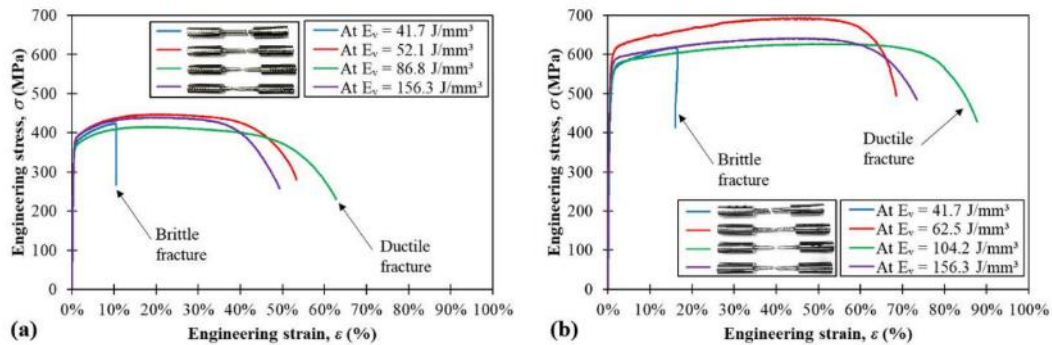


Figure 4.10: Stress-strain curves for (a) Invar 36, (b) SS 316L parts manufactured at various laser energy density levels.

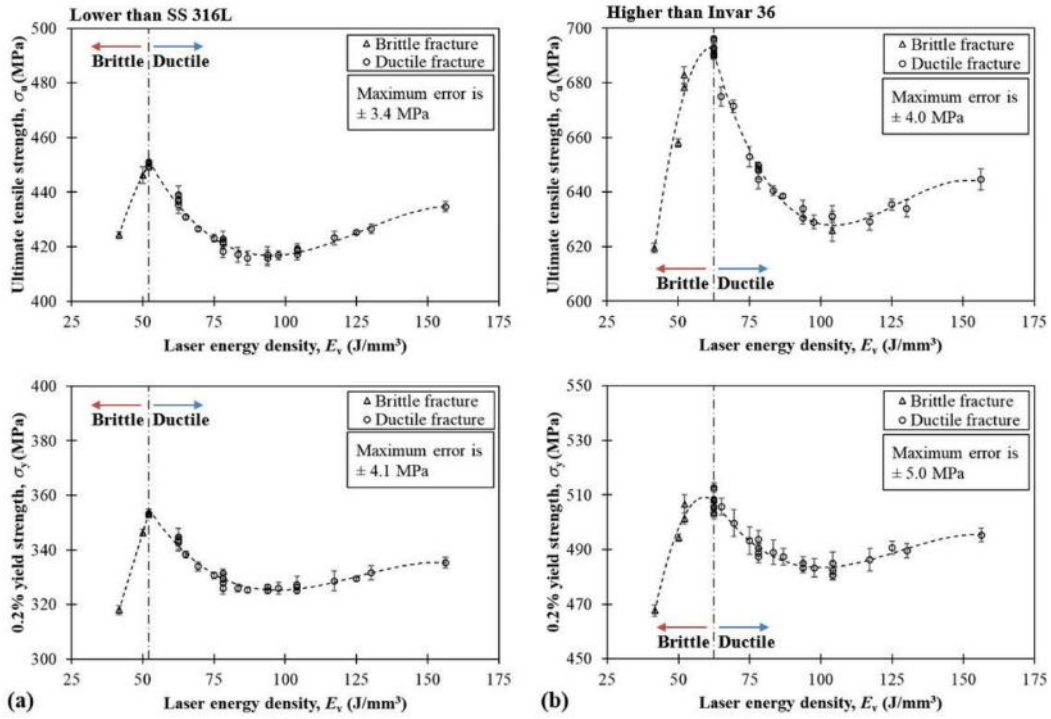


Figure 4.11: Ultimate tensile strength and yield strength of (a) Invar 36, (b) SS 316L parts produced at various laser energy densities.

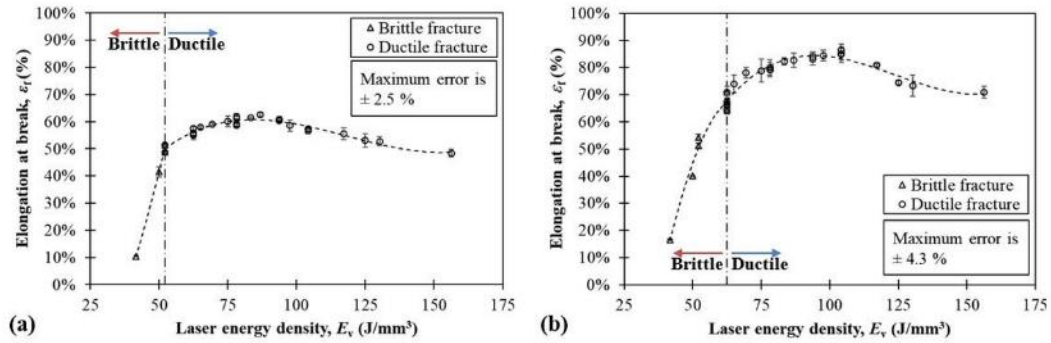


Figure 4.12: Maximum elongation at break of (a) Invar 36, (b) SS 316L parts produced at various laser energy densities.

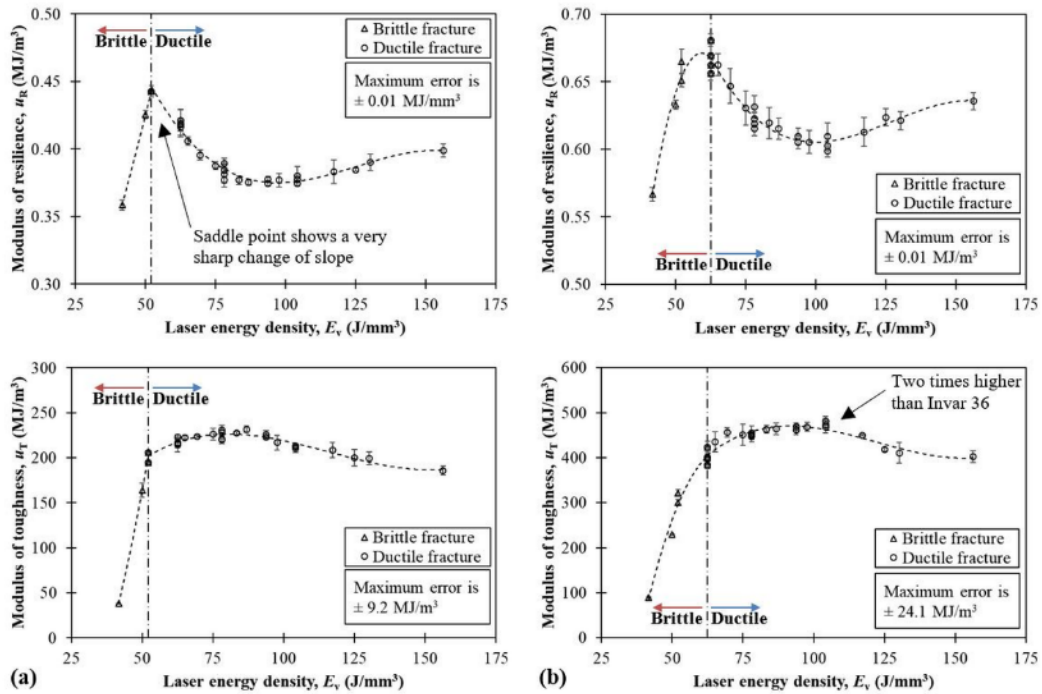


Figure 4.13: Approximate modulus of resilience and modulus of toughness of (a) Invar 36, (b) SS 316L parts produced at various laser energy densities.

From the tensile-test results, two laser energy density were introduced, brittle-ductile transition energy density, E_T , and critical laser energy density, E_C . The transition laser energy density is the laser energy at which the material transforms from brittle to ductile fracture. The critical laser energy density is the laser energy at which the part density and toughness start to decrease. It was found that E_T is 52.1 J/mm³ for Invar 36 and 62.5 J/mm³ for SS 316L, while E_C is 86.8 J/mm³ for Invar 36 and 104.2 J/mm³ for SS 316L. These two laser energy densities are material dependent, and they could be determined by statistically designed experiments. By screening the data, it was noticed that the trend that the mechanical properties took in the brittle fracture mode was different than the trend that they took in the ductile fracture mode. Two data sets were analyzed to examine the effect of the laser energy density on the mechanical properties: the first data set was for samples that were manufactured below E_T and the second data set was developed for samples that

were manufactured above E_T . The same regression model developed for the part density analysis, Eq. (5), was applied on each data set. Two empirical models were examined for each material: the first empirical model explains the mechanical properties changes during the brittle fracture mode and the second empirical model optimizes the mechanical properties during the ductile fracture mode for both materials. The regression analysis results for Invar 36 and SS 316L mechanical properties are shown in the *Appendix*. Table 4.10 shows a summary of the empirical “regression” models describing the mechanical properties for both materials based on laser energy density. For each mechanical property, the developed model (i.e. based on laser energy density) was compared with a model that combine the individual parameters (i.e. laser power, scanning speed, and hatch spacing). An ANOVA was conducted in which the regression models were tested for statistical significance. It was found that the regression model with the best statistical significance (i.e. high R^2 , small S, and small PRESS) was that based on laser energy density. The regression equations that were resulted from ANOVA are listed in Table 4.11. It was observed from the regression analysis that both materials showed similar behaviors during the tensile test. Both Invar 36 and SS 316L components manifested brittle fracture when melted at laser energy density lower than E_T . This was attributed to the formation of internal voids and cracks at laser energy densities below E_T . The parts manifested ductile fracture when melted at laser energy density higher than E_T . The ductile parts showed that increasing the laser energy density caused a reduction in the tensile and yield strength and an increase in the elongation and toughness. This was attributed to internal residual stresses induced in the parts when manufactured at laser energy densities higher than E_T . A tensile residual stress most likely caused a reduction in the ultimate and yield strength. Parts that were produced at E_C exhibited the lowest tensile strength but the highest toughness. Parts

that were produced at laser energy densities higher than E_C showed a reduction in the material toughness. This was attributed to changes in the material composition and unstable keyholes occurred during the melting process when using laser energy densities higher than E_C . These compositional changes are discussed in section 3.3.5.

Table 4.10: Summary of the ANOVA results for the tensile mechanical properties of Invar 36 and SS 316L.

	S	R ²	Adjusted R ²	Predicted R ²	PRESS
Invar 36 <i>$E_v \leq E_T$, where $E_T = 52.1 \text{ J/mm}^3$</i>					
Ultimate tensile strength	2.08309	96.98%	96.68%	96.01%	57.2963
0.2% offset yield strength	1.48357	99.14%	99.06%	98.62%	35.3670
Elongation at break	1.48765	99.31%	99.24%	99.13%	27.9777
Modulus of resilience	3.57795	99.12%	99.03%	98.62%	200.468
Modulus of toughness	6.32522	99.26%	99.18%	99.06%	505.028
Invar 36 <i>$E_v \geq E_T$, where $E_T = 52.1 \text{ J/mm}^3$</i>					
Ultimate tensile strength	2.65504	93.65%	93.38%	93.02%	550.317
0.2% offset yield strength	2.64951	91.51%	91.15%	90.55%	555.132
Elongation at break	1.68894	83.09%	82.37%	80.88%	228.954
Modulus of resilience	6.25093	91.76%	91.41%	90.83%	3089.60
Modulus of toughness	6.51664	74.49%	73.42%	71.14%	3411.47
SS 316L <i>$E_v \leq E_T$, where $E_T = 62.5 \text{ J/mm}^3$</i>					
Ultimate tensile strength	5.30730	95.80%	95.40%	94.65%	753.451
0.2% offset yield strength	4.29652	91.07%	90.22%	88.79%	486.469
Elongation at break	3.35542	96.63%	96.31%	95.85%	291.875
Modulus of resilience	11.2668	90.45%	89.54%	88.07%	3332.19
Modulus of toughness	21.2584	96.50%	96.16%	95.66%	11753.1
SS 316L <i>$E_v \geq E_T$, where $E_T = 62.5 \text{ J/mm}^3$</i>					
Ultimate tensile strength	3.91619	97.25%	97.12%	96.83%	1148.66
0.2% offset yield strength	3.93654	83.84%	83.09%	81.93%	1126.41
Elongation at break	3.04980	80.54%	79.64%	77.92%	685.880
Modulus of resilience	10.0793	83.93%	83.19%	82.02%	7388.62
Modulus of toughness	17.4631	68.04%	66.57%	63.67%	22533.7

Table 4.11: Empirical “regression” equations for the tensile mechanical properties of both Invar 36 and SS 316L.

Invar 36, where $E_T = 52.1 \text{ J/mm}^3$	
$E_v \leq E_T$	$\begin{aligned} \sigma_u &= 319.90 + 2.508 E_v \\ \sigma_y &= 176.64 + 3.3929 E_v \\ \varepsilon_f &= -60.09 + 0.04061 E_v^2 \\ u_R &= 22.4 + 8.067 E_v \\ u_T &= -250.5 + 0.16613 E_v^2 \end{aligned}$
$E_v \geq E_T$	$\begin{aligned} \sigma_u &= 652.5 - 6.206 E_v + 0.05225 E_v^2 - 0.000137 E_v^3 \\ \sigma_y &= 518.3 - 5.031 E_v + 0.04222 E_v^2 - 0.000112 E_v^3 \\ \varepsilon_f &= -40.62 + 2.948 E_v - 0.02715 E_v^2 + 0.000076 E_v^3 \\ u_R &= 840.9 - 12.169 E_v + 0.10240 E_v^2 - 0.000273 E_v^3 \\ u_T &= -45.0 + 8.195 E_v - 0.07796 E_v^2 + 0.000224 E_v^3 \end{aligned}$
SS 316L, where $E_T = 62.5 \text{ J/mm}^3$	
$E_v \leq E_T$	$\begin{aligned} \sigma_u &= -18.7 + 23.11 E_v - 0.1876 E_v^2 \\ \sigma_y &= 27.8 + 16.29 E_v - 0.1378 E_v^2 \\ \varepsilon_f &= -295.8 + 10.83 E_v - 0.0803 E_v^2 \\ u_R &= -533 + 40.68 E_v - 0.3435 E_v^2 \\ u_T &= -1787 + 64.7 E_v - 0.4752 E_v^2 \end{aligned}$
$E_v \geq E_T$	$\begin{aligned} \sigma_u &= 1233.8 - 15.067 E_v + 0.12187 E_v^2 - 0.000318 E_v^3 \\ \sigma_y &= 748.4 - 6.752 E_v + 0.05554 E_v^2 - 0.000145 E_v^3 \\ \varepsilon_f &= -136.7 + 5.901 E_v - 0.05052 E_v^2 + 0.000136 E_v^3 \\ u_R &= 1288.7 - 17.43 E_v + 0.1436 E_v^2 - 0.000376 E_v^3 \\ u_T &= -488 + 26.14 E_v - 0.2280 E_v^2 + 0.000621 E_v^3 \end{aligned}$

4.3.3 Microscopic residual stress via XRD method

Most of the observed stresses in the top and lateral surfaces were tensile in both materials. In Invar 36, the maximum principal stress in the horizontal direction ranged from 48.8 to 328.9 MPa and the minimum principal residual stress ranged from 11.3 to 209.2 MPa. Moreover, the maximum principal stress in the vertical direction ranged from 59.4 to 157.8 MPa and the minimum principal residual stress ranged from -3.9 to 78.8 MPa. In SS 316L, the maximum principal residual stress in the horizontal direction ranged from 73 to 444.7 MPa and the minimum principal stress ranged from -36.3 to 314.1 MPa. Also, the maximum principal residual stress in the vertical direction ranged from 85.6 to 197.4 MPa

and the minimum principal stress ranged from -3 to 90.6 MPa. Figure 4.14 shows the principal stresses on both top and lateral surfaces for both materials. The analysis showed that:

1. SS 316L samples showed higher residual stresses in both directions than Invar 36 samples that were manufactured at the same laser energy. Since all the observed stresses were tensile, they are most likely caused by thermal stresses induced during the melting and/or solidification process. This thermal stress is influenced by modulus of elasticity, CTE, and temperature difference. Thus, the lower the coefficient of thermal expansion the less the residual stress induced. However, CTE might be influenced by the laser energy density, which is considered in another study [42].
2. Both horizontal and vertical stresses increased when the laser energy density increased. This was attributed to the fact that higher energy density could cause higher temperature difference and consequently cause higher thermal stress. The thermal history and temperature difference strongly affect the amount of residual stress induced. The horizontal residual stresses induced in the parts, that were produced at laser energy densities higher than E_C , exceeded the yield strength of both materials (276 MPa for Invar 36 and 290 MPa for SS 316L). These parts showed noticeable plastic deformations during the SLM process as shown in Figure 4.15. Since the thermal stress exceeded the yield strength of the material, it was expected that the material underwent plastic deformations during the process as mentioned by Totten, et al. [43]. It was also observed that the plastic deformation in Invar 36 was lower than that in SS 316L as Invar 36 has lower residual stresses (as shown in Figure 4.14).

3. Maximum horizontal stress was observed along the scanning direction and minimum horizontal stress was observed along the hatch direction. Since the scanning direction changes after each layer due to the (67° degree) rotation of the scans between subsequent layers, the directions of the maximum and minimum horizontal stresses change in each deposited layer. This led to large amount of longitudinal and transverse macroscopic residual stresses in the longitudinal and lateral horizontal directions.

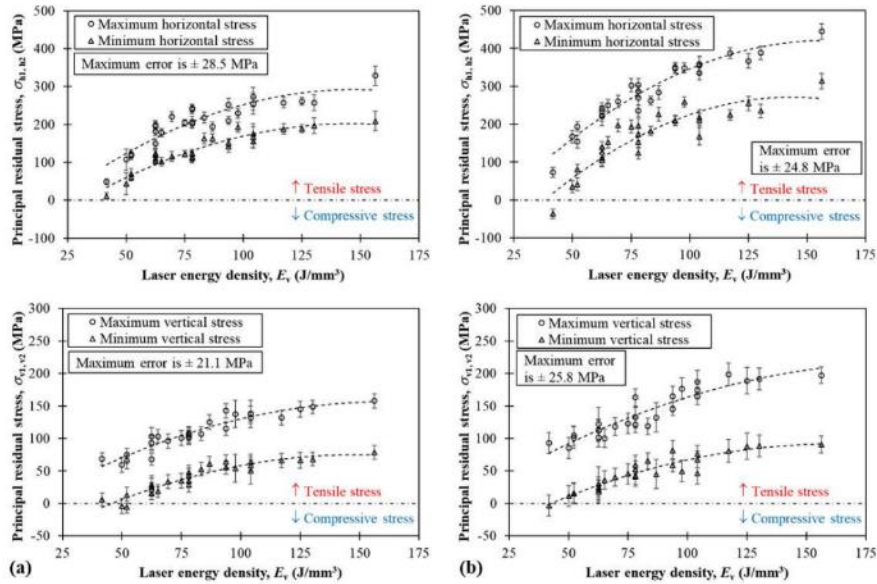


Figure 4.14: Horizontal and vertical principal residual stresses induced in (a) Invar 36 and (b) SS 316L samples produced at various laser energy densities.

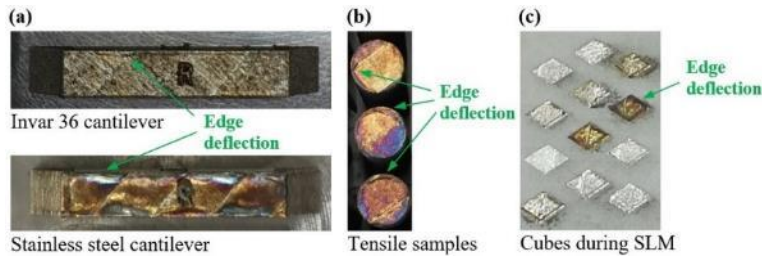


Figure 4.15: Plastic deformation of (a) cantilevers, (b) tensile test samples, and (c) cubes when melted at laser energy densities much higher than the critical laser energy density of each material.

By screening the data, it was found that the relationship between the residual stress and the laser energy density is a second order polynomial relationship. A regression model was developed to study the effect of the laser energy density on the residual stress as described in Eq. (4.6).

$$\sigma_{h1}, \sigma_{h2}, \sigma_{v1}, \sigma_{v2} = \beta_0 + \beta_1 E_v + \beta_{11} E_v^2 + e \quad (4.6)$$

The regression analysis results for the microscopic residual stresses in both Invar 36 and SS 316L parts is shown in the *Appendix*. The models were defined as statistically significant and showed high R^2 , small S, and small PRESS as listed in Table 4.12. The regression equations of microscopic residual stresses are listed Table 4.13. It was also observed that the residual stresses induced in SS 316L samples are approximately twice the residual stresses induced in invar 36 parts because of its highest CTE.

Table 4.12: Summary of the ANOVA results for the residual stress induced in Invar 36 and SS 316L.

	S	R ²	Adjusted R ²	Predicted R ²	PRESS
Invar 36					
Maximum horizontal stress	24.8852	83.91%	82.57%	60.11%	36854.2
Minimum horizontal stress	15.8926	90.17%	89.35%	86.49%	8327.96
Maximum vertical stress	9.11879	90.04%	89.21%	87.71%	2461.14
Minimum vertical stress	7.59393	90.26%	89.45%	85.90%	2003.10
SS 316L					
Maximum horizontal stress	23.3459	92.75%	92.15%	86.66%	24077.0
Minimum horizontal stress	33.0690	82.90%	81.48%	61.42%	59216.9
Maximum vertical stress	13.0254	87.65%	86.62%	80.73%	6352.42
Minimum vertical stress	9.13009	88.74%	87.80%	86.89%	2328.56

Table 4.13: Empirical “regression” equations for the residual stress induced in both Invar 36 and SS 316L.

Invar 36	SS 316L
$\sigma_{h1} = -95.1 + 5.263 E_v - 0.01789 E_v^2$	$\sigma_{h1} = -131.9 + 6.988 E_v - 0.02209 E_v^2$
$\sigma_{h2} = -126.5 + 4.490 E_v - 0.01534 E_v^2$	$\sigma_{h2} = -230.7 + 6.99 E_v - 0.02431 E_v^2$
$\sigma_{v1} = -23.5 + 2.220 E_v - 0.00684 E_v^2$	$\sigma_{v1} = -9.1 + 2.319 E_v - 0.00594 E_v^2$
$\sigma_{v2} = -82.0 + 2.116 E_v - 0.00714 E_v^2$	$\sigma_{v2} = -77.1 + 2.086 E_v - 0.00645 E_v^2$

4.3.4 Macroscopic residual stress via cantilever method

The deformation of each T-shape cantilever was measured using CMM. This deformation was most likely attributed to the relaxation of the residual stresses induced in the parts during the SLM process. Figure 4.16 shows the measured points along the length of the cantilever and the fitted parabolic curves for Invar 36 and SS 316L samples produced at the critical laser energy density. Although the critical laser energy density has the same effect on the part, both materials showed varied deflections due to their different CTE. The minimum height and average deflection of each cantilever were extracted from the parabolic curve. The minimum height was used to characterize the dimensional error in the cantilever and the average deflection was used to characterize the macroscopic residual stress using the FE model discussed in Section 4.2.5. It was observed that the dimensional errors and residual stresses induced in the SS 316L samples were higher than those induced in the Invar 36 samples, which agreed with the XRD microscopic residual stress. Yadroitsava and Yadroitsev [30] developed a similar finite element model to predict the residual stresses induced in titanium samples. Their simulation results agreed with the XRD measurements. They also studied the residual stress induced in SS 316L cubes and titanium samples produced at a laser energy density of 179 J/mm^3 (higher than the maximum laser energy density in this study) via XRD method. They found that the residual stress was between 300-700 MPa along the scanning direction at different locations. In the current study, the maximum observed horizontal residual stress was 444.7 MPa along the scanning direction in samples produced at 156.3 J/mm^3 . Using the developed models for SS 316L in the current study (Table 4.13 and Table 4.15), a laser energy density of 179 J/mm^3 is expected to produce 411 MPa maximum microscopic residual stress and 631 MPa maximum macroscopic residual stress (both values are within the range of their XRD

measurements that were between 300-700 MPa). In their study, they did not measure the macroscopic residual stress in SS 316L, which is the scope of the current paper. Their study also based on a very high energy density and did not cover other influencing factors (i.e. mechanical properties, material composition, etc.). It was observed that the cantilever deflection is influenced by the laser energy density that was used to manufacture the cantilever. Figure 4.17 shows the deflection of cantilevers that were manufactured at different laser energy densities from both materials. The nominal height of the cantilever was 10 mm. The parts that were manufactured at low energy densities showed fewer dimensional errors in the measured height as compared to the nominal height. By increasing the laser energy density, it was found that the height of the cantilever decreased. This was most likely attributed to the bending deflection that the cantilever exhibited at higher energy densities, and this was clearly visible after the wire EDM. The tensile residual stresses induced in both sides of cantilever were relieved after the wire EDM and caused tension in both sides and compression in the cantilever center. It was also observed that the cantilever deflection increased when increasing the laser energy density.

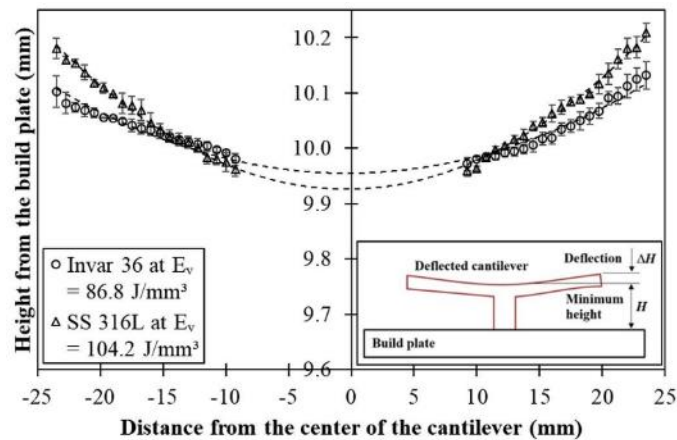


Figure 4.16: Deflections of Invar 36 and SS 316L cantilevers produced at the critical energy density (86.8 J/mm³ for Invar 36 and 104.2 J/mm³ for SS 316L).

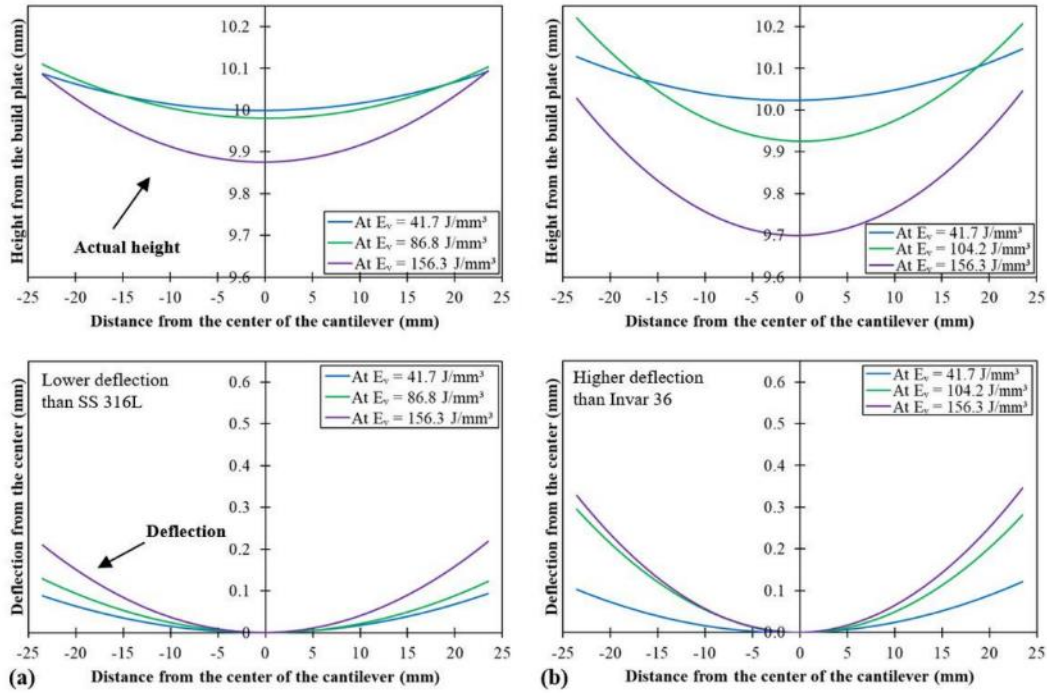


Figure 4.17: The height of the cantilever from the build plate and the cantilever deflection from the center of the cantilever for (a) Invar 36 and (b) SS 316L samples produced at various laser energy densities.

Figure 4.18 and Figure 4.19 show the deflection (ΔH), minimum height (H), and dimensional height error (e_H) for cantilevers manufactured at different laser energy densities from both materials. The uncertainties were calculated from the standard deviation of the three measurements taken at each point across the width of the cantilever.

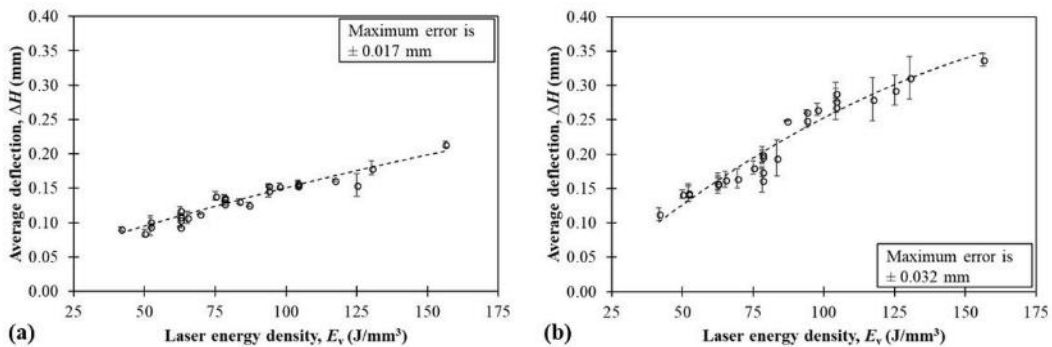


Figure 4.18: Average cantilever deflection for (a) Invar 36 and (b) SS 316L.

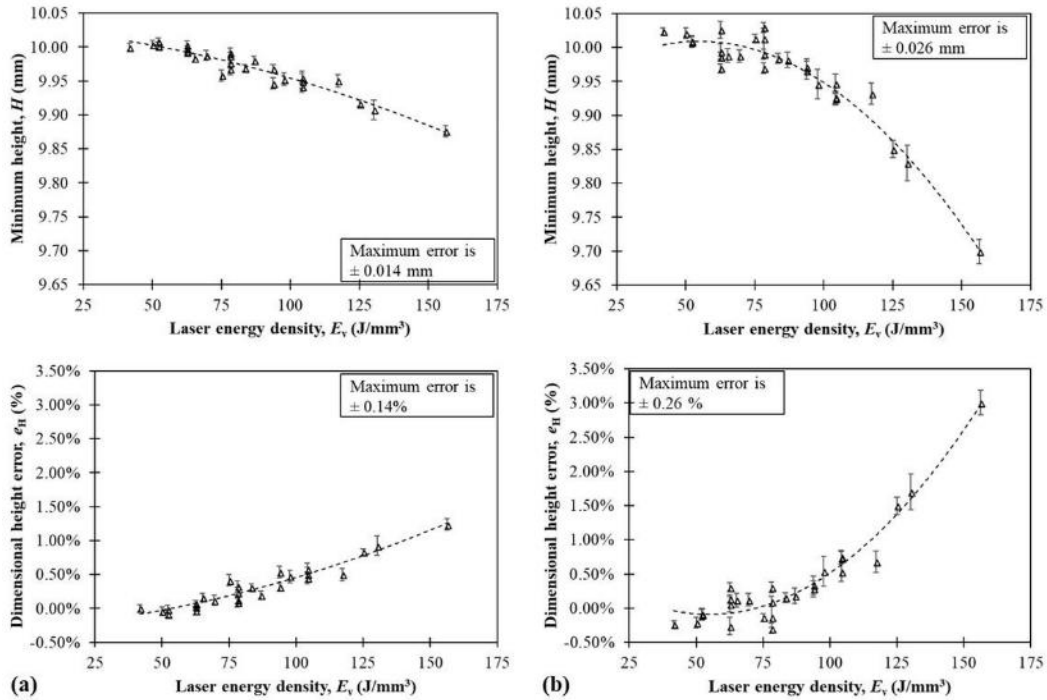


Figure 4.19: Minimum cantilever height and dimensional height error for (a) Invar 36 and (b) SS 316L.

These data measurements were imported into the FE model to predict the resultant stresses. The deformations were imported in the boundary conditions and the resultant stress tensors were determined. These stress tensors represent the residual stresses that were induced in the parts during the SLM process and were relieved after the support removal. The longitudinal horizontal, lateral horizontal, and vertical stresses (σ_{rh1} , σ_{rh2} , and σ_{rv} , respectively) were determined for each sample and plotted against the laser energy density that was used to produce that sample as shown in Figure 4.20. By screening the data, it was observed that the relationship of minimum height, average deflection, and macroscopic residual stress with the laser energy density is a second order polynomial equation. The same model that was developed for the microscopic residual stress data was used. It was found that the minimum height decreases as well as the deflection and residual stresses increase when increasing the laser energy density. The regression analysis results for the

cantilever deflection and the estimated residual stresses are shown in the *Appendix*. Table 4.14 summarizes the S, R², and PRESS values for each model, which all were considered statistically significant. Table 4.15 summarizes the regression equations that could be used to predict the expected deflection and residual stresses at each laser energy density level. The macroscopic residual stresses (Figure 4.20) resulted from the numerical model agreed with the microscopic residual stress (Figure 4.14) resulted from the XRD measurements. Table 4.16 shows a comparison between the XRD residual stresses and FE relieved stresses for both materials. The numerical results showed good agreement with the XRD experimental results, however the numerical model underpredicts the experimental measurements. The variation was most likely attributed to the diffraction errors in the XRD technique and the excessive surface roughness in the parts.

Table 4.14: Summary of the ANOVA results for the cantilever deflection and macroscopic residual stress induced in Invar 36 and SS 316L.

	S	R ²	Adjusted R ²	Predicted R ²	PRESS
Invar 36					
Maximum height	0.0093178	92.01%	91.69%	90.77%	0.0025077
Average deflection	0.0087387	91.86%	91.54%	90.42%	0.0022483
Longitudinal horizontal stress	11.2999	91.86%	91.54%	90.42%	3759.31
Lateral horizontal stress	4.38856	91.86%	91.54%	90.42%	567.028
Vertical stress	5.91128	91.86%	91.54%	90.42%	1028.78
SS 316L					
Maximum height	0.0186470	93.75%	93.23%	92.43%	0.0101001
Average deflection	0.0169626	93.40%	92.85%	91.09%	0.0093232
Longitudinal horizontal stress	28.8752	93.40%	92.85%	91.09%	27016.4
Lateral horizontal stress	9.43106	93.40%	92.85%	91.09%	2882.03
Vertical stress	14.4868	93.40%	92.85%	91.09%	6800.21

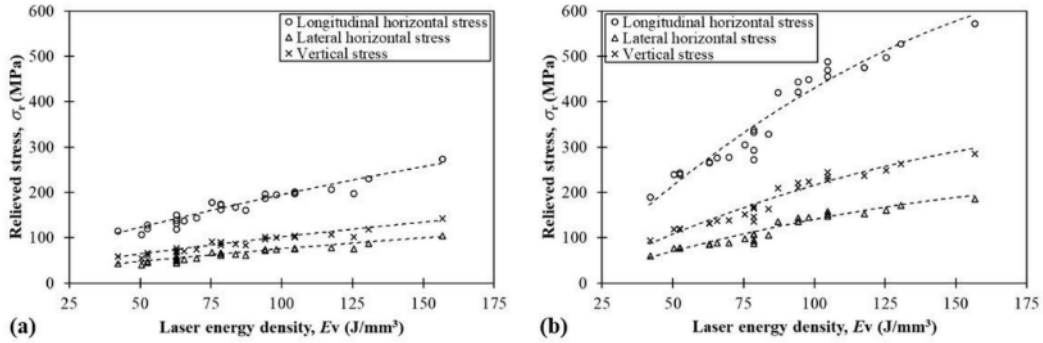


Figure 4.20: Simulation results for the relieved residual stress via cantilever deflection for (a) Invar 36 and (b) SS 316L.

Table 4.15: Empirical “regression” equations for the macroscopic residual stress induced in both Invar 36 and SS 316L.

Invar 36	SS 316L
$H = 10.0153 - 0.000006 E_v^2$ $\Delta H = 0.04400 + 0.001055 E_v$ $\sigma_{rh1} = 56.92 + 1.3641 E_v$ $\sigma_{rh2} = 22.10 + 0.5298 E_v$ $\sigma_{rv} = 29.77 + 0.7136 E_v$	$H = 9.9192 + 0.003277 E_v - 0.000030 E_v^2$ $\Delta H = -0.0400 + 0.003726 E_v - 0.000008 E_v^2$ $\sigma_{rh1} = -68.2 + 6.34 E_v - 0.01357 E_v^2$ $\sigma_{rh2} = -22.3 + 2.071 E_v - 0.00443 E_v^2$ $\sigma_{rv} = -34.2 + 3.182 E_v - 0.00681 E_v^2$

Table 4.16: Comparison between the experimental and numerical residual stress results.

	Invar 36		SS 316L	
	XRD residual stress	FE relieved stress	XRD residual stress	FE relieved stress
Longitudinal horizontal stress	48.8 to 328.9 MPa	117.5 to 276.4 MPa	73 to 444.7 MPa	192.1 to 574.3 MPa
Lateral horizontal stress	11.3 to 209.2 MPa	61.4 to 144.6 MPa	-36.3 to 314.1 MPa	96.4 to 288.1 MPa
Vertical stress	59.4 to 157.8 MPa	45.6 to 107.3 MPa	85.6 to 197.4 MPa	62.7 to 187.6 MPa

4.3.5 Fractography and material composition analyses

The fractography analysis of the tensile-test samples revealed that the parts produced at a laser energy density less than E_T (52.1 J/mm³ for invar 36, and 62.5 J/mm³ for SS 316L)

undergo brittle fracture (see Figure 4.21a) likely due to the formation of voids and internal cracks. Parts that were produced at E_T and above undergo ductile fracture as shown in Figure 4.21. Table 4.17 lists the material compositions of Invar 36 and SS 316L tensile-test samples produced at various laser energy densities, compared with the typical chemical composition of the wrought material. At laser energy densities higher than E_C (86.8 J/mm^3 for Invar 36 and 104.2 J/mm^3 for SS 316L), the EDX analysis showed vaporization and microsegregation of some alloying elements. The scale value of the EDX measurements was $\pm 0.01 \text{ wt.}\%$. The scanning rate was adjusted very low and many frames were collected (2000 frames were taken) to allow accurate measurements. The vaporization phenomenon was explained elsewhere in the work done by He, et al. [44], who studied the effect of the laser welding on the material composition. Yakout, et al. [2] also explained the soot formation that happens during the laser melting of nickel-based alloys. It was observed that using laser energy densities higher than E_C caused a reduction in the nickel, manganese, and chromium concentrations, and accordingly caused an increase in the silicon, iron, and molybdenum concentrations. This was attributed to the vaporization of nickel, manganese, and chromium during the melting process, as they have low boiling temperatures compared with other elements ($2913 \text{ }^\circ\text{C}$ for nickel, $2061 \text{ }^\circ\text{C}$ for manganese, and $2671 \text{ }^\circ\text{C}$ for chromium). The concentrations of the elements that have higher boiling temperatures were increased (e.g. molybdenum's boiling temperature is $4639 \text{ }^\circ\text{C}$). The increase in the ultimate tensile strength and the reduction in the elongation that were noticed above E_C were most likely attributed to the changes occurred in the material composition.

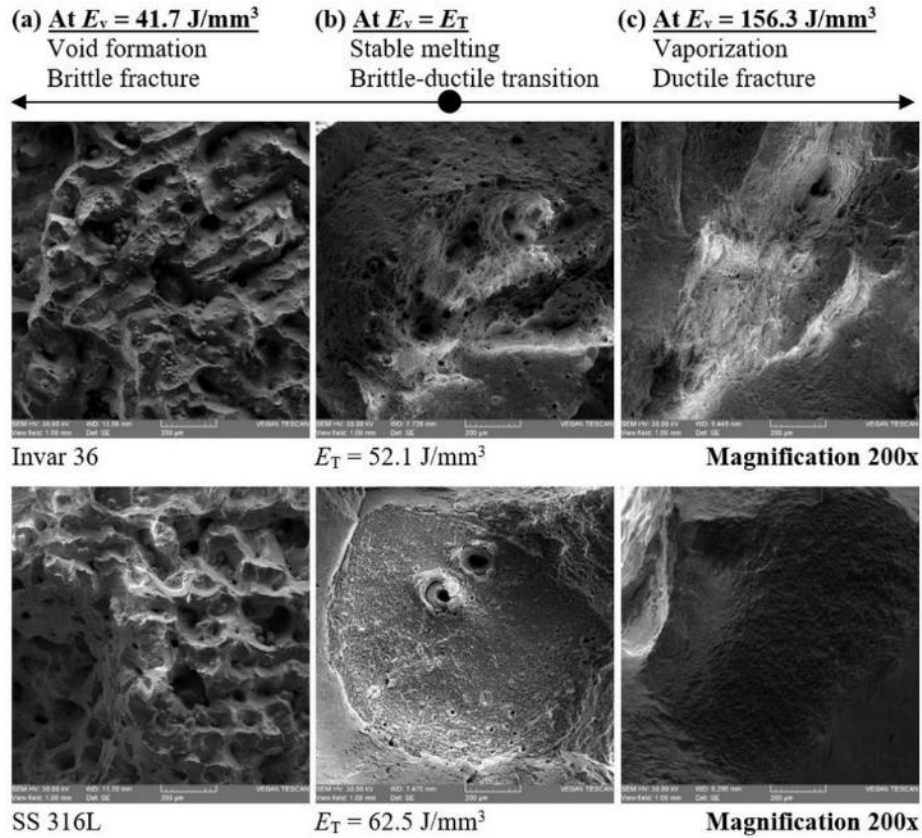


Figure 4.21: Fractography of Invar 36 and stainless steel 316L samples produced at laser energy density of (a) 41.7 J/mm^3 with more voids present “brittle fracture”, (b) 62.5 J/mm^3 with less voids present “the beginning of ductile fracture”, and (c) 156.3 J/mm^3 with over melting and mass loss.

Table 4.17: Material composition of Invar 36 and SS 316L tensile-test samples compared with the wrought material (wt.%) and powder composition.

Element	Fe		Ni		Mn	Si	Total
Wrought Invar 36	Bal.		35.5-36.5		<0.5	<0.25	
Virgin powder	63.97		35.62		0.23	0.18	100.00
Recycled powder	63.55		36.05		0.21	0.19	100.00
At 41.7 J/mm^3	63.35		36.20		0.24	0.21	100.00
At 86.8 J/mm^3	63.95		35.29		0.19	0.57	100.00
At 156.3 J/mm^3	66.33		32.41		0.15	1.11	100.00
Element	Fe	Cr	Ni	Mo	Mn	Si	Total
Wrought SS 316L	Bal.	16-18	10-14	2-3	<2	<1	
Virgin powder	67.59	17.13	10.69	1.62	1.84	1.13	100.00
Recycled powder	67.54	17.12	10.52	1.79	1.81	1.22	100.00
At 41.7 J/mm^3	66.87	17.66	10.23	2.24	1.61	1.39	100.00
At 104.2 J/mm^3	66.81	17.53	10.08	2.43	1.60	1.55	100.00
At 156.3 J/mm^3	68.22	17.07	8.62	2.64	1.49	1.96	100.00

4.3.6 Optimum SLM process parameters for Invar 36 and SS 316L

The density measurements, tensile-test results, residual stress measurements, and microstructure analysis were used to find the optimum SLM process parameters. In this study, two laser energy densities were introduced: E_T and E_C . Below E_T , the fractography analysis showed footprints of internal voids (Figure 4.21a) and the tensile test showed brittle fracture. The parts that were manufactured below E_T showed low toughness, low density, and low residual stresses. Parts that were produced between E_T and E_C showed stable melting, high density, high toughness, but moderate residual stress. The tensile-test results of these parts showed ductile fracture regime. Above E_C , alloying elements that have lower boiling temperatures were vaporized, ejected from the melt pool, and converted into soot. This vaporization phenomenon affected the material composition (see Table 4.17) and consequently the mechanical properties of the parts produced. These parts showed lower densities, lower toughness, and extensive residual stresses. Some parts showed plastic deformation as the internal residual stresses were higher than the yield strength of the material. Therefore, it can be summarized that the melting process is discontinuous below E_T , continuous between E_T and E_C , and unstable above E_C as shown in Figure 4.22. The low and high boundaries of laser energy density were determined from preliminary experiments by the authors. The recoater arm started to bump over the edge of an improperly melted layer and caused vibration when using laser energy densities higher than 156.3 J/mm^3 for both materials. It was also observed that powder particles do not bond properly when using laser energy densities lower than 41.7 J/mm^3 . Therefore, the melting process is considered unstable above the high boundary and insufficient below the low boundary of laser energy density. It was found that the SLM process shows stable melting when using any combinations of process parameters that could give an energy density

between 52.1 J/mm^3 and 86.8 J/mm^3 for Invar 36 and between 62.5 J/mm^3 and 104.2 J/mm^3 for SS 316L. Figure 4.22 shows the process map of laser power and scanning speed for both materials at hatch spacings of 0.08 mm, 0.10 mm, and 0.12 mm. Using any laser energy within the above-mentioned range would provide stable melting process as well as continuous beads and melting tracks. This, consequently, would provide high dense parts with high toughness and less residual stresses. Using energy densities above E_C would cause changes in the material composition, and it is expected that these parts will have CTE different than that of the wrought material, particularly for Invar. The CTE and magnetic properties of the two materials are described in another publication by the authors [42].

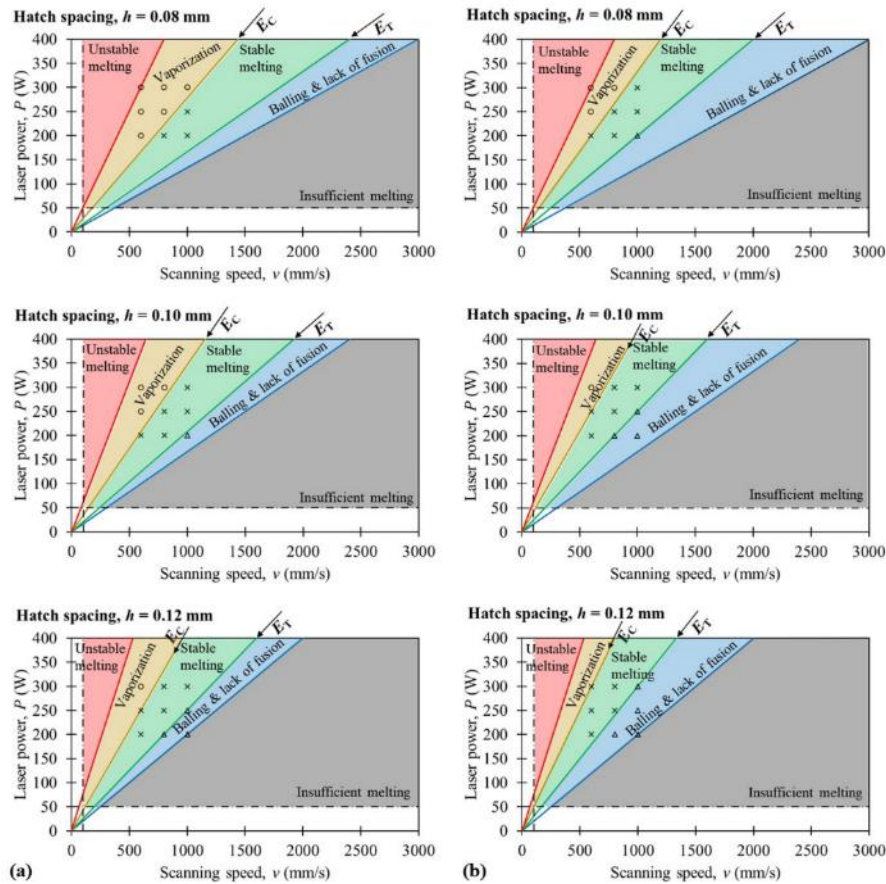


Figure 4.22: SLM process map for (a) Invar 36 and (b) SS 316L, showing the process parameters that could provide stable melting.

4.4 Conclusions

The current study deals with selective laser melting of Invar 36 and stainless steel 316L. Both materials are good candidates for welding and melting processes. Density measurements, tensile testing, internal microstructures, material compositions, and induced residual stresses were studied. The results showed that:

1. Using energy densities below the brittle-ductile transition energy density, E_T , caused brittle fracture in the parts produced due to void formation. The fractography of these parts showed voids footprints. The brittle-ductile transition energy density is 52.1 J/mm^3 for Invar 36 and 62.5 J/mm^3 for stainless steel 316L.
2. Between E_T and the critical energy density, E_C , the parts showed stable melting, continuous beads, and homogeneous melt tracks. These parts had the highest density and toughness, but medium residual stresses due to thermal history. The critical energy density is 86.8 J/mm^3 for Invar 36 and 104.2 J/mm^3 for stainless steel 316L.
3. Above E_C , the chemical compositions of the parts produced showed less concentration for some of the alloying elements that have low boiling temperatures. These alloying elements were vaporized during the melting process. Therefore, the mechanical properties of these parts were altered due to changes in the chemical composition. These parts showed less toughness, density, and very high internal residual stresses.

It was concluded that the process parameters of selective laser melting should be optimized for various alloys and careful considerations should be taken during the design stage. The paper explained the physics of void formation and vaporization phenomena as well as their relationship with the process parameters and their influence on the part characteristics and quality. The effect of the laser process parameters on other influencing factors is considered for future work.

4.5 References

- [1] DebRoy, T. *et al.*, "Additive manufacturing of metallic components – Process, structure and properties," *Progress in Materials Science*, vol. 92, pp. 112-224, 2018.
- [2] Yakout, M., Cadamuro, A., Elbestawi, M. A., and Veldhuis, S. C., "The selection of process parameters in additive manufacturing for aerospace alloys," *The International Journal of Advanced Manufacturing Technology*, vol. 92, no. 5-8, pp. 2081-2098, 2017.
- [3] Yakout, M., Elbestawi, M. A., and Veldhuis, S. C., "On the characterization of stainless steel 316L parts produced by selective laser melting," *The International Journal of Advanced Manufacturing Technology*, vol. 95, no. 5-8, pp. 1953-1974, 2018.
- [4] Qiu, C., Adkins, N. J. E., and Attallah, M. M., "Selective laser melting of Invar 36: Microstructure and properties," *Acta Materialia*, vol. 103, pp. 382-395, 2016.
- [5] Harrison, N. J., Todd, I., and Mumtaz, K., "Thermal expansion coefficients in Invar processed by selective laser melting," *Journal of Materials Science*, journal article vol. 52, no. 17, pp. 10517-10525, 2017.
- [6] Spierings, A. B. and Levy, G., "Comparison of density of stainless steel 316L parts produced with selective laser melting using different powder grades," in *The 20th Annual International Solid Freeform Fabrication Symposium*, Austin, Texas, USA, 2009, pp. 342-353: University of Texas in Austin.
- [7] Kamath, C., El-dasher, B., Gallegos, G. F., King, W. E., and Sisto, A., "Density of additively-manufactured, 316L SS parts using laser powder-bed fusion at powers up to 400 W," *The International Journal of Advanced Manufacturing Technology*, vol. 74, pp. 65-78, 2014.
- [8] Strauss, J. T. and Stucky, M. J., "Laser additive manufacturing processing of a mixture of iron and nickel powders," in *The 27th Annual International Solid Freeform Fabrication Symposium*, 2016.
- [9] Li, R., Liu, J., Shi, Y., Wang, L., and Jiang, W., "Balling behavior of stainless steel and nickel powder during selective laser melting process," *The International Journal of Advanced Manufacturing Technology*, vol. 59, pp. 1025-1035, 2012.
- [10] Miranda, G. *et al.*, "Predictive models for physical and mechanical properties of 316L stainless steel produced by selective laser melting," *Materials Science and Engineering A*, vol. 657, pp. 43-56, 2016.
- [11] Spierings, A. B., Herres, N., and Levy, G., "Influence of the particle size distribution on surface quality and mechanical properties in additive manufactured stainless steel parts," in *The 21st Annual International Solid Freeform Fabrication Symposium*, Austin, Texas, USA, 2010, pp. 397-406: University of Texas in Austin.

- [12] Kruth, J. P., Deckers, J., Yasa, E., and Wauthle, R., "Assessing influencing factors of residual stresses in selective laser melting using a novel analysis method," in *The 16th International Symposium on Electromachining (ISEM XVI)*, Shanghai, China, 2010.
- [13] Yasa, E., Craeghs, T., Badrossamay, M., and Kruth, J.-P., "Rapid manufacturing research at the catholic university of leuven," presented at the US Turkey Workshop on Rapid Technologies, Istanbul, Turkey, 2009.
- [14] Yusuf, S. M., Chen, Y., Boardman, R., Yang, S., and Gao, N., "Investigation on porosity and microhardness of 316L stainless steel fabricated by selective laser melting," *Metals*, vol. 7, pp. 64 (1-12), 2017.
- [15] Liu, B., Wildman, R., Tuck, C., Ashcroft, I., and Hague, R., "Investigation the effect of particle size distribution on processing parameters optimisation in selective laser melting process," in *The 22nd Annual International Solid Freeform Fabrication Symposium*, Texas, USA, 2011.
- [16] Casati, R., Lemke, J., and Vedani, M., "Microstructure and fracture behavior of 316L austenitic stainless steel produced by selective laser melting," *Journal of Materials Science and Technology*, vol. 32, pp. 738-744, 2016.
- [17] Kruth, J., Badrossamay, M., Yasa, E., Deckers, J., Thijs, L., and Humbeeck, J. V., "Part and material properties in selective laser melting of metals," in *The 16th International Symposium on Electromachining (ISEM XVI)*, Shanghai, China, 2010.
- [18] Dadbakhsh, S., Hao, L., and Sewell, N., "Effect of selective laser melting layout on the quality of stainless steel parts," *Rapid Prototyping Journal*, vol. 18, pp. 241-249, 2012.
- [19] Kurzynowski, T., Gruber, K., Stopyra, W., Kuźnicka, B., and Chlebus, E., "Correlation between process parameters, microstructure and properties of 316 L stainless steel processed by selective laser melting," *Materials Science and Engineering: A*, vol. 718, pp. 64-73, 2018.
- [20] Yadroitsev, I. and Smurov, I., "Selective laser melting technology: from the single laser melted track stability to 3d parts of complex shape," *Physics Procedia*, vol. 5, pp. 551-560, 2010.
- [21] Yasa, E., Deckers, J., Kruth, J.-P., Rombouts, M., and Luyten, J., "Investigation of sectoral scanning in selective laser melting " in *ASME 2010 10th Biennial Conference on Engineering Systems Design and Analysis*, Istanbul, Turkey, 2010, vol. 4, pp. 695-703.
- [22] Yasa, E., "Manufacturing by combining selective laser melting and selective laser erosion/laser re-melting," PhD Department of Mechanical Engineering, Katholieke Universiteit Leuven, Leuven, 2011.

- [23] Sun, Z., Tan, X., Tor, S. B., and Yeong, W. Y., "Selective laser melting of stainless steel 316L with low porosity and high build rates," *Materials and Design*, vol. 104, pp. 197-204, 2016.
- [24] Liverani, E., Toschi, S., Ceschini, L., and Fortunato, A., "Effect of selective laser melting (SLM) process parameters on microstructure and mechanical properties of 316L austenitic stainless steel," *Journal of Materials Processing Technology*, vol. 249, pp. 255-263, 2017.
- [25] Saeidi, K., "Stainless steels fabricated by laser melting, Scaled-down structural hierarchies and microstructural heterogeneities," PhD Department of Materials and Environmental Chemistry, Stockholm University, Stockholm, Sweden, 2016.
- [26] Yadroitsev, I. and Yadroitsava, I., "Evaluation of residual stress in stainless steel 316L and Ti6Al4V samples produced by selective laser melting," *Virtual and Physical Prototyping*, vol. 10, no. 2, pp. 67-76, 2015.
- [27] Liu, Y., Yang, Y., and Wang, D., "A study on the residual stress during selective laser melting (SLM) of metallic powder," *The International Journal of Advanced Manufacturing Technology*, vol. 87, pp. 647-656, 2016.
- [28] Yadroitsava, I. and Yadroitsev, I., "Evaluation of residual stress in selective laser melting of 316L steel," in *The 1st International Conference on Progress in Additive Manufacturing*, Singapore, 2014.
- [29] Shifeng, W., Shuai, L., Qingsong, W., Yan, C., Sheng, Z., and Yusheng, S., "Effect of molten pool boundaries on the mechanical properties of selective laser melting parts," *Journal of Materials Processing Technology*, vol. 214, pp. 2660-2667, 2014.
- [30] Yadroitsava, I. and Yadroitsev, I., "Residual stress in metal specimens produced by direct metal laser sintering," in *The 26th Annual International Solid Freeform Fabrication Symposium*, Texas, USA, 2015.
- [31] *Standard test methods for tension testing of metallic materials*, 2016.
- [32] *Standard guide for evaluating mechanical properties of metal materials made via additive manufacturing processes*, 2014.
- [33] Budynas, R. G., Nisbett, J. K., and Shigley, J. E., *Shigley's mechanical engineering design*. New York: McGraw-Hill, 2011.
- [34] Gusarov, A. V., Pavlov, M., and Smurov, I., "Residual Stresses at Laser Surface Remelting and Additive Manufacturing," *Physics Procedia*, vol. 12, pp. 248-254, 2011/01/01/ 2011.
- [35] Cheng, B., Shrestha, S., and Chou, K., "Stress and deformation evaluations of scanning strategy effect in selective laser melting," *Additive Manufacturing*, vol. 12, pp. 240-251, 2016.

- [36] Wang, L. *et al.*, "Graphene-copper composite with micro-layered grains and ultrahigh strength," *Scientific Reports*, Article vol. 7, p. 41896, 02/07/online 2017.
- [37] Zaeh, M. F. and Branner, G., "Investigations on residual stresses and deformations in selective laser melting," *Production Engineering*, journal article vol. 4, no. 1, pp. 35-45, 2010.
- [38] Vrancken, B., "Study of residual stresses in selective laser melting," PhD Degree, Faculty of Engineering Science, KU Leuven, Belgium, 2016.
- [39] *Standard specification for thermostat component alloys*, 2013.
- [40] *Standard specification for superstrength alloy steel forgings*, 2017.
- [41] *Standard specification for annealed or cold-worked austenitic stainless steel sheet, strip, plate, and flat bar*, 2015.
- [42] Yakout, M., Elbestawi, M. A., and Veldhuis, S. C., "A study of thermal expansion coefficients and microstructure during selective laser melting of Invar 36 and stainless steel 316L," *Additive Manufacturing*, 2018/10/13/ 2018.
- [43] Totten, G. E., Howes, M. A. H., and Inoue, T. (2002). *Handbook of residual stress and deformation of steel*. Available: <http://www.books24x7.com/marc.asp?bookid=42650>
- [44] He, X., DebRoy, T., and Fuerschbach, P. W., "Alloying element vaporization during laser spot welding of stainless steel," *Journal of Physics D: Applied Physics*, vol. 36, pp. 3079-3088, 2003.

Chapter 5

Thermal Expansion and Metallurgical Changes Associated with Selective Laser Melting of Invar 36 and Stainless Steel 316L

Complete Citation:

Yakout, M., Elbestawi, M.A., Veldhuis, S.C. (2018). A study of thermal expansion coefficients and microstructure during selective laser melting of Invar 36 and stainless steel 316L. *Additive Manufacturing*, Volume 24, pp 405-418. DOI: 10.1016/j.addma.2018.09.035

Copyright:

© 2018 The Authors Under CC BY-NC-ND 4.0 License. Published by Elsevier.

Relative Contributions:

- M. Yakout: Performed experiments, analysis, and data interpretation. Wrote the first draft of the manuscript. Helped with submitting the final manuscript to the journal (corresponding author).
- M. A. Elbestawi: Co-supervisor of M. Yakout. Revised the manuscript. Was responsible of submitting the final manuscript to the journal (corresponding author).
- S. C. Veldhuis: Co-supervisor of M. Yakout. Revised the manuscript.

Abstract:

This paper presents an experimental study on the metallurgical issues associated with selective laser melting of Invar 36 and stainless steel 316L and the resulting coefficient of thermal expansion. Invar 36 has been used in aircraft control systems, electronic devices, optical instruments, and medical instruments that are exposed to significant temperature changes. Stainless steel 316L is commonly used for applications that require high corrosion resistance in the aerospace, medical, and nuclear industries. Both Invar 36 and stainless steel 316L are weldable austenitic face-centered cubic crystal structures, but stainless steel 316L may experience chromium evaporation and Invar 36 may experience weld cracking during the welding process. Various laser process parameters were tested based on a full factorial design of experiments. The microstructure, material composition, coefficient of thermal expansion, and magnetic dipole moment were measured for both materials. It was found that there exists a critical laser energy density for each material, E_C , for which selective laser melting process is optimal for material properties. The critical laser energy density provides enough energy to induce stable melting, homogeneous microstructure and chemical composition, resulting in thermal expansion and magnetic properties in line with that expected for the wrought material. Below the critical energy, a lack of fusion due to insufficient melt tracks and discontinuous beads was observed. The melt track was also unstable above the critical energy due to vaporization and microsegregation of alloying elements. Both cases can generate stress risers and part flaws during manufacturing. These flaws could be avoided by finding the critical laser energy needed for each material. The critical laser energy density was determined to be 86.8 J/mm^3 for Invar 36 and 104.2 J/mm^3 for stainless steel 316L.

5.1 Introduction

Due to their unique properties, Invar 36 (*UNS K93600*) [1] and stainless steel 316L (*UNS S31603*) [2] have gained notable popularity in the aerospace industry. Invar 36 offers very low coefficient of **thermal expansion** (CTE) and **ferromagnetic properties** for applications up to its **Curie temperature** (279 °C) due to its 36% nickel content. Therefore, it has been used in applications that require high dimensional stability (e.g. precision measuring instruments, aerospace control devices, waveguide tubes, telescopes, ring laser gyroscopes, etc.) [1, 3-6]. Stainless steel 316L offers good **corrosion resistance** because of its chromium, nickel and molybdenum contents. Thus it has been used in applications that might be exposed to high corrosion rates (e.g. exhaust components, aircraft structures, helicopter blades, sandwich structures, etc.) [2, 7]. Although both alloys exhibit a single-phase austenite (γ -Fe) that have a face-centered cubic (FCC) crystal structure, they offer different mechanical, chemical, and magnetic characteristics due to the variations in their **chemical compositions**. For instance, Invar 36 exhibits ferromagnetic behavior below the Curie temperature and a paramagnetic behavior above this temperature, but stainless steel 316L is nonmagnetic unless it is cold hardened, where it becomes paramagnetic due to the martensitic phase transformation [1, 2, 8]. Austenitic alloys are relatively difficult-to-cut due to their high work hardening, high ductility, low heat conductivity and high built up edge formation, however they have good weldability [9-14]. Thus, both alloys are good candidates for metal additive manufacturing (AM). Selective laser melting (SLM) is one of the most powerful AM processes as it can produce functional components composed of a wide range of weldable materials for many industries, including the aerospace industry [15-17]. It is a powder-bed process in which a metal powder is evenly distributed on a build plate forming a layer that is melted according to a predefined computer aided design (CAD) using a focused laser beam as shown in Figure 5.1a. Parts produced via

SLM have been known to have defects and stress risers including, but not limited to, internal voids, partially melted/unmelted powder, macro/micro cracks, changes in chemical composition, and thermal stress. Accordingly, parametric studies have been suggested in the literature to better understand what happens during the SLM process and minimize these defects and stress risers [3, 7, 18-25]. The SLM process parameters include laser power, P in (W); average scanning speed, v in (mm/s); hatch spacing, h in (mm); layer thickness, t in (mm); stripe width, w in (mm); and stripe overlap, γ in (mm) as shown in Figure 5.1b. The volumetric laser energy density, E_v in (J/mm^3) combines the most effective parameters that affect the material properties as described by Equation (5.1). It has been reported in the literature that Invar 36 parts were produced using process parameters that give laser energy densities between 10 to 333 J/mm^3 , and stainless steel 316L were produced using parameters that give laser energy densities between 28 to 214 J/mm^3 , as listed in Table 5.1. However, it is not clear which of these process parameters could be used to produce high quality parts. Previous attempts at optimizing laser energy for part production, mainly focused on a one-factor-at-a-time (OFAT) and did not include the effect of material composition. Therefore, little insight into the physical mechanisms in defining optimal laser energy was presented [3-6, 26-52]. Qiu et al. [5] studied the CTE of Invar 36 parts produced using the SLM process and postprocessed using hot isostatic pressing. The authors showed that the hot isostatic pressing process caused a reduction in the CTE of the additively manufactured parts. However, their study is based on a sample size of three samples manufactured at laser energy density of 25 J/mm^3 . A full range of process parameters windows needs to be studied. Harrison et al. [4] reported that the CTE of the SLM Invar 36 is lower than that of wrought Invar 36. The authors found that the CTE of Invar 36 increases when an annealing postprocessing procedure is performed. In this work, the process-structure-property relationships for both materials were studied through experiments based on full factorial design.

$$E_v = \frac{P}{(v \times h \times t)} \quad (5.1)$$

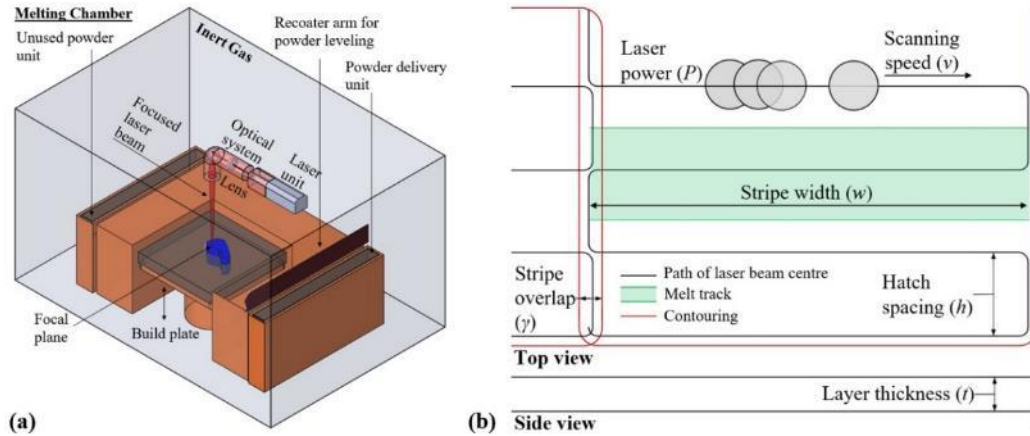


Figure 5.1: Illustration of (a) selective laser melting machine and (b) selective laser melting process parameters [3, 7, 16]. These process parameters were used for calculating the laser energy density E_v during this study.

5.2 Experimental procedures

5.2.1 Feedstock materials

Two gas-atomized powders, Invar 36 (Sandvik Osprey LTD) and stainless steel 316L (Carpenter Technology LTD), in the size range of 15-45 μm were used. ASTM F3049-14 [53] standard stated that “determining the properties of the feedstock powder used in these processes is a necessary condition for industry's confidence in powder selection and ability to produce consistent components with known and predictable properties”. Hence, the powder size distribution (PSD) of both virgin (as received) and recycled (as sieved) powders were measured using Malvern Mastersizer 2000 via the laser diffraction method according to ASTM B822-17 [54] and ASTM F3049-14 [53]. The powder morphology and chemical composition were identified using scanning electron microscopy (SEM) and energy dispersive X-ray spectroscopy (EDX) methods.

Table 5.1: Process parameters reported in the literature for producing Invar 36 and stainless steel 316L.

Heat source		Processing parameters					Ref.
AM platform (laser type)	Alloy	P (W)	v (mm/s)	t (mm)	h (mm)	E_v (J/mm ³)	
EOS M280 (Yb-fiber laser)	Invar 36 SS 316L	200-300	600-1000	0.040	0.080-0.120	42-156	Current study
Concept Laser M2 (Nd:YAG)	Invar 36	400	1800-4300	0.030	0.300	10-25	[5]
EOS M290 (Yb-fiber laser)	Invar 36	150-300	700-2200	0.040	0.080-0.320	23-93	[3]
Phenix PXM (Yb-fiber laser)	Invar 36	300	2500	0.030	0.090	44	[6]
Renishaw AM125 (Yb-fiber laser)	Invar 36	180-200	333-1000	0.020	0.090	100-333	[4]
Concept Laser M2 (Nd:YAG)	SS 316L	150-400	500-1800	0.030	0.150	28-74	[35]
HRPM-IIA (Yb-fiber laser)	SS 316L	190	800	0.050	0.150	32	[36]
SLM Solutions 125HL (Yb-fiber laser)	SS 316L	50-100	300-1250	0.030	0.070-0.140	32-80	[29]
Concept Laser M1 (Nd:YAG)	SS 316L	104	175-800	0.030-0.045	0.130	33-107	[26, 27]
Concept Laser M3 (Nd:YAG)	SS 316L	100	175-380	0.060	0.126	35-76	[37, 38]
EOS M280 (Yb-fiber laser)	SS 316L	150	1200	0.030	0.100	42	[50]
Concept Laser M2 (Nd:YAG)	SS 316L	200	1600	0.050	0.060	42	[39]
SLM-Realizer 100 (Yb-fiber laser)	SS 316L	50	100-300	0.050	0.080	42-125	[40]
Renishaw AM250 (Yb-fiber laser)	SS 316L	200	750	0.050	0.110	48	[7, 32]
Concept Laser M3 (Nd:YAG)	SS 316L	105	380	0.020-0.040	0.125	55-111	[41]
SLM-Realizer 250 (Yb-fiber laser)	SS 316L	87	150	0.075	0.130	59	[42]
SLM-Realizer 250 (Yb-fiber laser)	SS 316L	100-200	200-220	0.050	0.124	81-150	[43]
Phenix PM100 (Yb-fiber laser)	SS 316L	50	120	0.040	0.120	87	[44]
<i>in-house</i> SLM (Nd:YAG)	SS 316L	100	300	0.030	0.112-0.125	89-99	[46]
SLM Solutions 250HL (Yb-fiber laser)	SS 316L	380	625-3000	0.050	0.025-0.120	99-109	[28]
SISMA MYSINT100 (Yb-fiber laser)	SS 316L	100-150	700	0.020	0.050-0.070	102-214	[47]
DiMetal-100 (Yb-fiber laser)	SS 316L	200	400	0.040	0.080	156	[49]
HRPM-IIA (Yb-fiber laser)	SS 316L	180	900	0.020	0.060	167	[52]

5.2.2 Selective laser melting processing

An EOSINT M280 SLM machine, equipped with a 400 W ytterbium fiber laser and nitrogen air flow, was used to produce the test samples. Full factorial design of experiments (DOE) with three factors (P , v , h) at three levels was developed as listed in Table 5.2. The layer thickness, stripe width, stripe overlap, and scanning rotation between subsequent layers were maintained constant at 0.04 mm, 10 mm, 0.08 mm, and 67° respectively, and a stripe scanning strategy [7] was used. The contouring, up-skin, and down-skin parameters were deactivated during the process so that only the hatching parameters were considered in the current study. The focal plane of the laser was maintained at zero position, in which the surface being melted was in the focal plane as shown in Figure 5.1a. The DOE generates a matrix of 27 experimental runs with a wide range of laser energy density from 41.7 to 156.3 J/mm³. Each run of experiment was used to produce two cubes with an edge length of 10 mm from each material, in which a total of 54 cubes were produced from each material. The samples were fabricated directly on the build plate and did not undergo any post-processing procedures. The cubes were removed using a band saw with coolant applied to prevent overheating of the samples.

5.2.3 Microstructural analysis and phase identification

SEM and EDX methods were used to analyze the surface morphology and material composition of the parts produced. The surface morphology analysis identified the surface defects and the part deterioration. The analysis was performed on one cube from each run of experiments (27 cubes from each material) and included both top and lateral surfaces of each sample. The material phase of these samples was identified via X-ray diffraction (XRD) method based on lattice strain measurements. The lattice deformation was obtained using a $\text{CoK}\alpha$ (wavelength 1.79026 Å) radiation source, detector angle was 57.4° , and X-ray angles was 59.4° .

Table 5.2: SLM process parameters used in this study (DOE matrix based on full factorial design).

No	P (W)	v (mm/s)	h (mm)	E_v (J/mm ³)	No	P (W)	v (mm/s)	h (mm)	E_v (J/mm ³)
1	200	600	0.08	104.2 **	15	250	800	0.12	65.1
2	200	600	0.10	83.3	16	250	1000	0.08	78.1 ‡
3	200	600	0.12	69.4	17	250	1000	0.10	62.5 †
4	200	800	0.08	78.1 ‡	18	250	1000	0.12	52.1 *
5	200	800	0.10	62.5 †	19	300	600	0.08	156.3
6	200	800	0.12	52.1 *	20	300	600	0.10	125.0
7	200	1000	0.08	62.5 †	21	300	600	0.12	104.2 **
8	200	1000	0.10	50.0	22	300	800	0.08	117.2
9	200	1000	0.12	41.7	23	300	800	0.10	93.8 §
10	250	600	0.08	130.2	24	300	800	0.12	78.1 ‡
11	250	600	0.10	104.2 **	25	300	1000	0.08	93.8 §
12	250	600	0.12	86.8	26	300	1000	0.10	75.0
13	250	800	0.08	97.7	27	300	1000	0.12	62.5 †
14	250	800	0.10	78.1 ‡					
* † ‡ § ** indicate groups that have the same laser energy densities									

5.2.4 Magnetic and thermal testing

The magnetic dipole moment (j) of each sample was measured using Lake Shore 480 fluxmeter. In parallel to this, the second cube from each run of experiment was machined to the standard size of the CTE samples provided in the ASTM E831-14 standard (4 mm diameter and 10 mm length) [55, 56]. The BÄHR quenching dilatometer DIL 805A/D was used to perform the CTE measurements. The initial length of the samples (L_o) was measured using a Mitutoyo micrometer with a scale value of $\pm 1 \mu\text{m}$. The samples were heated via induction copper coil and the corresponding linear deflection (ΔL) was measured by a linear voltage displacement transducer (LVDT) through quartz push rods attached to the sample end. Simultaneously, the instantaneous temperature (T_i) was measured by a 0.1 mm diameter K-type thermocouple spot-welded to the sample. The samples were heated in inert helium atmosphere from room temperature ($T_o = 21^\circ\text{C}$) to 1000°C with a 0.1°C/s heating rate and allowed to cool to room temperature. The thermal expansion, ε_T in ($\mu\text{m/m}$),

coefficient of thermal expansion “CTE”, α in ($10^{-6} \text{ }^\circ\text{C}^{-1}$), temperature difference over which ΔL is measured, ΔT in ($^\circ\text{C}$), and average temperature, T_a in ($^\circ\text{C}$), were calculated as described by Equation (5.2).

$$\alpha = \left(\frac{\Delta L}{L_o \times \Delta T} \right) = \left(\frac{\varepsilon_T}{\Delta T} \right), \text{ where } \varepsilon_T = \left(\frac{\Delta L}{L_o} \right) \quad (5.2)$$

$$\Delta T = (T_{i+1} - T_i), \text{ and } T_a = \frac{T_{i+1} + T_i}{2}$$

5.3 Experimental results

5.3.1 Powder characterization

Figure 5.2a and b show the differential and cumulative PSD for both virgin and recycled powders. It was observed that the PSD curves overlap within the repeatability standard deviation ($\pm 1\%$), implying that the particle sizes for both materials were approximately identical. Table 5.3 lists the powder diameter (D_p) at three cumulative volumes of particles ($p = 10\%, 50\%, 90\%$). It was noted that 10-90% of both virgin and recycled Invar 36 powder were approximately between $17 \mu\text{m}$ to $49 \mu\text{m}$, while 10-90% of virgin stainless steel 316L powder was approximately between $18 \mu\text{m}$ to $47 \mu\text{m}$. In addition, 10-90% of recycled stainless steel 316L powder was approximately between $17 \mu\text{m}$ to $52 \mu\text{m}$. No large particles were observed, implying that the large agglomerated particles were sieved successfully. It is worth noting that both virgin and recycled powders were sieved before the SLM process via a 200-mesh sieve ($75 \mu\text{m}$). Figure 5.3 shows the microstructure of the virgin (as received) and recycled (as sieved) Invar 36 and stainless steel 316L powders. The analysis showed minimal difference between the virgin and recycled powders. The morphology of the virgin powders showed nearly identical spherical particles, while the recycled powders showed

agglomerated spherical particles within the size range of the typical powder (15-45 μm). No significant morphological changes between the virgin and recycled powders were observed.

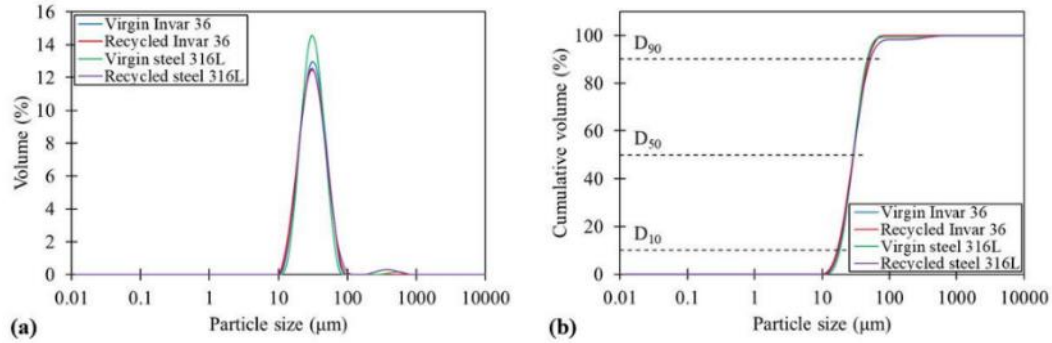


Figure 5.2: (a) Differential and (b) cumulative powder size distribution for both Invar 36 and stainless steel 316L powders.

Table 5.3: Powder diameter at cumulative volume percent of particles 10%, 50%, and 90% for both materials.

Powder	Virgin powder size (as received prior to SLM)			Recycled powder size (as sieved following SLM)		
	D ₁₀ (μm)	D ₅₀ (μm)	D ₉₀ (μm)	D ₁₀ (μm)	D ₅₀ (μm)	D ₉₀ (μm)
Invar 36	17.3 ± 0.2	29.3 ± 0.3	48.9 ± 0.3	16.7 ± 0.4	28.8 ± 0.2	49.2 ± 0.9
Steel 316L	18.3 ± 0.3	29.1 ± 0.5	46.5 ± 0.6	17.4 ± 0.3	29.3 ± 0.5	52.2 ± 0.5

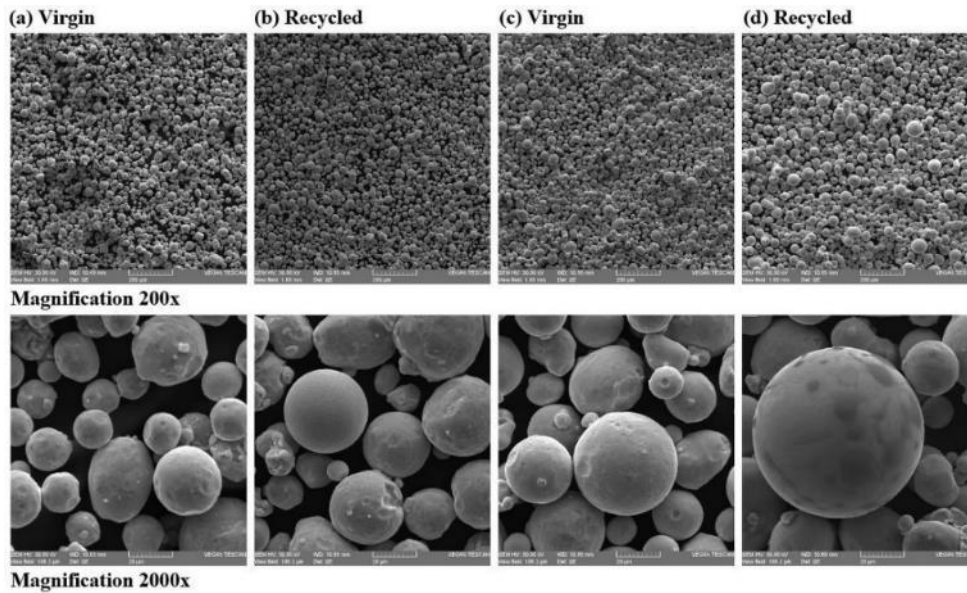


Figure 5.3: Microstructures of (a, b) virgin and recycled Invar 36 and (c, d) virgin and recycled stainless steel 316L powders.

5.3.2 Microstructural characterization

Invar 36 parts that were produced at a laser energy density of 41.7 J/mm^3 showed discontinuous beads that consequently formed voids, cracks, denudations, and balling phenomenon. These parts were also found to have unmelted powder particles adhering to the surface and cracks between subsequent layers as shown in Figure 5.4a and e. Therefore, parts that were produced at laser energy densities between 41.7 J/mm^3 and 52.1 J/mm^3 exhibited fewer voids and semi-continuous melt tracks. Parts that were produced at 86.8 J/mm^3 showed continuous melt tracks with no voids and balling formations. This microstructure showed stable melting with no cracks as shown in Figure 5.4c and g. Parts that were produced at 156.3 J/mm^3 exhibited keyhole pores and spatters (i.e. droplets of molten metal) as shown in Figure 5.4d and h. This could be attributed to the vaporization and ejection of some elements from the melting pool during the SLM process. Similarly, stainless steel 316L parts that were produced between 41.7 J/mm^3 and 62.5 J/mm^3 showed either discontinuous or semi-continuous beads. These parts were found to have voids, cracks, balling, denudations and unmelted powder particles adhering to the surface as shown in Figure 5.5a, b, e, and f. At a laser energy density of 104.2 J/mm^3 , stainless steel parts showed continuous melt tracks with no voids and balling formations as shown in Figure 5.5c and g. These parts showed the highest measured density with stable melting characteristics. Similar to Invar 36 parts, stainless steel parts that were produced at 156.3 J/mm^3 showed keyhole pores and metal spatters as shown in Figure 5.5d and h. A **critical laser energy density** (E_C) was defined for each material, in which the material undergoes unstable melting when exposed to laser energy densities above this critical energy density. The melting process is stable only when using the critical energy density ($E_C = 86.8 \text{ J/mm}^3$ for Invar 36 and $E_C = 104.2 \text{ J/mm}^3$ for stainless steel 316L).

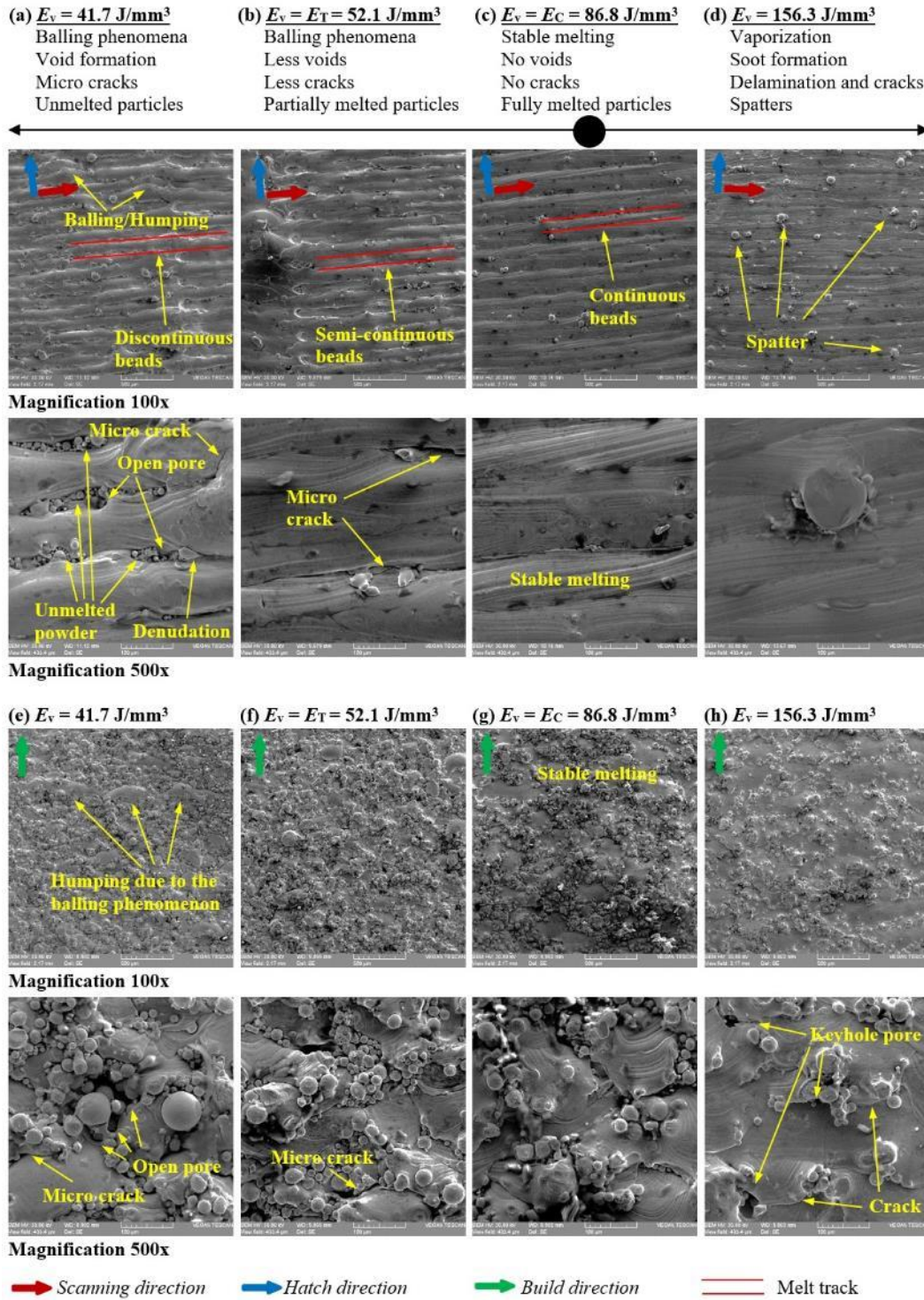


Figure 5.4: Microstructures of (a-d) top and (e-h) side surfaces of *Invar 36* parts produced at laser energy density of (a, e) 41.7 J/mm^3 , (b, f) 52.1 J/mm^3 , (c, g) 86.8 J/mm^3 , and (d, h) 156.3 J/mm^3 . 100x and 500x magnifications were used.

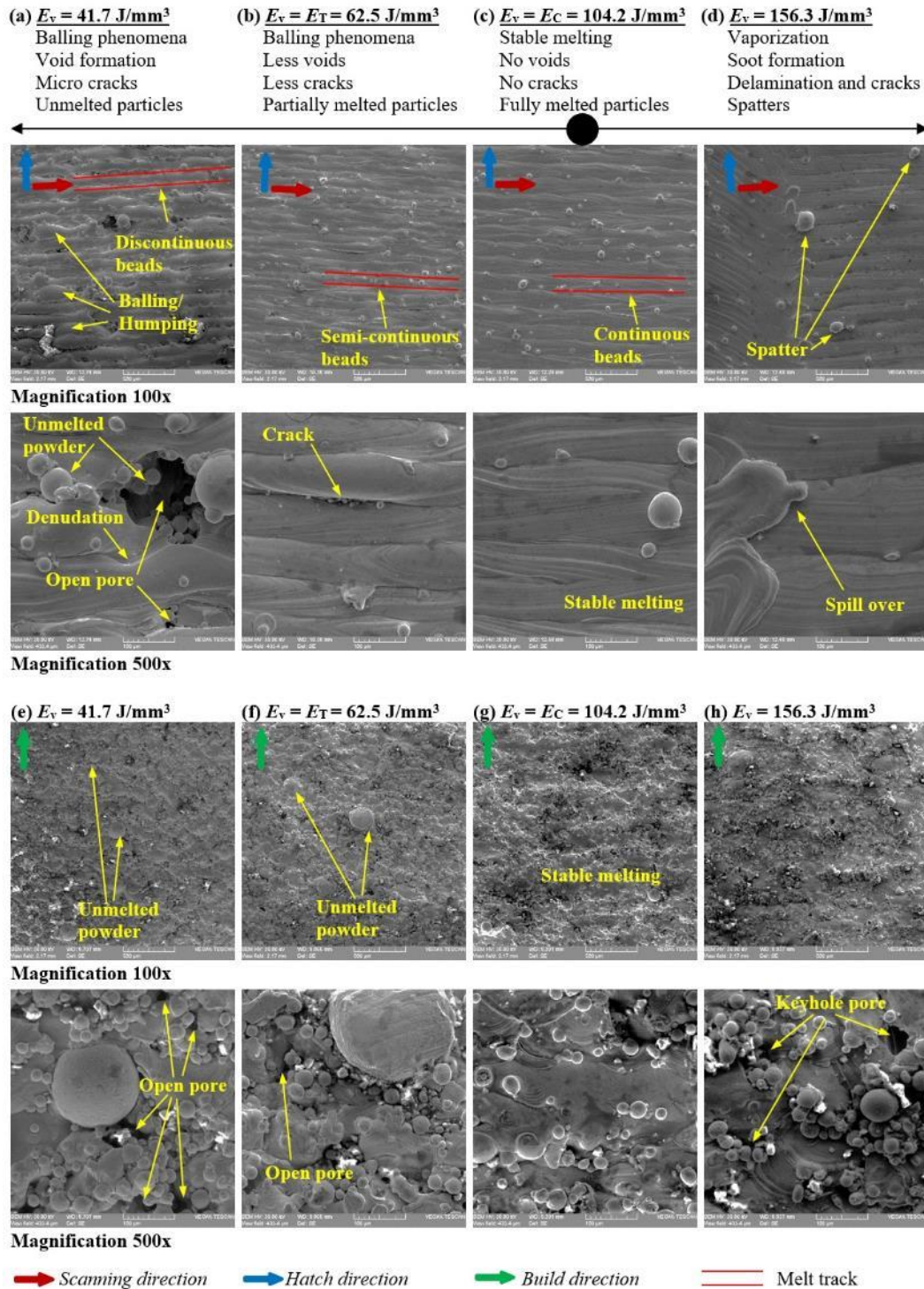


Figure 5.5: Microstructures of (a-d) top and (e-h) side surfaces of *stainless steel 316L* parts produced at laser energy density of (a, e) 41.7 J/mm^3 , (b, f) 62.5 J/mm^3 , (c, g) 104.2 J/mm^3 , and (d, h) 156.3 J/mm^3 . 100x and 500x magnifications were used.

5.3.3 Material composition

Table 5.4 and Table 5.5 list the material compositions of Invar 36 and stainless steel 316L samples produced at various laser energy densities, compared with the typical chemical composition of the wrought material. The scale value of the EDX measurements was ± 0.01 wt%. The scanning rate was adjusted very low and many frames were collected (20 frames, resolution of 2048×2048 pixels/frame, and scanning rate of 10^3 $\mu\text{s}/\text{pixel}$) to allow accurate measurements. The material composition of the parts that were produced at energy densities below E_C did not show that much difference from the wrought material. However, the parts that were produced at energy densities above E_C showed significant change in the concentration of some alloying elements. In Invar 36, it was observed that using laser energy densities higher than E_C caused a reduction in the nickel and manganese concentrations, and accordingly caused an increase in the silicon and iron concentrations. Similarly, the concentration of nickel, manganese, and chromium decreased, as well as the concentration of silicon, iron, and molybdenum increased in stainless steel 316L when using laser energy densities higher than E_C for stainless steel 316L.

Table 5.4: Material composition of Invar 36 parts (wt.%).

Element	Wrought material [57]	Powder		SLM Invar 36 cubes			
		Virgin	Recycled	41.7 J/mm ³	52.1 J/mm ³	86.8 J/mm ³	156.3 J/mm ³
Fe	Balance	63.97	63.55	63.92	63.85	63.45	64.82
Ni	35.5-36.5	35.62	36.05	35.66	35.21	35.11	33.34
Mn	<0.5	0.23	0.21	0.22	0.20	0.20	0.17
Si	<0.25	0.18	0.19	0.20	0.74	1.24	1.67
Total		100.00	100.00	100.00	100.00	100.00	100.00

Table 5.5: Material composition of stainless steel 316L parts (wt.%).

Element	Wrought material [55]	Powder		SLM stainless steel 316L cubes			
		Virgin	Recycled	41.7 J/mm ³	62.5 J/mm ³	104.2 J/mm ³	156.3 J/mm ³
Fe	Balance	67.59	67.54	67.74	67.87	67.88	68.21
Cr	16-18	17.13	17.12	17.10	17.09	17.11	17.05
Ni	10-14	10.69	10.52	10.10	9.98	9.69	8.66
Mo	2-3	1.62	1.79	1.74	1.90	2.30	2.79
Mn	<2	1.84	1.81	1.86	1.74	1.39	1.35
Si	<1	1.13	1.22	1.46	1.42	1.63	1.94
Total		100.00	100.00	100.00	100.00	100.00	100.00

5.3.4 Crystallographic characterization

Figure 5.6a and b show the XRD diffractograms of Invar 36 and stainless steel 316L samples that were produced at various laser energy densities. The results matched the typical austenitic steel (γ -Fe) structure shown in Figure 5.6c and no other phases were observed. However, significant differences in the intensities of both (1 1 1) and (2 0 0) planes were observed. Using high laser energy density caused an increase in the intensity of (2 0 0) plane and a reduction in the intensity of (1 1 1) plane. This could be attributed to either the microsegregation of some precipitates during the parts solidification when using very high laser energy density [58-64] or that (2 0 0) plane is the preferred growth direction during solidification of cubic materials. Some studies in the literature have reported that residual stresses due to phase transformation could be induced in the alloys that experience a martensitic transformation [7, 65, 66], but some other studies have reported residual stresses due to thermal stresses [67]. The residual stress measurements for Invar 36 and stainless steel 316L are considered in another work by the authors [68].

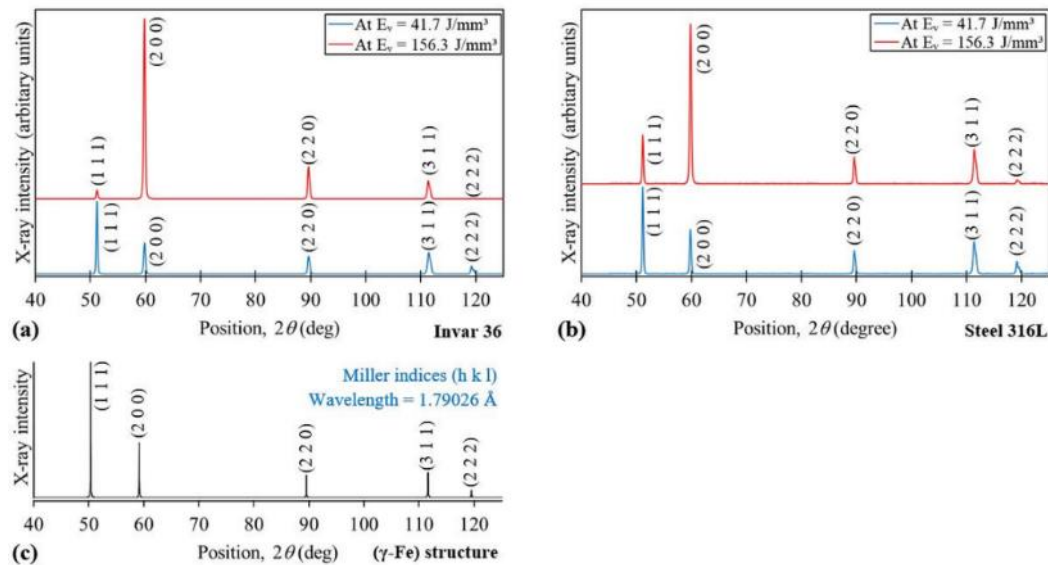


Figure 5.6: XRD diffractograms of (a) SLM Invar 36 samples, (b) SLM stainless steel 316L samples, and (c) typical austenite crystal.

5.3.5 Coefficient of thermal expansion

Figure 5.7 shows the dilatometer experimental results (i.e. thermal expansion and average linear CTE) for Invar 36 and stainless steel 316L parts produced at the critical laser energy density. The SLM parts showed linear CTE analogous to the wrought material, no significant changes were observed. The results were almost identical to those reported in the literature [4, 5]. The Invar effect occurs when the nickel content in the alloy is maintained at 36%, which manifests the lowest CTE compared with any other iron-nickel based alloy [69]. The CTE of Invar 36 is much lower than that of stainless steel 316L as shown in Figure 5.7. The CTE of Invar 36 starts to drastically increase after the Curie temperature ($T_C = 279\text{ }^\circ\text{C}$), but it is still lower than steels and other iron-based alloys. It was observed that the laser process parameters affect the CTE of the material, especially at low temperatures. For Invar 36, parts that were manufactured at 41.7 J/mm^3 and 156.3 J/mm^3 showed lower thermal expansion than parts that were manufactured at E_C (86.8 J/mm^3) at low temperatures as shown in Figure 5.8. Similarly, stainless steel 316L parts that were manufactured at E_C (104.2 J/mm^3) showed higher thermal expansion than parts that were manufactured at 41.7 J/mm^3 and 156.3 J/mm^3 at low temperatures. Figure 5.9 shows the thermal expansion of SLM parts at $50\text{ }^\circ\text{C}$ as a function of laser energy density. It was observed that increasing the laser energy density resulted in an increase in the thermal expansion until a peak was reached, after which it decreased. This peak energy density matches the critical energy density for each material. It was reported in the literature [5] that the SLM process does not affect the CTE of Invar 36, for a sample size of three samples manufactured with different orientations at laser energy density of 25 J/mm^3 . The work done in reference [5] did not include samples manufactured at laser energy densities higher than 25 J/mm^3 and therefore it is likely that all of the test data was below the critical laser energy density for their material. Another study [4] reported that

the CTE of the SLM Invar 36 is lower than that of wrought Invar 36. The authors concluded that an annealing procedure after the SLM process caused an increase in the CTE, however the authors in reference [5] showed that the hot isostatic pressing process caused a reduction in the CTE. Neither study covered the influence of the process parameters on the CTE. However, reference [4] mentioned that the CTE of an alloy is very sensitive to compositional changes in the alloy. In this study, it was observed that the trend of Invar 36 thermal expansion changed after the Curie temperature, which could be attributed to changes in the material magnetic properties after the Curie temperature. Thus, the range used in the statistical analysis was from room temperature to Curie temperature (279 °C). The relationship between the instantaneous temperature, T_i , and thermal expansion, ϵ_T , is considered to be a second order polynomial within the range from room temperature to Curie temperature as shown in Figure 5.7a. Equation (3) represents the empirical relationship between the thermal expansion and temperature, in which constants a , b , and c are material dependent. Since the SLM process parameters affect the material properties, so it was expected that these constants would depend on the SLM process parameters. A three-way interaction regression model that examines the effect of SLM process parameters on the thermal expansion was developed using Minitab software. The model included independent variables (P , v , h), quadratic variables and two-way interactions (P^2 , v^2 , h^2 , $P \times v$, $P \times h$, $v \times h$), three-way interaction ($P \times v \times h$), temperature variables (T , T^2), and interaction terms ($P \times T$, $v \times T$, $h \times T$, $P \times v \times T$, $P \times h \times T$, $v \times h \times T$). Table 5.6 shows the results of the regression models where, S is the standard deviation, R^2 is the coefficient of determination, and PRESS is the predicted residual error sum of squares. These models were accepted as statistically significant. Table 5.7 shows the regression equations of the thermal expansion for both materials.

$$\varepsilon_T = a + bT + cT^2 \quad (5.3)$$

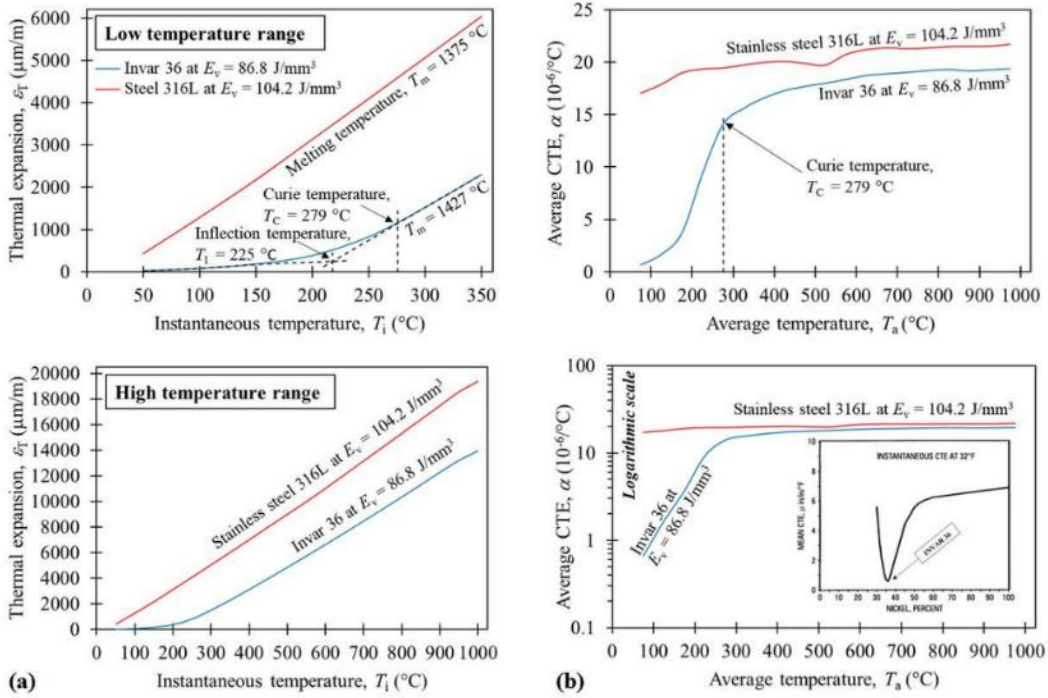


Figure 5.7: (a) thermal expansion and (b) average coefficient of thermal expansion for Invar 36 and stainless steel 316L samples manufactured at the critical laser energy density (E_C).

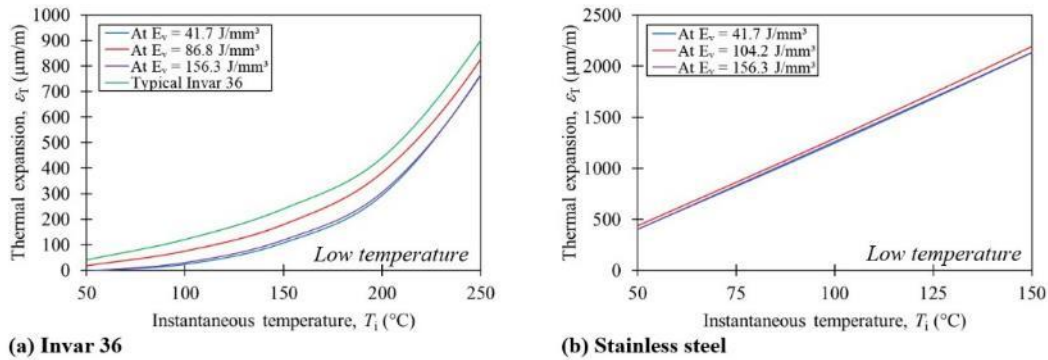


Figure 5.8: Thermal expansion of (a) Invar 36 and (b) stainless steel 316L samples manufactured at various laser energy densities.

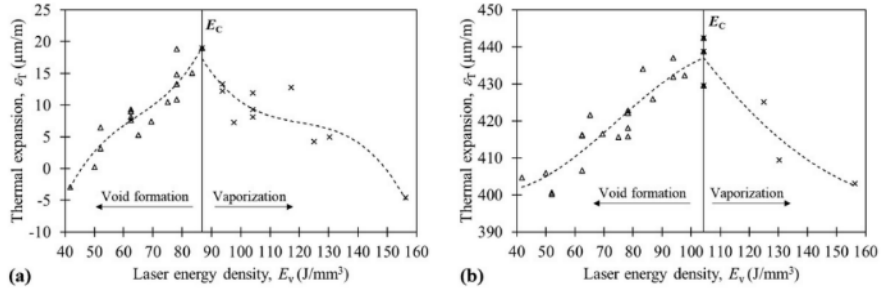


Figure 5.9: Thermal expansion of (a) Invar 36 and (b) stainless steel samples at instantaneous temperature $T_i = 50 \text{ }^\circ\text{C}$.

Table 5.6: Regression model for Invar 36 and stainless steel 316L thermal expansions.

Source	Degree of freedom	Contribution	Sum of squares	Mean sum of squares	F-value	p-value	t-value	Remarks	
Invar 36									
Regression	9	99.38%	1758838	195426	1737.99	0.000	-3.11	$\alpha = 0.05$ $F_{0.05, 9, 98} = 1.98$ $t_{0.025, 98} = 1.98$	
P	1	0.00%	21	805	7.16	0.009	2.68		
v	1	0.00%	29	1165	10.36	0.002	3.22		
T ²	1	96.89%	1714838	205158	1824.54	0.000	42.71		
P ²	1	0.04%	754	754	6.70	0.011	-2.59		
v ²	1	0.07%	1233	1233	10.96	0.001	-3.31		
P × T	1	0.95%	16825	34996	311.24	0.000	-17.64		
P × v × T	1	0.04%	753	17477	155.43	0.000	12.47		
P × h × T	1	0.02%	402	22389	199.11	0.000	14.11		
v × h × T	1	1.36%	23983	23983	213.29	0.000	-14.60		
Error	98	0.62%	11019	112					
Total	107	100.00%	1769857						
S = 10.6040, R ² = 99.38%, Adjusted R ² = 99.32%, Predicted R ² = 99.24%, PRESS = 13464.8									
Stainless steel 316L									
Regression	14	99.99%	108703202	7764514	83444.06	0.000		$\alpha = 0.05$ $F_{0.05, 14, 93} = 1.80$ $t_{0.025, 93} = 1.99$	
T	1	99.92%	108620843	64100	688.88	0.000	26.25		
P	1	0.00%	1899	1566	16.82	0.000	-4.10		
v	1	0.00%	4445	3542	38.06	0.000	-6.17		
h	1	0.00%	1597	949	10.20	0.002	-3.19		
T ²	1	0.06%	63693	63693	684.50	0.000	26.16		
P ²	1	0.00%	507	507	5.44	0.022	-2.33		
h ²	1	0.00%	415	415	4.46	0.037	-2.11		
P × T	1	0.00%	27	486	5.22	0.025	-2.28		
h × T	1	0.00%	0	525	5.64	0.020	-2.37		
P × v	1	0.00%	2055	4329	46.53	0.000	6.82		
P × h	1	0.00%	1646	2596	27.90	0.000	5.28		
v × h	1	0.00%	2023	2626	28.22	0.000	5.31		
P × h × T	1	0.00%	537	537	5.77	0.018	2.40		
P × v × h	1	0.00%	3512	3512	37.75	0.000	-6.14		
Error	93	0.01%	8654	93					
Total	107	100.00%	108711856						
S = 9.64627, R ² = 99.99%, Adjusted R ² = 99.99%, Predicted R ² = 99.99%, PRESS = 11785.3									

Table 5.7: Empirical “regression” equations for thermal expansion of both Invar 36 and stainless steel 316L parts.

Invar 36 ($T_C = 279\text{ }^\circ\text{C}$)	
$T_o \leq T \leq T_C$ $T_C = 279\text{ }^\circ\text{C}$	$\varepsilon_T = (0.015196) T^2 + (-0.012794 P + 0.000008 P \times v + 0.06248 P \times h - 0.01895 v \times h) T + (-200.4 + 1.167 P + 0.2826 v - 0.002242 P^2 - 0.000179 v^2)$ $a = 0.015196$ $b = -0.012794 P + 0.000008 P \times v + 0.06248 P \times h - 0.01895 v \times h$ $c = -200.4 + 1.167 P + 0.2826 v - 0.002242 P^2 - 0.000179 v^2$
Stainless steel 316L	
$T_o \leq T \leq T_C$ $T_C = 279\text{ }^\circ\text{C}$	$\varepsilon_T = (0.009714) T^2 + (16.954 - 0.00577 P - 14.98 h + 0.0599 P \times h) T + (452 - 3.557 P - 1.350 v - 6925 h - 0.001838 P^2 - 10399 h^2 + 0.005893 P \times v + 40.28 P \times h + 11.47 v \times h - 0.05238 P \times v \times h)$ $a = 0.009714$ $b = 16.954 - 0.00577 P - 14.98 h + 0.0599 P \times h$ $c = 452 - 3.557 P - 1.350 v - 6925 h - 0.001838 P^2 - 10399 h^2 + 0.005893 P \times v + 40.28 P \times h + 11.47 v \times h - 0.05238 P \times v \times h$

Invar 36 sometimes shows negative CTE below Curie temperature due to interaction between lattice vibration and magnetic degree of freedom. Both void formation and compositional changes affect the CTE of Invar 36 [70]. It was found that parts that have internal voids and/or parts that exhibit alloying element vaporization might have negative CTE as shown in Figure 5.9. This is not the case in stainless steel 316L parts that have very high CTE compared with Invar 36. The study showed that Invar 36 parts produced by SLM process have significant dependency on the laser energy density variation than stainless steel 316L parts. Figure 5.10 shows the effects of hatch spacing, scanning speed, and laser power on the thermal expansion of both materials at 200 °C (below the Curie temperature). It can be concluded that:

1. At low laser power (laser energy density below E_C), increasing the scanning speed and/or hatch spacing led to a decrease in the laser energy density and consequently a decrease in the thermal expansion. This could be attributed to the void formation at high scanning speed and large hatch spacing. These results conformed with the microstructure analysis that showed voids below the critical energy density (see Figure 5.4a, e, and Figure 5.5a, e).
2. At high laser power (laser energy density above E_C), decreasing the scanning speed and/or hatch spacing led to an increase in the laser energy density and consequently a decrease in the thermal expansion. This could be attributed to the mass loss and composition change occurred above the critical energy density. These results conformed with the composition analysis that showed reduction in some elements concentration (Table 5.5 and Table 5.6).

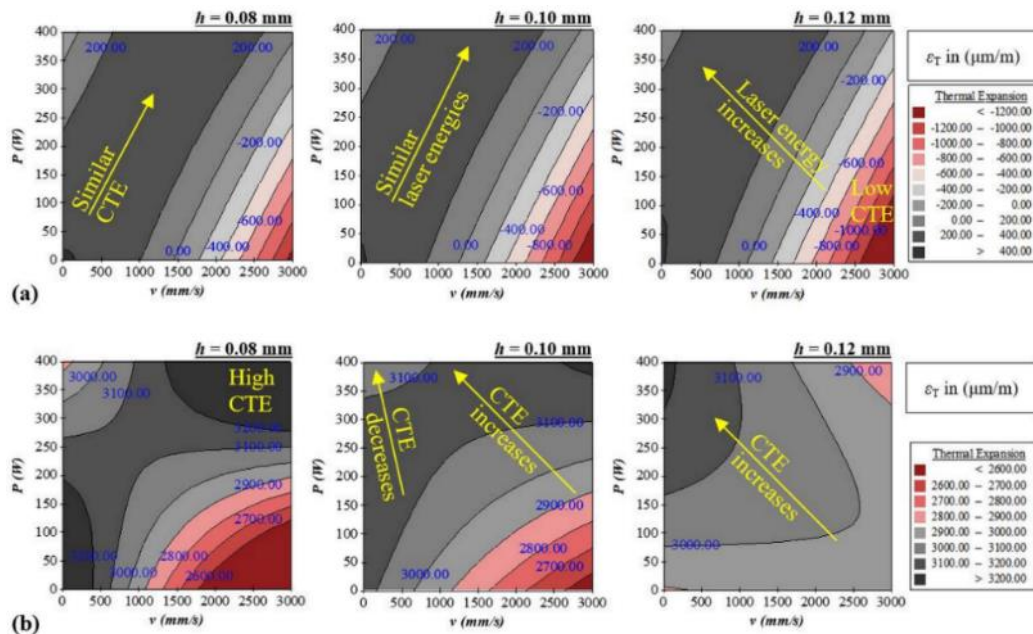


Figure 5.10: Contour plots for the thermal expansion of (a) Invar 36 and (b) stainless steel 316L samples at temperature of 200 °C. The plots show the effect of laser power and scanning speed on thermal expansion at hatch spacings of 0.08, 0.10, and 0.12 mm.

5.3.6 Magnetic dipole moment

Introducing pores into the microstructure causes a transgranular fracture through the grain boundaries and consequently an increase in the magnetic properties of the material due to weak grain boundaries [71, 72]. Any compositional change could also affect the magnetic properties of the material [73-76]. Increasing silicon concentration is one of the compositional changes that could increase the magnetic moment [77]. Table 5.8 lists the magnetic dipole moment in the Invar 36 and stainless steel 316L samples that were produced at various laser energy densities. It was found that increasing the laser energy density caused a reduction in the magnetic dipole moment until the critical energy density is reached, after which the magnetic dipole moment started to increase. Below the critical energy density, increasing the laser energy density caused a reduction in the void formation and consequently caused a reduction in the magnetic dipole moment. Above the critical energy density, increasing the laser energy density caused an increase in the silicon concentration (i.e. microsegregation of some alloying elements) and consequently an increase in the magnetic dipole moment. The magnetic properties of the material are affected by either void formation in the microstructure (i.e. grain boundaries) [71, 72] or changes in the material composition [73-76]. Stainless steel 316L is nonmagnetic material (low magnetic dipole moment) and Invar 36 is ferromagnetic material that demagnetize above the Curie temperature. For ferromagnetic metals, the coefficient of thermal expansion increases, and magnetization decreases as temperature increases [78]. It was found that SLM parts that were produced at laser energy densities below E_C have low coefficient of thermal expansion and high magnetic properties due to void formation. In addition, parts that were produced at laser energy densities above E_C have also low coefficient of thermal expansion and high magnetic properties due to changes in the material composition. Only parts that were produced at the critical energy density showed the highest coefficient of thermal expansion and the lowest magnetic dipole moment.

Table 5.8: Magnetic dipole moment of Invar 36 and stainless steel 316L samples.

Invar 36		Stainless steel 316L	
Produced at E_V	Magnetic dipole moment, j (Wb.cm)	Produced at E_V	Magnetic dipole moment, j (Wb.cm)
41.7 J/mm ³	34.9285	41.7 J/mm ³	0.1542
52.1 J/mm ³	31.4332	52.1 J/mm ³	0.1199
86.8 J/mm ³	23.5939	104.2 J/mm ³	0.1079
156.3 J/mm ³	28.1234	156.3 J/mm ³	0.1448

5.4 Discussion

SLM parts can exhibit stress risers and number of dislocations as compared with other traditional manufacturing methods as shown in Figure 5.11. The SLM process generates highly localized changes in both heating rate during the powder melting and cooling rate during the part solidification process. These thermal changes could cause void formation, changes in the composition, and variations in the thermal expansion [3, 7, 18-21, 79-81]. These three mechanisms significantly affect the mechanical properties and material properties of the parts produced [49, 50, 82-88]. The laser process parameters should be optimized in an early stage during manufacturing to avoid these stress risers for better manufacturing quality. Furthermore, how the laser energy correlate to the physics of these three mechanisms was discussed in this paper by means of experimental observations and statistical analyses.

5.4.1 Void formation

It was observed that using laser energy density lower than the critical energy density (E_c) can cause the formation of voids, partially melted/unmelted powder particles, cracks between subsequent layers, powder denudations, and balling phenomenon. Figure 5.12a shows the different types of voids and cracks; keyhole pores formed due to high penetration of laser in the deposited layer, gas pores formed due to entrapped gas either inside powder particles or inside the melt pool, lack-of-fusion pores formed due to improper connection between melt

pools, balling phenomenon happens due to discontinuous or semi-continuous beads (melt tracks), cracks between subsequent layers due to improper amount of heat [21, 89-91].

Void formation is not exclusively restricted to low laser energy; rather, it is widely dependent on the stability of the melt track. Voids could be formed from either gas pores, lack-of fusion pores, or keyhole induced porosity [3, 19, 21, 39]. At laser energy densities lower than E_c , the voids could be either gas pores or lack-of fusion pores. The gas pores are almost spherical in shape and formed due to entrapped gases either inside the powder particles during the powder atomization process or inside the melting pool during the SLM process. The lack-of-fusion pores are formed due to inadequate penetration of the melt pool into a previously deposited layer. At laser energy densities higher than E_c , the keyhole pores could be formed due to entrapped alloy vapors inside the melting pool [21].

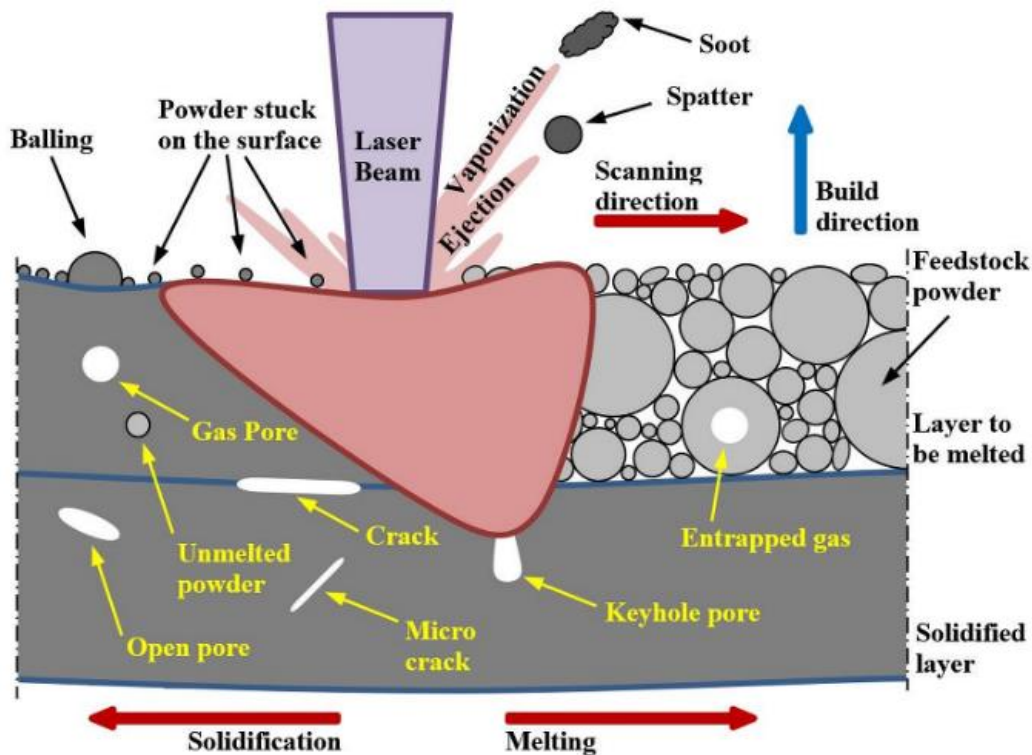


Figure 5.11: Illustration of SLM melt pool formation highlighting the expected defects.

Balling phenomenon is described by the Plateau-Rayleigh capillary instability [21, 36, 66], which occurs when the melt track tends to break up into spherical balls and becomes discontinuous. Using laser energy density lower than E_C could lead to balling phenomenon due to surface tension accompanied with decreased wettability.

Powder denudation is the apparent clearing of powder particles around the melt track. It usually accompanied with elongated pores due to surface tension. The powder denudation causes an accumulation of surface roughness between layers. When the laser energy is not sufficient to rapidly fully melt the powder particles, wetting occurs and the surface tension acts to pull melted particles into the melt pool. This phenomenon is reported in the literature as powder denudation and is commonly known in laser welding process [92-95]. Some of the pores showed in the microstructure analysis were accompanied with powder denudations.

5.4.2 Vaporization phenomenon

From the microstructure analysis, it was observed that using laser energy densities higher than E_C caused footprints of spilled over molten metal. This molten metal on the surface supports the conclusion that the layers were over melted. If the laser energy density exceeded E_C during the melting of a certain layer, the layer would be over melted, and the molten metal would spill over the sides, leaving marks on the preceding layers as shown in Figure 5.4d and Figure 5.5d. This high amount of energy density caused: (i) vaporization of some elements that converted into soot goes to the filter, (ii) ejection of molten particles that converted into droplet spatters on the surface, and (iii) ejection of unmelted powder particles that converted into powder spatters stuck on the surface as shown in Figure 5.12b. The vaporization and microsegregation of alloying elements affected the chemical composition of the parts produced as discussed earlier in section 5.3.3. Table 5.9 shows the

melting and boiling temperatures, linear thermal expansion, and functionality of the dominant alloying elements in Invar 36 and stainless steel 316L. It can be summarized that manganese improves the hardness and tensile strength but reduces the weldability and ductility of the material, chromium improves the hardenability and corrosion resistance and reduces plasticity, nickel improves toughness and corrosion resistance and stabilizes austenite in the material, silicon tends to increase strength and hardness but reduces ductility, and molybdenum increases hardness and strength [96, 97]. It was observed that the concentrations of manganese, chromium, and nickel, elements that have the lowest boiling temperatures, decreased, as well as the concentrations of molybdenum, silicon, and iron, elements that have the highest boiling temperatures, increased when using laser energy densities higher than E_C for both materials. Iron, manganese, chromium, and nickel are the main alloying elements that vaporized in steel alloys [98]. Although iron has lower boiling point than nickel, but iron was preserved while nickel was vaporized at high energy density. This could be attributed to that iron is the base alloying element in both alloys (62-69% Fe in stainless steel 316L and 63-64% Fe in Invar 36).

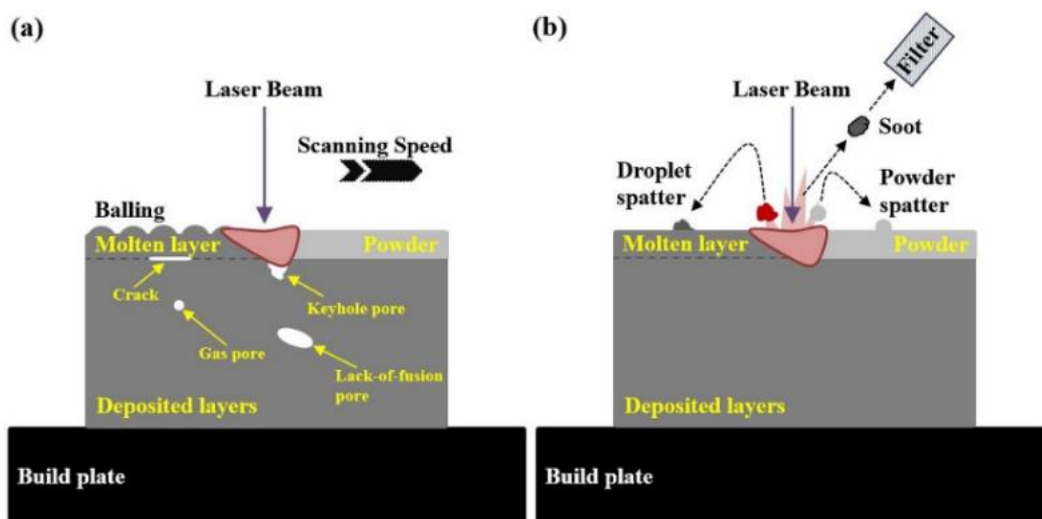


Figure 5.12: Physics of (a) void formation and (b) particles vaporization.

Table 5.9: Material properties of alloying elements [96, 97].

Element	α ($^{\circ}\text{C}$) at 25 $^{\circ}\text{C}$	T_m ($^{\circ}\text{C}$)	T_b ($^{\circ}\text{C}$)	Hardness	Tensile strength	Yield	Ductility	Corrosion
Mn	21.7×10^{-6}	1246	2061	+	+	+	-	
Cr	4.9×10^{-6}	1907	2671	+		+		+
Ni	13.4×10^{-6}	1455	2913	+	+	+	+	+
Fe	11.8×10^{-6}	1538	2861	+	+	+	+	
Si	0.0	1414	3265	+	+	+	-	
Mo	4.8×10^{-6}	2622	4639	+	+		-	+

(α) is the coefficient of thermal expansion, (T_m) is melting temperature, (T_b) is the boiling temperature, (+) means that the alloying element improves this property, and (-) means that it reduces this property

5.4.3 Thermal expansion variation

This mechanism is a consequence of the other two mechanisms because thermal expansion mainly depends on temperature, material composition, porosity/part density, crystallographic direction, grain growth, and phase transitions [99]. It was observed that increasing the laser energy density caused an increase in the thermal expansion below E_C and a decrease in thermal expansion above E_C . The void formation at energy densities lower than E_C caused a reduction in the thermal expansion of these parts [66, 99-101]. Alternatively, the vaporization of manganese and nickel (that have very high CTE as listed in Table 5.9) and the more concentration of molybdenum and silicon (that have very low CTE), that happened when using energy densities higher than E_C , caused a reduction in the thermal expansion of the parts produced. Magnetic dipole moments and magnetizations mainly depend on material composition, Curie temperature, crystal structure, and thermal expansion [63, 101]. Consequently, increasing the thermal expansion below E_C was accompanied by a reduction in the magnetic dipole moment and vice versa above E_C . It can be concluded that any compositional change and void formation could affect the thermal expansion and the magnetic properties of the material, and consequently could affect the mechanical properties of the parts produced [69]. This paper does not include the effect of the heat treatment, as it mainly studies the influence of the processing conditions

on the CTE and magnetic properties of Invar 36 and stainless steel 316L parts produced by SLM process. The effect of heat treatment on the thermal and magnetic properties of parts produced at the critical laser energy density is recommended for future work.

5.5 Conclusions

Invar 36 and stainless steel 316L powders, size 15-45 μm , were used to produce samples according to a full factorial design of experiments. The analyses showed that:

1. A critical energy density, E_C , exists for each material. This critical energy density was found to be 86.8 J/mm^3 for Invar 36 and 104.2 J/mm^3 for stainless steel 316L.
2. Using laser energy densities lower than E_C caused void formation due to either gas pores or balling phenomenon or discontinuous melt tracks. These voids caused a reduction in the coefficient of thermal expansion and an increase in the magnetic dipole moment. By increasing the laser energy, the amount of voids decreases, and consequently the coefficient of thermal expansion increases along with a reduction in the magnetic dipole moment.
3. Vaporization and microsegregation of some alloying elements is expected when using laser energy densities higher than E_C . This vaporization caused a reduction in the manganese, chromium, and nickel concentrations accompanied with increased concentrations of molybdenum, silicon, and iron. Since silicon and molybdenum have very low thermal expansion, a reduction in the coefficient of thermal expansion of the SLM parts was measured.

It is concluded that any combination of process parameters that can generate the critical energy density would provide a stable melting. The effect of this critical energy density on other influencing factors (i.e. residual stress and mechanical strength) is considered for future work.

5.6 References

- [1] Corbacho, J. L., Suárez, J. C., and Molleda, F., "Welding of invar Fe-36Ni alloy for tooling of composite materials," *Welding International*, vol. 12, no. 12, pp. 966-971, 1998.
- [2] Pentair, "The benefits of stainless steel," Pentair, Hoffman and Design 2015.
- [3] Yakout, M., Cadamuro, A., Elbestawi, M. A., and Veldhuis, S. C., "The selection of process parameters in additive manufacturing for aerospace alloys," *The International Journal of Advanced Manufacturing Technology*, vol. 92, no. 5-8, pp. 2081-2098, 2017.
- [4] Harrison, N. J., Todd, I., and Mumtaz, K., "Thermal expansion coefficients in Invar processed by selective laser melting," *Journal of Materials Science*, journal article vol. 52, no. 17, pp. 10517-10525, 2017.
- [5] Qiu, C., Adkins, N. J. E., and Attallah, M. M., "Selective laser melting of Invar 36: Microstructure and properties," *Acta Materialia*, vol. 103, pp. 382-395, 2016.
- [6] Strauss, J. T. and Stucky, M. J., "Laser additive manufacturing processing of a mixture of iron and nickel powders," in *The 27th Annual International Solid Freeform Fabrication Symposium*, 2016.
- [7] Yakout, M., Elbestawi, M. A., and Veldhuis, S. C., "On the characterization of stainless steel 316L parts produced by selective laser melting," *The International Journal of Advanced Manufacturing Technology*, vol. 95, no. 5-8, pp. 1953-1974, 2018.
- [8] Hidalgo, J., Jiménez-Morales, A., Barriere, T., Gelin, J. C., and Torralba, J. M., "Mechanical and functional properties of Invar alloy for μ -MIM," *Powder Metallurgy*, vol. 57, no. 2, pp. 127-136, 2014.
- [9] Kaladhar, M., Subbaiah, K. V., and Rao, C. H. S., "Machining of austenitic stainless steels – a review," *International Journal of Machining and Machinability of Materials*, vol. 12, no. 1-2, pp. 178-192, 2012.
- [10] Kim, S.-H., Choi, S.-G., Choi, W.-K., and Lee, E.-S., "Surface Characteristics of Invar alloy according to micro-pulse electrochemical machining," *Materials and Technology*, vol. 51, pp. 745–749, 2017.
- [11] Smith, R. J., Lewi, G. J., and Yates, D. H., "Development and Application of Nickel Alloys in Aerospace Engineering," *Aircraft Engineering and Aerospace Technology*, vol. 73, no. 2, pp. 138-147, 2001.
- [12] Jasthi, B. K., Arbegast, W. J., and Howard, S. M., "Thermal expansion coefficient and mechanical properties of friction stir welded Invar (Fe-36%Ni)," *Journal of Materials Engineering and Performance*, vol. 18, no. 7, pp. 925-934, 2009.

- [13] Zhao, Y., Wu, A., Yao, W., Wang, Z., Sato, Y. S., and Kokawa, H., "Microstructure and Mechanical Properties of Nd:YAG Laser Welded Invar 36 Alloy," *Materials Science Forum*, vol. 675-677, pp. 739-742, 2011.
- [14] Zhao, Y. *et al.*, "Temperature and Force Response Characteristics of Friction Stir Welding on Invar 36 Alloy," *Science and Technology of Welding and Joining*, vol. 18, no. 3, pp. 232-238, 2013.
- [15] Herzog, D., Seyda, V., Wycisk, E., and Emmelmann, C., "Additive manufacturing of metals," *Acta Materialia*, vol. 117, pp. 371-392, 2016.
- [16] Yakout, M., Elbestawi, M. A., and Veldhuis, S. C., "A review of metal additive manufacturing technologies," *Solid State Phenomena*, vol. 278, pp. 1-14, 2018.
- [17] Bartolomeu, F. *et al.*, "316L stainless steel mechanical and tribological behavior—A comparison between selective laser melting, hot pressing and conventional casting," *Additive Manufacturing*, vol. 16, pp. 81-89, 2017.
- [18] Song, B. *et al.*, "Differences in microstructure and properties between selective laser melting and traditional manufacturing for fabrication of metal parts: a review," *Frontiers of Mechanical Engineering*, vol. 10, no. 2, pp. 111-125, 2015.
- [19] Thijs, L., Verhaeghe, F., Craeghs, T., Humbeeck, J. V., and Kruth, J.-P., "A Study of the Microstructural Evolution during Selective Laser Melting of Ti-6Al-4V," *Acta Materialia*, vol. 58, pp. 3303-3312, 2010.
- [20] Cherry, J. A., Davies, H. M., Mehmood, S., Lavery, N. P., Brown, S. G. R., and Sienz, J., "Investigation into the effect of process parameters on microstructural and physical properties of 316L stainless steel parts by selective laser melting," *The International Journal of Advanced Manufacturing Technology*, journal article vol. 76, no. 5, pp. 869-879, 2015.
- [21] DebRoy, T. *et al.*, "Additive manufacturing of metallic components – Process, structure and properties," *Progress in Materials Science*, vol. 92, pp. 112-224, 2018.
- [22] Saedi, S., Shayesteh Moghaddam, N., Amerinatanzi, A., Elahinia, M., and Karaca, H. E., "On the effects of selective laser melting process parameters on microstructure and thermomechanical response of Ni-rich NiTi," *Acta Materialia*, vol. 144, pp. 552-560, 2018.
- [23] Dilip, J. J. S., Ram, G. D. J., Starr, T. L., and Stucker, B., "Selective laser melting of HY100 steel: Process parameters, microstructure and mechanical properties," *Additive Manufacturing*, vol. 13, pp. 49-60, 2017.
- [24] Yakout, M. and Elbestawi, M., "Additive manufacturing of composite materials: an overview," in *The 6th International Conference on Virtual Machining Process Technology (VMPT)*, Montréal, Canada, 2017.

- [25] Yakout, M., Elbestawi, M. A., and Veldhuis, S. C., "Process-Structure-Property relationship for selective laser melting of aerospace alloys," in *The 7th International Conference on Virtual Machining Process Technology (VMPT)*, Hamilton, Canada, 2018.
- [26] Spierings, A. B., Herres, N., and Levy, G., "Influence of the particle size distribution on surface quality and mechanical properties in additive manufactured stainless steel parts," in *The 21st Annual International Solid Freeform Fabrication Symposium*, Austin, Texas, USA, 2010, pp. 397-406: University of Texas in Austin.
- [27] Spierings, A. B. and Levy, G., "Comparison of density of stainless steel 316L parts produced with selective laser melting using different powder grades," in *The 20th Annual International Solid Freeform Fabrication Symposium*, Austin, Texas, USA, 2009, pp. 342-353: University of Texas in Austin.
- [28] Sun, Z., Tan, X., Tor, S. B., and Yeong, W. Y., "Selective laser melting of stainless steel 316L with low porosity and high build rates," *Materials and Design*, vol. 104, pp. 197-204, 2016.
- [29] Miranda, G. *et al.*, "Predictive models for physical and mechanical properties of 316L stainless steel produced by selective laser melting," *Materials Science and Engineering: A*, vol. 657, pp. 43-56, 2016.
- [30] Kruth, J. P., Froyen, L., Vaerenbergh, J. V., Mercelis, P., Rombouts, M., and Lauwers, B., "Selective laser melting of iron-based powder," *Journal of Materials Processing Technology* vol. 149, pp. 616-622, 2004.
- [31] DEWIDAR, M. M., KHALIL, K. A., and LIM, J. K., "Processing and mechanical properties of porous 316L stainless steel for biomedical applications " *Transactions of Nonferrous Metals Society of China* vol. 17, pp. 468-473, 2007.
- [32] Casati, R., Lemke, J., and Vedani, M., "Microstructure and fracture behavior of 316L austenitic stainless steel produced by selective laser melting," *Journal of Materials Science & Technology*, vol. 32, pp. 738-744, 2016.
- [33] Fitzgerald, E. and Everhart, W., "The effect of location on the structure and mechanical properties of selective laser melted 316L stainless steel," in *The 27th Annual International Solid Freeform Fabrication Symposium*, Texas, USA, 2016.
- [34] Zhang, Y., Liu, F., Chen, J., and Yuan, Y., "Effects of surface quality on corrosion resistance of 316L stainless steel parts manufactured via SLM," *Journal of Laser Applications*, vol. 29, no. 2, pp. 022306 (1-2), 2017.
- [35] Kamath, C., El-dasher, B., Gallegos, G. F., King, W. E., and Sisto, A., "Density of additively-manufactured, 316L SS parts using laser powder-bed fusion at powers up to 400 W," *The International Journal of Advanced Manufacturing Technology*, vol. 74, pp. 65-78, 2014.

- [36] Li, R., Liu, J., Shi, Y., Wang, L., and Jiang, W., "Balling behavior of stainless steel and nickel powder during selective laser melting process," *The International Journal of Advanced Manufacturing Technology*, vol. 59, pp. 1025-1035, 2012.
- [37] Kruth, J. P., Deckers, J., Yasa, E., and Wauthle, R., "Assessing influencing factors of residual stresses in selective laser melting using a novel analysis method," in *The 16th International Symposium on Electromachining (ISEM XVI)*, Shanghai, China, 2010.
- [38] Yasa, E., Craeghs, T., Badrossamay, M., and Kruth, J.-P., "Rapid manufacturing research at the catholic university of leuven," presented at the US Turkey Workshop on Rapid Technologies, Istanbul, Turkey, 2009.
- [39] Yusuf, S. M., Chen, Y., Boardman, R., Yang, S., and Gao, N., "Investigation on porosity and microhardness of 316L stainless steel fabricated by selective laser melting," *Metals*, vol. 7, pp. 64 (1-12), 2017.
- [40] Liu, B., Wildman, R., Tuck, C., Ashcroft, I., and Hague, R., "Investigation the effect of particle size distribution on processing parameters optimisation in selective laser melting process," in *The 22nd Annual International Solid Freeform Fabrication Symposium*, Texas, USA, 2011.
- [41] Kruth, J., Badrossamay, M., Yasa, E., Deckers, J., Thijs, L., and Humbeeck, J. V., "Part and material properties in selective laser melting of metals," in *The 16th International Symposium on Electromachining (ISEM XVI)*, Shanghai, China, 2010.
- [42] Dadbakhsh, S., Hao, L., and Sewell, N., "Effect of selective laser melting layout on the quality of stainless steel parts," *Rapid Prototyping Journal*, vol. 18, pp. 241-249, 2012.
- [43] Kurzynowski, T., Gruber, K., Stopyra, W., Kuźnicka, B., and Chlebus, E., "Correlation between process parameters, microstructure and properties of 316 L stainless steel processed by selective laser melting," *Materials Science and Engineering: A*, vol. 718, pp. 64-73, 2018.
- [44] Yadroitsev, I. and Smurov, I., "Selective laser melting technology: from the single laser melted track stability to 3d parts of complex shape," *Physics Procedia*, vol. 5, pp. 551-560, 2010.
- [45] Yasa, E., Deckers, J., Kruth, J.-P., Rombouts, M., and Luyten, J., "Investigation of sectoral scanning in selective laser melting " in *ASME 2010 10th Biennial Conference on Engineering Systems Design and Analysis*, Istanbul, Turkey, 2010, vol. 4, pp. 695-703.
- [46] Yasa, E., "Manufacturing by combining selective laser melting and selective laser erosion/laser re-melting," PhD Department of Mechanical Engineering, Katholieke Universiteit Leuven, Leuven, 2011.
- [47] Liverani, E., Toschi, S., Ceschini, L., and Fortunato, A., "Effect of selective laser melting (SLM) process parameters on microstructure and mechanical properties of

- 316L austenitic stainless steel," *Journal of Materials Processing Technology*, vol. 249, pp. 255-263, 2017.
- [48] Saeidi, K., "Stainless steels fabricated by laser melting, Scaled-down structural hierarchies and microstructural heterogeneities," PhD Department of Materials and Environmental Chemistry, Stockholm University, Stockholm, Sweden, 2016.
- [49] Liu, Y., Yang, Y., and Wang, D., "A study on the residual stress during selective laser melting (SLM) of metallic powder," *The International Journal of Advanced Manufacturing Technology*, vol. 87, pp. 647-656, 2016.
- [50] Yadroitsev, I. and Yadroitsava, I., "Evaluation of residual stress in stainless steel 316L and Ti6Al4V samples produced by selective laser melting," *Virtual and Physical Prototyping*, vol. 10, no. 2, pp. 67-76, 2015.
- [51] Yadroitsava, I. and Yadroitsev, I., "Evaluation of residual stress in selective laser melting of 316L steel," in *The 1st International Conference on Progress in Additive Manufacturing*, Singapore, 2014.
- [52] Shifeng, W., Shuai, L., Qingsong, W., Yan, C., Sheng, Z., and Yusheng, S., "Effect of molten pool boundaries on the mechanical properties of selective laser melting parts," *Journal of Materials Processing Technology*, vol. 214, pp. 2660-2667, 2014.
- [53] *Standard guide for characterizing properties of metal powders used for additive manufacturing processes*, 2014.
- [54] *Standard Test Method for Particle Size Distribution of Metal Powders and Related Compounds by Light Scattering*, 2017.
- [55] *Standard test method for linear thermal expansion of solid materials by thermomechanical analysis*, 2014.
- [56] James, J. D., Spittle, J. A., Brown, S. G. R., and Evans, R. W., "A review of measurement techniques for the thermal expansion coefficient of metals and alloys at elevated temperatures," *Measurement Science and Technology*, vol. 12, no. 3, p. R1, 2001.
- [57] *Standard specification for thermostat component alloys*, 2013.
- [58] Seede, R., Mostafa, A., Brailovski, V., Jahazi, M., and Medraj, M., "Microstructural and microhardness evolution from homogenization and hot isostatic pressing on selective laser melted Inconel 718: structure, texture, and phases," *Journal of Manufacturing and Materials Processing*, vol. 2, no. 2, p. 30, 2018.
- [59] Jia'an, W., Jiahe, W., and Zhongxiao, S., "Microstructures and microsegregation of directionally solidified Mg-1.5Gd magnesium alloy with different growth rates," *Rare Metal Materials and Engineering*, vol. 46, no. 1, pp. 12-16, 2017.

- [60] Amato, K. N. *et al.*, "Microstructures and mechanical behavior of Inconel 718 fabricated by selective laser melting," *Acta Materialia*, vol. 60, no. 5, pp. 2229-2239, 2012.
- [61] Savage, W. F. and Krantz, B. M., "Microsegregation in autogenous hastelloy X welds," *Welding Journal*, vol. 50, no. 7, pp. 292-303, 1971.
- [62] Inoue, M. and Hirasawa, I., "The relationship between crystal morphology and XRD peak intensity on CaSO₄·2H₂O," *Journal of Crystal Growth*, vol. 380, pp. 169-175, 2013.
- [63] Yao, W. J., Bao, G. H., Niu, X. L., Wang, N., and Lee, J. H., "Growth characteristics of TiC_xN_y ceramics under laser melting conditions," *Materials and Manufacturing Processes*, vol. 29, no. 6, pp. 715-720, 2014.
- [64] Kenel, C. *et al.*, "In situ investigation of phase transformations in Ti-6Al-4V under additive manufacturing conditions combining laser melting and high-speed micro-X-ray diffraction," *Scientific Reports*, vol. 7, no. 1, p. 16358, 2017.
- [65] Coupard, D., Palin-luc, T., Bristiel, P., Ji, V., and Dumas, C., "Residual stresses in surface induction hardening of steels: Comparison between experiment and simulation," *Materials Science and Engineering: A*, vol. 487, no. 1, pp. 328-339, 2008.
- [66] Arisoy, Y. M., Criales, L. E., Özel, T., Lane, B., Moylan, S., and Donmez, A., "Influence of scan strategy and process parameters on microstructure and its optimization in additively manufactured nickel alloy 625 via laser powder bed fusion," *The International Journal of Advanced Manufacturing Technology*, journal article vol. 90, no. 5, pp. 1393-1417, 2017.
- [67] Simson, T., Emmel, A., Dwars, A., and Böhm, J., "Residual stress measurements on AISI 316L samples manufactured by selective laser melting," *Additive Manufacturing*, vol. 17, pp. 183-189, 2017.
- [68] Yakout, M., Elbestawi, M. A., and Veldhuis, S. C., "Density and mechanical properties in selective laser melting of Invar 36 and stainless steel 316L," *Manuscript submitted for publication*, 2018.
- [69] van Schilfgaarde, M., Abrikosov, I. A., and Johansson, B., "Origin of the Invar effect in iron–nickel alloys," *Nature*, vol. 400, p. 46, 1999.
- [70] Al-Dabbagh, J. B., Al-Faluji, I. K., and Hashim, Y. B., "Negative Thermal Expansion in Ferromagnetic Fe-Ni Invar Alloys," in *Proceedings of ICSSST2010: 3rd International Conference on Solid State Science & Technology*, Kuching, Sarawak, Malaysia, 2010.
- [71] Witherspoon, C., Zheng, P., Chmielus, M., Dunand, D. C., and Müllner, P., "Effect of porosity on the magneto-mechanical behavior of polycrystalline magnetic shape-memory Ni–Mn–Ga foams," *Acta Materialia*, vol. 92, pp. 64-71, 2015.

- [72] Zhang, X. X., Witherspoon, C., Müllner, P., and Dunand, D. C., "Effect of pore architecture on magnetic-field-induced strain in polycrystalline Ni–Mn–Ga," *Acta Materialia*, vol. 59, no. 5, pp. 2229-2239, 2011.
- [73] Brink, B. K., Ståhl, K., Christiansen, T. L., Frandsen, C., Hansen, M. F., and Somers, M. A. J., "Composition-dependent variation of magnetic properties and interstitial ordering in homogeneous expanded austenite," *Acta Materialia*, vol. 106, pp. 32-39, 2016.
- [74] Özöğüt, U. C. and Çakır, A., "Investigation of temperature dependent magnetization and elastic modulus in Si-doped Fe₆₅Ni₃₅ invar alloys," *Journal of Alloys and Compounds*, vol. 705, pp. 126-130, 2017.
- [75] Liu, D., Wu, C., Yan, M., and Wang, J., "Correlating the microstructure, growth mechanism and magnetic properties of FeSiAl soft magnetic composites fabricated via HNO₃ oxidation," *Acta Materialia*, vol. 146, pp. 294-303, 2018.
- [76] Gebhardt, T. *et al.*, "Influence of chemical composition and magnetic effects on the elastic properties of fcc Fe–Mn alloys," *Acta Materialia*, vol. 59, no. 4, pp. 1493-1501, 2011.
- [77] Garibaldi, M., Ashcroft, I., Simonelli, M., and Hague, R., "Metallurgy of high-silicon steel parts produced using Selective Laser Melting," *Acta Materialia*, vol. 110, pp. 207-216, 2016.
- [78] Podgornykh, S. M., Kazantsev, V. A. J. T. P. o. M., and Metallography, "Relationship between the heat capacity, thermal expansion coefficient, and spontaneous magnetization in the invarlike compound YFe₁₀Mo₂," journal article vol. 109, no. 3, pp. 247-254, March 01 2010.
- [79] Anwar, A. B. and Pham, Q.-C., "Study of the spatter distribution on the powder bed during selective laser melting," *Additive Manufacturing*, vol. 22, pp. 86-97, 2018.
- [80] Taheri Andani, M., Dehghani, R., Karamooz-Ravari, M. R., Mirzaeifar, R., and Ni, J., "A study on the effect of energy input on spatter particles creation during selective laser melting process," *Additive Manufacturing*, vol. 20, pp. 33-43, 2018.
- [81] Ho, I. T., Chen, Y.-T., Yeh, A.-C., Chen, C.-P., and Jen, K.-K., "Microstructure evolution induced by inoculants during the selective laser melting of IN718," *Additive Manufacturing*, vol. 21, pp. 465-471, 2018.
- [82] Shiomi, M., Osakada, K., Nakamura, K., Yamashita, T., and Abe, F., "Residual stress within metallic model made by selective laser melting process," *CIRP Annals - Manufacturing Technology*, vol. 53, no. 1, pp. 195-198, 2004.
- [83] Mercelis, P. and Kruth, J.-P., "Residual stresses in selective laser sintering and selective laser melting," *Rapid Prototyping Journal*, vol. 12, no. 5, pp. 254-265, 2006.

- [84] Casavola, C., Campanelli, S. L., and Pappalettere, C., "Experimental analysis of residual stresses in the selective laser melting process," in *Proceedings of the XIth International Congress and Exposition*, Orlando, Florida USA, 2008: Society for Experimental Mechanics Inc.
- [85] Belle, L. V., Boyer, J.-C., and Vansteenkiste, G., "Investigation of residual stresses induced during the selective laser melting process," *Key Engineering Materials*, vol. 554-557, pp. 1828-1834, 2013.
- [86] Mishurova, T. *et al.*, "An assessment of subsurface residual stress analysis in SLM Ti-6Al-4V," *Materials*, vol. 10, no. 4, pp. 348 (1-14), 2017.
- [87] Vrancken, B., "Study of residual stresses in selective laser melting," PhD Degree, Faculty of Engineering Science, KU Leuven, Belgium, 2016.
- [88] Gu, D., Shi, Q., Lin, K., and Xi, L., "Microstructure and performance evolution and underlying thermal mechanisms of Ni-based parts fabricated by selective laser melting," *Additive Manufacturing*, vol. 22, pp. 265-278, 2018.
- [89] Peng, T. and Chen, C., "Influence of energy density on energy demand and porosity of 316L stainless steel fabricated by selective laser melting," *International Journal of Precision Engineering and Manufacturing-Green Technology*, journal article vol. 5, no. 1, pp. 55-62, 2018.
- [90] H., M. and Ch., H., "Experimental studies on selective laser melting of metallic parts," *Materialwissenschaft und Werkstofftechnik*, vol. 39, no. 9, pp. 665-670, 2008.
- [91] Qiu, C., Panwisawas, C., Ward, M., Basoalto, H. C., Brooks, J. W., and Attallah, M. M., "On the role of melt flow into the surface structure and porosity development during selective laser melting," *Acta Materialia*, vol. 96, pp. 72-79, 2015.
- [92] Matthews, M. J., Guss, G., Khairallah, S. A., Rubenchik, A. M., Depond, P. J., and King, W. E., "Denudation of metal powder layers in laser powder bed fusion processes," *Acta Materialia*, vol. 114, pp. 33-42, 2016.
- [93] Khairallah, S. A., Anderson, A. T., Rubenchik, A., and King, W. E., "Laser powder-bed fusion additive manufacturing: Physics of complex melt flow and formation mechanisms of pores, spatter, and denudation zones," *Acta Materialia*, vol. 108, pp. 36-45, 2016.
- [94] Xia, M., Gu, D., Yu, G., Dai, D., Chen, H., and Shi, Q., "Porosity evolution and its thermodynamic mechanism of randomly packed powder-bed during selective laser melting of Inconel 718 alloy," *International Journal of Machine Tools and Manufacture*, vol. 116, pp. 96-106, 2017.
- [95] Panwisawas, C. *et al.*, "Mesoscale modelling of selective laser melting: Thermal fluid dynamics and microstructural evolution," *Computational Materials Science*, vol. 126, pp. 479-490, 2017.

- [96] Rumble, J. R., *CRC handbook of chemistry and physics*, 99th ed. CRC Press, 2018.
- [97] Totten, G. E., Xie, L., and Funatani, K., *Handbook of Mechanical Alloy Design*. CRC press: Taylor & Francis, 2003.
- [98] Fuerschbach, P. W., Norris, J. T., He, X., and DebRoy, T., "Understanding Metal Vaporization from Laser Welding ", Sandia National Laboratories SAND2003-34902003.
- [99] Cverna, F., *ASM Ready Reference: Thermal properties of metals*. ASM International, 2002.
- [100] Ghabezloo, S., "Effect of porosity on the thermal expansion coefficient: A discussion of the paper 'Effects of mineral admixtures on the thermal expansion properties of hardened cement paste' by Z.H. Shui, R. Zhang, W. Chen, D. Xuan, *Constr. Build. Mater.* 24 (9) (2010) 1761–1767," *Construction and Building Materials*, vol. 24, no. 9, pp. 1796-1798, 2010.
- [101] Ghabezloo, S., "Micromechanical analysis of the effect of porosity on the thermal expansion coefficient of heterogeneous porous materials," *International Journal of Rock Mechanics and Mining Sciences*, p. 97, 2012.

Chapter 6

Thermal Expansion and Residual Stresses During Selective Laser Melting of Ti-6Al-4V

Complete Citation:

Yakout, M., Elbestawi, M.A., Veldhuis, S.C. A study of the relationship between thermal expansion and residual stresses in selective laser melting of Ti-6Al-4V. *Submitted for publication*, 2018.

Copyright:

© The Authors.

Relative Contributions:

M. Yakout: Performed experiments, analysis, and data interpretation. Wrote the first draft of the manuscript. Helped with submitting the final manuscript to the journal (first and corresponding author).

M. A. Elbestawi: Co-supervisor of M. Yakout. Revised the manuscript. Was responsible of submitting the final manuscript to the journal (corresponding author).

S. C. Veldhuis: Co-supervisor of M. Yakout. Revised the manuscript.

Abstract:

Selective laser melting of Ti-6Al-4V is associated with residual stress generation, thermal expansion, and metallurgical changes due to high heating and cooling rates. These manufacturing flaws affect the microstructure and mechanical properties of the parts produced. In this work, process mapping is presented for producing Ti-6Al-4V using the selective laser melting process. Combinations of process parameters that lead to stable melting are statistically identified. These process maps represent the density, coefficient of thermal expansion, and deflection of parts produced in terms of laser process parameters. As a result, an optimum process window to minimize manufacturing flaws and provide stable melting is presented. The effect of selective laser melting process parameters on the coefficient of thermal expansion of the as-deposited Ti-6Al-4V parts is investigated. A critical laser energy density of 86.8 J/mm^3 , E_C , is introduced based on the stability of the melting process. Stable melting of Ti-6Al-4V occurs at any combination of process parameters that generates laser energy density at E_C . This stable melting provides homogeneous microstructure, high density of 99.9%, and a thermal expansion coefficient in line with that of the wrought material. The induced residual stresses and part deflections at the optimal conditions are studied. Above E_C , high tensile residual stresses are observed due to variations in the coefficient of thermal expansion, temperature differential, and material composition. Lack of fusion and void formation occur below E_C .

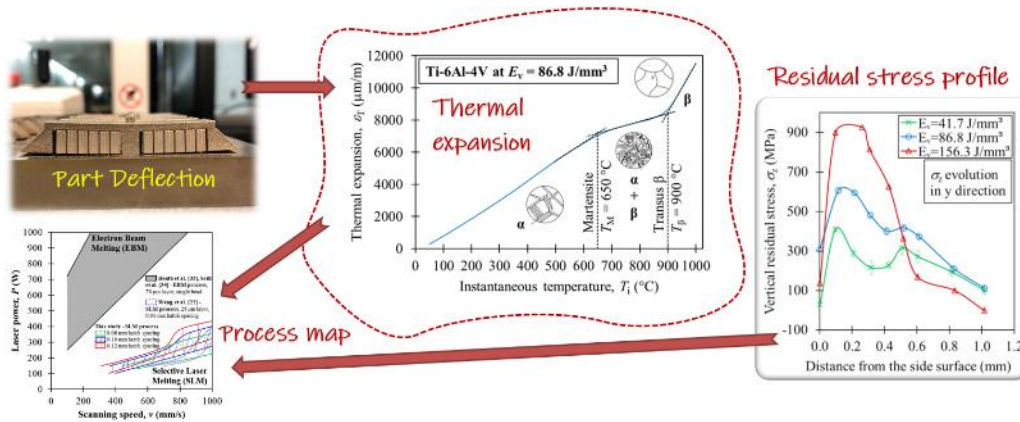
Keywords:

Selective laser melting; Ti-6Al-4V; Stable melting; Metallurgical changes; Thermal expansion.

Highlights:

- Stress risers in selective laser melting of Ti-6Al-4V.
- Coefficient of thermal expansion of additive manufacturing parts is important.
- Density, part deflection, thermal expansion, residual stresses were characterized.
- Optimum process maps for Ti-6Al-4V were determined based on stable melting.
- Critical laser energy density, E_c , for Ti-6Al-4V.

Graphical Abstract:



Acknowledgments:

This work was supported by the Natural Sciences and Engineering Research Council of Canada (NSERC), Grant: RGPIN-2016-06268. The authors also thank Marta Aniolek, Manufacturing Technologist at CanmetMATERIALS, Natural Resources Canada in Hamilton, Ontario, Canada for her assistance during the thermal expansion measurements.

6.1 Introduction

Ti-6Al-4V (UNS R56400) is commonly used in several applications in the aerospace, automotive, and biomedical industries due to its high strength-to-weight ratio, outstanding corrosion resistance, and excellent mechanical properties [1]. Often the shapes of components in these industries are complex and thus selective laser melting (SLM) can be implemented to manufacture these complex shapes using Ti-6Al-4V. Several studies are available in the open literature for SLM of Ti-6Al-4V [2-17]. Most of these studies focused on the metallurgical issues associated with SLM of Ti-6Al-4V and post processing of Ti-6Al-4V parts. Consequently, several recommended SLM process parameters have been reported in the literature for Ti-6Al-4V including, but not limited to, the process parameters illustrated in Table 6.1.

Table 6.1: Process parameters reported in the literature for selective laser melting of Ti-6Al-4V.

Reference	Laser power, P (W)	Scanning speed, v (mm/s)	Layer thickness, t (mm)	Hatch spacing, h (mm)	Laser energy density, E_v (J/mm ³)
[5]	40-160	360-1200	0.030	0.100	11-148
[4]	175-375	686-1029	0.030-0.090	0.120-0.180	34-68
[2]	75	150-1000	0.025	0.077	39-260
[6]	400	40-100	0.200	0.500	40-100
[7]	150	1200	0.030	0.100	42
[8]	117-170	225-1250	0.030	0.100-0.180	45-96
[9]	175	200-1100	0.030	0.100	53-292
[12]	110	200	0.050	0.100	110
[13]	200	227	0.050	0.100	176
[17]	175	600	0.03	0.04	243

The SLM process is associated with void formation, crack initiation, microsegregation, residual stresses, changes in the material composition, delamination, and phase transformation. These manufacturing flaws lead to degradations in the mechanical properties and fatigue performance of the parts produced [18-25]. Song et al. [12] studied the effect of the scanning speed on the density and microhardness of Ti-6Al-4V parts.

Kasperovich et al. [9] studied the influence of the processing parameters, particularly the laser energy density, on the porosity distribution in the parts produced. Some studies were reported in the open literature for characterizing the morphology, metallurgical issues, and phase transformations associated with SLM of Ti-6Al-4V [6, 17, 22, 26, 27]. These studies aimed at improving the performance and mechanical properties of Ti-6Al-4V parts using post-processing methods. In addition, residual stresses induced in Ti-6Al-4V parts produced via SLM are reported in the literature [7, 16, 28].

The coefficient of thermal expansion (CTE) is an important thermal property of the material that affects the generation of tensile residual stresses in laser-based manufacturing processes [29, 30]. Induced thermal stresses depend on the CTE and the temperature differential in the material as described in Equation (6.1). A material with low CTE will likely generate low thermal stresses, and consequently, low residual stresses during the SLM process [29, 31]. Since the wrought Ti-6Al-4V has a high CTE ($8.6 \mu\text{m}/\text{m}\cdot^\circ\text{C}$), high residual stresses are likely generated during the SLM process. Ali et al. [16] studied the development of residual stresses in SLM of Ti-6Al-4V by numerical simulations and the influence of various process parameters on the induced residual stresses. They found that the laser process variables affect the induced residual stresses. The open literature lacks information on the influence of the SLM process parameters on the CTE of Ti-6Al-4V. Since any variation in the thermal expansion of the parts produced could affect the resulting residual stresses [32], this paper contributes to the understanding of the relationship between the CTE and residual stresses development in SLM of Ti-6Al-4V. Test coupons were produced at various process parameters based on full factorial design of experiments (DOE). The density, thermal expansion, residual stresses, and microstructure were measured. Statistical analysis was used to optimize the SLM

process parameters for Ti-6Al-4V and provide process maps for stable melting, homogeneous microstructure, and fewer manufacturing flaws. The process maps were compared with those obtained by Wang et al. [22] for ductility and density of parts produced using SLM process, as well as those obtained by Beuth et al. [33] and Seifi et al. [34] for density and melt pool physics of parts produced using electron beam melting (EBM) process. Compared to the SLM process, the EBM process uses a beam of high electrons power (e.g., 3000 W) [35]. In the current study, the relationship between the microstructure, thermal expansion, residual stresses, and density of the parts produced at several combinations of SLM process parameters was investigated.

$$\sigma_T = \alpha E (T - T_{ref}) \quad (6.1)$$

where σ_T is thermal stress in (MPa), α is coefficient of thermal expansion at temperature T in (m/m.°C), E is modulus of elasticity in (MPa), and T_{ref} is reference temperature in (°C).

6.2 Experimental work

6.2.1 Feedstock, test samples, and methods

The feedstock material was Ti-6Al-4V Grade 23 powder in the size range of 15-45 μm supplied by Renishaw Canada. The powder morphology was inspected via scanning electron microscopy (SEM) in which no morphological deteriorations were observed as shown in Figure 6.1. In this study, laser power, P , average scanning speed, v , and hatch spacing, h were considered process variables as listed in Table 6.2. The scanning speed, v , was varied by varying the exposure time, θ , in Equation (6.2). The point distance, d , and time delay, θ_d , were maintained constant at 60 μm and 10 μs , respectively. The volumetric laser energy density, E_v in (J/mm^3), was calculated using Equation (6.2).

$$E_v = \frac{P}{v \times h \times t}, \text{ where } v = \frac{1000 \times d}{\theta + \theta_d} \quad (6.2)$$

where v is average scanning speed in (mm/s), d is point distance in (μm), θ is exposure time in (μs), θ_d is time delay between exposures of adjacent points in (μs), P is laser power in (W), h is hatch spacing in (mm), t is layer thickness in (mm), and E_v is volumetric laser energy density in (J/mm^3).

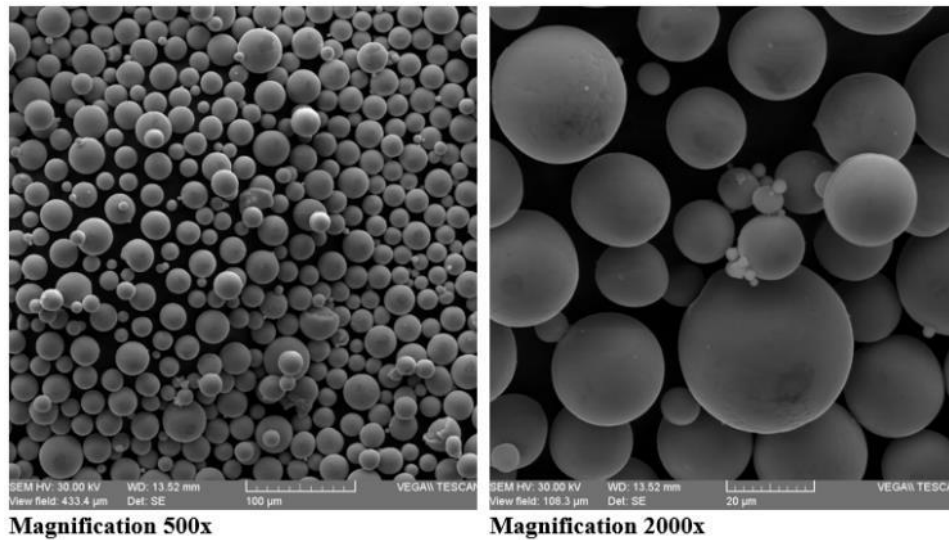


Figure 6.1: Morphology of Ti-6Al-4V Grade 23 powder used in this study.

Table 6.2: Laser process parameters used in this study.

No	P (W)	θ (μs)	v (mm/s)	h (mm)	E_v (J/mm^3)	No	P (W)	θ (μs)	v (mm/s)	h (mm)	E_v (J/mm^3)
1	200	90	600	0.08	104.2 *	16	250	50	1000	0.08	78.1 x
2	200	90	600	0.10	83.3	17	250	50	1000	0.10	62.5 #
3	200	90	600	0.12	69.4	18	250	50	1000	0.12	52.1 +
4	200	65	800	0.08	78.1 x	19	300	90	600	0.08	156.3
5	200	65	800	0.10	62.5 #	20	300	90	600	0.10	125.0
6	200	65	800	0.12	52.1 +	21	300	90	600	0.12	104.2 *
7	200	50	1000	0.08	62.5 #	22	300	65	800	0.08	117.2
8	200	50	1000	0.10	50.0	23	300	65	800	0.10	93.8 &
9	200	50	1000	0.12	41.7	24	300	65	800	0.12	78.1 x
10	250	90	600	0.08	130.2	25	300	50	1000	0.08	93.8 &
11	250	90	600	0.10	104.2 *	26	300	50	1000	0.10	75.0
12	250	90	600	0.12	86.8	27	300	50	1000	0.12	62.5 #
13	250	65	800	0.08	97.7	* x # + & indicate groups that have the same laser energy densities					
14	250	65	800	0.10	78.1 x						
15	250	65	800	0.12	65.1						

The laser energy density has been reported in the literature as a process mapping tool for SLM of various alloys [1, 2, 36-38]. Mahmoudi et al. [39] found that the linear energy density in (J/mm), P/v , is a better design parameter for identifying the material printability and volumetric energy density in (J/mm³) is for studying the transformation behavior of the material. Volumetric laser energy density is an important design tool but not sufficient for optimization [40]. To be used in the optimization process, the volumetric energy density equation, Equation (6.2), has to be modified to include the scanning parameters (e.g., scanning pattern and material properties) [41]. The contouring, up-skin, and down-skin parameters were deactivated in the current study to minimize the effect of the scanning parameters. Bertoli et al. [42] studied the limitation of the volumetric laser energy density and they concluded that it can serve as a broad guideline for parameter selection and to provide useful information on the effects of power, speed, layer thickness, and beam size combinations. However, the volumetric laser energy density does not capture melt pool physics and track morphology. Wang et al. [38] explained the dimensionless volumetric laser energy density, E_v^* , required to melt the powder that include the material properties and the material absorptivity. The dimensionless laser power, P^* , dimensionless scanning speed, v^* , dimensionless layer thickness, t^* , and dimensionless hatch spacing, h^* , were determined using Equation (6.3).

$$E_v^* = \frac{P^*}{v^* \times h^* \times t^*}, \text{ where } P^* = \frac{A \times P}{\varphi \times k \times (T_m - T_o)}, v^* = \frac{v \times \varphi}{D}, h^* = \frac{h}{\varphi}, t^* = \frac{2t}{\varphi} \quad (6.3)$$

where A is surface absorptivity, P is laser power in (W), φ is beam radius in (m), k is thermal conductivity in (W/m.K), T_m is melting temperature in (K), T_o is ambient temperature in (K), v is scanning speed in (m/s), D is material diffusivity in (m²/s), t is layer thickness in (m), and h is hatch spacing in (m).

The layer thickness, t , stripe width, w , stripe overlap, γ , and scanning rotation between subsequent layers were maintained constant at 0.04 mm, 10 mm, 0.08 mm, and 67° , respectively. Each run of experiment was used to produce the test coupons; one cantilever and four cubes as shown in Figure 6.2. Test coupons were manufactured using a Renishaw AM400 machine equipped with a 400 W ytterbium fiber laser and argon gas flow. In the current study, maps of process parameter combinations were determined with more methods than just using the laser energy density as an optimization tool. An optimization map of laser individual process parameters was determined. A parametric study was performed to find an optimum threshold of laser energy density based on the optimization results. These process maps optimize the laser power and scanning speed at each hatch spacing to achieve parts with high density, low thermal expansion, high cantilever height, and small cantilever deflection. The optimization process was based on:

1. Relative density higher than 99%.
2. Thermal expansion lower than $795 \mu\text{m/m}$ at 100°C .
3. Cantilever height more than 10 mm.
4. Cantilever deflection less than 0.48 mm.

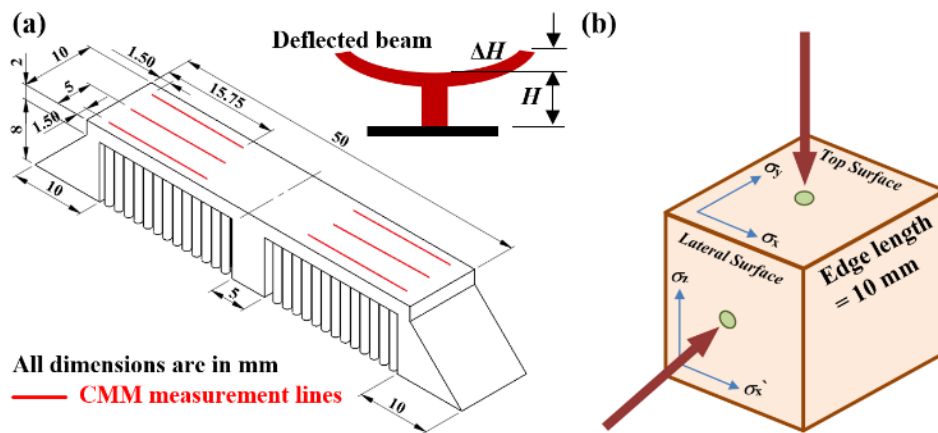


Figure 6.2: Dimensions of test coupons: (a) cantilevers, and (b) cubes.

These optimization criteria can vary by application, however the optimization procedure focused on achieving properties close to the wrought material [43].

6.2.2 Density measurement

The density of the cubes was measured at ambient temperature and pressure using the Archimedes principle [2, 37]. The density of a metal block can be calculated using its weight in air and its apparent weight when immersed in distilled water, as described in Equation (6.4).

$$\rho = \rho_w \times \frac{W_1}{W_1 - W_2}, \rho_r \% = \frac{\rho}{\rho_{bulk}} \%, \Delta\rho = \rho \times \sqrt{\left(\frac{\Delta W_1}{W_1}\right)^2 + \left(\frac{\sqrt{(\Delta W_1)^2 + (\Delta W_2)^2}}{W_1 - W_2}\right)^2} \quad (6.4)$$

where ρ is part density in (g/cm^3), ρ_r is relative density in %, $\Delta\rho$ is density error in (g/cm^3), W_1 is weight in the air in (gram), W_2 is apparent weight in the water in (gram), ρ_w is water density ($1 \text{ g}/\text{cm}^3$), ρ_{bulk} is Ti-6Al-4V bulk density ($4.42 \text{ g}/\text{cm}^3$). The resolution of the scale was $\pm 0.01 \text{ g}$ ($\Delta W_1 = \Delta W_2 = 0.01 \text{ g}$).

6.2.3 Thermal expansion measurement

One cube from each run of experiment was machined to the standard size of the CTE samples (4 mm diameter and 10 mm length) [31, 44, 45] and a BÄHR dilatometer (DIL 805A/D) was used to measure the CTE of each sample. The sample was heated using an induction Cu coil in vacuum atmosphere from room temperature ($T_0 = 21^\circ\text{C}$) to 1000°C with a $0.1^\circ\text{C}/\text{s}$ heating rate and naturally cooled down to room temperature. The change in length (ΔL) was measured by a linear voltage displacement transducer (LVDT) through quartz push rods attached to the sample end and the instantaneous temperature (T_i) was measured by a 0.1 mm diameter S-type Platinum Rhodium thermocouple spot-welded to the sample. The CTE, α in ($10^{-6} \text{ }^\circ\text{C}^{-1}$), and thermal expansion, ε_T in ($\mu\text{m}/\text{m}$), were measured using Equation (6.5).

$$\alpha = \left(\frac{\Delta L}{L_o \times \Delta T} \right) = \left(\frac{\varepsilon_T}{\Delta T} \right), \text{ where } \varepsilon_T = \left(\frac{\Delta L}{L_o} \right) \quad (6.5)$$

where ΔL is change in length in (μm), ΔT is temperature difference over which ΔL is measured in ($^{\circ}\text{C}$), L_o is initial length in (m), and ε_T is thermal expansion in ($\mu\text{m}/\text{m}$).

6.2.4 Part deflection characterization

The wire electrical discharge machining (EDM) was used to cut the supports of the cantilevers from the build plate, leaving the cantilevers attached to the build plate by the middle web. A coordinate measuring machine (CMM) was used to measure the height of 40 measurement locations along the 50 mm length of the top surface of the part, as shown in Figure 6.2a. The height of each measurement location was taken as the average of three measurements along the width of the cantilever to minimize the effect of surface roughness. The cantilever deflection, ΔH in (mm), and minimum height, H in (mm), were recorded.

6.2.5 Residual stress characterization

Based on the density results, the part with the closest density to wrought material was selected for residual stress analysis, in addition to one cube of a lower energy density ($41.7 \text{ J}/\text{mm}^3$) and one cube of a higher energy density ($156.3 \text{ J}/\text{mm}^3$). Depth residual stress profiles were measured at both top and side surfaces using the X-ray diffraction (XRD) method, as shown in Figure 6.2b. The lattice deformation at each depth was obtained using 22 different tilting angles (up to 25°), a Bragg angle of 142° for the crystallographic plane (2 1 3), and a $\text{CuK}\alpha$ (wavelength 1.541838 \AA) radiation source. The top surface measurements represent the profiles of the longitudinal and transverse horizontal residual stresses, σ_x and σ_y , in the vertical (build) direction. The side surface measurements

represent the profiles of the vertical and horizontal residual stresses, σ_z and σ_x , in the horizontal (layer) direction.

6.2.6 Metallurgical analysis

The residual stress samples were mounted in bakelite, polished, and chemically etched for approximately 15-20 seconds. The etchant formula was a solution of 5 ml (6.25%) of hydrogen fluoride (HF), 25 ml (31.25%) of nitric acid (HNO₃), and 50 ml (62.50%) of distilled water (H₂O). The etched sections were examined using an optical microscope (OM).

6.3 Results and analysis

6.3.1 Part density

The density measurements showed that the laser energy density had a strong influence on the relative density of Ti-6Al-4V parts as shown in Figure 6.3. A regression model that examines the influence of three independent variables (P , v , h) on part density (ρ_r) was developed using Minitab software. The model included independent variables (P , v , h), quadratic variables (P^2 , v^2 , h^2), two-way interactions ($P \times v$, $P \times h$, $v \times h$), and three-way interaction ($P \times v \times h$). The insignificant parameters were removed by a stepwise backward elimination of terms with less than 95% confidence interval. The overall significance of the regression model was tested by p-value, F-test, and t-test. Figure 6.4 shows the relationship between the relative density of Ti-6Al-4V and the various interactions between laser process parameters. It was found that parts produced using any combination of process parameters that gives an energy density of 86.8 J/mm³ have the highest part density (99.9%).

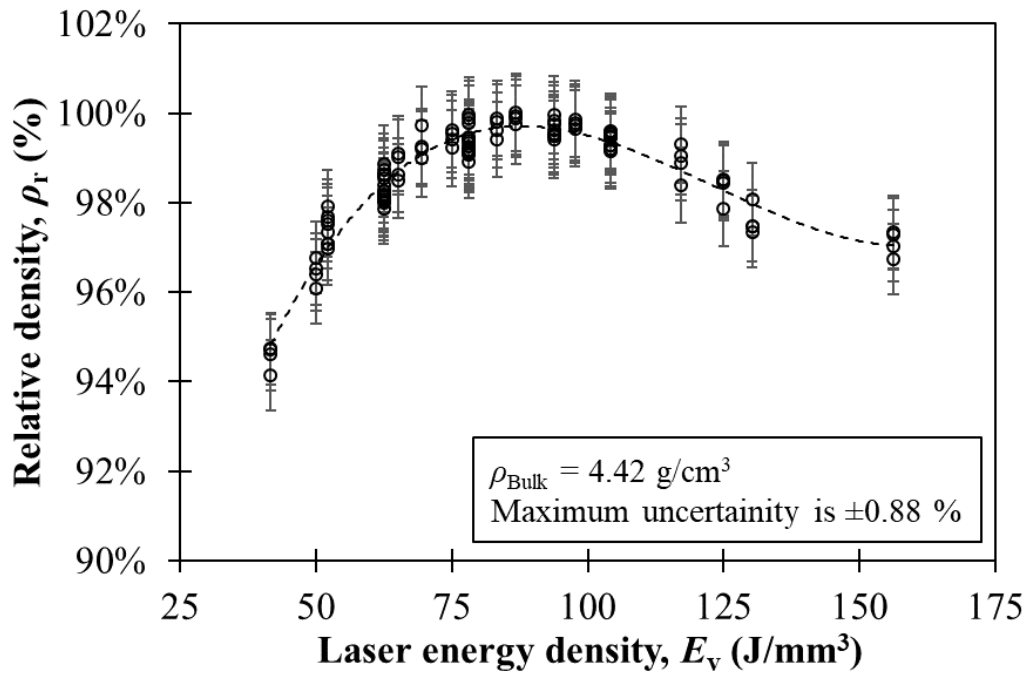


Figure 6.3: Relative density of Ti-6Al-4V as a function of laser energy density.

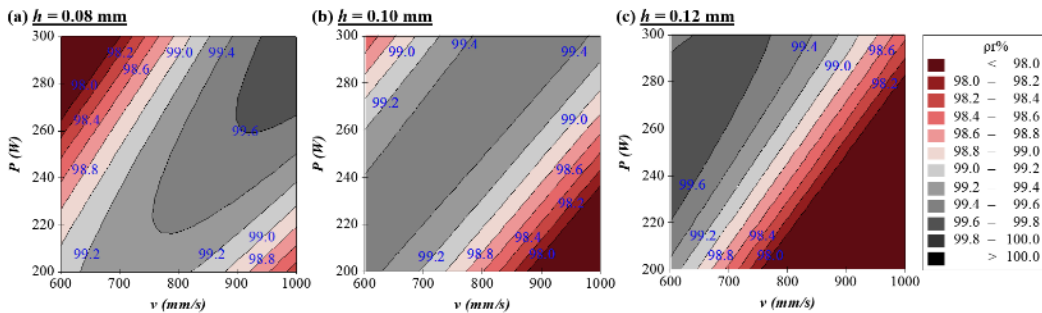


Figure 6.4: Effect of laser power and scanning speed on the relative density of Ti-6Al-4V at hatch spacing of (a) 0.08 mm, (b) 0.10 mm, and (c) 0.12 mm.

6.3.2 Thermal expansion

Thermal expansion and average linear CTE of SLM parts produced at various laser energy densities are shown in Figure 6.5a and b. It was observed that the laser process parameters significantly affect the CTE of the material. Figure 6.6a shows the thermal expansion curve of the part produced at laser energy density of 86.8 J/mm³, as this part showed the highest

bulk density and stable melting. Martensite starts to form at temperature of $T_M = 650$ °C and the alpha phase (α) transforms to the beta phase (β) at temperature of $T_\beta = 900$ °C. After solidification, Ti-6Al-4V forms $\alpha+\beta$ dual-phase, in which the dual phase distribution is affected by the laser processing conditions used during SLM [3]. Consequently, the CTE curve of Ti-6Al-4V parts produced using SLM is affected by the laser processing conditions. Figure 6.5b and Figure 6.6b shows the CTE and thermal expansion curves of three samples produced at laser energy densities of 41.7 J/mm³, 86.8 J/mm³, and 156.3 J/mm³. It was observed that parts produced at laser energy densities below 86.8 J/mm³ exhibited less thermal expansion than those produced at laser energy densities above 86.8 J/mm³. This is likely attributed to void formation at lower laser energy densities [46]. Figure 6.7a and b shows the thermal expansion of SLM parts as a function of laser energy density at 100 °C and 200 °C, respectively. It was observed that increasing the laser energy density caused an increase in the thermal expansion until 86.8 J/mm³, at which point the curve approximately flattened. This peak energy density is defined as the critical laser energy density, $E_C = 86.8$ J/mm³. The critical laser energy density is used to produce parts of high density and thermal expansion in line with that of the wrought material [31]. Below E_C , the parts displayed lower densities and lower thermal expansion due to void formation and crack initiation. Above E_C , the part density was seen to decrease where thermal expansion values levelled off. Phase transformations and keyhole formations are expected above E_C . The critical laser energy density, E_C , was explained by the authors for Invar 36 and stainless steel 316L [31, 37].

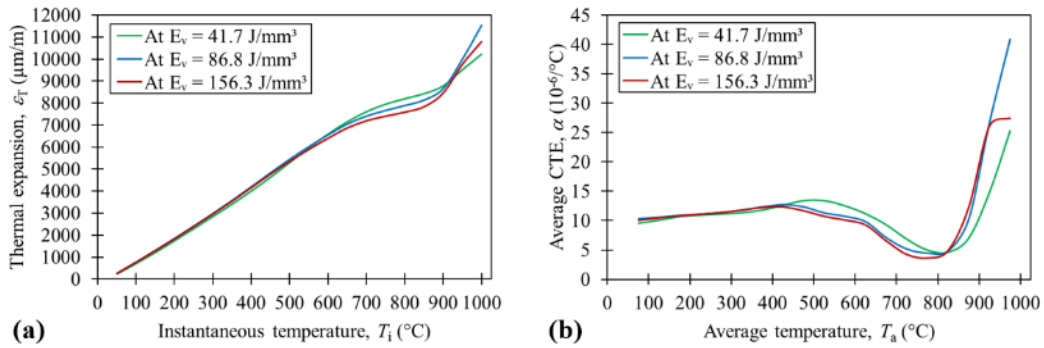


Figure 6.5: (a) Linear thermal expansion, and (b) average coefficient of thermal expansion of Ti-6Al-4V parts manufactured at various laser energy densities.

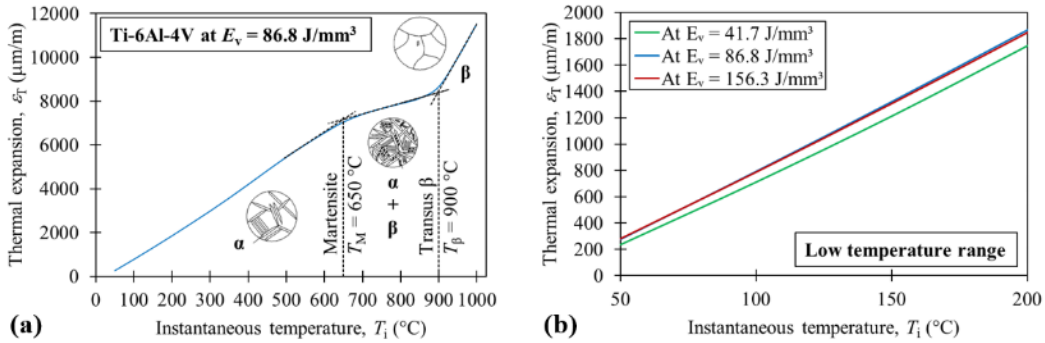


Figure 6.6: Thermal expansion of Ti-6Al-4V samples produced (a) at the critical laser energy density E_C , and (b) at various laser energy densities.

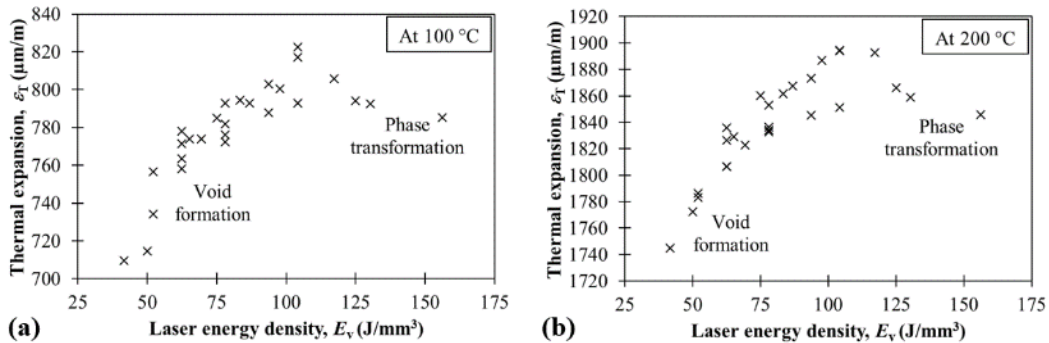


Figure 6.7: Thermal expansion of Ti-6Al-4V samples (a) at 100 $^{\circ}\text{C}$, and (b) at 200 $^{\circ}\text{C}$ as a function of laser energy density.

The statistical model developed for density analysis was used to determine the relationship between thermal expansions at 50 °C, 100 °C, 150 °C, and 200 °C and laser process parameters. The model included independent variables, quadratic and interactions variables, and 3-way interaction. A stepwise backward elimination method was used to eliminate the insignificant terms with less than 95% confidence interval. Contour plots were used to identify the interactions between the process parameters and thermal expansion. Figure 6.8 shows the effects of hatch spacing, scanning speed, and laser power on the part thermal expansion at 100 °C. It was observed that either increasing the laser power or reducing the laser scanning speed led to an increase in the thermal expansion at low temperature (from room temperature to 200 °C), which means that decreasing the laser energy density led to a reduction in the thermal expansion. However, decreasing the laser energy density led also to a reduction in the part density and an increase rate of void formation. Accordingly, an optimum range of process parameters that produce dense parts with low thermal expansion was determined in this study.

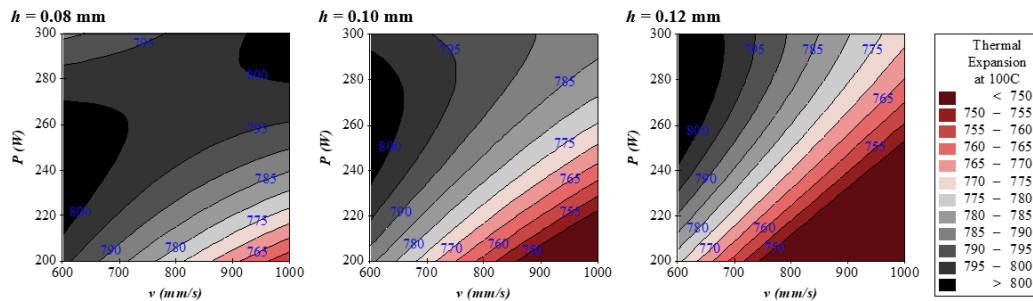


Figure 6.8: Effect of laser power, scanning speed, and hatch spacing on the thermal expansion of Ti-6Al-4V at 100 °C.

6.3.3 Part deflection

The deformation of each cantilever was measured using a CMM. Figure 6.9a shows the measured points along the length of the cantilever and the fitted parabolic curve for the cantilever that was produced at the critical laser energy density. Fitted parabolic curves of cantilevers produced at various laser energy densities are shown in Figure 6.9b. The minimum height and average deflection of each cantilever were extracted from the parabolic curve and plotted against the laser energy density as shown in Figure 6.10. The nominal height of the cantilever was 10 mm. The height of the cantilevers that were manufactured below the critical laser energy density were higher than this nominal height. By increasing the laser energy density, it was found that the height of the cantilever decreased and the cantilever deflection increased. This is likely attributed to the bending deflection that the cantilever exhibited at higher energy densities. The same statistical model developed for density analysis and thermal expansion was used for cantilever deflection and cantilever height. Figure 6.11 and Figure 6.12 show the effect of the laser process parameters on the cantilever height and cantilever deflection, respectively.

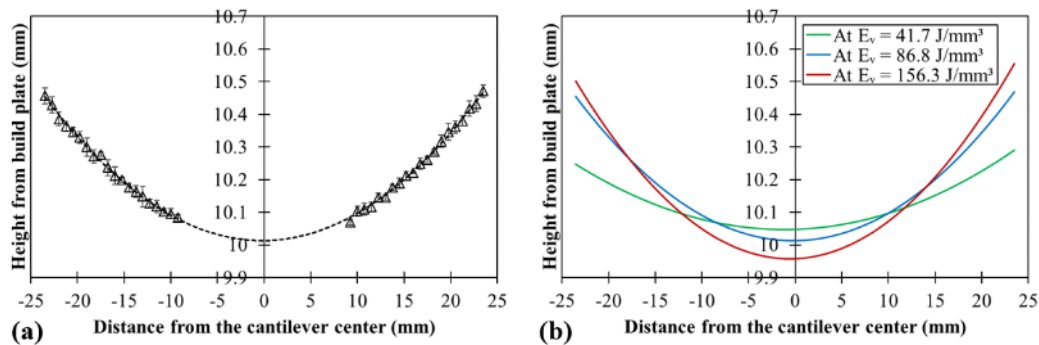


Figure 6.9: Deflection of cantilevers produced (a) at the critical laser energy density, and (b) at various laser energy densities.

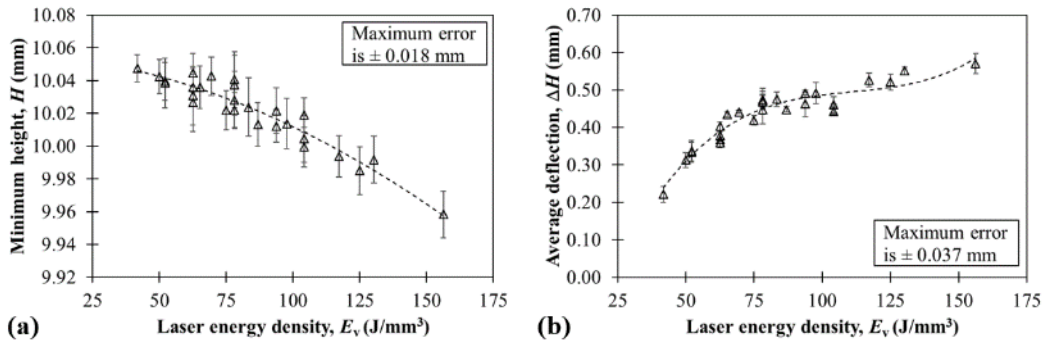


Figure 6.10: (a) Minimum height, and (b) average deflection of cantilevers produced at various laser energy densities.

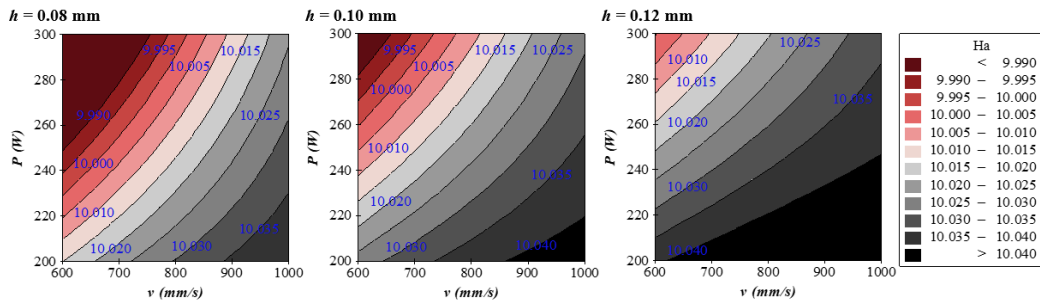


Figure 6.11: Relationship between laser processing parameters and Ti-6Al-4V cantilever height.

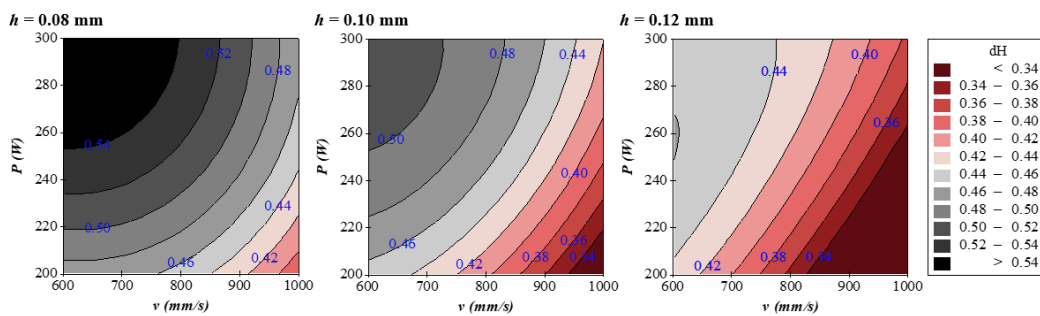


Figure 6.12: Relationship between laser processing parameters and Ti-6Al-4V cantilever deflection.

6.3.4 Residual stress

Most of the observed stresses in the top and lateral surfaces were tensile residual stresses in 1 mm depth. Figure 6.13 shows the longitudinal and transverse horizontal residual stress profiles, σ_x and σ_y , along the vertical (build) direction. These residual stress profiles showed the variation in the horizontal residual stresses in the top 25 layers (layer thickness of 0.04 mm). Figure 6.14 shows the vertical and horizontal residual stress profiles, σ_z and σ_x , along the horizontal (layer) direction. These profiles showed the variation in the horizontal and vertical residual stresses for approximately 8-12 scan tracks in the same layer (hatch spacing of 0.08-0.12 mm). The part produced above E_C showed peak horizontal tensile stresses ($\sigma_x = +528 \pm 12$ MPa and $\sigma_y = +445 \pm 10$ MPa) at 0.4 mm below the top surface. Then, the horizontal residual stresses shifted from high tensile stress to approximately zero stress at a location of 1 mm below the top surface ($\sigma_x = +20 \pm 21$ MPa and $\sigma_y = +50 \pm 23$ MPa). These high tensile stresses are likely attributed to phase transformation (β transus) that occur when using very high laser energy density. However, the part produced below E_C showed peak tensile stresses ($\sigma_x = +510 \pm 64$ MPa and $\sigma_y = +448 \pm 30$ MPa) at the top surface and remained in high tension ($\sigma_x = +264 \pm 22$ MPa and $\sigma_y = +237 \pm 22$ MPa) at 1 mm below the top surface. These retained high tension zones are likely attributed to the void formation that occur when using very low laser energy density. At E_C , low tensile stress values ($\sigma_x = +205 \pm 26$ MPa and $\sigma_y = +51 \pm 26$ MPa) were seen at the top surface, and these values increased to almost double ($\sigma_x = +409 \pm 26$ MPa and $\sigma_y = +334 \pm 21$ MPa) at locations 1 mm below the top surface. These low tensile regions at the surface are attributed to the stable melting that occurs when using critical laser energy density. The vertical residual stresses were $+409 \pm 10$ MPa, $+606 \pm 15$ MPa, and $+926 \pm 14$ MPa at the very near subsurface of parts produced below E_C , at E_C , and above E_C , respectively. In the

same layer, these high vertical tensile stresses started to shift to compressive stresses after a few scan tracks. Similarly, the horizontal residual stresses started with high tensile values at the very near subsurface and shifted to compressive stresses after a few scan tracks from the edge. These stresses are attributed to the temperature gradient between subsequent layers which is higher at the edges (surrounded by loose powder) compared to the region from a few scan tracks (surrounded by molten metal) to the center of the layer.

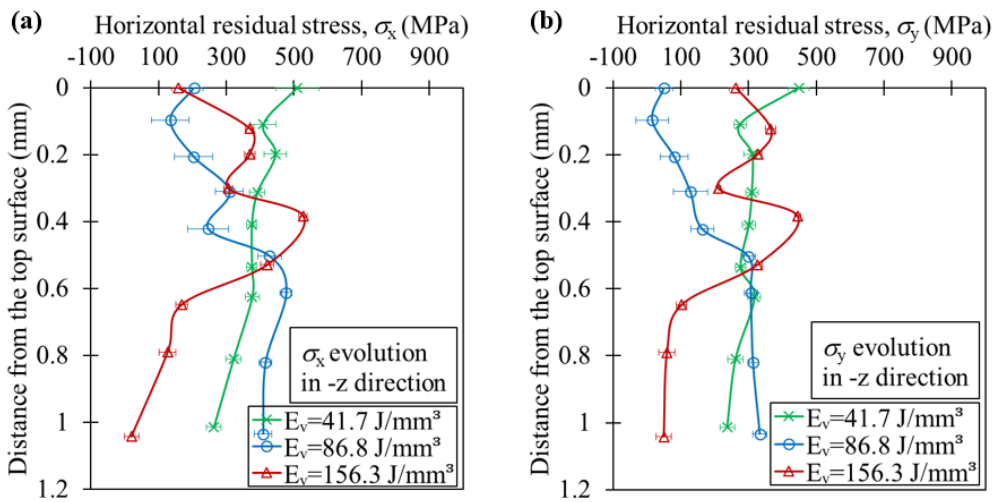


Figure 6.13: (a) Longitudinal horizontal, and (b) transverse horizontal residual stress profiles in the build direction of Ti-6Al-4V samples produced at various laser energy densities.

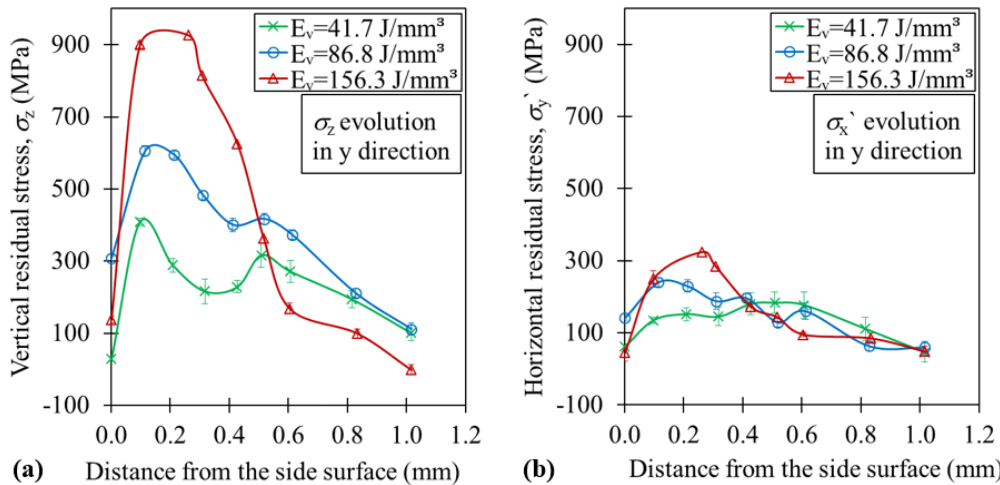


Figure 6.14: (a) Vertical, and (b) horizontal residual stress profiles in the layer direction of Ti-6Al-4V samples produced at various laser energy densities.

6.3.5 Internal microstructures

Figure 6.15 shows optical micrographs of the top cross-sections of three samples produced at 41.7 J/mm^3 , 86.8 J/mm^3 , and 156.3 J/mm^3 . The SLM parts usually have prior columnar β grain boundary and acicular α/α' microstructures [3, 27, 47, 48]. Voids and discontinuous beads were observed in the sample that was produced at 41.7 J/mm^3 . This sample showed prior columnar β grain boundary and mainly α needles, as shown in Figure 6.15. Large α' plates and elongated primary α -grains were observed in the sample that was produced above E_C at 156.3 J/mm^3 . The sample that was produced at $E_C = 86.8 \text{ J/mm}^3$ showed continuous melt tracks with no voids and large α' plates. This microstructure showed stable melting with mainly primary α -grains in columnar β grain boundary. The vertical cross-section of this sample illustrates the melt pool lines with equiaxed α -grains, Figure 6.15.

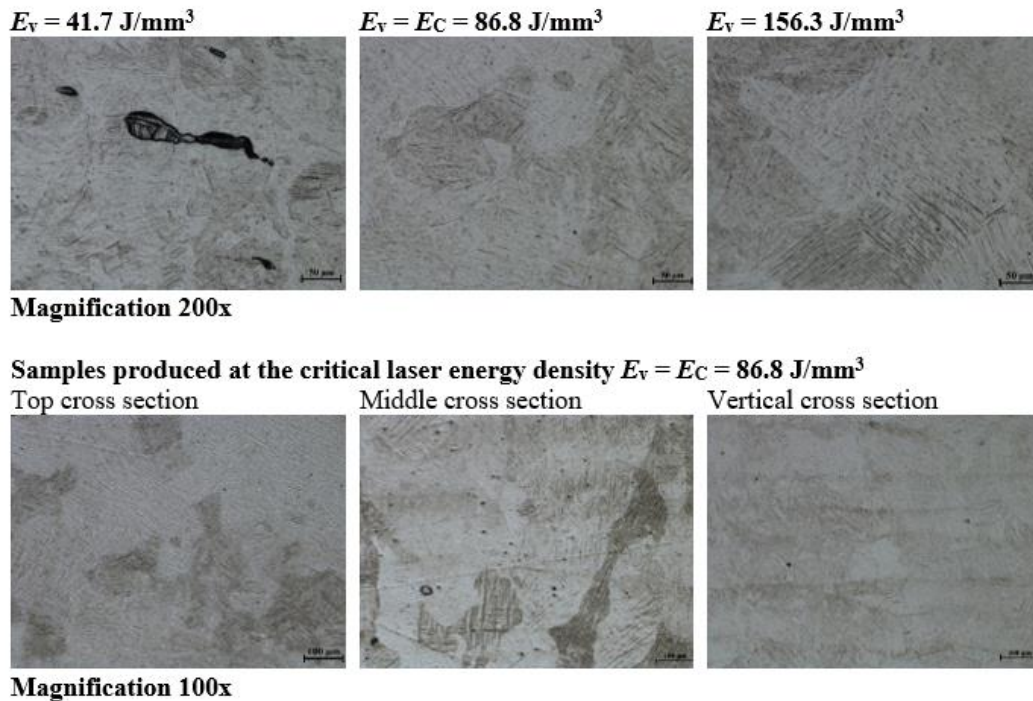


Figure 6.15: Micrographs of etched cross-sections of samples produced at different laser energy densities.

6.4 Discussion

6.4.1 Process-Property relationship

The contour plots and statistical analysis of the metallurgical properties: density (Figure 6.4), thermal expansion (Figure 6.8), cantilever height (Figure 6.11), and cantilever deflection (Figure 6.12) were used to determine process maps for Ti-6Al-4V. These optimum process maps were determined as discussed in Section 6.2.1.

Minitab software was used to determine the regression models of each response factor: part density, thermal expansion at 100 °C, cantilever height, and cantilever deflection. These regression models were used to determine the process maps shown in Figure 6.16. The highlighted ranges show the optimum combinations of laser power and scanning speed at hatch spacings of 0.08 mm, 0.10 mm, and 0.12 mm. This optimal range provides higher part density of 99%, thermal expansion lower than 795 $\mu\text{m/m}$ at 100 °C, and part deflection less than 0.48 mm. It was found that the optimum range of process parameters at hatch spacing of 0.08 mm provides laser energy densities between 70.8-86.5 J/mm^3 . In addition, the optimum range at hatch spacing of 0.10 mm provides laser energy densities between 68-86.1 J/mm^3 , while the optimum range at hatch spacing of 0.12 mm provides laser energy densities between 65-85 J/mm^3 . This laser energy density range does not exceed E_C for Ti-6Al-4V, i.e. 86.8 J/mm^3 , as shown in Figure 6.16d. The optimum range shown in Figure 6.16 was compared with the optimum range obtained by Wang et al. [22] for ductility and density of parts produced using the SLM process. The optimal range of SLM process parameters was compared with the optimal range of EBM process parameters obtained by Beuth et al. [33] and Seifi et al. [34] as shown in Figure 6.17. It was observed that the optimal range of process parameters obtained by Wang et al. [22] at layer thickness of 25 μm and hatch spacing of 0.08 mm was similar to those obtained in

the current study. Figure 6.17 shows the process maps of laser power and scanning speed obtained in the current study at a layer thickness of 40 μm and a hatch spacing of 0.08 mm, 0.10 mm, and 0.12 mm. Compared to SLM, the EBM of Ti-6Al-4V uses higher power density but lower scanning speed to achieve stable melting for a single bead [49]. The optimum EBM process parameters range presented in Figure 6.17 could change when using full hatch scanning instead of only one single bead.

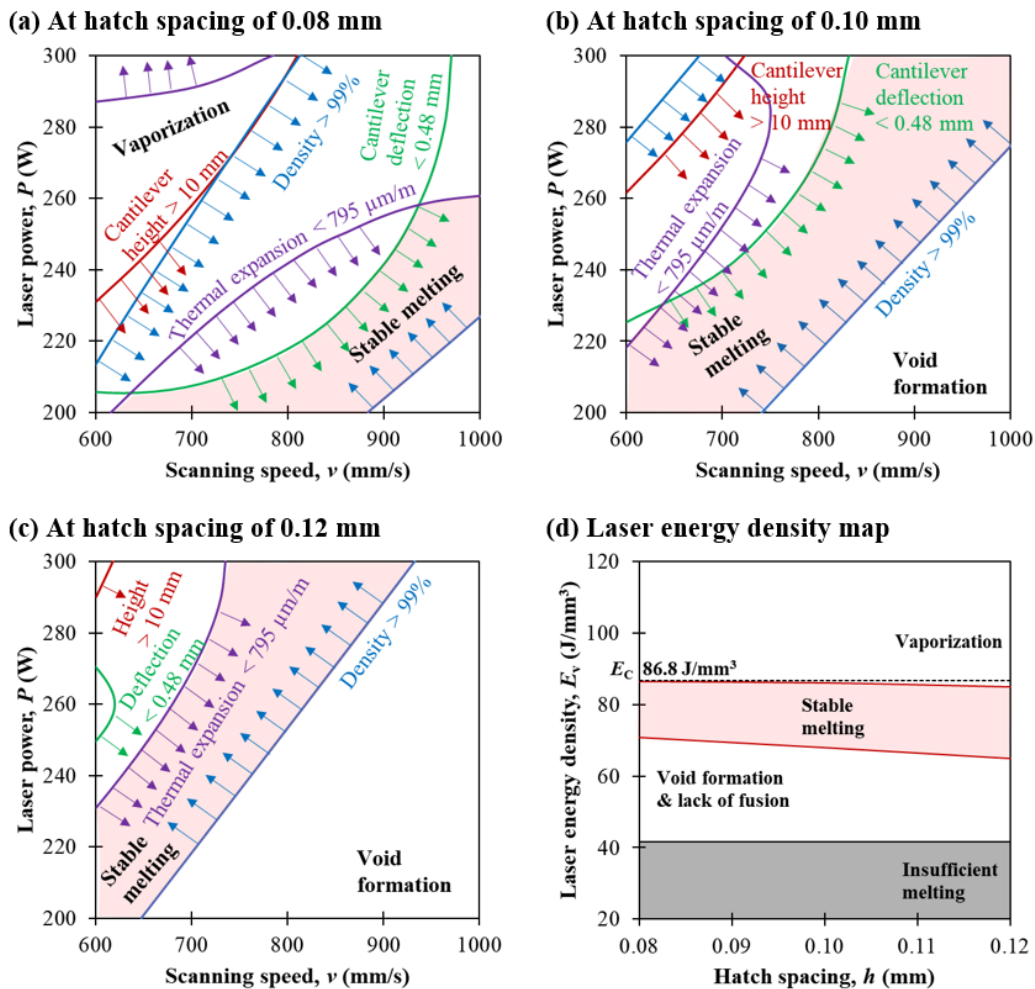


Figure 6.16: Relationship between laser processing parameters and Ti-6Al-4V cantilever deflection.

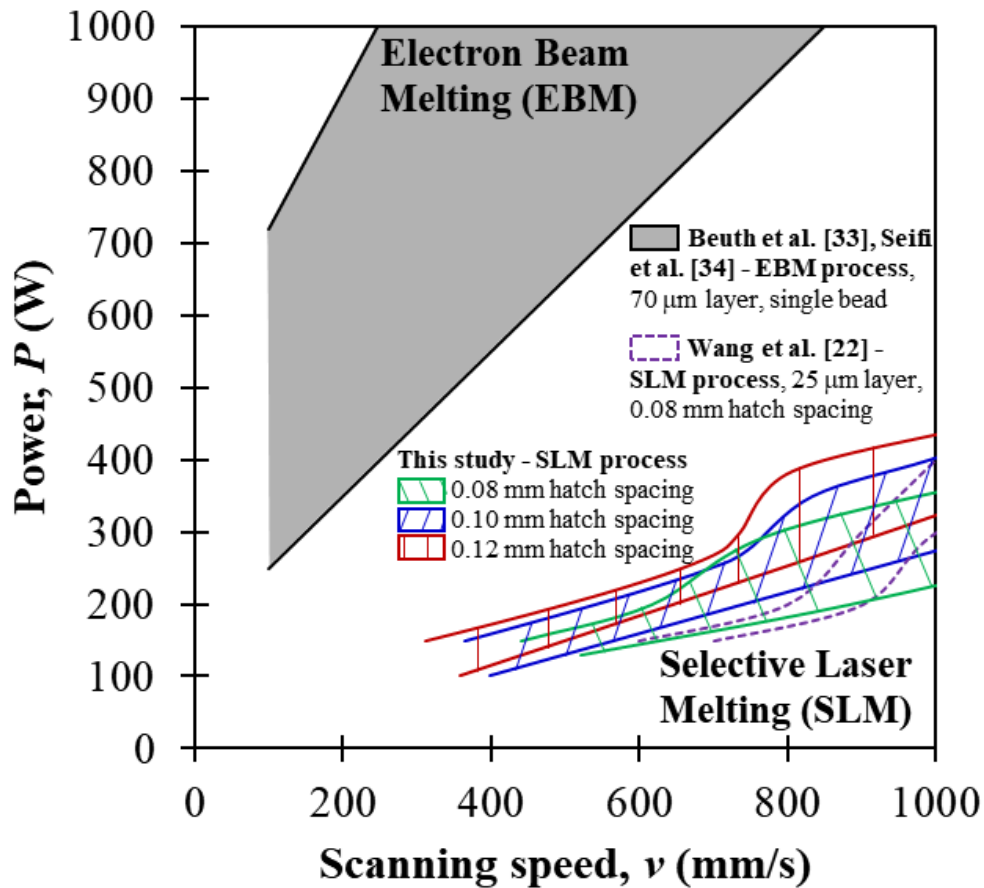


Figure 6.17: Relationship between laser processing parameters and Ti-6Al-4V cantilever deflection.

6.4.2 Process-Structure relationship

The residual stress analysis showed that:

- The vertical residual stress induced in parts that were produced above E_C exceeded the yield strength of the material, i.e. 795 MPa for Ti-6Al-4V Grade 23. These parts showed noticeable plastic deformation during the SLM process. This explains the large cantilever deflection that was found in parts produced above the critical energy density.

- The vertical and horizontal residual stress profiles in the layer direction are influenced by the dimension of the scan track (hatch spacing), but the horizontal residual stress profiles in the build direction are influenced by void formation and phase transformation.
- Residual stress profiles in SLM parts are strongly affected by the process parameters that were used to produce these parts.
- Increasing the laser energy density caused an increase in the vertical and horizontal residual stresses along the layer direction. This is most likely attributed to the temperature gradients between subsequent layers that increase by increasing the laser energy density.
- The vertical residual stress is almost twice the horizontal residual stress in SLM Ti-6Al-4V parts produced. The temperature gradient in the vertical direction, between unmelted and melted layers, is much higher than the temperature gradient in the horizontal direction, between scan tracks in the same layer.

Residual stresses are induced in SLM Ti-6Al-4V via two main mechanisms: (1) thermal stress due to temperature gradient, and (2) phase transformation due to solidification. The former mechanism is the main driving mechanism behind the formation of large residual stresses in the vertical direction as a result of the high temperature gradients between subsequent layers. The latter mechanism affects the induced residual stress, mainly in the horizontal direction, when using high energy densities. Above the critical laser energy density, the body-centered cubic β phase transforms into hexagonal martensite α' . The martensitic phase contains a high density of dislocations. This martensitic transformation leads to an increase in the residual stress and a reduction in the part ductility as explained in [4, 11, 50].

6.5 Conclusions

The relationships between density, thermal expansion, and deflection for Ti-6Al-4V parts produced using selective laser melting are discussed in this paper. It was found that increasing the laser energy density leads to an increase in the part density and thermal expansion up to a maximum point after which they decrease. The peak values occurred at the critical laser energy density, E_C . The part density decreases as phase transformation occurred and unstable melting existed above the critical laser energy density. Below the critical laser energy, the reduction in the part density was attributed to void formation. Thermal expansion of Ti-6Al-4V increased by increasing the laser energy density until it reached to a maximum limit at E_C . This maximum limit of thermal expansion is comparable with the thermal expansion of the wrought material. In addition, high residual stresses and large part distortions were found above the critical laser energy density. Based on statistical analyses, an optimum range of process parameters was established for Ti-6Al-4V. This optimum range provides laser energy densities between 65-86.8 J/mm³. The critical laser energy density, E_C , was found to be 86.8 J/mm³ for Ti-6Al-4V. Martensitic phase transformation was not observed, and less residual stress was induced when producing Ti-6Al-4V parts at process conditions that generate laser energy densities below the critical laser energy density.

6.6 References

- [1] Casalino, G., Mortello, M., and Campanelli, S. L., "Ytterbium fiber laser welding of Ti6Al4V alloy," *Journal of Manufacturing Processes*, vol. 20, pp. 250-256, 2015.
- [2] Pal, S., Lojen, G., Kokol, V., and Drstvensek, I., "Evolution of metallurgical properties of Ti-6Al-4V alloy fabricated in different energy densities in the Selective Laser Melting technique," *Journal of Manufacturing Processes*, vol. 35, pp. 538-546, 2018.

- [3] Zafari, A. and Xia, K., "High Ductility in a fully martensitic microstructure: a paradox in a Ti alloy produced by selective laser melting," *Materials Research Letters*, vol. 6, no. 11, pp. 627-633, 2018.
- [4] Xu, W. *et al.*, "Additive manufacturing of strong and ductile Ti–6Al–4V by selective laser melting via in situ martensite decomposition," *Acta Materialia*, vol. 85, pp. 74-84, 2015.
- [5] Gong, H., Rafi, H., Starr, T., and Stucker, B., "The Effects of Processing Parameters on Defect Regularity in Ti-6Al-4V Parts Fabricated By Selective Laser Melting and Electron Beam Melting," in *24th Annual International Solid Freeform Fabrication Symposium*, Austin TX, 2013, pp. 424-439: University of Texas.
- [6] Shi, X. *et al.*, "Performance of High Layer Thickness in Selective Laser Melting of Ti6Al4V," *Materials*, vol. 9, no. 12, p. 975, 2016.
- [7] Yadroitsev, I. and Yadroitsava, I., "Evaluation of residual stress in stainless steel 316L and Ti6Al4V samples produced by selective laser melting," *Virtual and Physical Prototyping*, vol. 10, no. 2, pp. 67-76, 2015.
- [8] Fogagnolo, J., Sallica-Leva, E., Najjar Lopes, E. S., Jardini, A., and Caram, R., "The effect of the laser process parameters in the microstructure and mechanical properties of Ti6Al4V produced by selective laser sintering/melting," in *21st International Conference on Metallurgy and Materials (Metal 2012)*, Czech Republic, 2012, pp. 1234-1238.
- [9] Kasperovich, G., Haubrich, J., Gussone, J., and Requena, G., "Correlation between porosity and processing parameters in TiAl6V4 produced by selective laser melting," *Materials & Design*, vol. 105, pp. 160-170, 2016.
- [10] Thijs, L., Verhaeghe, F., Craeghs, T., Humbeeck, J. V., and Kruth, J.-P., "A Study of the Microstructural Evolution during Selective Laser Melting of Ti–6Al–4V," *Acta Materialia*, vol. 58, pp. 3303–3312, 2010.
- [11] Tan, X. *et al.*, "Revealing martensitic transformation and α/β interface evolution in electron beam melting three-dimensional-printed Ti-6Al-4V," *Scientific Reports*, vol. 6, p. 26039, 2016.
- [12] Song, B., Dong, S., Liao, H., and Coddet, C. J. T. I. J. o. A. M. T., "Process parameter selection for selective laser melting of Ti6Al4V based on temperature distribution simulation and experimental sintering," *The International Journal of Advanced Manufacturing Technology*, vol. 61, no. 9, pp. 967-974, 2012.
- [13] Simonelli, M., Tse, Y., and Tuck, C., "Further understanding of ti-6al-4v selective laser melting using texture analysis," in *23rd Annual International Solid Freeform Fabrication Symposium*, Austin TX, 2012, pp. 480-491: University of Texas.
- [14] Mishurova, T. *et al.*, "An assessment of subsurface residual stress analysis in SLM Ti-6Al-4V," *Materials*, vol. 10, no. 4, p. 348, 2017.

- [15] Kenel, C. *et al.*, "In situ investigation of phase transformations in Ti-6Al-4V under additive manufacturing conditions combining laser melting and high-speed micro-X-ray diffraction," *Scientific Reports*, vol. 7, no. 1, p. 16358, 2017.
- [16] Ali, H., Ghadbeigi, H., and Mumtaz, K. J. T. I. J. o. A. M. T., "Residual stress development in selective laser-melted Ti6Al4V: a parametric thermal modelling approach," *The International Journal of Advanced Manufacturing Technology*, vol. 97, no. 5, pp. 2621-2633, 2018.
- [17] Barriobero-Vila, P. *et al.*, "Inducing Stable $\alpha + \beta$ Microstructures during Selective Laser Melting of Ti-6Al-4V Using Intensified Intrinsic Heat Treatments," *Materials*, vol. 10, no. 3, p. 268, 2017.
- [18] DebRoy, T. *et al.*, "Additive manufacturing of metallic components – Process, structure and properties," *Progress in Materials Science*, vol. 92, pp. 112-224, 2018.
- [19] Shifeng, W., Shuai, L., Qingsong, W., Yan, C., Sheng, Z., and Yusheng, S., "Effect of molten pool boundaries on the mechanical properties of selective laser melting parts," *Journal of Materials Processing Technology*, vol. 214, pp. 2660-2667, 2014.
- [20] Thompson, M. K. *et al.*, "Design for Additive Manufacturing: Trends, opportunities, considerations, and constraints," *CIRP Annals*, vol. 65, no. 2, pp. 737-760, 2016.
- [21] Yakout, M., Cadamuro, A., Elbestawi, M. A., and Veldhuis, S. C., "The selection of process parameters in additive manufacturing for aerospace alloys," *The International Journal of Advanced Manufacturing Technology*, vol. 92, no. 5-8, pp. 2081-2098, 2017.
- [22] Wang, D., Dou, W., and Yang, Y., "Research on Selective Laser Melting of Ti6Al4V: Surface Morphologies, Optimized Processing Zone, and Ductility Improvement Mechanism," *Metals*, vol. 8, no. 7, p. 471, 2018.
- [23] Van Hooreweder, B. and Kruth, J.-P., "Advanced fatigue analysis of metal lattice structures produced by Selective Laser Melting," *CIRP Annals*, vol. 66, no. 1, pp. 221-224, 2017.
- [24] Wu, B. *et al.*, "A review of the wire arc additive manufacturing of metals: properties, defects and quality improvement," *Journal of Manufacturing Processes*, vol. 35, pp. 127-139, 2018.
- [25] Yakout, M., Elbestawi, M. A., and Veldhuis, S. C., "On the characterization of stainless steel 316L parts produced by selective laser melting," *The International Journal of Advanced Manufacturing Technology*, journal article vol. 95, no. 5-8, pp. 1953-1974, March 01 2018.
- [26] Han, J. *et al.*, "Microstructure and mechanical property of selective laser melted Ti6Al4V dependence on laser energy density," *Rapid Prototyping Journal*, vol. 23, no. 2, pp. 217-226, 2017.

- [27] Ter Haar, G. and Becker, T., "Selective Laser Melting Produced Ti-6Al-4V: Post-Process Heat Treatments to Achieve Superior Tensile Properties," *Materials*, vol. 11, no. 1, p. 146, 2018.
- [28] Ahmad, B., van der Veen, S. O., Fitzpatrick, M. E., and Guo, H., "Residual stress evaluation in selective-laser-melting additively manufactured titanium (Ti-6Al-4V) and inconel 718 using the contour method and numerical simulation," *Additive Manufacturing*, vol. 22, pp. 571-582, 2018.
- [29] Armentani, E., Esposito, R., and Sepe, R., "The effect of thermal properties and weld efficiency on residual stresses in welding," *Journal of Achievements in Materials and Manufacturing Engineering*, vol. 20, no. 1-2, pp. 319-322, 2007.
- [30] Zhukovskii, V. K. and Gokhman, A. R., "Relation between a linear thermal expansion coefficient and residual stresses," *Technical Physics*, vol. 54, no. 4, pp. 535-541, 2009.
- [31] Yakout, M., Elbestawi, M. A., and Veldhuis, S. C., "A study of thermal expansion coefficients and microstructure during selective laser melting of invar 36 and stainless steel 316L," *Additive Manufacturing*, vol. 24, pp. 405-418, 2018.
- [32] Malzbender, J., "Stress profile and thermal expansion of layered materials determined from surface stresses," *Applied Physics Letters*, vol. 84, no. 23, pp. 4661-4662, 2004.
- [33] Beuth, J. *et al.*, "Process mapping for qualification across multiple direct metal additive manufacturing processes," in *24th International Solid Freeform Fabrication Symposium*, Austin TX, 2013, pp. 655-665: University of Texas.
- [34] Seifi, M., Christiansen, D., Beuth, J., Harrysson, O., and Lewandowski, J. J., "Process Mapping, Fracture and Fatigue Behavior of Ti-6Al-4V Produced by EBM Additive Manufacturing," in *Proceedings of the 13th World Conference on Titanium*, V. Venkatesh *et al.*, Eds.: TMS/Wiley, 2016.
- [35] Gockel, J., Beuth, J., and Taminger, K., "Integrated control of solidification microstructure and melt pool dimensions in electron beam wire feed additive manufacturing of Ti-6Al-4V," *Additive Manufacturing*, vol. 1-4, pp. 119-126, 2014.
- [36] Wang, L.-z., Wang, S., and Hong, X., "Pulsed SLM-manufactured AlSi10Mg alloy: Mechanical properties and microstructural effects of designed laser energy densities," *Journal of Manufacturing Processes*, vol. 35, pp. 492-499, 2018.
- [37] Yakout, M., Elbestawi, M. A., and Veldhuis, S. C., "Density and mechanical properties in selective laser melting of Invar 36 and stainless steel 316L," *Journal of Materials Processing Technology*, vol. 266, pp. 397-420, 2019.
- [38] Wang, Y., Kamath, C., Voisin, T., and Li, Z., "A processing diagram for high-density Ti-6Al-4V by selective laser melting," *Rapid Prototyping Journal*, vol. 24, no. 9, pp. 1469-1478, 2018.

- [39] Mahmoudi, M. *et al.*, "On the printability and transformation behavior of nickel-titanium shape memory alloys fabricated using laser powder-bed fusion additive manufacturing," *Journal of Manufacturing Processes*, vol. 35, pp. 672-680, 2018.
- [40] Hitzler, L., Hirsch, J., Heine, B., Merkel, M., Hall, W., and Öchsner, A., "On the Anisotropic Mechanical Properties of Selective Laser-Melted Stainless Steel," *Materials*, vol. 10, no. 10, p. 1136, 2017.
- [41] Prashanth, K. G., Scudino, S., Maity, T., Das, J., and Eckert, J., "Is the energy density a reliable parameter for materials synthesis by selective laser melting?," *Materials Research Letters*, vol. 5, no. 6, pp. 386-390, 2017.
- [42] Scipioni Bertoli, U., Wolfer, A. J., Matthews, M. J., Delplanque, J.-P. R., and Schoenung, J. M., "On the limitations of Volumetric Energy Density as a design parameter for Selective Laser Melting," *Materials & Design*, vol. 113, pp. 331-340, 2017.
- [43] International, A. S. M. and Handbook, C., *ASM handbook. Volume 2, Volume 2*. Materials Park, OH: ASM International, 1990.
- [44] *Standard test method for linear thermal expansion of solid materials by thermomechanical analysis*, 2014.
- [45] James, J. D., Spittle, J. A., Brown, S. G. R., and Evans, R. W., "A review of measurement techniques for the thermal expansion coefficient of metals and alloys at elevated temperatures," *Measurement Science and Technology*, vol. 12, no. 3, p. R1, 2001.
- [46] Mukherjee, T. and DebRoy, T., "Mitigation of lack of fusion defects in powder bed fusion additive manufacturing," *Journal of Manufacturing Processes*, vol. 36, pp. 442-449, 2018.
- [47] Wysocki, B., Maj, P., Sitek, R., Buhagiar, J., Kurzydłowski, K., and Świążkowski, W., "Laser and Electron Beam Additive Manufacturing Methods of Fabricating Titanium Bone Implants," *Applied Sciences*, vol. 7, no. 7, p. 657, 2017.
- [48] Rahman Rashid, R. A., Palanisamy, S., Attar, H., Bermingham, M., and Dargusch, M. S., "Metallurgical features of direct laser-deposited Ti6Al4V with trace boron," *Journal of Manufacturing Processes*, vol. 35, pp. 651-656, 2018.
- [49] Loeber, L. *et al.*, "Comparison of selective laser and electron beam melted titanium aluminides," in *22nd International Solid Freeform Fabrication Symposium Austin TX*, 2011: University of Texas.
- [50] Ali, H., Ma, L., Ghadbeigi, H., and Mumtaz, K., "In-situ residual stress reduction, martensitic decomposition and mechanical properties enhancement through high temperature powder bed pre-heating of Selective Laser Melted Ti6Al4V," *Materials Science and Engineering: A*, vol. 695, pp. 211-220, 2017.

Chapter 7

Residual Stresses and Dimensional Distortions

During Selective Laser Melting of Invar 36,

Stainless Steel 316L, and Ti-6Al-4V

Complete Citation:

Yakout, M., Elbestawi, M.A., Veldhuis, S.C., Nangle-Smith, S. Influence of thermal properties on residual stresses in SLM of aerospace alloys. *Submitted for publication*, 2018.

Copyright:

© Authors.

Relative Contributions:

M. Yakout: Performed experiments, analysis, and data interpretation. Wrote the first draft of the manuscript. Helped with submitting the final manuscript to the journal (first and corresponding author).

M. A. Elbestawi: Co-supervisor of M. Yakout. Revised the manuscript. Was responsible of submitting the final manuscript to the journal (corresponding author).

S. C. Veldhuis: Co-supervisor of M. Yakout. Revised the manuscript.

S. Nangle-Smith: Was involved in calculating the heat transfer boundary conditions.

Abstract:

Purpose – Residual stresses are induced during selective laser melting (SLM) due to rapid melting, solidification, and build plate removal. In this paper, the thermal cycle, residual stresses, and part distortions are examined for selected aerospace materials (i.e. Ti-6Al-4V, stainless steel 316L, and Invar 36) using a thermo-mechanical finite element model.

Design/methodology/approach –The model predicts the residual stress and part distortion after build plate removal. The residual stress field is validated using X-ray diffraction method and the part distortion is validated using dimensional measurements. Additionally, real-time measurements were taken using pyrometer and high-speed camera during the SLM process.

Findings – The trends found in the numerical results agree with those found experimentally. Invar 36 had the lowest tensile residual stresses due to its lowest coefficient of thermal expansion. The residual stresses of stainless steel 316L were lower than those of Ti-6Al-4V due to its higher thermal diffusivity.

Research limitations/implications – The model predicts residual stresses at the optimal SLM process parameters. However, using any other process conditions could cause void formation and/or alloying element vaporization which would require the inclusion of melt pool physics in the model.

Originality/value – The paper explains the influence of the coefficient of thermal expansion and thermal diffusivity on the induced thermal stresses. The methodology can

be used to predict the dimensional distortions and residual stresses in complex designs of any of the three materials under optimal SLM process parameters.

Keywords:

Selective laser melting (SLM), Finite element analysis, Residual stress, Thermal diffusivity, Aerospace industry, Melting.

Acknowledgment:

This work was supported by the Natural Sciences and Engineering Research Council of Canada (NSERC), Grant: RGPIN-2016-06268. The authors also thank Mr. Roman Duplak of SimuTech Group Inc. for supporting this project.

7.1 Introduction

Selective laser melting (SLM), a powder-bed additive manufacturing (AM) process, is associated with void formation, crack propagation, alloying elements vaporization, and high temperature gradients. The mechanical, optical, and electrical properties of various AM materials, as well as the expected defects including porosity, cracking, distortion, delamination, and degradation of surface finish have been reported in the open literature [1, 2]. SLM induces residual stresses and part flaws, that consequently affect the mechanical properties and fatigue performance of parts produced [3-5]. This paper contributes to the understanding of the physical mechanisms of residual stresses formation in Ti-6Al-4V, stainless steel 316L, and Invar 36 parts produced using SLM. These three alloys are widely used in the aerospace and biomedical industries because of their unique properties. Ti-6Al-4V offers high strength-to-weight ratio and is biocompatible, stainless steel 316L offers corrosion resistance and high strength, and Invar 36 is a ferromagnetic alloy that has a very low coefficient of thermal expansion for applications below its Curie temperature (279 °C). Ti-6Al-4V, stainless steel 316L, and Invar 36 produced using SLM can develop tensile residual stresses up to 920 MPa [5, 6], 450 MPa [7], and 350 MPa [7], respectively. Induced thermal stresses depend on the coefficient of thermal expansion and the temperature differential in the material as described in Equation (7.1). Consequently, the lower a material's coefficient of thermal expansion, the lower the thermal stresses induced, and therefore lower residual stresses will develop [8]. SLM parts are deformed by thermal stresses due to rapid heating and cooling. These thermal stresses induce tensile residual stresses in the parts [9]. SLM parts should be post processed to minimize residual stresses as the generation of residual stresses is inevitable in the SLM process [10]. Finite element (FE) models are used when designing for additive manufacturing to predict residual stresses and part flaws [11].

$$\sigma_T = \alpha_T E (T - T_{ref}) \tag{7.1}$$

where σ_T is thermal stress in (MPa), T is temperature in (K), α_T is coefficient of thermal expansion at temperature T in (m/m.°C), E is modulus of elasticity in (MPa). Subscript $_{ref}$ represents reference.

In this paper, residual stresses and dimensional distortions of Ti-6Al-4V, stainless steel 316L, and Invar 36 are investigated experimentally and numerically. An X-ray diffraction (XRD) instrument and a coordinate measuring machine (CMM) are used for residual stress and dimensional distortion measurements, respectively. ANSYS© 19.2 Workbench Additive, coupled thermal-mechanical FE module, is used to predict residual stresses and part distortions during SLM as described in Figure 7.1. The main contribution of the present study is to analyse and quantify the residual stresses induced in Ti-6Al-4V, stainless steel 316L, and Invar 36 during the SLM process and investigate their relationship with the material thermal properties.

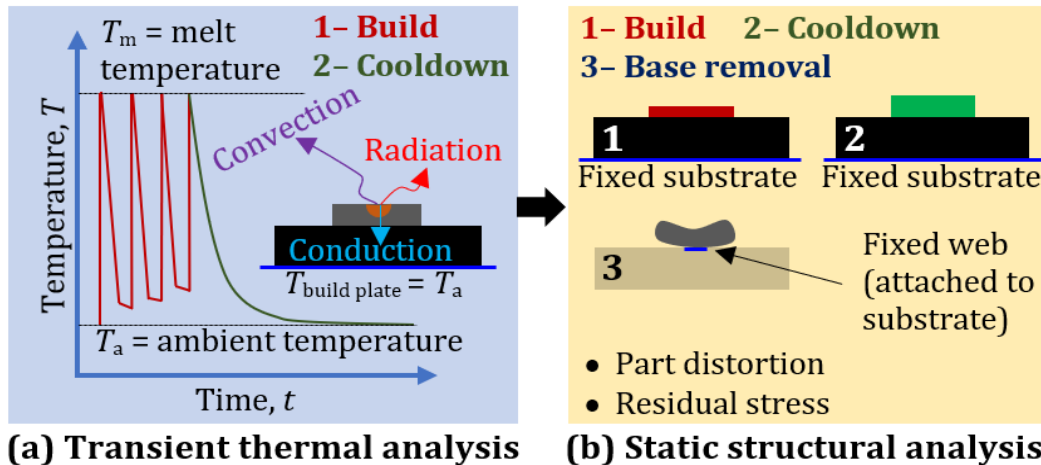


Figure 7.1: Schematic of (a) transient thermal, (b) static structural models.

7.2 Methodology

7.2.1 Test parts and experiments

A cantilever beam, Figure 7.2a, was designed to measure the dimensional distortions, and a cube, Figure 7.2b, was designed to measure the residual stress evolution. The cantilever beam method is commonly used [12-14] to assess distortions of SLM parts. Table 7.1 shows the optimal SLM process conditions for Ti-6Al-4V, stainless steel 316L, and Invar 36 parts for minimal defect evolution as reported in the literature [7, 15, 16]. These optimal process conditions provide stable melting and can be used to produce dense parts with high mechanical properties and minimal defects. Figure 7.5 shows the influence of the laser energy density on the relative density of parts produced. Voids and internal cracks are formed below these optimal conditions and alloying elements vaporize above these optimal conditions [7, 17, 18]. Gas-atomized powders in the size range of 15-45 μm , were processed at these optimal conditions. The main process parameters are listed in Table 7.1. A stripe scanning strategy was used, with stripe width, stripe overlap, scanning rotation between subsequent layers of 10 mm, 0.08 mm, and 67° , respectively. No contouring was used. Parts produced using these process conditions do not manifest any void formation, significant changes in the material composition, or phase transformation [7, 15, 16, 19]. Ti-6Al-4V parts were produced on titanium build plate using a Renishaw AM400 machine equipped with argon gas flow. Invar 36 and stainless steel 316L parts were produced on 18Ni-500 build plates using an EOSINT M280 machine equipped with nitrogen gas flow. Wire electrical discharge machining (EDM) was used to cut the part from the build plate whereby the middle web was left attached as shown in Figure 7.4.

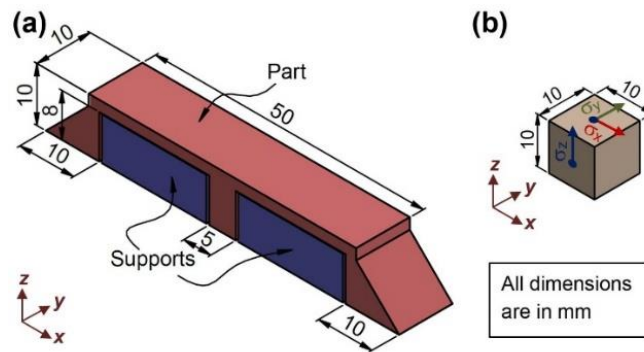


Figure 7.2: Dimensions of (a) cantilever beams and (b) cubes for residual stress measurements.

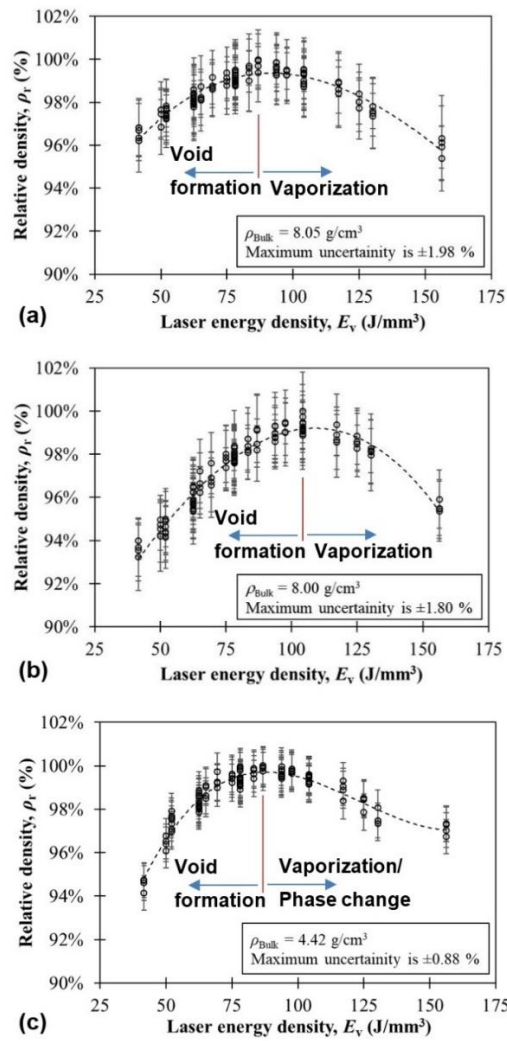


Figure 7.3: Relative density as a function of laser energy density for (a) Invar 36 [7, 17], (b) stainless steel 316L [7, 17, 20], and (c) Ti-6Al-4V [18].

Table 7.1: SLM process conditions for Ti-6Al-4V, stainless steel 316L, and Invar 36.

Process parameter (unit)	Ti-6Al-4V	Steel 316L	Invar 36
Laser power P (W)	250	250	250
Scanning speed v (mm/s)	600	600	600
Hatch spacing h (mm)	0.12	0.10	0.12
Layer thickness t (mm)	0.04	0.04	0.04
Laser energy density E_v (J/mm ³)	86.8	104.2	86.8
Dwell time t_D (s)	10	10	10
Preheat temperature T_a (°C)	40	40	40

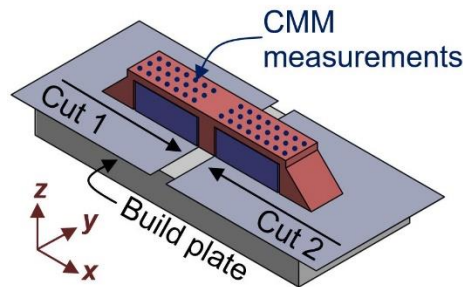


Figure 7.4: CMM measurements highlighting EDM cut planes.

7.2.2 Model development and boundary conditions

The SLM process was modelled using an orthogonal Cartesian mesh consisting of superlayers, which are an average of multiple scan layers. The model does not explicitly consider the melt pool physics, rather each element was added at the melt temperature, ($T_{new\ element} = T_m$), with zero strain and the thermal stress accumulated as the part was cooled down and reheated again. If the effect of scanning strategy is to be determined, melt pool physics should be explicitly modelled. For example, the microscale scan model of Li et al. [21] considered the moving laser heat source as a Gaussian heat flux. In the current study, the FE model included; (i) macroscale approach to predict the part distortion due to the removal of the build plate, and (ii) mesoscale approach to predict the residual stress evolution due to heating and cooling. As such, the thermal stresses predicted by the model accurately reflect parts made with optimal SLM process conditions that do not overheat or underheat the part. The FE model coupled a transient thermal analysis with static structural analysis in a multi-staged approach as shown in Figure 7.1. The sequence includes a build step where elements

are added, a dwell step between the end of one layer to the start of the subsequent layer, and a cooldown step during which the laser was off, where the part cooled down to ambient temperature. The final step of the static structural analysis was the removal of the build-plate according to Figure 7.4. The transient thermal model was governed by the 3D Fourier heat conduction equations as described in Equation (7.2). The model assumed homogenous and isotropic material properties that vary with temperature. The part size was 66 mm × 10 mm × 10 mm. The bottom of the build plate was set to have a constant temperature boundary condition of 40°C ($T_{z=0} = 40 \text{ }^\circ\text{C}$). The sides of the part are given a Neumann zero heat flux boundary condition as heat loss to the loose powder bed on the sides of the part was assumed negligible. Heat is lost via convection and radiation to the inert gas environment, Equation (7.3), and correlations were used to determine these heat transfer coefficients [22], Equations (7.4), (7.5), and (7.6). During the build step, the part was cooled via forced convection and radiation to the 40°C chamber gas, which flowed at 5.5 m/s [23]. During the cooldown step, the part was cooled via natural convection and radiation to the stagnant chamber gas. The surface temperature used for the correlations was an average bulk temperature over the build time estimated by averaging the heat content in the plate and the part using the rule of mixtures. All gas properties were evaluated at the film temperature, T_{film} . The emissivity of the parts was assumed to be 0.2 [22]. Table 7.2 summarises the values that were used to calculate the heat transfer coefficients during both build and cooldown steps for each material. The stress distribution was determined in the static structural model using Equations (7.7) and (7.8). Plastic deformation was modelled using the bilinear isotropic hardening approach. The bottom of the build plate was set as a fixed boundary condition during the build step. However, only the web of the cantilever was set as a fixed boundary condition, to mimic the experimental setup during the build plate removal step.

$$\left(\frac{\rho C_p}{k}\right) \frac{\partial T}{\partial t} = \frac{\partial^2 T}{\partial x^2} + \frac{\partial^2 T}{\partial y^2} + \frac{\partial^2 T}{\partial z^2} \quad (7.2)$$

$$-k \left. \frac{\partial T}{\partial z} \right|_{z=\text{layer height}} = h_c (T_s - T_{ch}) + h_r (T_s - T_{ch}) \quad (7.3)$$

where C_p is specific heat capacity in (J/kg.K), k is thermal conductivity in (W/m.K), ρ is bulk density in (kg/m³), T is temperature in (K), t is time in (s), h is heat transfer coefficient in (W/m².K). Directions x , y , z are scanning and build directions. Subscripts c , r , s , ch represent convection, radiation, surface, and chamber, respectively.

$$h_c|_{\text{build}} = \frac{k}{L} (0.664 R_e^{0.5} P_r^{1/3}), \text{ where } R_e = \frac{U_{ch} L}{\eta_{ch}} \quad (7.4)$$

$$h_c|_{\text{cooldown}} = \frac{k}{L/2} (0.54 R_a^{0.4}), \text{ where } R_a = \left(\frac{g \alpha (T_s - T_{ch}) \left(\frac{L}{2}\right)^3}{\eta_{ch}^2} \right) P_r \quad (7.5)$$

$$h_r = \epsilon C_{st} (T_s + T_{ch}) (T_s^2 + T_{ch}^2) \quad (7.6)$$

where P_r is Prandtl number, R_e is Reynolds number, R_a is Rayleigh number, ϵ is emissivity, U is velocity in (m/s), η is kinematic viscosity in (m²/s), α is coefficient of thermal expansion in (m/m.°C), g is standard acceleration due to gravity (9.81 m/s²), C_{st} is Stefan-Boltzmann constant (5.67 x 10⁻⁸ W/m².K⁴).

$$\begin{Bmatrix} \varepsilon_x \\ \varepsilon_y \\ \varepsilon_z \end{Bmatrix} = \frac{1}{E} \begin{bmatrix} 1 & -\nu & -\nu \\ -\nu & 1 & -\nu \\ -\nu & -\nu & 1 \end{bmatrix} \begin{Bmatrix} \sigma_x \\ \sigma_y \\ \sigma_z \end{Bmatrix} + \begin{bmatrix} 1 & 0 & 0 \\ 0 & 1 & 0 \\ 0 & 0 & 1 \end{bmatrix} \begin{Bmatrix} \varepsilon_x^P \\ \varepsilon_y^P \\ \varepsilon_z^P \end{Bmatrix} + \alpha (T - T_{ref}) \quad (7.7)$$

$$\gamma_{xy} = \frac{\tau_{xy}}{2G} + \gamma_{xy}^P; \quad \gamma_{xz} = \frac{\tau_{xz}}{2G} + \gamma_{xz}^P; \quad \gamma_{yz} = \frac{\tau_{yz}}{2G} + \gamma_{yz}^P \quad (7.8)$$

where ε is normal strain, γ is shear strain, σ is normal stress in (MPa), τ is shear stress in (MPa), E is modulus of elasticity in (MPa), G is modulus of rigidity in (MPa), ν is Poisson's ratio. Superscript P represents plastic deformation.

Table 7.2: Build conditions used to calculate heat transfer coefficients.

Property (unit)	Ti-6Al-4V	Steel 316L	Invar 36
T_m (°C)	1605	1375	1427
Build plate	Ti-6Al-4V	18Ni-500	18Ni-500
Gas	Argon	Nitrogen	Nitrogen
T_s (°C)	295	280	298
T_{ch} (°C)	40	40	40
T_{film}	168	160	169
h_r (W/m.K)	2.25	2.04	2.29
U_{ch} (m/s)	5.5	5.5	5.5
η_{ch} (m ² /s)	0.00002851	0.00003075	0.00003184
P_r	0.6655	0.7241	0.7277
R_e	48229	44715	43185
$h_{c build}$ (W/m.K)	12.38	17.35	17.37
R_a	9086981	8127456	8025262
$h_{c cooldown}$ (W/m.K)	5.77	7.93	8.05
$h _{build}$ (W/m.K)	14.63	19.39	19.66
$h _{cooldown}$ (W/m.K)	8.02	9.97	10.34

Mesh sensitivity analysis was performed, and mesh independence was achieved at a mesh size of 0.34 mm for part and supports, and a 5 mm for build plate. The superlayer in the model represents 8.5 build layers (layer thickness of 0.04 mm).

7.3 Results

7.3.1 Thermal cycle

Figure 7.5a shows the temperature history during the build and cooldown steps for Ti-6Al-4V. During the build of each superlayer, material is added at the melt temperature, T_m , as shown in Figure 7.5b. When all layers are built, the part cools to thermal equilibrium, T_{room} . Stainless steel 316L and Invar 36 showed similar thermal cycles bounded by their melt temperatures. A high-temperature fiber-optic infrared pyrometer (Fluke Endurance®) was

used to determine the temperature history of Ti-6Al-4V. The repeatability error of the pyrometer was ± 1 °C and the pyrometer’s accuracy was $\pm 0.3\%$ of the measured temperature +2°C bias. The operating range of the pyrometer was set between 1000 °C and 3200 °C. Figure 7.6a shows the temperature profile of the first three layers measured during the SLM of Ti-6Al-4V. It was found that the temperature reaches to 2300 °C in the first layer and drops to 2100 °C in the third layer, showing temperatures higher than the melting temperature, $T_m = 1605$ °C. The temperature measurements showed that these SLM process conditions generates enough heat to fully melt the parts. The shape of the melt pool was also inspected using a high-speed camera system (Photron FASTCAM MC2.1) as shown in Figure 7.6b.

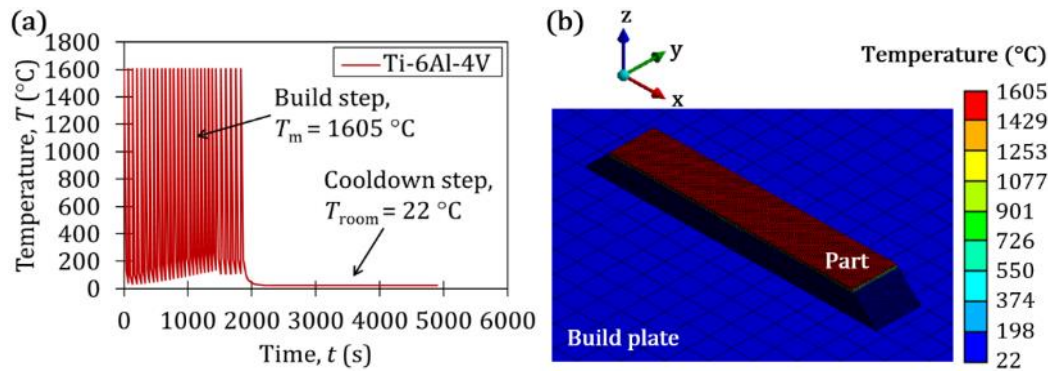


Figure 7.5: (a) Thermal cycles, (b) temperature profile of Ti-6Al-4V.

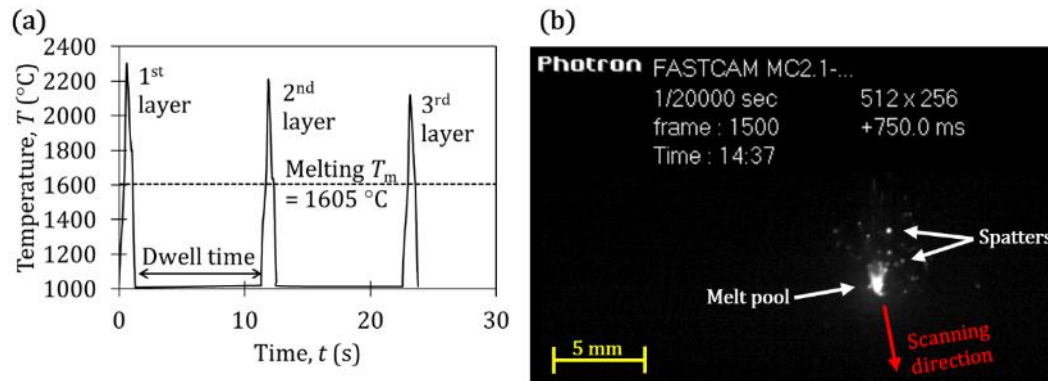


Figure 7.6: (a) Ti-6Al-4V thermal cycles using two-colour pyrometer, (b) melt pool shape visualization.

7.3.2 Dimensional distortion

The dimensional deflection that occurred after wire EDM was measured using a CMM, with a resolution of $0.1 \mu\text{m}$. The measurements were taken every 0.75 mm , resulting in 40 measurement locations along the 50 mm length (direction x) as shown in Figure 7.4. Three measurements were taken along the width of the cantilever (direction y) and averaged to minimize the effect of surface roughness. Figure 7.7a and b show the cantilever deflections measured experimentally and predicted by the model, respectively. The cantilevers were deflected downward in a convex shape as a result of stress relaxation after removing the build plate. More detail on the predicted deflection shapes can be seen in Figure 7.8b-d, and these shapes agree well with the experimental observations. Figure 7.8a shows that the model underpredicts the experimental deflections. This variation could be attributed to factors that were not considered in the model such as melt pool physics, changes in material composition, and phase transformation. The model was able to illustrate the relative differences in the deflection trends observed for the three materials. Both experimental and numerical results showed that the deformation due to residual stress of Ti-6Al-4V cantilever was more than twice that of stainless steel 316L. Invar 36 cantilever had the lowest deformation, and accordingly the lowest residual stresses.

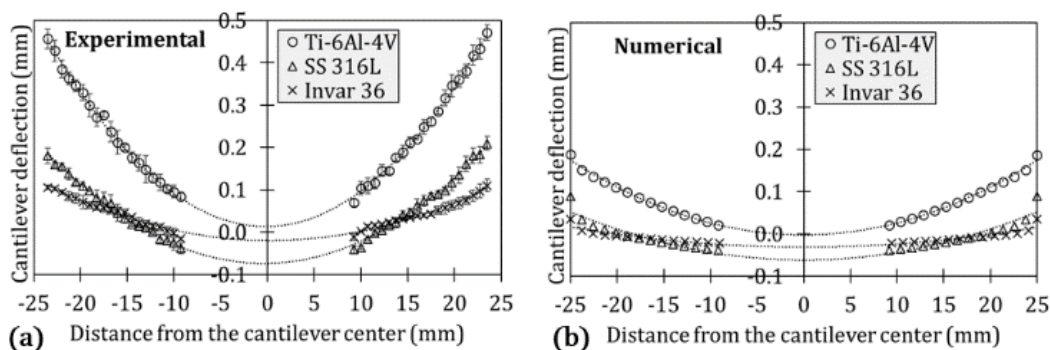


Figure 7.7: Average deflections on the top surfaces of the cantilevers: (a) measured by using CMM, (b) predicted by using the ANSYS© model.

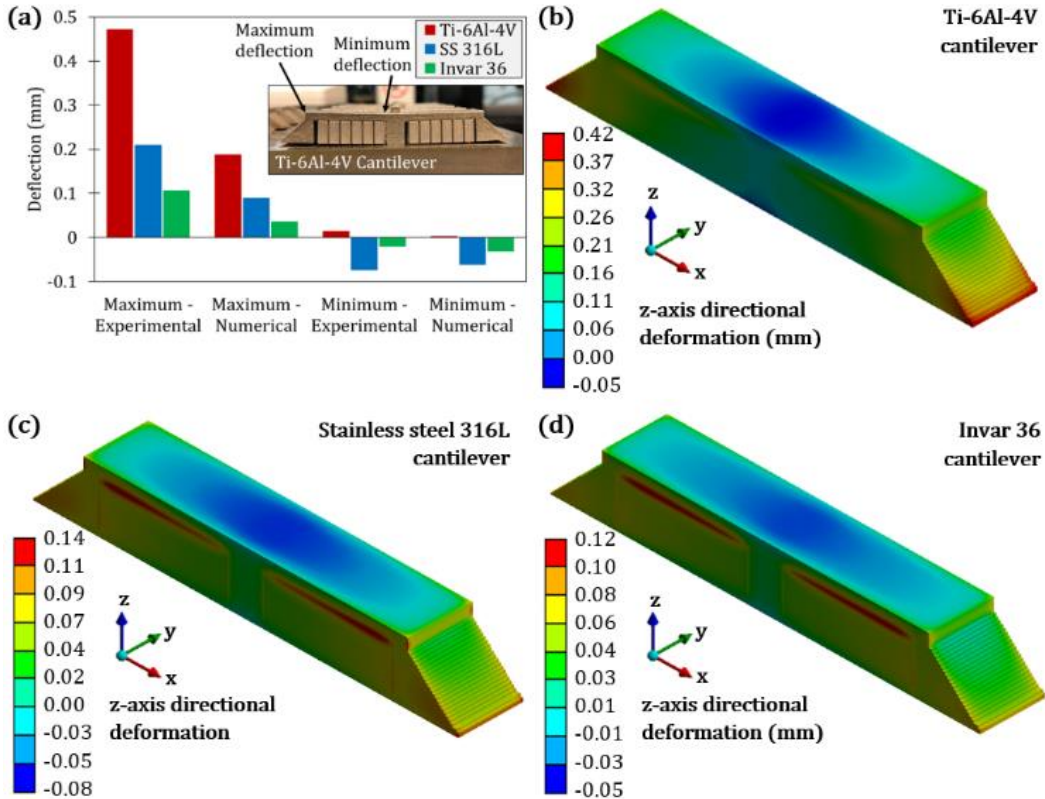


Figure 7.8: (a) Comparison between the numerical and experimental deflections, in which maximum deflection represents the edges of the top surface and minimum deflection represents the centre of the top surface; (b-d) directional deformation profiles (z-axis) of Ti-6Al-4V, stainless steel 316L, and Invar 36 cantilevers predicted by using the ANSYS© model.

7.3.3 Residual stress evolution

The directional residual stress was measured on the cubes using the XRD method, which determines the stress tensor based on lattice strain measurements. The measurements were taken on the top and lateral surfaces of each cube as shown in Figure 7.2b. Two directional stresses were measured in ten sub-surfaces for each point. The top surface measurements represent the horizontal residual stresses (σ_x , σ_y), and the lateral surface measurement represents the vertical residual stress (σ_z). Figure 7.9a shows the evolution of residual

stresses as measured using the XRD method and Figure 7.9b shows the evolution of residual stresses as predicted using the ANSYS© model. The trends seen in the numerical results agreed with the experimental results, but the prediction accuracy for the simulations was found to be better for the vertical residual stresses rather than the horizontal residual stresses. As XRD method is affected by surface roughness, this could be attributed to the roughness of the top surface [4]. The vertical residual stress profile showed high tensile stress at the lateral surface, transitioning to compressive stresses at a depth of approximately 1 mm as shown in Figure 7.9c. Similarly, the horizontal residual stresses are tensile at the top surface and transition to compression after approximately 25 layers or 1 mm from the top surface. This could be attributed to the high temperature differences at the surfaces that were surrounded by loose powders. It was found that residual stresses induced in Ti-6Al-4V samples were higher than those induced in stainless steel 316L samples. Invar 36 samples had the lowest stress values. This can be attributed to its lower coefficient of thermal expansion.

7.4 Discussion and conclusions

A comparison between Ti-6Al-4V, stainless steel 316L, and Invar 36 in selective laser melting was investigated. The comparison included residual stresses and part distortions using both analytical and experimental findings. Invar 36 had the lowest dimensional distortions and tensile residual stresses of the three materials. The dimensional distortions and residual stresses of stainless steel 316L were lower than those of Ti-6Al-4V. The model can be used to predict the dimensional distortions and residual stresses in complex designs of any of the three materials under optimal SLM process parameters, which could not be measured experimentally.

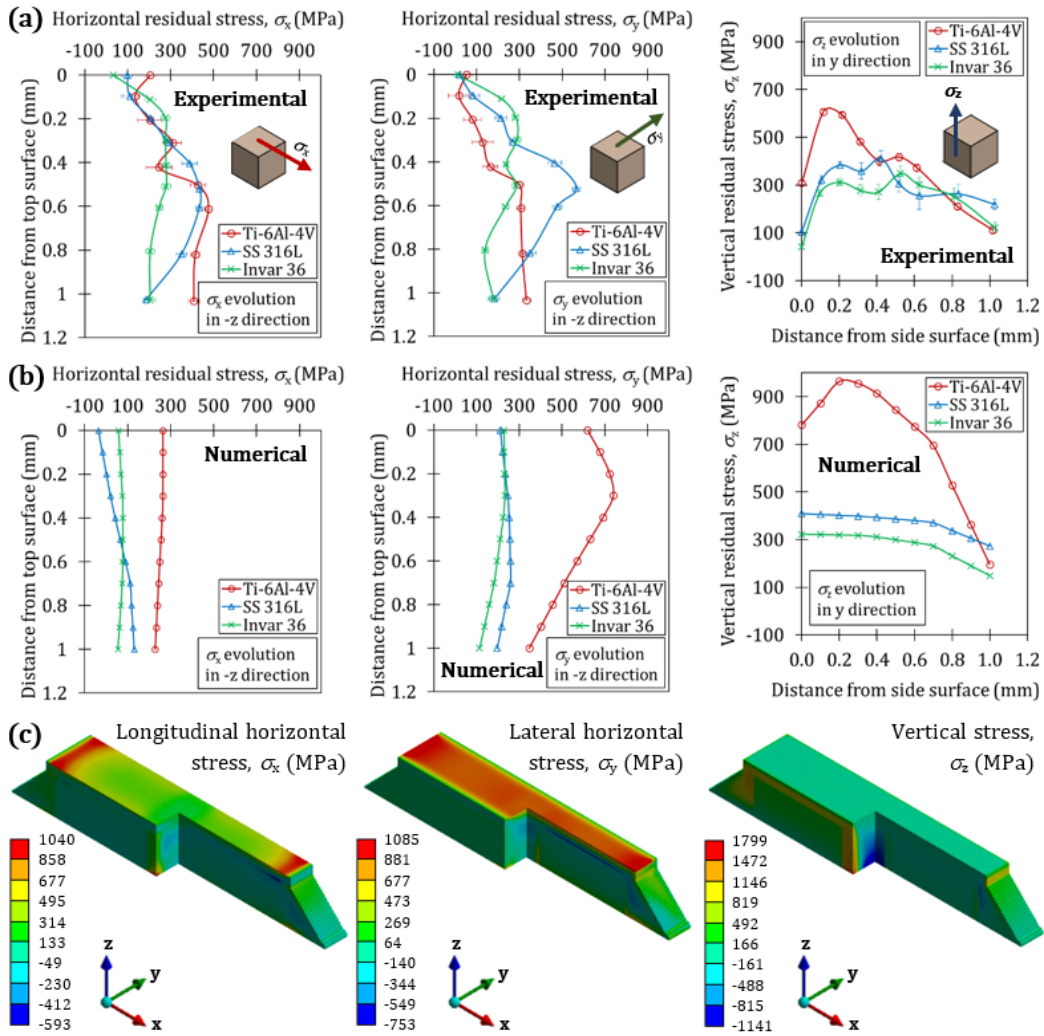


Figure 7.9: (a-b) Experimental and numerical evolutions of longitudinal horizontal, lateral horizontal, and vertical residual stresses (σ_x , σ_y , σ_z), (c) residual stress profiles of Ti-6Al-4V.

A key research objective of this paper was to investigate, contrast, and assess the mechanisms of residual stresses induced during selective laser melting. Two main properties affect the thermal stresses: (i) coefficient of thermal expansion, CTE and (ii) thermal diffusivity, D_T . Table 7.3 shows the thermal properties of the three alloys. The thermal diffusivity of the material, Equation (7.9), is important. The higher the thermal

diffusivity, the quicker the heat moves through the material reducing its thermal stresses, Equation (7.2). It is a material property which governs how quickly heat conducts through the material, and thus how temperature uniformity is established.

$$D_T = \frac{k}{\rho C_p} \tag{7.9}$$

where D_T is thermal diffusivity in (m^2/s), ρ is bulk density in (kg/m^3), C_p is specific heat capacity in ($J/kg.K$), k is thermal conductivity in ($W/m.K$).

Table 7.3: Thermal properties at room temperature.

Property (unit)	Ti-6Al-4V	Steel 316L	Invar 36
Linear CTE, α_T ($\mu m/m.^{\circ}C$)	8.6	16	1.3
Thermal diffusivity, D_T (mm^2/s)	2.9	3.5	2.5

Invar 36 has a much lower CTE which resulted in the lowest thermal stresses, and thus residual stresses. Although the CTE of stainless steel 316L is higher than that of Ti-6Al-4V, they are of the same order of magnitude and stainless steel 316L exhibited lower stresses than Ti-6Al-4V. This is likely due to the higher thermal diffusivity of stainless steel 316L which allows for the heat to dissipate faster through the material ensuring a lower temperature differential in the part, and consequently lower thermal stress. This analysis concerns dimensional distortions and residual stresses of the three materials when produced at the optimal process parameters. Producing these materials at any other process conditions could cause void formation, spatter generation, or evaporative compositional change which would require the inclusion of melt pool physics in the numerical modelling [24].

7.5 References

- [1] Bourell, D. *et al.*, "Materials for additive manufacturing," *CIRP Annals*, vol. 66, no. 2, pp. 659-681, 2017.
- [2] Schmutzler, C., Stiehl, T. H., and Zaeh, M. F., "Empirical process model for shrinkage-induced warpage in 3D printing," *Rapid Prototyping Journal*, 2019.
- [3] Van Hooreweder, B. and Kruth, J.-P., "Advanced fatigue analysis of metal lattice structures produced by Selective Laser Melting," *CIRP Annals*, vol. 66, no. 1, pp. 221-224, 2017.
- [4] Mercelis, P. and Kruth, J. P., "Residual stresses in selective laser sintering and selective laser melting," *Rapid Prototyping Journal*, vol. 12, no. 5, pp. 254-265, 2006.
- [5] Han, J. *et al.*, "Microstructure and mechanical property of selective laser melted Ti6Al4V dependence on laser energy density," *Rapid Prototyping Journal*, vol. 23, no. 2, pp. 217-226, 2017.
- [6] Ahmad, B., van der Veen, S. O., Fitzpatrick, M. E., and Guo, H., "Residual stress evaluation in selective-laser-melting additively manufactured titanium (Ti-6Al-4V) and inconel 718 using the contour method and numerical simulation," *Additive Manufacturing*, vol. 22, pp. 571-582, 2018.
- [7] Yakout, M., Elbestawi, M. A., and Veldhuis, S. C., "Density and mechanical properties in selective laser melting of Invar 36 and stainless steel 316L," *Journal of Materials Processing Technology*, vol. 266, pp. 397-420, 2019.
- [8] Armentani, E., Esposito, R., and Sepe, R., "The effect of thermal properties and weld efficiency on residual stresses in welding," *Journal of Achievements in Materials and Manufacturing Engineering*, vol. 20, no. 1-2, pp. 319-322, 2007.
- [9] Shiomi, M., Osakada, K., Nakamura, K., Yamashita, T., and Abe, F., "Residual Stress within Metallic Model Made by Selective Laser Melting Process," *CIRP Annals*, vol. 53, no. 1, pp. 195-198, 2004.
- [10] Furumoto, T., Ueda, T., Alkahari, M. R., and Hosokawa, A., "Investigation of laser consolidation process for metal powder by two-color pyrometer and high-speed video camera," *CIRP Annals*, vol. 62, no. 1, pp. 223-226, 2013.
- [11] Thompson, M. K. *et al.*, "Design for Additive Manufacturing: Trends, opportunities, considerations, and constraints," *CIRP Annals*, vol. 65, no. 2, pp. 737-760, 2016.
- [12] Papadakis, L., Loizou, A., Risse, J., and Schrage, J., "Numerical Computation of Component Shape Distortion Manufactured by Selective Laser Melting," *Procedia CIRP*, vol. 18, pp. 90-95, 2014.

- [13] Li, C., Liu, J. F., Fang, X. Y., and Guo, Y. B., "Efficient predictive model of part distortion and residual stress in selective laser melting," *Additive Manufacturing*, vol. 17, pp. 157-168, 2017/10/01/ 2017.
- [14] Mugwagwa, L., Dimitrov, D., Matope, S., and Yadroitsev, I., "Influence of process parameters on residual stress related distortions in selective laser melting," *Procedia Manufacturing*, vol. 21, pp. 92-99, 2018/01/01/ 2018.
- [15] Liu, Z. Y., Li, C., Fang, X. Y., and Guo, Y. B., "Energy Consumption in Additive Manufacturing of Metal Parts," *Procedia Manufacturing*, vol. 26, pp. 834-845, 2018.
- [16] Wang, Y., Kamath, C., Voisin, T., and Li, Z., "A processing diagram for high-density Ti-6Al-4V by selective laser melting," *Rapid Prototyping Journal*, vol. 24, no. 9, pp. 1469-1478, 2018.
- [17] Yakout, M., Elbestawi, M. A., and Veldhuis, S. C., "A study of thermal expansion coefficients and microstructure during selective laser melting of invar 36 and stainless steel 316L," *Additive Manufacturing*, vol. 24, pp. 405-418, 2018.
- [18] Yakout, M., Elbestawi, M. A., and veldhuis, S. C., "A study of the relationship between thermal expansion and residual stresses in selective laser melting of Ti 6Al 4V," *under review*, 2019.
- [19] Yakout, M., Cadamuro, A., Elbestawi, M. A., and Veldhuis, S. C., "The selection of process parameters in additive manufacturing for aerospace alloys," *The International Journal of Advanced Manufacturing Technology*, vol. 92, no. 5-8, pp. 2081-2098, 2017.
- [20] Yakout, M., Elbestawi, M. A., and Veldhuis, S. C., "On the characterization of stainless steel 316L parts produced by selective laser melting," *The International Journal of Advanced Manufacturing Technology*, journal article vol. 95, no. 5-8, pp. 1953-1974, March 01 2018.
- [21] Li, C., Guo, Y., Fang, X., and Fang, F., "A scalable predictive model and validation for residual stress and distortion in selective laser melting," *CIRP Annals*, vol. 67, no. 1, pp. 249-252, 2018.
- [22] Incropera, F. P., DeWitt, D. P., Bergman, T. L., and Lavine, A. S., *Fundamentals of Heat and Mass Transfer*, 6th ed. John Wiley, 2007.
- [23] Bugatti, M. and Semeraro, Q., "Limitations of the inherent strain method in simulating powder bed fusion processes," *Additive Manufacturing*, vol. 23, pp. 329-346, 2018/10/01/ 2018.
- [24] Furumoto, T., Egashira, K., Munekage, K., and Abe, S., "Experimental investigation of melt pool behaviour during selective laser melting by high speed imaging," *CIRP Annals*, vol. 67, no. 1, pp. 253-256, 2018/01/01/ 2018.

Chapter 8

Conclusions and Closing Remarks

Since its discovery in 1920, Invar 36 has gained considerable popularity in the aerospace industry because of its low coefficient of thermal expansion. It is a 36% nickel-iron alloy that has been used for applications that require high dimensional stability when the temperature changes, such as in radio and electronic devices, aircraft control systems, optical devices, etc. Stainless steel 316L has an advantage over other stainless steels because it contains nickel and molybdenum elements that increase its corrosion resistance. Furthermore, the relatively low carbon percentage enhances its welding characteristics. For example, turbine blades have been produced using materials that have high temperature resistance, corrosion resistance, fatigue strength, tensile strength, and bending strength.

This thesis contributes to the process-structure-property relationships in selective laser melting of Invar 36, stainless steel 316L, and Ti-6Al-4V. Both Invar 36 and stainless steel 316L materials have a single-phase austenite (γ -Fe) crystal structure, but Ti-6Al-4V have columnar β grain boundary and acicular α/α' microstructures. While wrought Invar 36 has low coefficient of thermal expansion ($1.3 \mu\text{m}/\text{m}\cdot^\circ\text{C}$) and low thermal diffusivity ($2.5 \text{ mm}^2/\text{s}$), stainless steel 316L has high coefficient of thermal expansion ($16 \mu\text{m}/\text{m}\cdot^\circ\text{C}$) and high thermal diffusivity ($3.5 \text{ mm}^2/\text{s}$). Although Ti-6Al-4V has a high coefficient of thermal expansion ($8.6 \mu\text{m}/\text{m}\cdot^\circ\text{C}$), its thermal diffusivity ($2.9 \text{ mm}^2/\text{s}$) is low compared to

stainless steel 316L. Accordingly, the three alloys were chosen in this study. By studying the selective laser melting of Invar 36, stainless steel 316L, Ti-6Al-4V at various process parameters based on full factorial design of experiments, it was found that:

1. A brittle-ductile transition energy density, E_T , exists for each material (52.1 J/mm³ for Invar 36, 62.5 J/mm³ for stainless steel 316L, and 65 J/mm³ for Ti-6Al-4V).
2. A critical energy density, E_C , exists for each material (86.8 J/mm³ for Invar 36, 104.2 J/mm³ for stainless steel 316L, and 86.8 J/mm³ for Ti-6Al-4V).
3. Below E_T , brittle fracture was observed in the parts because of void formation due to either gas pores or balling phenomenon or discontinuous melt tracks. These voids caused a reduction in the coefficient of thermal expansion and an increase in the magnetic dipole moment. The part density increases when the laser energy density increases, until reaching a certain limit associated with melting (E_C).
4. Between E_T and E_C , the parts showed stable melting, continuous beads, and homogeneous melt tracks. These parts had the highest density and toughness, but medium residual stresses due to thermal history.
5. Above E_C , the chemical compositions of the Invar 36 and stainless steel 316L parts showed vaporization of some of the alloying elements that have low boiling temperatures. This vaporization caused a reduction in the manganese, chromium, and nickel concentrations accompanied with increased concentrations of molybdenum, silicon, and iron. Since silicon and molybdenum have very low thermal expansion, a reduction in the coefficient of thermal expansion of the SLM parts was measured. These parts showed less toughness, density, and very high internal residual stresses. No vaporization was observed in the Ti-6Al-4V parts. In addition, high residual stresses and large part distortions were found above the critical laser energy density.

It was concluded that any combination of process parameters that can generate the critical energy density would provide a stable melting. The residual stresses were mainly induced during the selective laser melting process by either thermal stresses or phase transformation. An optimum range of process parameters was established for each of the three materials. Martensitic phase transformation was not observed, and less residual stress was induced when producing parts at process conditions that generate laser energy densities below the critical laser energy density. A comparison between Invar 36, stainless steel 316L, and Ti-6Al-4V in selective laser melting was investigated.

Two main properties affect the thermal stresses: (i) coefficient of thermal expansion, CTE and (ii) thermal diffusivity. The thermal stresses increase by increasing the CTE of the material. However, the higher the thermal diffusivity, the quicker the heat moves through the material reducing its thermal stresses. It is a material property which governs how quickly heat conducts through the material, and thus how temperature uniformity is established.

Invar 36 has a much lower CTE which resulted in the lowest thermal stresses, and thus residual stresses. Although the CTE of stainless steel 316L is higher than that of Ti-6Al-4V, they are of the same order of magnitude and stainless steel 316L exhibited lower stresses than Ti-6Al-4V. This is likely due to the higher thermal diffusivity of stainless steel 316L which allows for the heat to dissipate faster through the material ensuring a lower temperature differential in the part, and consequently lower thermal stress. This analysis concerns dimensional distortions and residual stresses of the three materials when produced at the optimal process parameters.

During the selective laser melting of stainless steel 316L at the same process parameters but at different location on the build plate, it was found that:

1. At the center of the build plate, some alloying elements microsegregated and some particles were ejected from the melting pool and converted into soot. This may occur at the center of the build plate due to the built-up energy originating from the surrounding parts. This built-up energy also caused a martensitic transformation in the parts produced, which induced a high amount of residual stresses.
2. At the side of the build plate, the wettability of the molten metal decreases, resulting in the occurrence of a balling phenomenon on the surface. The balling phenomenon has two effects: (i) the molten metal will not be able to complete the scan track with full melting and (ii) the profile error will be affected, causing geometrical distortions in the parts.
3. The temperature gradient during the melting process will cause thermal stresses during the process. These thermal stresses are one of the main causes for residual stresses in the parts produced.

In addition, a coupled thermal-mechanical finite element module (i.e., ANSYS© 19.2 Workbench Additive) was used to predict residual stresses and part distortions during selective laser melting of these three alloys. The model does not count for void formation, spatter generation, or evaporative compositional change which would require the inclusion of melt pool physics in the numerical modelling. This part is considered for future work. In this study, a pyrometer and high-speed camera were used to identify the thermal cycles during the process. However, the online monitoring and control of process parameters during the selective laser melting process of aerospace alloys is also considered for future work.